2008

Experimental and theoretical investigations in rare earth-triel-tetrel polar intermetallic systems: composition-structure-properties relationships

Tae-soo You
Iowa State University

Experimental and theoretical investigations in rare earth-triel-tetrel polar intermetallic systems: Composition-structure-properties relationships

by

Tae-Soo You

A dissertation submitted to the graduate faculty

in partial fulfillment of the requirements for the degree of

DOCTOR OF PHILOSOPHY

Major: Inorganic Chemistry

Program of Study Committee:
Gordon J. Miller, Major Professor
John D. Corbett
L. Keith Woo
Victor S.-Y. Lin
Theresa Windus

Iowa State University

Ames, Iowa

2008

To my beloved wife Hyun-Jung

and

parents

"Be anxious for nothing, but in everything by prayer and supplication with thanksgiving let your requests be made known to God. And the peace of God, which surpasses all comprehension, will guard your hearts and your minds in Christ Jesus."

- Philippians 4:6 - 7

TABLE OF CONTENTS

CHAPTER 1

Introduction and Motivation

1.1 Introduction

One of the major goals of solid state chemists has been to achieve a comprehensive understanding of the interrelationships among stoichiometry, crystal structure, and physical properties of solid state compounds.[1-3] Based on fundamental understanding of these relationships, we can create intermetallic materials which show precisely designed crystal structures with properties specifically tuned for certain purposes. Intermetallic compounds are basically chemical substances formed when two or more metallic elements combine with definite compositions.[4] These compounds typically show smaller heats of formation (ca. −50 to −10 kJ/mol) than those of salts or polymeric compounds (ca. −500 to −1000 kJ/mol) and frequently show a homogeneity width.[4] The combination of metallic elements with different atomic sizes, electronic configurations, and electronegativities results in a large collection of intermetallic compounds with known or novel structure types.[5]

There exist several schemes to classify these observed intermetallic structure types and explain their structural features based on the idea of valence electron concentration per atom (*vec*). Two most thoroughly investigated intermetallic systems using this idea are the Hume-Rothery electron phases and Zintl phases. The Hume-Rothery phases represent intermetallic compounds which correspond to $1 < vec < 2$,[6] whereas Zintl phases include compounds whose structures are determined by the octet rule and correspond to $vec > 4$ for the electronegative components. The *vec* is determined in two different ways depending on the intermetallic phase as follow:

a) Hume-Rothery phases (e^-/atom): The *vec* is the ratio of the total number of valence electrons contributed by all atom species present to the total number of all atoms per formula.

b) Zintl phases (e^-/electronegative atom): The *vec* is the ratio of the total number of valence electrons contributed by all atom species present to the total number of electronegative atoms per formula.

There is another class of intermetallics, which is considered as an intermediate between Hume-Rothery phases and Zintl phases. This class of compounds is polar intermetallics. Since these three classes of compounds are fundamentally correlated to my doctoral research and frequently referred in this dissertation, a brief description of each phase is shown below.

Hume-Rothery Phases

The Hume-Rothery phases can be classified as intermetallic compounds which correspond to a narrow range of *vec* between 1 and 2. This class of compounds is composed of late transition metals (Group 8-12) through the post-transition metals, and their structure types are determined by the average valence electron concentration per atom. For instance, compounds adopting the β-brass structure with the body centered cubic structure (b.c.c.), such as CuZn, Cu_3Al and Cu_5Sn, have the ratio of valence electrons to atoms of 3:2 (*vec* = 1.5).[7] On the other hand, compounds forming γ-brass structure in the Cu-Zn and Cu-Al series, such as Cu_5Zb_8, Cu_9Al_4 and $Cu_{31}Sn_8$, show the ratio of valence electrons to atoms of 21:13 (*vec* = 1.61).[8] Moreover, many binary compounds, which contain Cu, Ag or Au, adopt the ε-phase with the hexagonal closest packed (h.c.p) structure and show the ratio of valence electrons to atoms of 7:4 (*vec* = 1.75).[9] Structures of the Hume-Rothery phases are more complex than those of corresponding elements, and the different atomic sizes of the elements provide higher packing efficiencies for these compounds.[10]

Table 1. Summary of Hume-Rothery phases with $1.0 < vec < 2.0$[11]

Phase Type	Structure	*vec* range
α	f.c.c.	1.0-1.42
β	b.c.c.	1.36-1.59
μ	cubic	1.40-1.54
γ	b.c.c.	1.54-1.70
δ	cubic	1.55-2.00
ξ	h.c.p.	1.32-1.83
ε	h.c.p.	1.65-1.89
η	h.c.p.	1.93-2.0

Moreover, Hume-Rothery phases frequently show homogeneity widths, which are finite ranges in composition for a single phase. Table 1 summarizes the structure types with corresponding ranges in *vec* of Hume-Rothery phases.

Zintl Phase

In 1929, Eduard Zintl published one simple, but quite significant note after he discovered intermetallic compounds that did not behave like typical Hume-Rothery phases, but rather showed salt-like properties, such as higher melting points than either elemental component, high heats of formation, poor conductivities and greater brittleness than normal metal alloys.[12] Although the widely-known Hume-Rothery rules had revealed the correlation between structure and valence electron concentration for many intermetallic phases, many other intermetallic compounds that Zintl investigated could not be rationalized using the Hume-Rothery rules. Zintl attributed these unusual properties to the electron transfer occurring from the electropositive active atoms to the electronegative atoms. NaTl is an excellent example (see Figure 1) of Zintl phases in which the electron transfer occurs from the electropositive Na atoms to the electronegative Tl atoms resulting in the formula of $Na^{+}Tl^{-}$.[13] Therefore, this structure can be described as a combination of tetravalent Tl^{-} anions forming a diamond-like three-dimensional network and the void-filling Na^{+} cations.

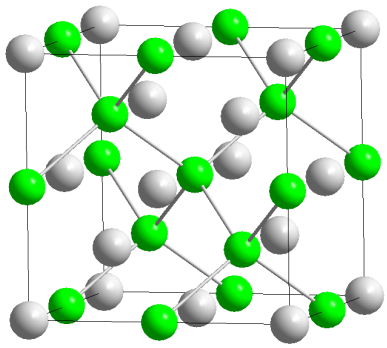

Figure 1. Crystal structure of NaTl. Na: gray; Tl: green.

As the "Zintl concept" became widely recognized, solid state chemists have been synthesizing and characterizing numerous intermetallic compounds to probe their unusual

salt-like properties. Intermetallic Zintl phases offer a large collection of structures and interesting electronic properties to investigate[14-16] and can be classified as an intermediate between typical intermetallic compounds and classical ionic compounds. Zintl phases are typically composed of electropositive elements, such as alkali or alkaline-earth metals (Group 1, 2) or rare-earth metals, and electronegative elements, such as post-transition metals (Group 13-15). They adopt closed-shell electronic configurations and follow the Zintl-Klemm electron counting rules,[17-19] which involve formal electron transfer from electropositive elements to electropositive elements.[20] Moreover, because of the closed-shell configuration, Zintl phases typically show diamagnetic and semiconducting characteristics. However, they can be differentiated from typical semiconductors by the distinct role of the electropositive elements.[21] Electropositive elements in Zintl phases formally donate electrons to electronegative elements, which form the polyanion networks using covalent bonds, and are not participated in the covalent structures, but rather involved in ionic interaction with anions.[12]

Although most Zintl phases are semiconductors, many recent reports indicate that metallic behavior is also observed when there is substantial "cation covalency"[12,21], which indicates a covalency between the empty *d*-states of cationic elements and the occupied *p*-states of anionic elements. One such example is $EuGe_2$ (Figure 2, left), which has divalent Eu atoms and shows metallic behavior with antiferromagnetic ordering at ca. 50 K[22]. The ten-electron $[Ge_2]^{2-}$ substructure form a puckered three-bonded, two-dimensional nets which stack in an eclipsed fashion along the *c*-axis with Eu^{2+} sitting above and below these puckered hexagonal rings. According to the Zintl-Klemm formalism,[20,23] this three-bonded, two-dimensional net with local trigonal pyramidal environments are well suited for five valence electrons per Ge atom, i.e., "Ge^{-}." One theoretical study[22] showed that Eu 6*s* and 5*d* orbitals drop below the Fermi level through Eu-Ge orbital interactions and provide the rationale for the metallic character.

$EuGa_2$ is another example of a metallic Zintl phase (Figure 2, right), which adopts the orthorhombic KHg_2-type structure with a four-bonded, three-dimensional net $[Ga_2]^{2-}$ and satisfies the Zintl-Klemm formalism. This eight-electron network shows optimized Ga-Ga

bonding and is intrinsically metallic due to the presence of four-membered rings propagating along the *b*-axis.[24]

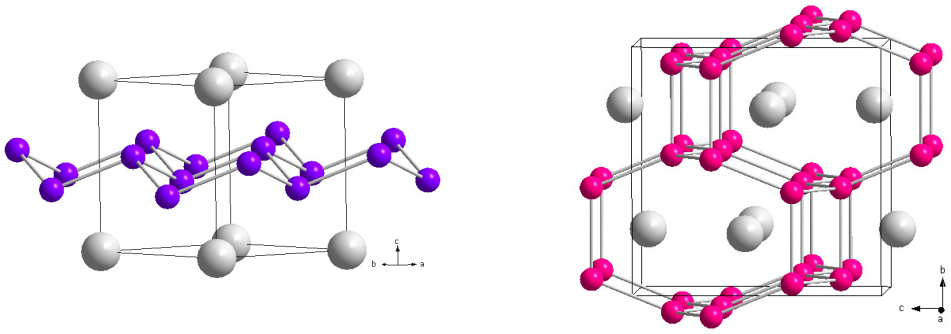

Figure 2. Crystal structure of $EuGe_2$ (left) and $EuGa_2$ (right). Eu: gray; Ge: purple; Ga: red.

Polar Intermetallics

This class of compounds consists of electropositive elements, typically from one of the first three groups of the Periodic Table, including the rare-earth elements, combined with the more electropositive metals or semimetals found near the end and immediately following the transition series. The electronegative elements form structural fragments that often conform to simple electron counting rules, such as the Zintl-Klemm formalism,[20,21,25] and give rise to an electronic structure characterized by a pseudogap in the electronic density of states (DOS) curve and optimized orbital interactions at the Fermi level.[12] These orbital interactions are evaluated by the crystal orbital Hamilton population (COHP) analysis which allows states to be identified according to bonding, nonbonding, or antibonding character of the interatomic orbital interactions.[26] On the other hand, the electropositive metals act like cations, which simply donate valence electrons to the electronegative components as in classical valence compounds or Zintl phases. However, in polar intermetallic compounds the electron transfer is not the full complement of valence electrons, but it provides "lattice stabilization" via orbital interactions between cation-anion.[21,26] The presence of the pseudogap at the Fermi level can lead to potentially interesting physical properties, especially if rare-earth metals serve as the active metal because of partially filled 4*f* bands.[27] In general, polar intermetallics can be considered as a bridge compounds between classical intermetallic

compounds on the one side, e.g., Hume-Rothery phases and Laves phases, and Zintl phases on the other side.[20,21,25]

1.2 Preview of Research Project

In my research, I have systematically investigated the Eu($M_{1-x}M'_x$)$_2$ phases, where *M* and *M'* are elements from Group 12-14, to study interrelationships among atomic, electronic, and possible magnetic structures in various $[(M_{1-x}M'_x)]^{2-}$ networks by changing either atomic size or valence electron count, or both. Throughout this investigation, I have characterized: 1) the nine-electron series EuGa*Tt* (*Tt* = Si, Ge, Sn) as only atomic sizes were changed by substituting *Tt*; 2) a systematic structural variation within the Eu($Zn_{1-x}Ge_x$)$_2$ series as valence electron count varied by altering stoichiometry; and 3) different structural trends for two isoelectronic Eu($Ga_{1-x}Tt_x$)$_2$ (*Tt* = Si, Ge) series as two controllable factors varied simultaneously. The overall systems covered in this investigation are illustrated in Figure 3. Other parts of my research focused on the coloring problem in the $YMg_{1-x}Zn_{1+x}$ and YMg*Tr* (*Tr* = Al, Ga, In) series, and the phase width and site preferences in the $EuMg_xGa_{4-x}$ series. During these experiments, several different conventional, high-temperature solid-state synthetic methods were carried out to produce the target compounds.

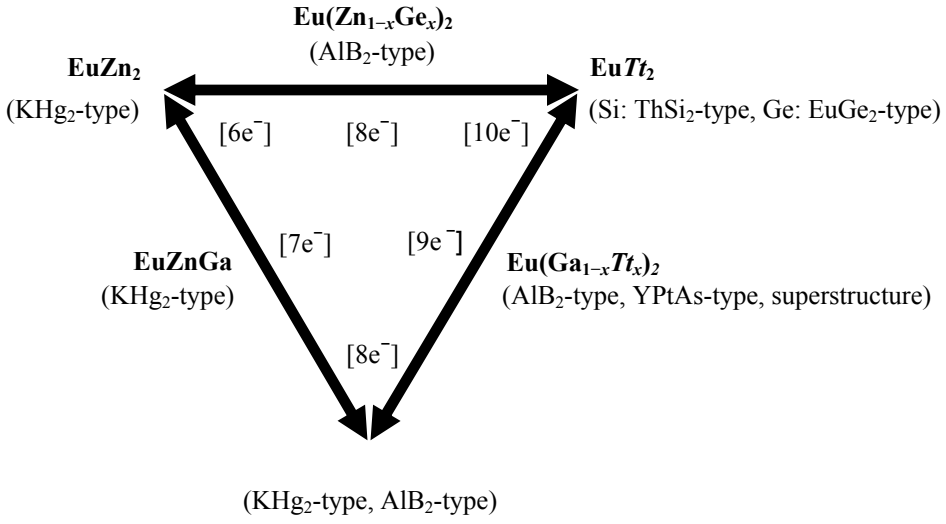

Figure 3. Schematic diagram of the Eu($M_{1-x}M'_x$)$_2$ series

These include arc-melting under an argon atmosphere, induction-melting under vacuum (ca. 5×10^{-5} Torr) and regular melting using a high temperature resistance furnace. For induction-melting and regular melting methods, Ta ampoules, which were sealed by arc-melting and then enclosed in evacuated silica jackets, were used as reaction containers. Annealing procedures were conducted when it was necessary. More detailed experimental procedures are described in the following chapters.

Synthesized compounds were characterized by both powder and single crystal X-ray diffraction, either at low or room temperature, for crystal structure determination as well as by various chemical and physical property measurements, which include energy-dispersive X-ray spectroscopy (EDXS) for chemical compositions, X-ray absorption spectroscopy (XAS) for the oxidation state of the Eu atoms, temperature-dependent magnetic susceptibility for magnetic ordering and the oxidation state of Eu atoms, and temperature-dependent resistivity. Quantum-mechanical calculations were performed to gain insights into the electronic structures and chemical bondings of observed and hypothetical structure models using *ab-initio* methods, such as tight-binding, linear muffin-tin orbital (TB-LMTO) and Vienna *ab-initio* simulation package (VASP) codes, and a semi-empirical method, such as the extended Hückel code. Computational calculation results were carefully analyzed based on the band structure, density of states (DOS), crystal orbital Hamilton population (COHP) curves, electron localization function (ELF) and valence electronic density maps.

This dissertation consists of eight chapters, all of which include experimental and theoretical studies as well as physical property investigations for novel polar intermetallics and Zintl phases. A brief summary of each chapter is described below:

Chapter 2: Experimental and theoretical studies of the EuGa*Tt* (*Tt* = Si, Ge, Sn) series as atomic sizes was changed by substituting *Tt* to see the influence of atomic size for layered structures

Chapter 3: Experimental studies of the $Eu(Zn_{1-x}Ge_x)_2$ ($0 \leq x \leq 1$) series as valence electron count varied by altering stoichiometry, and application and limitation of the Zintl-Klemm concept to understand an observed systematic structural variation

Chapter 4: Theoretical studies for the $Eu(Zn_{1-x}Ge_x)_2$ ($0 \leq x \leq 1$) series using TB-LMTO and VASP codes for observed and hypothetical structure models to understand the phase width and site preferences

Chapter 5: Investigation of the $Eu(Ga_{1-x}Tt_x)$ (*Tt* = Si, Ge; $0 \leq x \leq 1$) series as two controllable factors (atomic sizes and valence electron count) varied simultaneously, and the results comparison with two previously investigated series

Chapter 6: A study of the coloring problem in the $YMg_{1-x}Zn_{1+x}$ and $YMgTr$ (*Tr* = Al, Ga, In) series using experimental and theoretical methods

Chapter 7: Experimental and theoretical investigations for the $EuMg_xGa_{4-x}$ series from the perspective of particular chemical bondings to understand observed phase width and site preferences

References

[1] Westbrook, J. H.; Fleischer, R. L. *Intermetallic Compounds: Principles and Practice*; John Wiley & Sons: West Sussex, **1995,** Vol. 1-2.

[2] Sauthoff, G. *Intermetallics*; VCH Publishers Inc.: New York, **1995**.

[3] Hafner, J.; Hulliger, F.; Jensen, W. B.; Majewski, J. A.; Mathis, K.; Villars, P.; Vogl, P. *The Structure of Binary Compounds*; de Boer, F. R. and Pettifor, D. G., Ed.; Elsevier Science Publishing Company, Inc.: New York, **1989,** Vol. 2.

[4] Gourdon, O.; Gout, D.; Miller, G. J. "Electronic states of intermetallic compounds," *encyclopedia of Condensed Matter Physics*; G. Bassani, G. Liedl, and P. Wyder, Ed.; Elsevier Inc.: Amsterdam, Netherlands, **2005,** 409.

[5] Villars, P.; Calvert, L. D. *Pearson's Handbook of Crystallographic Data for Intermetallic Phase*; 2nd ed Ed.; ASM International, Metals Park OH.; **1991**.

[6] Hume-Rothery, W. *J. Inst. Metals* **1926**, 35.

[7] Hume-Rothery, W. *The Metallic State*, Oxford; Clarendon, **1931**, 328; Hume-Rothery, W.; Raynor, G. V. *The Structure of Metals and Alloys*, London; *The Inst. of Metals,* 1st ed. **1936**.

[8] Bradley, A. J.; Thewlis, J. *Proc. Roy. Soc*. A112, **1926**, 678; Bradley, A. J. *Phil. Mag*. **1926**, *6*, 878.

[9] Westgren, A. F.; Phragmen, G. *Z. Mtallounde* **1926**, *18*, 279.

[10] C.-S. Lee, *Doctoral Dissertation*, **2000**. 2.

[11] Barrett, C.: Massalski, T. B.; *Structure of Metals*, Pergamon Press, 3rd ed. **1980**, 248.

[12] Miller, G. J.; Lee, C.-S.; Choe, W. "Structure and Bonding Around the Zintl Border," *Highlights in Inorganic Chemistry*, Ed. G. Meyer, Wiley-VCH, **2002**, 21-54.

[13] Zintl, E.; Woltersdorf, G. *Z. Elektrochem*. **1935**, *41*, 876.

[14] Zintl, E.; Dullenkopf, W. *Z. Phy. Chem*. **1932**, *B12*, 183.

[15] Zintl, E.; Brauer, G. *Z. Phy. Chem*. **1933**, *B20*, 245.

[16] Zintl, E. *Angew.Chem*. **1939**, *52*, 1.

[17] Schafer, H.; Eisenmann, B.; Muller, W. *Angew. Chem. Intl. Ed. Engl*., **1973**, *12*, 694.

[18] Schafer, H.; Eisenmann, B.; Muller, W. *Rev. Inorg. Chem*. **1981**, *3*, 29.

[19] von Schnering, H. G. *Nova Acta Leopold*., 264, **1985**, *59*, 165.

[20] Miller, G. J. In *Chemistry, Structure, and Bonding of Zintl Phases and Ions*; Kauzlarich, S. M., Ed.; VCH Publishers; New York, **1996,** 1-59.

[21] Klem, M. T.; Vaughy, J. T.; Harp, J.G.; Corbett, J. D. *Inorg.Chem*.**2001**, *40*, 7020.

[22] Bobev, S.; Bauer, E. D.; Thomson, J. D.; Sarrao, J. L.; Miller, G. J.; Eck, B.; Dronskowski, R. *J. Solid State Chem*. **2004**, *177*, 3545.

[23] Nesper, R., *Prog. Solid State Chem*. **1990**, *20*, 1.

[24] Nuspl, G.; Polborn, K.; Evers, J.; Landrum, G.A.; Hoffmann, R. *Inorg.Chem.* **1996**, *35*, 6922-6932.

[25] Schäfer, H. *Ann. Rev. Mater. Sci.* **1985**, *5*, 1.

[26] Gout, D.; Barker, T. J.; Gourdon, O.; Miller, G. J. *Chem. Mater*. **2005**, *17*, 3661-3667.

[27] Gout, D.; Benbow, E.; Gourdon, O.; Miller, G. J. *J. Solid State Chem*. **2003**, *176,* 538−54.

CHAPTER 2

Planar vs. Puckered Nets in the Polar Intermetallic Series EuGa*Tt* (*Tt* = Si, Ge, Sn)

Modified from a paper published in *Inorganic Chemistry*

Tae-Soo You,[2,4] Yuri Grin,[3] and Gordon J. Miller[2,5]

2.1 Abstract

The ternary polar intermetallic compounds EuGa*Tt* (*Tt* = Si, Ge, Sn) have been synthesized and characterized experimentally as well as theoretically. EuGaSi crystallizes in the hexagonal AlB_2-type structure (space group *P6/mmm*, Z = 1, Pearson symbol *hP*3) with randomly distributed Ga and Si atoms on the graphite-type planes; *a* = 4.1687(6) Å, *c* = 4.5543(9) Å. On the other hand, EuGaGe and EuGaSn adopt the hexagonal YPtAs-type structure (space group $P6_3/mmc$, Z = 4, Pearson symbol *hP*12): *a* = 4.2646(6) Å and *c* = 18.041(5) Å for EuGaGe; *a* = 4.5243(5) Å and *c* = 18.067(3) Å for EuGaSn. The three crystal structures contain formally $[GaTt]^{2-}$ polyanionic 3-bonded, hexagonal networks, which change from planar to puckered and exhibit a significant decrease in interlayer Ga-Ga distances as the size of *Tt* increases. Magnetic susceptibility measurements of this series of compounds show Curie-Weiss behavior above 86(5) K, 95(5) K and 116(5) K with the magnetic moments of 7.93μ_B, 7.97μ_B, and 7.99μ_B for EuGaSi, EuGaGe and EuGaSn, respectively, indicating a $4f^7$ electronic configuration (Eu^{2+}) for Eu atoms. X-ray absorption spectra (XAS) are also consistent with these magnetic properties. Electronic structure

---

[1]Reproduced with permission from *Inorganic Chemistry*, 2007, 46, 8801-8811. Copyright 2007 American Chemical Society.

[2]Graduate student and Professor, respectively, Department of Chemistry, Iowa State University

[3] Professor, Max-Planck-Institute für Chemische Physik fester Stoffe, Dresden, Germany

[4] Primary researcher and author

[5] Author for correspondence

calculations supplemented by a crystal orbital Hamilton population (COHP) analysis identifies the synergy between atomic sizes, from both Eu and *Tt* atoms, and the orbital contributions from Eu toward influencing the structural features of EuGa*Tt*. A multi-centered interaction between planes of Eu atoms and the $[GaTt]^{2-}$ layers rather than through-space Ga-Ga bonding is seen in electron localization function (ELF) distributions.

2.2 Introduction

Polar intermetallic compounds offer a growing collection of diverse structures and interesting physical properties to investigate.[1-3] These compounds consist of an electropositive metal, typically from one of the first three groups of the Periodic Table, including the rare-earth elements, combined with the more electronegative metals found around the Zintl line. As a classification of chemical compounds, such phases can be considered as a bridge between intermetallic compounds like Hume-Rothery phases or Laves phases on the one side,[2] and Zintl phases on the other side.[4] Although most Zintl phases are semiconducting, many recent reports indicate that metallic behavior is common when there is substantial "cation covalency".[5,6] One such example is $EuGe_2$, which shows metallic behavior with antiferromagnetic ordering at ca. 50 K and divalent Eu.[7] The ten-electron $[Ge_2]^{2-}$ network forms puckered 3-connected layers stacked in an eclipsed fashion with Eu atoms sitting above/below the puckered six-membered rings. According to the Zintl-Klemm-Busmann electron counting scheme,[4,8] the three-bonded, pyramidal environment surrounding each Ge atom is well suited for five valence electrons per Ge atom, i.e., "Ge^{-}." A previous theoretical study showed that crystal orbitals with substantial Eu 5*d* orbital contributions drop below the Fermi level through Eu-Ge orbital interactions to provide the rationale for its metallic character.[7] Another example is $EuGa_2$, which adopts the orthorhombic KHg_2 structure, with a 3D, 4-connected net $[Ga_2]^{2-}$. The 8-electron network shows optimized bonding and is intrinsically metallic due to the presence of four-membered rings.[9]

As part of an investigation of $Eu(M_{1-x}M'_x)_2$ phases, where M and M′ are elements from Group 12-14, to study the interrelationships among valence electron count, magnetic order and chemical bonding in various $[(M_{1-x}M'_x)_2]^{2-}$ networks, we have characterized the nine-electron series EuGa*Tt* (*Tt* = Si, Ge, Sn). Recent studies on the series of ternary

silicides *AE*GaSi (*AE* = Ca, Sr, Ba),[10] which are isoelectronic to EuGaGe, revealed that these compounds adopt the AlB_2-type structure with no preferred ordering of Ga and Si atoms in the graphite-type network.[11-15] These compounds are related to the superconducting *AE*AlSi (*AE* = Ca and Sr), which are being investigated for their similarities to superconducting MgB_2.[16] As reported herein, puckering of the graphite-type sheet occurs for the heavier tetralides *Tt*, and we discuss the influence of atomic size and electronic factors on the structural features of EuGa*Tt* compounds.

2.3 Experimental

2.3.1 Synthesis and Chemical Analysis.

EuGaSi, EuGaGe and EuGaSn were synthesized from the pure elements in the molar ratio Eu:Ga:*Tt* (*Tt* = Si, Ge, Sn) = 1:1:1; Eu (Ames Laboratory, rod, 99.99%), Ga (Ames Laboratory, ingot, 99.99%), Si (Aldrich, piece, 99.999%), Ge (Alfa, piece, 99.999%) and Sn (Ames Laboratory, ingot, 99.99%). Pellets weighing 1.0 ± 0.2 g and containing stoichiometric mixtures of the corresponding elements were arc-melted under a high purity argon atmosphere on a water-cooled copper hearth, and was re-melted six times after turning to ensure homogeneity. During this procedure, we observed weight losses of ca. 0.4-0.7 weight percent; preparation of these materials in sealed Ta ampoules using either a high-frequency induction furnace or a conventional tube furnace yielded identical products, but crystals extracted from these products were less suitable for subsequent diffraction experiments (see supporting information for further details about preparation methods and characterization of these products). During this series of experiments, we found that $Eu(Ga_{1-x}Si_x)_2$ showed a homogeneity range for the AlB_2-type structure. Thus, eight additional samples with different compositions ($0 \leq x \leq 1$) were prepared to check the range of substitution. Moreover, $Eu(Ga_{1-x}Ge_x)_2$ displays structural sensitivity depending upon the different compositions ($0 \leq x \leq 1$). However, we focus here just on compounds with equiatomic composition; the others will be discussed in a subsequent paper. Based on powder X-ray diffraction patterns for these equiatomic products, EuGaSi and EuGaSn products showed proper crystallinities to obtain accurate lattice parameters and to pursue single crystal X-ray diffraction investigations, whereas the EuGaGe product showed poor crystallinity.

Therefore, only the EuGaGe pellet was wrapped with tantalum foil and annealed at 350 ºC in an evacuated fused silica jacket for one week to improve its crystallinity. After heating, the furnace was turned off and allowed to cool down to room temperature. All three products appear to be stable to exposure to both air and moisture over several weeks. Analysis by energy-dispersive X-ray spectroscopy (EDXS) was conducted on a Hitachi S-2460N variable-pressure scanning electron microscope (SEM) with an Oxford Instruments Link Isis Model 200 X-ray analyzer. The corresponding pure elements were used as standards for intensity references.

2.3.2 Crystal Structure Determination

EuGa*Tt* (*Tt* = Si, Ge, Sn) were characterized by both powder and single crystal X-ray diffraction. Phase purity and lattice parameters were carried out on a Huber G670 Guinier image-plate powder diffraction camera applying monochromatic Cu $K\alpha_1$ radiation (λ = 1.54059 Å). The step size was set at 0.005°, and the exposure time was 2 hours. Data acquisition was controlled via the *in situ* program. The powder pattern of EuGaSn compound showed a trace of Eu_2O_3 impurity. However, the lattice parameters obtained from the Rietveld refinements of the three X-ray patterns using program *Rietica*[17] were in very good agreement to the results of single crystal X-ray diffraction.

For single crystal X-ray diffraction experiments, several silvery plate- and needle-shaped crystals were selected from crushed samples. The crystals were checked for crystal quality by a rapid scan on a Bruker SMART Apex CCD diffractometer with Mo $K\alpha_1$ radiation (λ = 0.71073 Å), and then the best crystals were chosen for further data collection at 293(2) K. Single crystal X-ray diffraction data of EuGaGe and EuGaSn were collected from three sets of 606 frames on a full sphere with 0.3° scans in ω and with an exposure time of 10 sec per frame. Single crystal X-ray diffraction data of EuGaSi were collected on a STOE IPDS diffractometer from two sets of 180 frames with an exposure time of 1 min for each frame. The angular range of 2θ was 4-56° for EuGaGe and EuGaSn and 4-70° for EuGaSi.

Intensities were extracted and then corrected for Lorentz and polarization effects using the *SAINT* program.[18] The program *SADABS*[18] was used for empirical absorption correction. The entire sets of reflections of the three compounds were matched with the

hexagonal crystal system. After further analysis, the space group *P*6/*mmm* was chosen for EuGaSi, whereas $P6_3/mmc$ was selected for EuGaGe and EuGaSn. The structures were solved by direct methods and refined on F^2 by full-matrix least-squares methods using the *SHELXTL* software package.[19] During the refinement process of EuGaGe, the Ga and Ge atoms could not be distinguished because the X-ray scattering factors for Ga and Ge atoms differ by at most 3.1%. Interatomic distances within a unit cell were also not useful to distinguish Ga and Ge atoms because of their similar covalent radii: *r*(Ga) = 1.25 Å and *r*(Ge) = 1.22 Å.[20] However, electronic structure calculations performed on several structural models with different possible Ga and Ge atomic positions indicate that the atomic coordinates reported in Table 2 create the most energetically favorable structure. Details of those calculations are discussed in a subsequent section. In addition, evaluating corresponding displacement parameters indicates preference for the distribution seen in EuGaSn, (see the "Discussion" section below). The chemical composition obtained from EDXS analysis, $Eu_{1.00(1)}Ga_{1.01(2)}Ge_{0.99(3)}$, very well matched the loading composition.

2.3.3 X-ray Absorption Spectroscopy (XAS)

XAS measurements on the Eu L_{III} edge were conducted at the EXAFS beam-line A1 of HASYLAB at DESY (Hamburg, Germany). Samples were ground together with dry B_4C powder before the measurements. Wavelength selection was realized by means of a double-crystal Si(111) monochromator of four crystal modes with digitally stabilized components. The resolution was about 2 eV (FWHM) at the Eu L_{III} edge of 6977 eV. Eu_2O_3 was used as a reference during the measurement.

2.3.4 Magnetic Susceptibility Measurement

Temperature dependent magnetic susceptibility measurements were conducted using a Quantum Design, MPMS-5 SQUID magnetometer. The measured temperature range was 1.8 K−300 K with a magnetic field range of 0.1−5.5 T. Magnetic measurements were carried out on bulk samples (approximately 300 mg) from the same preparations as the one used for powder diffraction experiments.

2.3.5 Computational Details

Tight-binding, linear muffin-tin orbital (TB-LMTO) calculations[21] were carried out in the atomic sphere approximation (ASA) using the Stuttgart program.[28] Exchange and correlation were treated by the local spin density approximation (LSDA).[22] All relativistic effects except spin-orbit coupling were taken into account by using a scalar relativistic approximation.[23]

In the ASA method, space is filled with overlapping Wigner-Seitz (WS) atomic spheres. The symmetry of the potential is considered spherical inside each WS sphere, and a combined correction is used to take into account the overlapping part.[24] The radii of WS spheres were obtained by requiring that the overlapping potential be the best possible approximation to the full potential, and were determined by an automatic procedure.[24] This overlap should not be too large because the error in kinetic energy introduced by the combined correction is proportional to the fourth power of the relative sphere overlap. No empty spheres (ES)[21] were used, but the overlapping maximum was adjusted to fill up the interstitial space in the unit cell of EuGaGe and EuGaSn. The WS radii are as follows: for EuGaSi, Eu = 2.22 Å, Ga = 1.35 Å and Si = 1.44 Å; for EuGaGe, Eu1 = 2.24 Å, Eu2 = 2.14 Å, Ga = 1.45 Å and Ge = 1.49 Å; for EuGaSn, Eu1 = 2.11 Å, Eu2 = 2.09 Å, Ga = 1.62 Å and Sn = 1.77 Å. The basis sets included 6*s*, 6*p* and 5*d* orbitals for Eu; 4*s*, 4*p* and 4*d* orbitals for Ga; 3*s*, 3*p* and 3*d* orbitals for Si; 4*s*, 4*p* and 4*d* orbitals for Ge; 5*s*, 5*p* and 5*d* orbitals for Sn. The Eu 6*p*, Ga 4*d*, Si 3*d*, Ge 4*d* and Sn 5*d* orbitals were treated by the Löwdin downfolding technique;[21-23] and the Eu 4*f* wavefunctions were treated as core functions occupied by 7 electrons. The crystal orbital Hamilton populations (COHP) curves[25] and the integrated COHP values (ICOHPs) were calculated to determine the relative influences of various interatomic orbital interactions. For the computation of electronic densities of states (DOS), band structures and COHP curves, the 4*f* electrons of Eu were treated as core electrons. The *k*-space integrations were performed by the tetrahedron method.[26] The self-consistent charge density was obtained using 210 irreducible *k*-points in the Brillouin zone for the hexagonal cell. The contribution of the nonspherical part of the charge density to the potential was neglected. The spin-polarized calculations have been performed on each structure.

The electron localization function[27a] (ELF, η) was evaluated within the TB-LMTO-ASA program package[28] with an ELF module already implemented. To better understand features of chemical bonding in these phases, a topological analysis of ELF was conducted with the program *Basin*.[29] The integrated electron density in each basin, which is defined by the surface of zero flux in the ELF gradient, analogous to the procedure proposed by Bader for the electron density,[30] provides the basic information of electron counts for each basin, and additionally describes the bonding situation. The software *Amira*[31] was used to visualize ELF distributions.

2.4 Results and Discussion

2.4.1 Structures

EuGa*Tt* (*Tt* = Si, Ge, Sn) crystallize in two different types of structures correlating to the different atomic sizes of *Tt*: (1) the AlB_2-type structure for EuGaSi and (2) the YPtAs-type structure for EuGaGe and EuGaSn. Important crystallographic data, atomic positions, selected interatomic distances and thermal displacement parameters for EuGaSi, EuGaGe and EuGaSn are listed in Tables 1-3.

EuGaSi. EuGaSi adopts a ternary version of the hexagonal AlB_2-type structure with a honeycomb-like $^{2}_{\infty}[GaSi]$ planar layer as shown in Figure 1; the separation between adjacent planes is 4.5543(9) Å. During this investigation, we observed that EuGaSi is one example of a homogeneity range, $Eu(Ga_{1-x}Si_x)_2$ with x = 0.165-0.862, adopting the AlB_2-type structure.[32] Ga and Si atoms randomly occupy the 2*d* site in the unit cell. Therefore, many different local environments at each atomic site are possible. If Ga-Si interactions are preferred over Ga-Ga and Si-Si interactions, then we would expect to observe a superstructure with a *c*-axis length twice the observed value[33] and space group $P6_3/mmc$ as in ZrBeSi.[34] However, we find no additional X-ray reflections to suggest a doubling of the *c*-axis. For the possibility of in-plane ordering, the unit cell can be refined in the space group $P\bar{6}m2$,[34] which is the highest *translationengleiche* subgroup of *P*6/*mmm* in which the 2*d* site of *P*6/*mmm* splits into two distinct sites, 1*d* and 1*f*. However, for EuGaSi in $P\bar{6}m2$, each site was refined as the same 50:50 mixture of Ga and Si atoms.

Table 1. Crystallographic data for EuGa*Tt* (*Tt* = Si, Ge, Sn).

	EuGaSi	EuGaGe	EuGaSn
Formula mass (g mol^{-1})	249.77	294.27	340.37
Space group	*P*6/*mmm* (no.191)	*P*6$_3$/*mmc* (no.194)	*P*6$_3$/*mmc* (no.194)
Lattice parameters (Å)	*a* = 4.1687(6)	*a* = 4.2646(6)	*a* = 4.5243(5)
	c = 4.5543(9)	*c* = 18.041(5)	*c* = 18.067(3)
Volume (Å^3)	68.541(19)	284.15(9)	320.27(7)
Z	1	4	4
Density calc. (g cm^{-3})	6.051	6.879	7.059
Diffractometer	STOE IPDS	SMART Apex	SMART Apex
2θ range (º)	4.48-69.64	4.48-55.94	5.0-55.88
Index ranges	$-6 \le h \le 6$, $-6 \le k \le 6$, $-6 \le l \le 7$	$-5 \le h \le 5$, $-5 \le k \le 5$, $-23 \le l \le 23$	$-5 \le h \le 5$, $-5 \le k \le 5$, $-20 \le l \le 23$
Reflections collected	1988	2203	1713
Independent reflections	86 [R_{init} = 0.076]	169 [R_{init} = 0.043]	185 [R_{init} = 0.030]
Data/Refined parameters	86/7	169/12	185/11
Goodness-of-fit on F^2	1.185	1.259	1.297
Final R indices [$I > 2\sigma(I)$]	R1 = 0.015, wR2 = 0.032	R1 = 0.025, wR2 = 0.050	R1 = 0.029, wR2 = 0.057
R indices (all data)	R1 = 0.015, wR2 = 0.032	R1 = 0.032, wR2 = 0.053	R1 = 0.036, wR2 = 0.059
Largest diff. peak and hole (e$^-$/Å^3)	0.844 / –0.705	0.800 / –0.969	1.496 / –2.123

Table 2. Atomic coordinates and equivalent displacement parameters for EuGa*Tt* (*Tt* = Si, Ge, Sn).

Atom	Wyckoff position	*x*	*y*	*z*	U_{eq} [a]
			EuGaSi		
Eu	1*a*	0	0	0	0.010(1)
Ga/Si	2*d*	1/3	2/3	1/2	0.017(1)
			EuGaGe		
Eu(1)	2*a*	0	0	0	0.010(1)
Eu(2)	2*b*	0	0	1/4	0.010(1)
Ga	4*f*	2/3	1/3	0.1467(1)	0.014(1)
Ge	4*f*	1/3	2/3	0.1142(1)	0.010(1)
			EuGaSn		
Eu(1)	2*a*	0	0	0	0.013(1)
Eu(2)	2*b*	0	0	1/4	0.010(1)
Ga	4*f*	2/3	1/3	0.1620(1)	0.014(1)
Sn	4*f*	1/3	2/3	0.1168(1)	0.011(1)

[a] U_{eq} is defined as one third of the trace of the orthogonalized U_{ij} tensor.

Table 3. Selected interatomic distances, bond and torsion angles for EuGa*Tt* (*Tt* = Si, Ge, Sn).

	EuGaSi		EuGaGe	EuGaSn
Ga-*Tt* (Å)	2.4068(3)		2.5312(7)	2.7369(7)
Ga-Ga (Å)	4.5543(9)		3.726(1)	3.178(1)
Eu-Ga/Si (Å)	3.3133(4)	Eu(1)-Ga (Å)	3.615(1)	3.924(1)
		Eu(1)-*Tt* (Å)	3.210(1)	3.3585(7)
		Eu(2)-Ga (Å)	3.088(1)	3.057(1)
		Eu(2)-*Tt* (Å)	3.474(1)	3.5512(8)
Ga-*Tt*-Ga (°)	120.0		114.79(4)	111.49(4)
Torsion Angle (Ga-*Tt*-Ga-*Tt*; °)	0		43.8	54.7

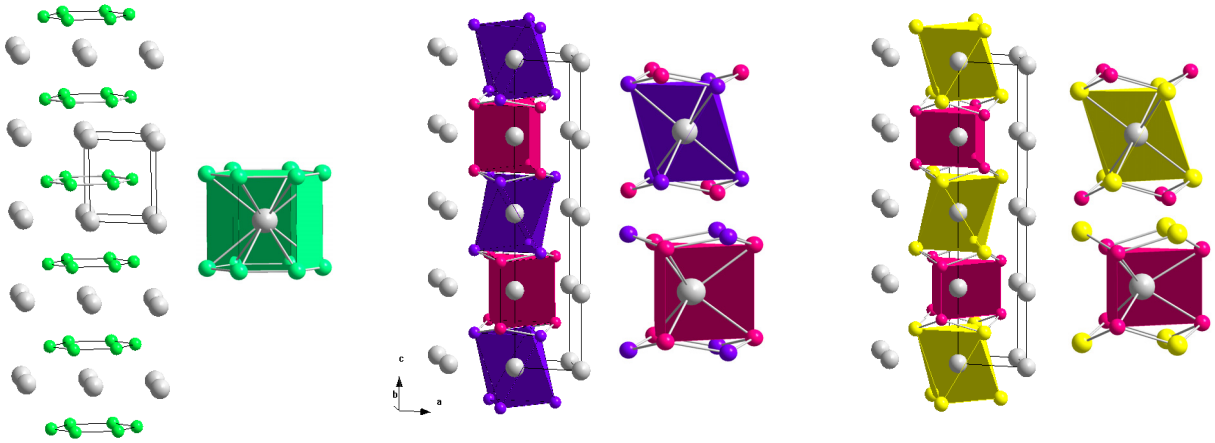

Figure 1. Crystal structures of EuGaSi, EuGaGe and EuGaSn and coordination environments at the Eu atoms. Eu: gray; Ga/Si: green; Ga: red; Ge: purple; Sn: yellow.

The U_{33}/U_{11} ratio for the Ga/Si mixed site is large, which can indicate a tendency toward puckering the 6^3 anionic nets. To check the possibility of puckering, we refined the structure in space group $P\bar{3}m1$, which allowed the z-coordinate of the Ga/Si sites to refine: the result is $z = 0.5002(3)$. Therefore, we describe the unit cell of EuGaSi in the space group *P6/mmm* where Ga and Si atoms are randomly distributed within the honeycomb net. Each Ga or Si atom is surrounded by three other main group atoms at the distance of 2.4068(3) Å. This distance is shorter than the sum of covalent radii of Ga and Si, which is 2.42 Å (r(Ga) = 1.25 Å, r(Si) = 1.17 Å[20]), implying significant interactions exist within the hexagonal layer.

EuGaGe and EuGaSn. EuGaGe and EuGaSn crystallize in the hexagonal YPtAs type of crystal structure which can be described as a puckered derivative of the AlB_2-type structure (see Figure 1).[35,36] The Ga and Ge/Sn atoms form puckered three-bonded, alternating hexagonal layers. Furthermore, the observed puckering mode locates Ga atoms closer (3.726(1) and 3.178(1) Å, respectively, for EuGaGe and EuGaSn) and Ge/Sn atoms farther to each other between adjacent layers. These Ga-*Tt* distances increase from EuGaGe to EuGaSn

(see Table 3). Thus, as the Ga-*Tt* distance increases within the puckered sheets, the Ga-Ga distance decreases between adjacent sheets.

Since we observed a relatively high U_{33}/U_{11} ratio at the Ga site in EuGaGe, we attempted to refine a structure with a split Ga site. Although we were able to lower the *R* value from 2.45% to 2.40% with two additional parameters, a Hamilton significance test[37] suggested that the decrease of *R* value related to the additional parameters was not a significant improvement. Therefore, in the absence of any other reason to split the Ga site, we will use the originally refined structure.

The indistinguishable atomic positions for Ga and Ge in EuGaGe can be differentiated for Ga and Sn in EuGaSn and agree with total energies obtained from electronic structure calculations. However, we could distinguish Ga and Ge atomic positions based on the differential isotropic thermal displacement parameters, U_{11}, at two 4*f* sites. Refinements of structures with either *only* Ge atoms or *only* Ga atoms at the two 4*f* sites in the asymmetric unit produced smaller U_{11} values at the Ga site than at the Ge site by 25% and 33%, respectively, suggesting lower electron accumulation at the Ga site. However, we observed equal U_{11} values at the two 4*f* sites when we differentiated the Ga and Ge atomic positions as shown in Supplementary Material (Table S2).

There are two distinct coordination environments at the Eu sites, as also shown in Figure 1: Eu(1) is surrounded by an octahedron of six Ge or Sn atoms; whereas Eu(2) is surrounded by six Ga atoms forming a trigonal prism. As listed in Table 3, the nearest neighbor distances of these two Eu coordination polyhedra change in opposing fashion: Eu-Ge/Sn distances for the octahedra increase while Eu-Ga distances in the trigonal prisms decrease from EuGaGe to EuGaSn.

Along the entire EuGa*Tt* series, as the size of the *Tt* atom increases, the torsion angle of the polyanion layer increases indicating the change from planar to moderately puckered, then strongly puckered layers. The torsion angles of the puckered hexagonal layers in EuGaGe and EuGaSn can be compared with several known analogues, such as CaGaGe and SrGaSn.[38] These compounds show increasing torsion angles from 42.20° (CaGaGe) and 43.80° (EuGaGe) to 54.70° (EuGaSn) and 56.07° (SrGaSn) as the size of active metal or *Tt* atom increases (ionic radii: $r(Ca^{2+})$ = 1.06Å, $r(Eu^{2+})$ = 1.12Å, $r(Sr^{2+})$ = 1.27Å; covalent radii:

r(Ge) = 1.22 Å, *r*(Sn) = 1.40Å).[20] In addition, going from EuGaSi to EuGaGe and EuGaSn, the lattice parameter *a* increases whereas the average separation between $^{2}_{\infty}[\mathrm{Ga}Tt]$ sheets, as measured either by *c* for EuGaSi or *c*/4 for EuGaGe and EuGaSn, decreases. The interlayer Ga-Ga distance between adjacent hexagonal layers significantly decreases as the size of *Tt* atom increases.

For comparison, the gallium monochalcogenides, GaS,[39] GaSe,[40] HT-GaTe,[41] represent a series isoelectronic with Eu$\mathrm{Ga}Tt$ (HT-GaTe is reported as the "high temperature" form; at ambient conditions, the crystal structure of GaTe is monoclinic[42]). These binary compounds adopt structures closely related to the [GaGe] and [GaSn] networks in EuGaGe and EuGaSn, but not the [GaSi] framework in EuGaSi. In $\mathrm{Ga}X$ (*X* = S, Se, Te), however, the $^{2}_{\infty}[\mathrm{Ga}X]$ sheets are significantly more puckered as evidenced by the Ga-*X*-Ga angles (all ca. 100°) and their corresponding torsion angles (all ca 76°). As the size of *X* increases, the Ga-*X* distances increase from 2.332 Å (GaS) to 2.453 Å (GaSe) to 2.612 Å (GaTe), whereas the Ga-Ga separation varies as 2.449 Å (GaS), 2.444 Å (GaSe), and 2.714 Å (GaTe). Therefore, the Ga-*Tt* distances in Eu$\mathrm{Ga}Tt$ fall in a similar range to the Ga-*X* contacts in $\mathrm{Ga}X$, but the corresponding Ga-Ga distances are much longer in the Eu$\mathrm{Ga}Tt$ series. We will explore the chemical bonding issues in Eu$\mathrm{Ga}Tt$ in a subsequent section of this paper.

2.4.2 Magnetic Susceptibilities

Temperature dependent magnetic susceptibilities and reciprocal susceptibilities of all three compounds are measured at 0.1 T and shown in Figure 2. The susceptibility curves show essentially Curie-Weiss behavior in the corresponding paramagnetic regions with ferromagnetic (FM) behavior for EuGaSi and EuGaGe and antiferromagnetic (AFM) behavior for EuGaSn at low temperatures. Magnetization measurements as a function of external field (0-5.5 T) at 2 K confirmed these magnetic ordering characteristics for each compound. Fitting linear $1/\chi$ vs. *T* curves above ca. 120 K give effective magnetic moments to be 7.93(1)μ_B for EuGaSi, 7.97(1)μ_B for EuGaGe, and 7.99(1)μ_B for EuGaSn, moments which are all very close to the value of the Eu^{2+} free ion, 7.94 μ_B, to indicate a $4f^7$ electronic configuration for Eu.

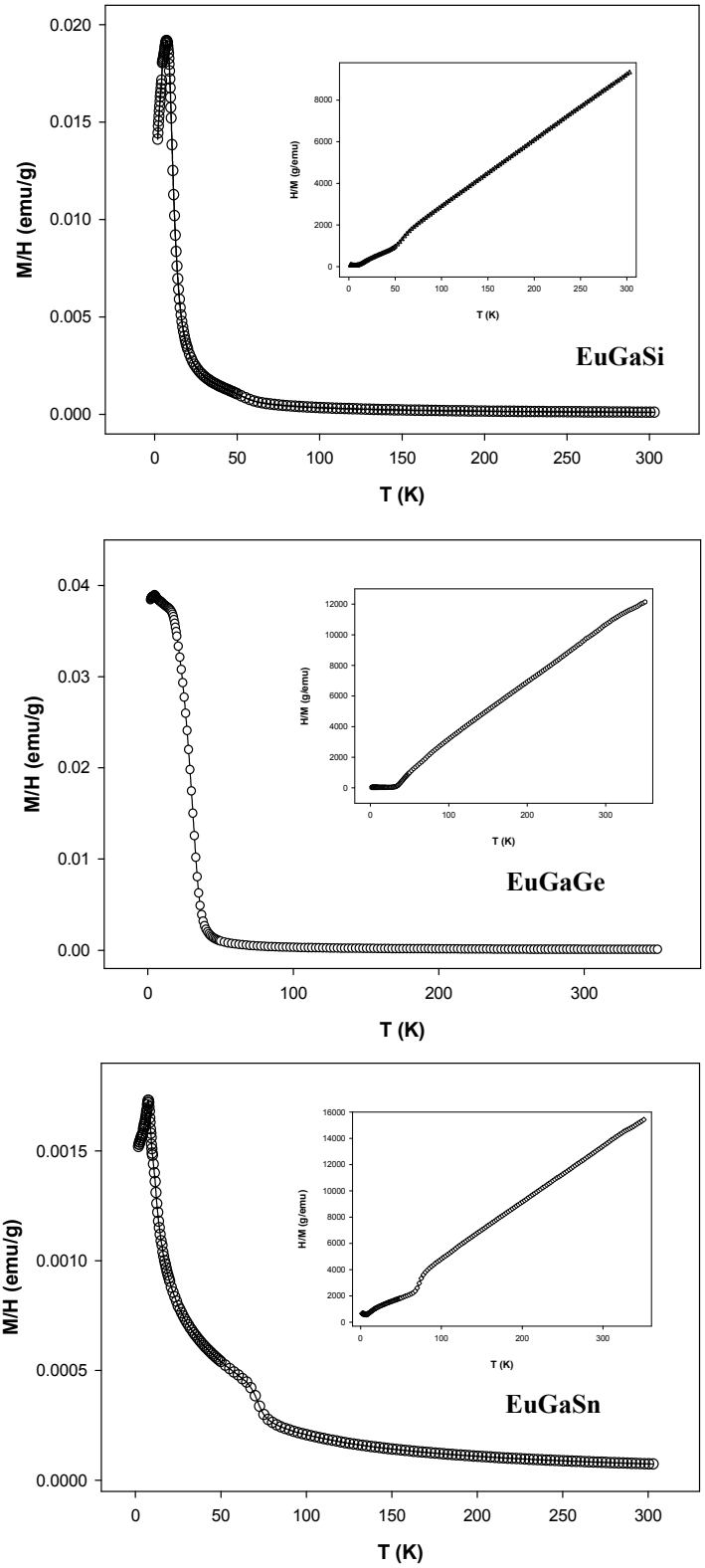

Figure 2. Temperature dependence of the magnetic susceptibilities and the reciprocal susceptibilities for EuGaSi, EuGaGe and EuGaSn.

Small shoulders observed in the $\chi(T)$ curves for EuGaSi and EuGaSn arise from trace amounts of EuO, which is reported to show FM ordering at ca. 70 K.[43-45] This impurity can also be observed in the powder X-ray diffraction pattern of EuGaSn, but it is not noticeable in the pattern of EuGaSi. Since a small amount of EuO exists in products (according to powder X-ray pattern), it can not significantly affect the results of magnetic susceptibility measurements of major phases. Both EuGaSi and EuGaGe show Curie-Weiss behavior, respectively, at temperature above 86(5) K and 95(5) K. Below those temperatures, the susceptibilities become dependent on the external magnetic field and show FM ordering with $\theta_p = +8.8(5)$ K for EuGaSi and with $\theta_p = +14.5(5)$ K for EuGaGe. EuGaSn is Curie-Weiss paramagnetic above 116(5) K, but shows AFM ordering with $\theta_p = -15.2(5)$ K.

2.4.3 Eu L_{III} XAS Measurements

As shown in Figure 3, sharp absorption maxima are observed at ca. 6977 eV for all three EuGa*Tt* (*Tt* = Si, Ge, Sn) samples, which indicates a $4f^7$ electronic configuration at the Eu atoms for the entire series.

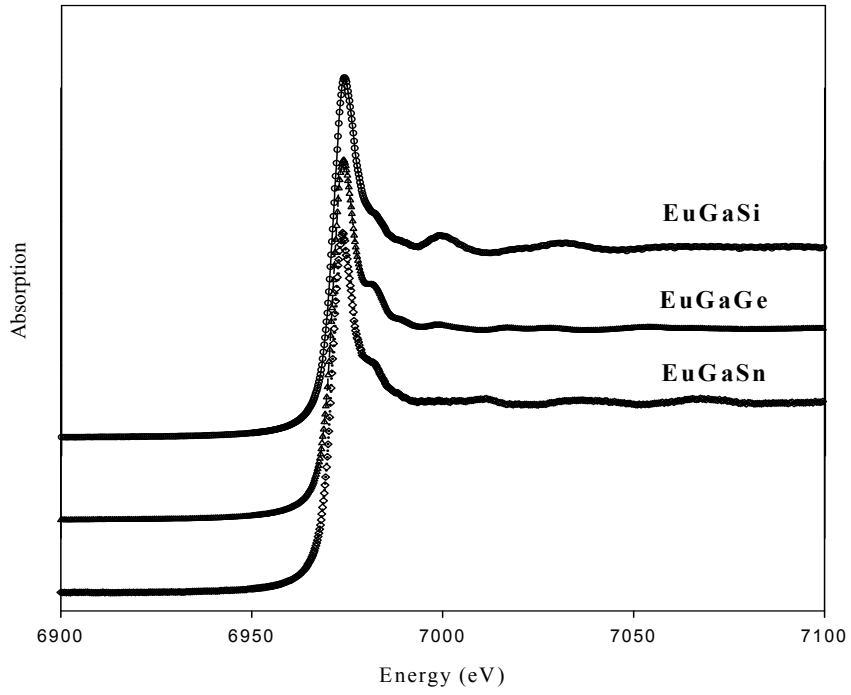

Figure 3. XAS spectra of EuGa*Tt* (*Tt* = Si,Ge,Sn).

These results are consistent with the magnetic susceptibility data. Small shoulders observed at approximately 10 eV higher than the main absorption peak are due to the existence of small traces of other form of Eu impurity which is Eu_2O_3 (electronic configuration $4f^6$, Eu^{3+}) in all three samples.

2.4.4 Electronic Structure Calculations

To investigate the electronic structure and chemical bonding features that contribute to the structural trends and atomic distributions in EuGa*Tt*, TB-LMTO-ASA electronic structure calculations using spin-polarized LSDA were carried out on observed crystal structures as well as on several hypothetical structural models. For these systems, the DOS curves for the majority and minority spin states differed only slightly, so subsequent DOS curves illustrate their superpositions.

EuGaSi. X-ray diffraction results concluded complete absence of ordering of Ga and Si in this AlB_2-type structure. Therefore, we constructed three ordered, model structures for EuGaSi, which are illustrated in Figure 4. In all three models we fixed every $^{2}_{\infty}[GaSi]$ layer to be ordered with only Ga-Si contacts (an alternant 6^3 net). For the isoelectronic system, *M*AlSi (*M* = Ca, Sr), Mazin and Papaconstantopoulos investigated the influence of in-plane ordering using the virtual crystal approximation to average Al and Si. They concluded that in-plane Al-Si ordering did not affect the band structures or DOS curves of these systems significantly.[46]

Our three models differ from each other in how these alternant 6^3 sheets stack along the *c*-axis: (1) alternating to create just Ga···Si interactions between planes; space group $P6_3/mmc$, $Z = 2$; (2) eclipsed to create Ga···Ga and Si···Si interactions between planes; space group $P\bar{6}m2$, $Z = 1$; and (3) 1:1 intergrowth of models (1) and (2) to create Ga···Si, Ga···Ga, and Si···Si interactions between planes; space group $P6_3/mmc$, $Z = 4$. Model 3 has a unit cell that resembles most closely the structures of EuGaGe and EuGaSn. The calculated total energies give Model 1 as slightly more energetically favorable than both Model 2, by just 0.75 meV/formula unit (f.u.), and Model 3 by 0.14 meV/f.u.

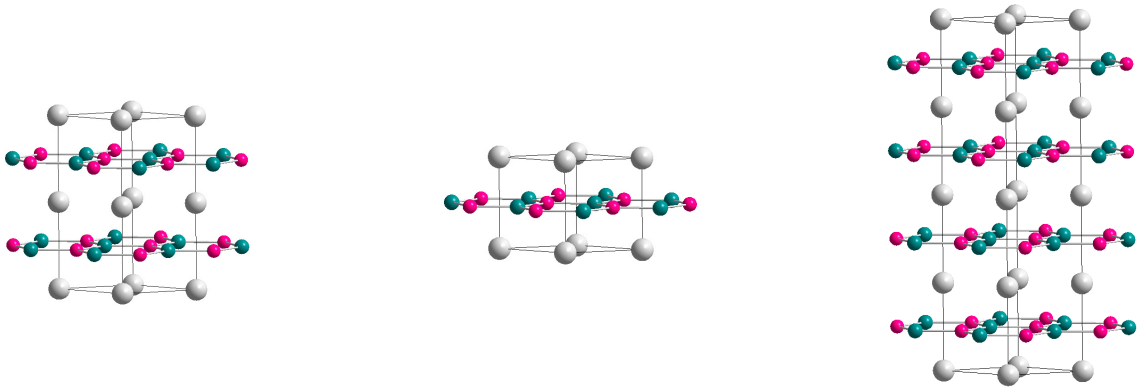

Model 1 ($P6_3/mmc$, $Z = 2$) **Model 2** ($P\bar{6}m2$, $Z = 1$) **Model 3** ($P6_3/mmc$, $Z = 4$)

Figure 4. Three structural models of EuGaSi. See text for detailed descriptions. Eu: gray; Ga: red; Si: green.

Figure 5 illustrates DOS and –COHP curves for Model 1, where the Fermi level (E_F) is the reference energy value in these curves. Throughout the entire DOS curve, there is significant mixing between valence orbitals of Eu and Ga/Si atoms. The region below ca. −1.0 eV displays significant contributions from Ga and Si atoms, whereas the region above ca. −1.0 eV is dominated by valence orbitals at Eu. In the occupied region of the DOS curve, there are three principal segments: (a) a bonding valence 3*s*-4*s* band between ca. 8.0 and 10.5 eV below E_F; (b) a bonding 3*p*-4*p* band between ca. 1.0 and 7.0 eV below E_F; and (c) a Eu 5*d* band around E_F. A deep minimum (almost a "pseudogap") in the DOS curve at ca. 1.0 eV below E_F corresponds to a valence band filling of 8 valence electrons per formula unit, which nearly matches the top of the Ga-Si bonding states shown in the adjacent –COHP curve.

In fact, the Fermi level for EuGaSi falls in the Ga-Si nonbonding region, whereas the Eu-Ga and Eu-Si –COHP curves indicate bonding states at the Fermi level. Interrogation of the DOS curve and the electronic band structure (available in Supplementary Material) reveals that Ga-Si σ-bonding bands span the region between ca. 1.0 and 7.0 eV below E_F (segment (b) above), and Ga-Si π-bonding bands start ca. 5 eV below E_F. Orbital interactions between $^{2}_{\infty}[\mathrm{GaSi}]$ planes along the *c*-axis take place primarily via the intervening Eu atoms, such that a Eu 5*d* band drops below E_F. Therefore, Ga-Si orbital interactions are predominantly two-dimensional in character.[47]

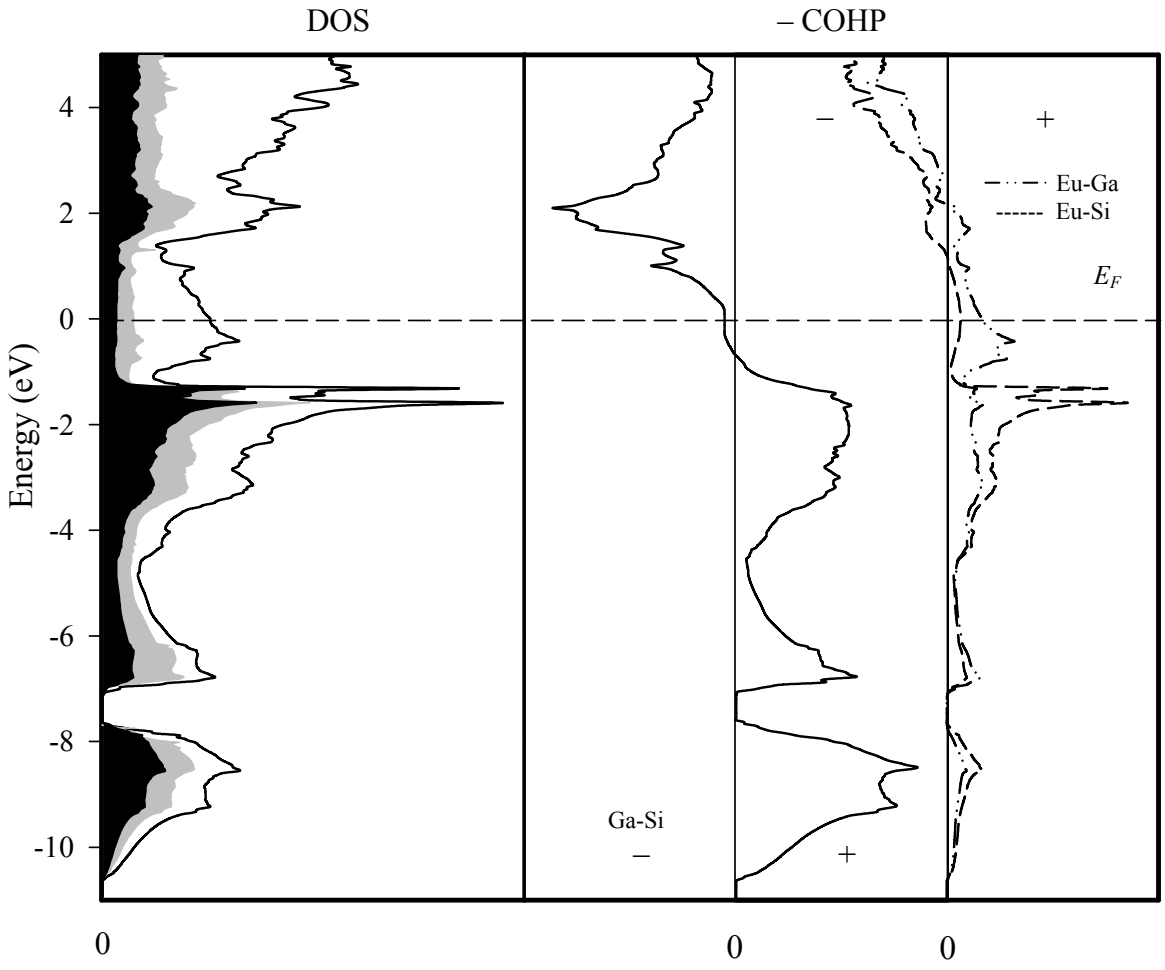

Figure 5. DOS and –COHP curves for EuGaSi. (Left) Total DOS (solid line), Eu PDOS (white region), Ga PDOS (gray region) and Si PDOS (black region). (Right) Ga-Si, Eu-Ga and Eu-Si COHP curves. The Fermi level is indicated by the dashed line and is the energetic reference (0 eV).

The strong doubled peak in the DOS has two origins: (1) from a nearly flat band composed of valence p_x and p_y orbitals from Ga and Si along the ΓM line in the first Brillouin zone, a band that remains relatively flat up to the AL line at the zone boundary; and (2) a nearly dispersionless band valence p_z orbitals from Ga and Si along the ΓK line. This second band shows nearly zero dispersion through changing overlap with Eu 5*d* orbitals along the ΓK direction. A "fatband" analysis [21,28] of the electronic band structure for EuGaSi is available in Supplementary material. These peaks are a distinct feature of the DOS curves for

AlB_2-type structures with large "cations," e.g., BaAlSi,[48] A study of the electronic structures of *AE*AlSi (*AE* = Ca, Sr, Ba)[44] showed a distinct change in corresponding DOS curves as the size of *AE* changed. In BaAlSi, an energy gap opened for 8 valence electrons, with a sharp double peak in the DOS just below this gap.

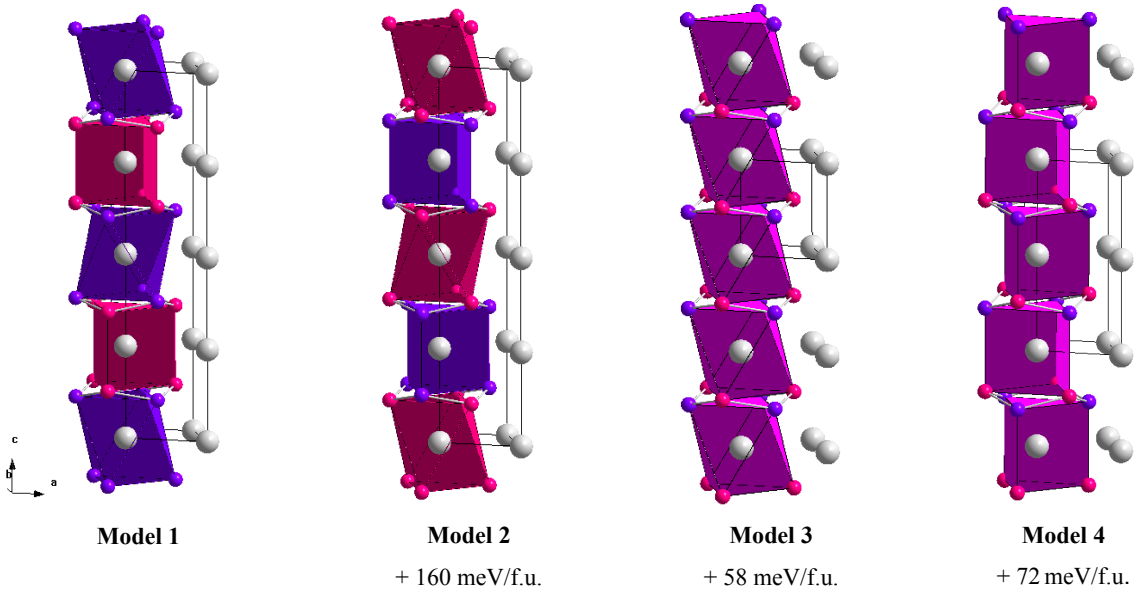

Figure 6. Four structural models of EuGaGe. See text for detailed descriptions. Eu: gray; Ga: red; Ge: purple.

The DOS curves for SrAlSi and CaAlSi showed no energy gap and a much reduced peak. Reasons for the differences in *AE*AlSi include (a) decreasing bandwidths for the occupied valence bands as the *AE* size increases due to smaller Al-Si orbital overlaps; and (b) increased orbital mixing between the valence p_z orbitals of the Al-Si network and the valence *d* orbitals of the *AE* atoms. We continue to investigate how such subtle interactions can impact structural features and physical properties in these and related polar intermetallic systems.

EuGaGe and EuGaSn. Both EuGaGe and EuGaSn, which are isoelectronic to EuGaSi, crystallize in the YPtAs-type structure instead of the AlB_2-type structure. The $^{2}_{\infty}[GaTt]$ sheets are no longer planar, and interlayer Ga···Ga contacts at 3.726(1) and 3.178(1) Å in

EuGaGe and EuGaSn, respectively, suggest an attractive, albeit weak, interaction at least for EuGaSn.

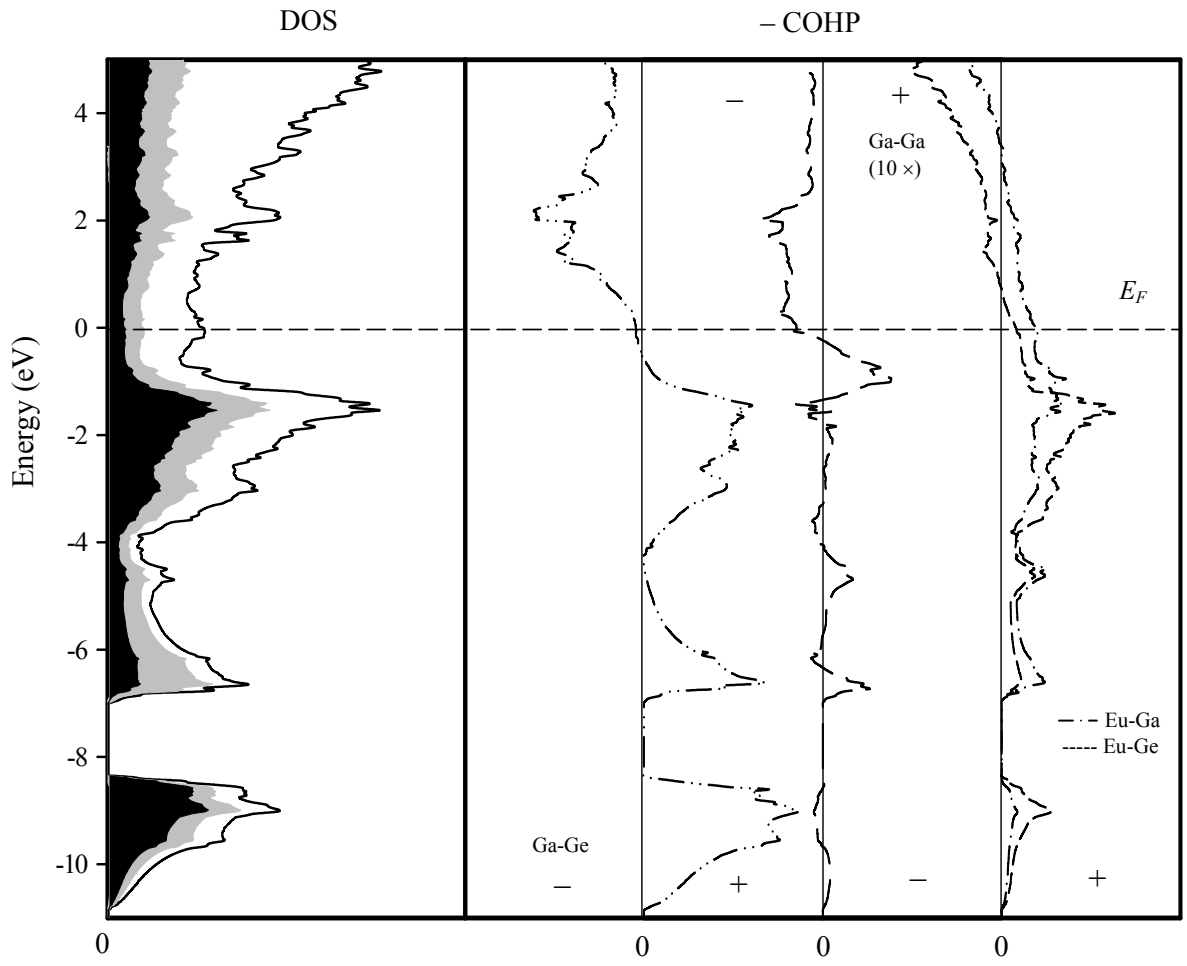

Figure 7. DOS and COHP curves for EuGaGe. (Left) Total DOS (solid line), Eu PDOS (white region), Ge PDOS (black region) and Ga PDOS (gray region). (Right) Ga-Ge, Ga-Ga, Eu-Ga and Eu-Ge COHP curves. Ga-Ga −COHP curve is magnified by ten times for comparison. The Fermi level is indicated by the dashed line and is the energetic reference (0 eV).

To explore these distinct features as well as to identify the most favorable atomic distributions, the total energies of four structural models of EuGa*Tt* shown in Figure 6 have been calculated by TB-LMTO-ASA calculations. the corresponding –COHP curves are quite similar to those for EuGaSi: the Ga-Ge and Eu-Ge contacts are nearly optimized in both. To understand the origin of the energy difference between Models (1) and (2), the corresponding

ICOHP values are listed in Table 4 to compare the various orbital interactions within each model. According to these results, Ga-Ge, Eu-Ge and Eu-Ga interactions are attractive in both models, whereas the Ga-Ga interaction between $^{2}_{\infty}[GaGe]$ sheets only in Model (1) is (weakly) attractive. The Ga-Ga –COHP curve (see Figure 7) crosses from bonding to antibonding states at the Fermi level. These interactions lead to the different coordination environments at the Eu sites, and the observed puckering of the $^{2}_{\infty}[GaGe]$ sheets.

Table 4. Integrated crystal orbital Hamiltonian population (ICOHP) values per bond for Models 1 and 2 of EuGaGe. Negative and positive ICOHP values represent, respectively, net bonding and antibonding interactions.

Model 1			Model 2		
Bond	Distance (Å)	ICOHP	Bond	Distance (Å)	ICOHP
Ga-Ge	2.5314(7)	− 0.2007	Ga-Ge	2.5314(7)	− 0.2022
Ga-Ga	3.726(1)	− 0.0109	Ga-Ga	4.800(1)	+ 0.0024
Ge-Ge	4.800(1)	+ 0.0043	Ge-Ge	3.726(1)	+ 0.0034
Eu(2)-Ga	3.087(1)	− 0.0560	Eu(1)-Ga	3.087(1)	− 0.0590
Eu(1)-Ge	3.210(1)	− 0.0645	Eu(2)-Ge	3.210(1)	− 0.0626

2.4.5 Chemical Bonding Analysis

Polar intermetallic compounds, like the EuGa*Tt* examples reported in this work, often adopt structures in accord with the Zintl-Klemm concept.[4,8] The success of this electron counting rule is high when the compounds show semiconducting (nonmetallic) behavior, but frequently require modification or explanation when the compounds are metallic – such is the anticipated case for EuGa*Tt*. Magnetic and spectroscopic measurements confirm the $4f^7$ configuration at the Eu sites, so we can formulate the main group component as $[GaTt]^{2-}$, which is assigned 9 valence electrons. According to the Zintl-Klemm concept,[8] the three-connected 6^3 nets would then be formulated as $[(3b)Ga^{2-}(3b)Tt^{-}] = [GaTt]^{3-}$, which is

optimized for 10 valence electrons. For *planar* 6^3 nets, as in graphite, the following formulation becomes more realistic as π-interactions become influential: [('4b')Ga^{-}('4b')Tt^{0}] = [Ga*Tt*]$^{-}$, and is optimized for 8 valence electrons. Clearly, the EuGa*Tt* series is an intermediate case.

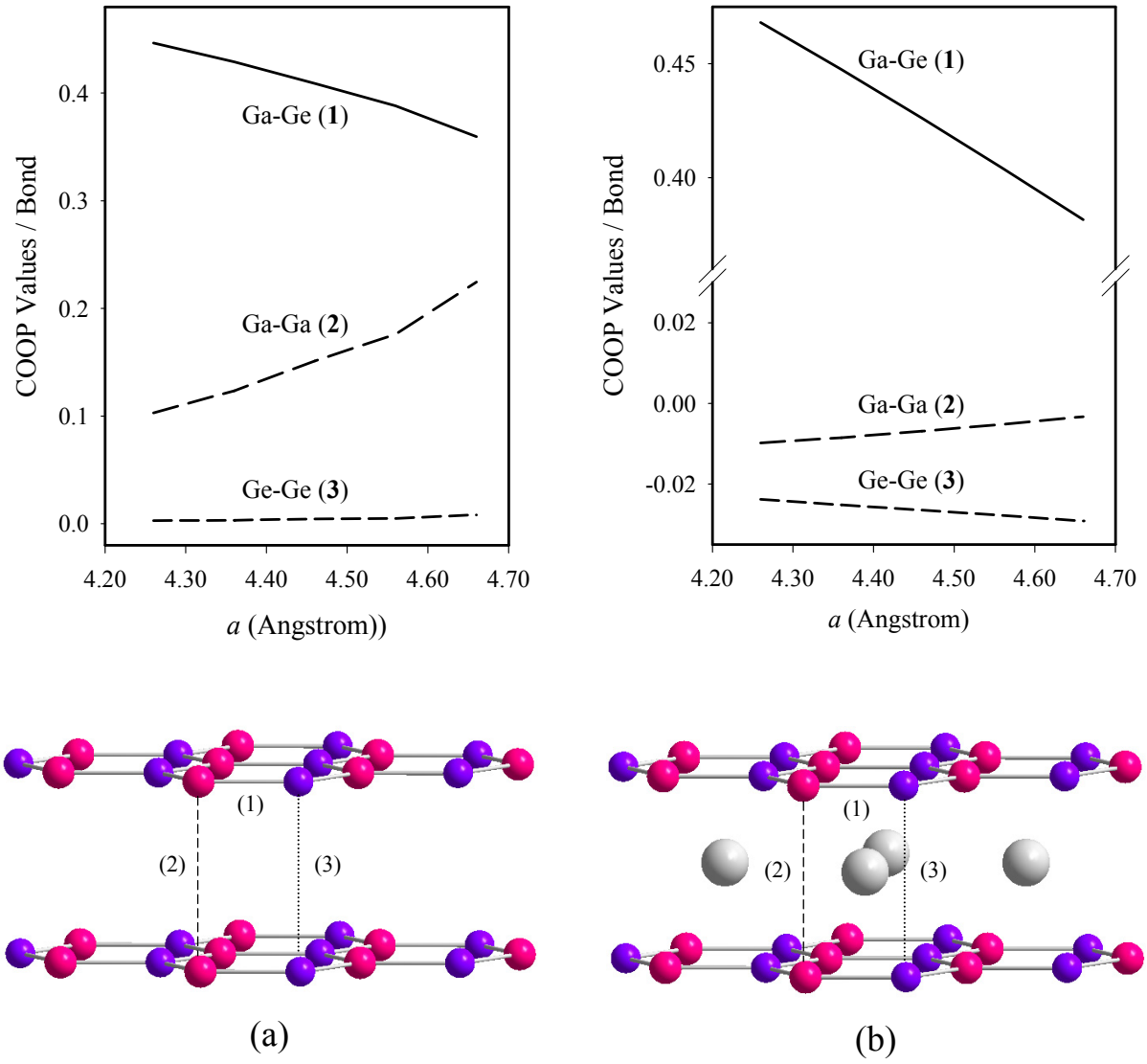

Figure 8. (a) Model structure, $^{2}_{\infty}\left[(GaGe)_2\right]^{4-}$ and (b) model structure, $^{2}_{\infty}\left[Eu(GaGe)_2\right]^{4-}$ with corresponding COOP analysis of Ga-Ge, Ga···Ga, and Ge···Ge contacts as the unit cell parameter *a* varies.

The DOS curves for EuGa*Tt* all show minima in the DOS at 8 valence electrons, and is deepest for EuGaSi, which partially substantiates the simple electron counting rule. EuGaSi differs from EuGaGe and EuGaSn in how the additional valence electron is used for chemical bonding: puckering of the 9-electron $[GaGe]^{2-}$ and $[GaSn]^{2-}$ sheets to give Ga···Ga contacts implies the formulations $[(4b)Ga^{-}(3b)Ge^{-}]$ and $[(4b)Ga^{-}(3b)Sn^{-}]$.

However, these Ga···Ga contacts exceed 3.0 Å, which is not consistent with 2-center, 2-electron bonding between these Ga atoms. No such distortion occurs in EuGaSi, which resembles the situation in 9-electron AlB_2. The isoelectronic gallium monochalcogenides, Ga*X* (*X* = S, Se, Te), follow the Zintl-Klemm formalism more closely than EuGa*Tt*: the Ga-Ga distances are less than 2.75 Å, so the formulation would be $[(4b)Ga^{-}(3b)X^{+}]$. However, the formal charges assigned to each site violate expectations from electronegativity arguments. The limiting ionic formulation is $Ga^{2+}X^{2-}$. Since there are no *Tt*-*Tt* contacts in EuGa*Tt*, we may consider the formulation $Eu^{2+}Ga^{2+}Tt^{4-}$, but this is certainly an extremely, and highly unrealistic picture of the bonding situation.[8]

Extended Hückel (EHT) calculations[49,50] on two model structures derived from EuGaGe can provide some preliminary insights into the factors influencing how these layers shift away from planar configurations. These model structures consist of two planar, alternant ${}^{2}_{\infty}[GaGe]^{2-}\,6^3$ nets stacked in an eclipsed fashion to give inter-planar Ga···Ga and Ge···Ge contacts (see Figure 8); the two cases differ by whether or not there are Eu atoms inserted between these planes. For the calculations, the inter-planar distance was kept fixed at 4.00 Å, while the *a*-axis was varied. Trends in crystal orbital overlap population (COOP) values for Ga-Ge, Ga···Ga and Ge···Ge contacts are plotted as a function of lattice constant. When no Eu atoms occur between these planes, the results show that as the Ga-Ge distance increases, the corresponding inter-planar Ga···Ga overlap population is significantly bonding and also increases while the Ge···Ge overlap population remains nearly zero, i.e., essentially nonbonding. With inserted Eu atoms, the Ga···Ga overlap populations drop to nonbonding values. In this case, both Ga···Ga and Ge···Ge contacts are weakly repulsive, with the stronger orbital repulsions occurring within the Ge···Ge contacts. Thus, this semi-empirical

analysis suggests that the puckering is influenced by Eu-Ga and Eu-Ge interactions rather than through-space Ga···Ga interactions.

2.4.6 Bonding Analysis by the Electron Localization Function (ELF)

Because the formation of an electron pair is the key element of the models for the chemical bond, it becomes possible to describe chemical bonding using so-called bonding-detector functions, e.g., the Electron Localization Function (ELF)[27a] or the Electron Localizability Indicator (ELI)[27b], both of which are related to the motion of electron pairs in a chemical system. In this bonding analysis of EuGa*Tt*, we use the system of tools based on ELF. In the ELF representation, the elements of chemical bonding are consequently derived by employing the topological features of the bonding-detector function. The directed interaction between atoms in a chemical structure, i.e., a molecule or extended solid, can be distinguished in real space. Maxima of the ELF in the valence region (valence shells) or/and structurization of the penultimate (outer core) shell[27c] provide signatures for directed (covalent) bonding. The ELF tools are especially suitable to detect directed (covalent) bonding in materials with bands that are not fully occupied or are strongly overlapping, a situation which is typical for intermetallic compounds. The analysis of the topology of ELF can be combined with the consecutive integration of the electron density in "basins," which are bound by zero-flux surfaces in the ELF gradient field. This procedure, similar to the one proposed for electron density,[30] allows assignment of an electron count for each basin, revealing basic information about chemical bonding. This combined application of ELF together with electron density offers the possibility of Zintl-like electron counts for a large group of intermetallic phases and of getting access to a bond definition in real space for complex structures. Reviews on the application of ELF for different kinds of bonding situations are available;[27d] for more details, see http://www.cpfs.mpg.de/ELF.

The ELF can be illustrated in two distinct ways: (1) as surfaces corresponding to a single ELF value ("isosurfaces"); and (2) as a slice through the structure. To achieve further insights into the valence region along the EuGa*Tt* series, especially between Ga atoms, the ELF has been analyzed in detail for EuGaSi and EuGaSn (EuGaSn was selected because the interlayer Ga···Ga contact is significantly shorter than the corresponding distance in EuGaGe).

To have a reference system with puckered main group 6^3 nets for comparison, an ELF analysis on $EuGe_2$ was also conducted.

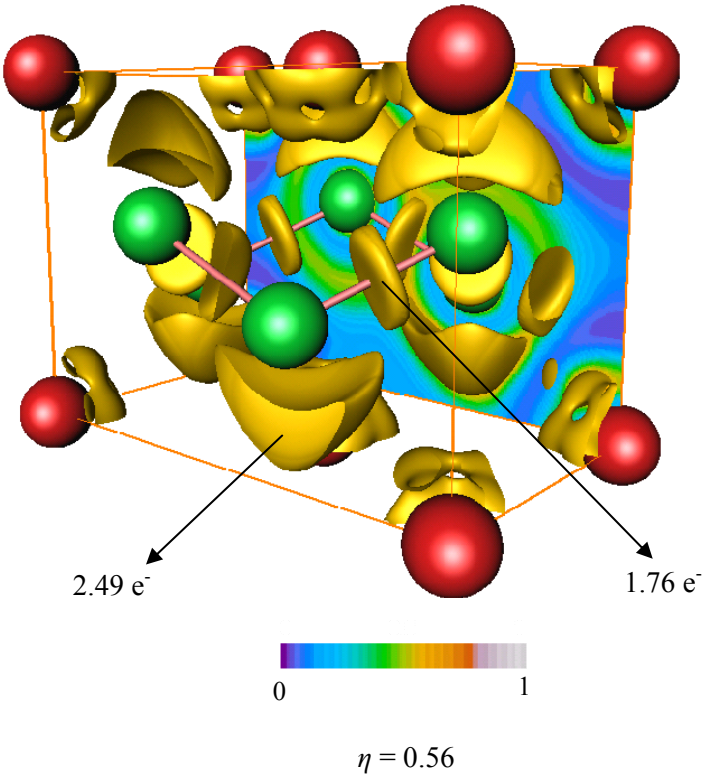

Figure 9. ELF distribution (color scale indicated) in $EuGe_2$; Eu sites: red spheres; Ge sites: green spheres. ELF isosurfaces (η = 0.56), colored in yellow, produce lone pair attractors (2.49 e^-) and Ge-Ge bond pair attractors (1.76 e^-). A (110) ELF surface is also illustrated.

$EuGe_2$. The topological analysis of ELF reveals four attractors, which are defined as local maxima of ELF values, around each three-bonded Ge atom as shown in Figure 9. One lone pair-like attractor is located above (or below) the atom along [001] and three other attractors are symmetrically located at Ge-Ge contacts within the hexagonal layer. Integration of the total electron density within each basin, which is defined by zero-flux surfaces in the ELF gradient, gives the valence electron counts of 2.49 electrons for the lone pair-like attractor and 1.76 electrons for the Ge-Ge bond attractors. Thus, the total valence electron count for

valence shell basin sets is 5.13 electrons per Ge atom (= 2.49 e^- ("lone pair") + 3 × 1.76 e^- / 2 ("bond pairs")), which can be written as $Ge^{1.13}$.

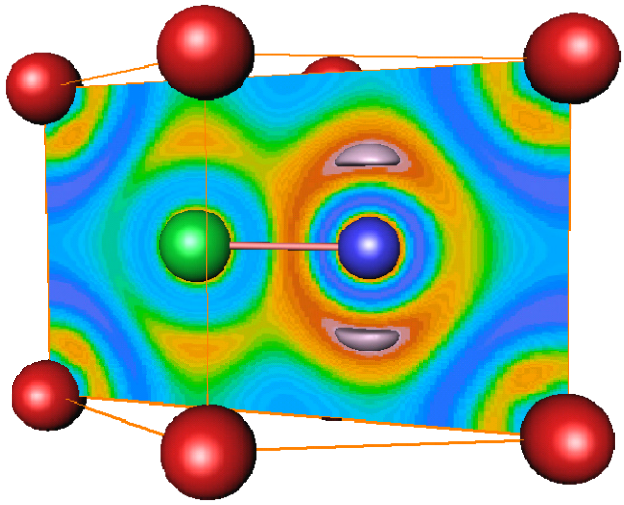

$\eta = 0.80$

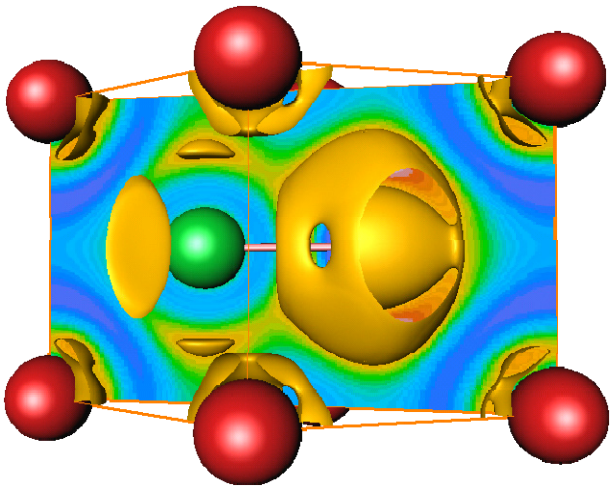

$\eta = 0.57$

Figure 10. ELF distribution (color scale indicated) in EuGaSi; Eu sites: red spheres; Ga sites: green spheres; Si sites: blue spheres. ELF isosurfaces (η = 0.80 and 0.57), colored, respectively, in white and yellow, produce attractors associated with Si and Ga atoms. A (110) ELF surface is also illustrated.

As a result, the bonding situation in $EuGe_2$ may be described as $Eu^{2.26+}[Ge^{1.13-}]_2$, which agrees reasonably well with a Zintl-Klemm representation as $Eu^{2+}[Ge^{-}]_2$.

EuGaSi. (Figure 10) ELF attractors are located around the three-bonded Ga and Si atoms within the planar polyanionic layers. Unlike $EuGe_2$, lone pair-like attractors are observed symmetrically above and below both Ga and Si atoms along [001] together with bond attractors on each Ga-Si bond. Integration of the total electron density of lone-like attractors around Ga and Si atom and the Ga-Si bond attractors results in values of 3.81 electrons for the valence shell basins of Ga and 5.32 electrons for the valence shell basins of Si for a formulation of $Eu^{2.13+}[Ga^{0.81-}Si^{1.32-}]$ with roughly divalent Eu atoms.

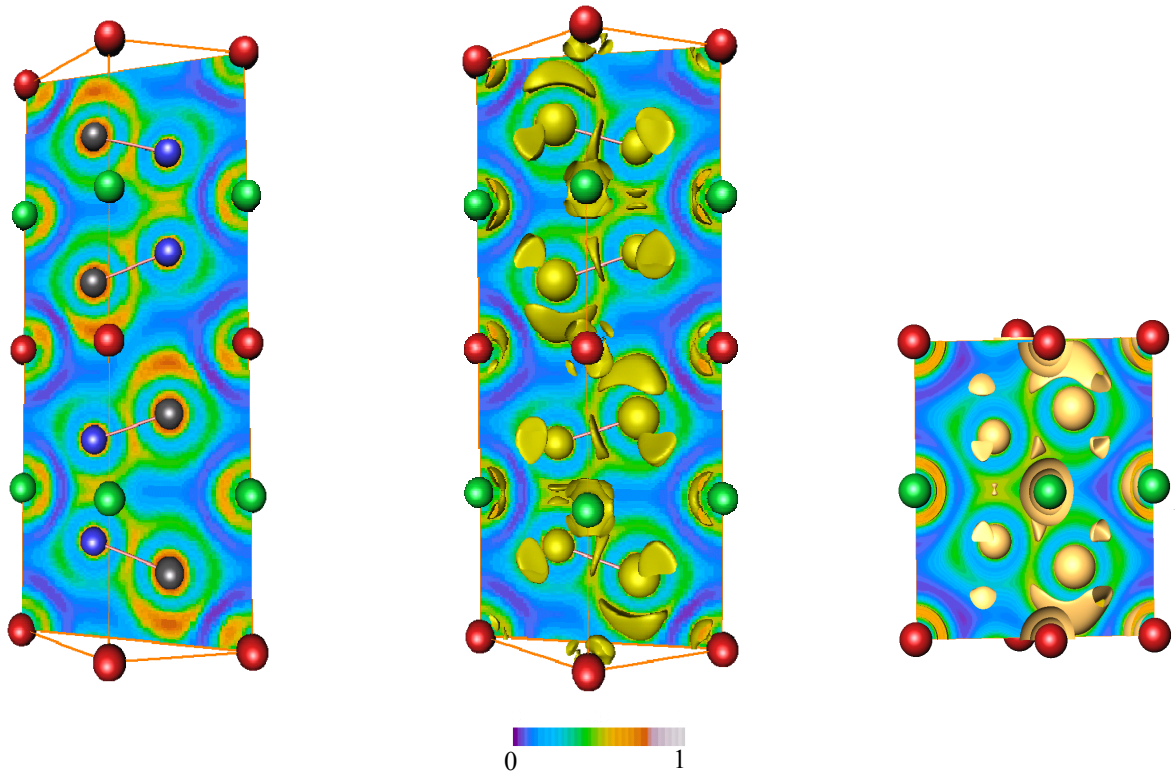

(110) contour map (a) $\eta = 0.53$ (b) $\eta = 0.51$ (c)

Figure 11. (a) ELF distribution of EuGaSn (LMTO calculations) in the (110) plane; (b) ELF isosurface (η = 0.53) interspersed with (110) ELF distribution; (c) One-half of a unit cell of EuGaSn with ELF isosurface (η = 0.51) based on a FPLO calculation. Eu(1) sites: red spheres; Eu(2) sites: green spheres; Ga sites: blue spheres; Sn sites: black spheres.

EuGaSn. (Figure 11) The positions of ELF bond attractors around three-bonded Ga and Sn atoms are similar to those in $EuGe_2$ and EuGaSi. Since the extent of puckering for each $^{2}_{\infty}[GaSn]$ layer is between that of $EuGe_2$ and EuGaSi, we observe lone pair-like attractors on Ga and Sn atoms along [001]. The lone pair-like attractors at each Ga site face each other as shown in Figure 11b and show two maxima within this pair. Clearly, the Ga···Ga contact does not show a bond attractor as seen for the Ga-Sn contacts. Integration of the total valence electron density in the basins was performed as described earlier for $EuGe_2$ and EuGaSi and formulated EuGaSn to be $Eu^{2.12+}[Ga^{0.54-}Sn^{1.58-}]$. This type of interaction is also observed in a full-potential local orbital calculation (FPLO), which confirms the existence of two separate attractors between Ga atoms as shown in Figure 11c. Therefore, this interaction cannot be identified as a two-center, two-electron bond. Rather, we suggest these interlayer Ga···Ga interactions to be described as two distinct four-center interactions involving one Ga atom and three Eu atoms forming a distorted tetrahedral surrounding of this attractor. This is well in accord with the population analysis from both TB-LMTO-ASA and EHT revealing a pronounced Eu-Ga and Eu-Ge interaction and an essentially nonbonding Ga-Ga interaction. We continue to explore this unusual interaction with theoretical calculations and high pressure experiments on EuGa*Tt*.

2.5 Summary

Three ternary compounds EuGa*Tt* (*Tt* = Si, Ge, Sn) were prepared and their crystal structures were characterized by powder and single crystal X-ray diffraction. EuGaSi crystallizes in the AlB_2-type structure with a planar hexagonal layer consisting of randomly distributed Ga and Si atoms, whereas EuGaGe and EuGaSn adopt the YPtAs-type of crystal structure with puckered polyanionic layers composed of ordered Ga and Ge/Sn atoms. Based on the crystal structure refinement, two distinct coordination environments at Eu, octahedral and trigonal prismatic, were found in EuGaGe and EuGaSn. Electronic factors are influential to direct the distribution of Ga and *Tt* atoms in these structures, which also affect local structural distortions. An unusual four-center interaction is revealed by ELF calculations.

Acknowledgement

This work was supported by NSF DMR 02-41092 and 06-05949. The authors are grateful to Dr. Warren Straszheim for the EDXS measurements, to Dr. Sergey Bud'ko for magnetization measurements at Iowa State University, to Dr. Ulrich Burkhardt for XAS measurements, to Dr. Alexei Baranov for FPLO calculations as well as to Dr. Frank Wagner and to Dr. Miroslav Kohout at Max-Planck-Institute for Chemical Physics of Solids in Dresden, Germany for a fruitful discussion concerning bonding analysis in real space. Tae-Soo You also wishes to thank MPI-CPFS in Dresden, Germany for financial support.

References

[1] Häussermann, U.; Amerioun, S.; Eriksson, L.; Lee, C.-S.; Miller, G. J. *J. Amer. Chem. Soc*. **2002**, *124*, 4371−4383.

[2] Westbrook, J. H.; Fleischer, R. L., Ed.; *Intermetallic Compounds: Principle and Practice*, Wiley, New York, 1995.

[3] Schäfer, H. *Ann. Rev. Mater. Sci.* **1985**, *5*, 1.

[4] Nesper, R., *Prog. Solid State Chem*. **1990**, *20*, 1.

[5] Miller, G. J.; Lee, C.-S.; Choe, W. In *Inorganic Chemistry Highlights*; Meyer, G., Naumann, D., Wesemann, L., Ed.; Wiley-VCH, Berlin, 2002.

[6] Klem, M. T.; Vaughy, J. T.; Harp, J.G.; Corbett, J. D. *Inorg.Chem.***2001**, *40*, 7020−7026.

[7] Bobev, S.; Bauer, E. D.; Thompson, J. D.; Sarrao, J. L.; Miller, G. J.; Eck, B.; Dronskow-ski, R. *J. Solid State Chem*. **2004**, *177,* 3545−3552.

[8] Miller, G. J. In *Chemistry, Structure, and Bonding of Zintl Phases and Ions*; Kauzlarich, S. M., Ed.; VCH Publishers; New York, 1996; pp 1−59.

[9] Nuspl, G.; Polborn, K.; Evers, J.; Landrum, G.A.; Hoffmann, R. *Inorg.Chem*. **1996**, *35*, 6922-6932.

[10] Meng, R. L.; Lorenz, B.; Wang, Y. S.; Cmaidalka, J.; Sun, Y. Y.; Xue, Y. Y.; Meen, J. K.; Chu, C. W. *Physica C* **2002**, *382*, 113-116.

[11] Imai, M.; Abe, E.; Ye, J.; Nishida, K.; Kimura, T.; Honma, K.; Abe, H,; Kitazawa, H. *Phys. Rev. Lett*. **2001**, *87*, 077003.

[12] Imai, M.; Nishida, K.; Kimura, T.; Abe, H. *Appl. Phys. Lett*. **2002**, *80*, 1019−1021.

[13] Imai, M.; Nishida, K.; Kimura, T.; Abe, H. *Physica C* **2002**, *377*, 96−100.

[14] Imai, M.; Nishida, K.; Kimura, T.; Kitazawa, H.; Abe, H.; Kito, H.; Yoshii, K. *Physica C* **2002**, *382*, 361−366.

[15] Lorenz, B.; Lenzi, J.; Cmaidalka, J.; Meng, R. L.; Sun, Y. Y; Xue, Y. Y.; Chu, C. W. *Physica C* **2002**, *383*, 191−196.

[16] Nagamatsu. J.; Nakagawa, N.; Muranaka, T.; Zenitani, Y.; Akimitsu J. *Nature* **2001**, *410*, 63−64.

[17] Hunter, B. A.; Howard, C. J. *Rietica*; Australian Nuclear Science and Technology Organization: Menai, Australia, 2000.

[18] XRD single crystal software. Bruker Analytical X-ray System: Madison, WI, **2002**.

[19] *SHELXTL*, version 5.1; Bruker AXS Inc.: Madison, WI, **1998.**

[20] Emsley, J. *The Elements*; Clarendon press: Oxford, **1998.**

[21] Anderson, O. K. *Phys. Rev. B* **1986**, *34*, 2439.

[22] Anderson, O. K.; Jepsen, O. *Phys. Rev. Lett.* **1984***, 53*, 2571−2574.

[23] Andersen, O. K.; Jepsen, O.; Glötzel, D. In *Highlights of condensed matter theory*; F. Bassani, F. Fumi, M.Tosi, Eds.; New York, North-Holland, Lambrecht, W. R. L., **1985.**

[24] Jepsen, O.; Anderson, O. K. *Z. Phys. B* **1995**, *97*, 35.

[25] Dronskowski, R.; Blochl, P. *J. Phys. Chem*. **1993**, *97*, 8617−8624.

[26] Blöchl, P. E.; Jepsen, O.; Anderson, O. K. *Phys. Rev. B* **1994**, 49, 16223−16233.

[27] (a) Savin, A.; Flad, H. J.; Preuss, H.; von Schnering, H. G. *Angew. Chem.* **1992**, *104*, 185; *Angew. Chem., Int. Ed. Engl.* **1992**, *31*, 185; (b) Kohout, M. *Int. J. Quantum Chem.* **2004,** 97, 651; (c) Kohout, M.; Wagner, F. R.; Grin, Yu. *Theor. Chem. Acc.* **2002**, 108, 150; (d) Gatti, C. *Z. Kristallogr.* **2005**, 220**,** 399.

[28] Jepsen, O.; Burkhardt, A.; Andersen, O. K. *The TB-LMTO-ASA Program*, version 4.7; Max-Planck-Institut für Festkörperforschung: Stuttgart, Germany, 1999.

[29] Kohout, M. *BASIN*, version 2.3; Max-Planck-Institut für Chemische Physik fester Stoffe: Dresden, Germany, 2001.

[30] Bader, R. F. W. *Atoms in molecules: a quantum theory*; Oxford University Press: Oxford, 1999.

[31] *Amira* visualization software; Konrad-Zuse-Zentrum für Informationstechnik Berlin (ZIB): Berlin, Germany, 2003.

[32] T.-S. You, G. J. Miller, to be published

[33] Wenski, G.; Mewis, A. *Z. Anorg. Allg. Chem*. **1986**, *535*, 110-122.

[34] Nielsen, J. W.; Baenziger, N. C.: Acta Crystallogr. **1954**, *7*, 132-133.

[35] Hoffmann, R.; Pöttgen, R. *Z. Kristallogr*. **2001**, *216*, 127.

[36] Burdett, J. K.; Miller, G. J. *Chem. Mater*. **1990**, *2*, 12-26.

[37] Hamilton, C. W. *Acta Cryst*. **1965**, *18*, 502-510.

[38] Czybulka, A.; Pinger, B.; Schuster, H. *Z. Anorg. Allg. Chem*. **1989**, *579*, 151-157.

[39] Kuhn, A.; Bourdon, A.; Rigoult, J.; Rimsky, A. *Phys. Rev. B* **1982**, *25*, 4081-4088.

[40] Benazeth, S.; Dung, N.H.; Guittard, M.; Laruelle, P. *Acta Crystallogr., Sect. C* **1988**, *44*, 234-236.

[41] Semiletov, S.A.; Vlasov, V.A. *Kristallografiya* **1963**, *8*, 877-883.

[42] Julien-Pouzol, M.; Jaulmes, S.; Guittard, M.; Alapini, F. *Acta Crystallogr., Sect. B* **1979**, *35*, 2848-2851.

[43] Pöttgen, R.; Johrendt, D. *Chem. Mater*. **2000**, *12*, 875-897.

[44] McWhan, D.; Souers, P.; Jura. G. *Phys. Rev*. **1966**, *143*, 385-389

[45] Stroka, B.; Wosnitza, J.; Scheer, E.; Löhneysen, H.; Park, W.; Fischer, K. *Z. Phys. Condens. Matter*. **1992**, *89*, 32.

[46] Mazin, I. I. ; Papaconstantopoulos, D. A. *Phys. Rev. B* **2003**, *68*, 220504(R).

[47] Giantomassi, M.; Boeri, L.; Bachelet, G. *Phys. Rev. B* **2005**, *72*, 224512.

[48] Huang, G. Q.; Chen, L. F.; Liu, M.; Xing, D. Y. *Phys. Rev. B* **2004**, *69*, 064509.

[49] (a) Hoffmann, R. *J. Chem. Phys.* **1963**, *39*, 1397; (b) Hoffmann, R.; Lipscomb, W.N. *J. Chem. Phys.* **1962**, *36*, 2179; (c) Whangbo, M.-H.; Hoffmann, R.; Woodward, R.B. *Proc. R. Soc. London* **1979**, *A366*, 23.

[50] EHT calculations included orbital overlaps within second nearest neighbor unit cell with Hamiltonian matrix elements calculated by the weighted Wolfsberg-Helmholz expression.[51] Integrated COOP values were evaluated by 200 **k**-points in the first Brillouin zone. Atomic orbital parameters are: Ga 4*s*, H_{ii} = –14.58 eV, ζ = 1.77; Ga 4*p*, H_{ii} = –6.75 eV, ζ = 1.55; Ge 4*s*, H_{ii} = –16.00 eV, ζ = 2.16; Ge 4*p*, H_{ii} = –9.00 eV, ζ = 1.85; Eu 6*s*, H_{ii} = –8.13 eV, ζ = 1.74, Eu 6*p*, H_{ii} = –5.13 eV, ζ = 1.70, Eu 5*d*, H_{ii} = –8.32 eV, ζ_1 = 1.56 (0.8316), ζ_2 = 3.55 (0.3041).

[51] Ammeter, J.H.; Bürgi, H.-B.; Thibeault, J.C.; Hoffman, R. *J. Am. Chem. Soc.* **1978**, *100*, 3686.

Supplementary Material

Comment S1. Alternative Synthetic Approaches and Characterization

A certain amount of weight loss is inevitable during arc-melting (ca. 0.4-0.7 wt % loss out of total 1 ± 0.2 g samples), although low current was used (20 A) for these experiments due to potential volatility of Eu. Based on the X-ray diffraction analysis and chemical analysis (e.g. EDS), all of the compounds crystallized in single phase products with equiatomic compositions.

In addition, all three compounds were prepared in sealed Ta tubes using a high-frequency (HF) induction furnace or a conventional tube furnace at elevated temperatures. However, this approach did not generally obtain a homogeneous product or better crystallinity for the target compositions. No difference was observed between products from arc-melting and sealed tubes in terms of the crystal structure and the composition for EuGaGe. It is possible that optimizing synthetic or annealing temperatures could be achieved to obtain homogeneous target compounds, but the arc-melted products provided samples suitable for subsequent characterization. However, at this time, we are not certain whether observed, mixed-phase products are due to inaccurate temperature profiles or intrinsic properties of the components. Moreover, unlike EuPtGe where Eu boils (1537 °C) even before Pt melts (1769 °C) resulting in inaccurate compositions of the product, the melting points of Si, Ga, Ge and Sn are lower than the boiling point of Eu. Thus, weight loss of products seems to occur mainly after each ternary compound was produced. Experimental methods and powder X-ray patterns, which are not included in a manuscript, are summarized below for comparison.

EuGaSi

- Method 1: arc-melting (20 A)
- Method 2: HF induction furnace (1500 °C, 15 min)
- Powder X-ray pattern comparison: Two patterns are almost identical except small peaks around $2\theta = 31°$ and 38° in method 2. Method 1 gives a single phase product.

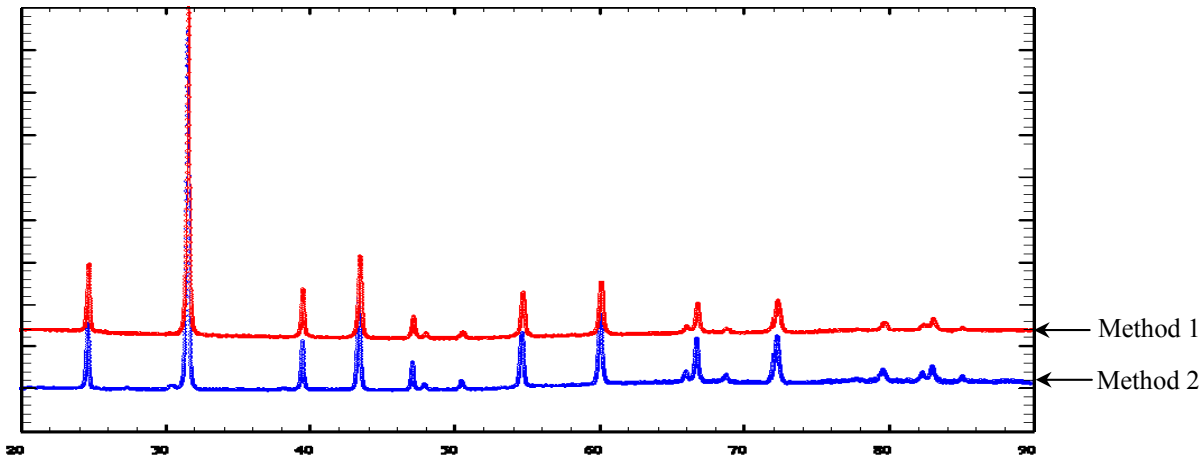

EuGaGe

- Method 1: arc-melting (20 A) + annealing (350°C, 7 days)
- Method 2: cylinder-furnace

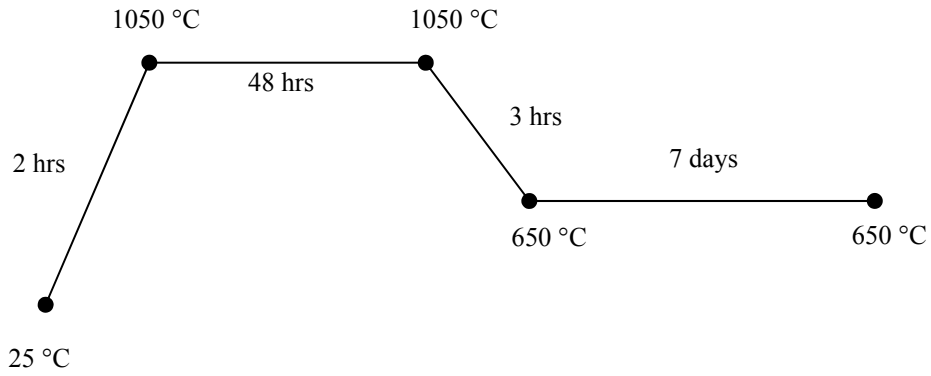

- Method 3: HF induction furnace (1100°C, 15 min) + annealing (650°C, 3 hrs)
- Powder X-ray pattern comparison: Method 1 and 2 show almost identical single phase powder patterns. However, method 3 gives mixed phases.

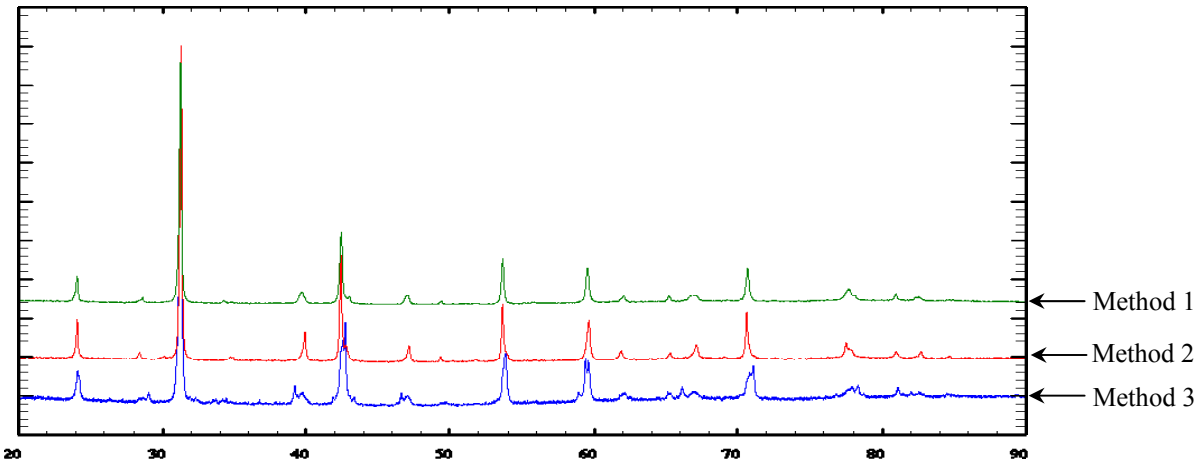

EuGaSn

- Method 1: arc-melting (20 A)
- Method 2: HF induction furnace (950 °C, 15 min) + annealing (500°C, 2 hrs)
- Powder X-ray pattern comparison: Mixed phases are observed in methods 2. Method 1 gives a single phase of target compound.

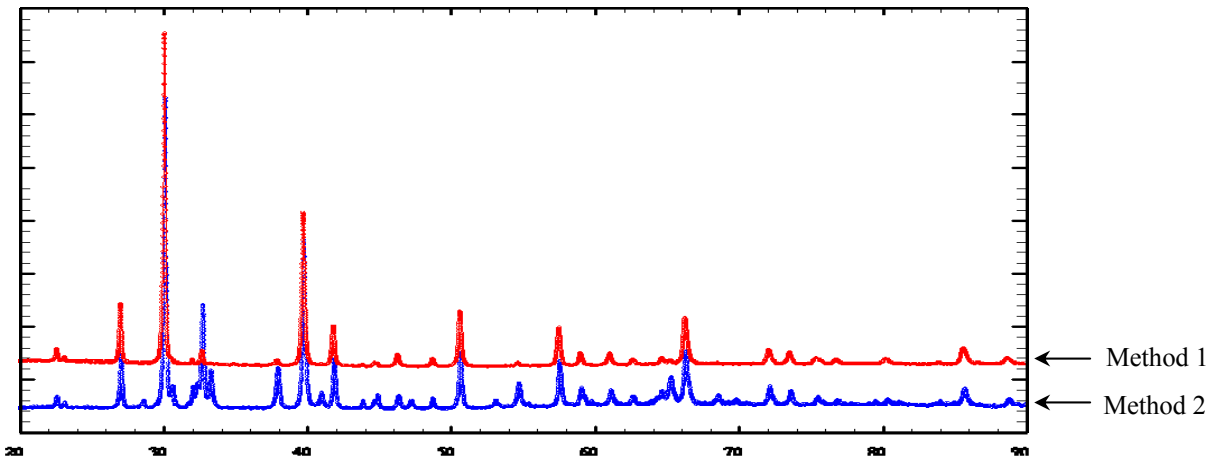

Table S2. Lattice constants as determined by single crystal and powder X-ray diffraction for EuGa*Tt* (*Tt* = Si, Ge, Sn).

Compound	EuGaSi		EuGaGe		EuGaSn	
Analysis	$Eu_{1.00}Ga_{1.00}Si_{1.00}$		$Eu_{1.00}Ga_{1.00}Ge_{1.00}$		$Eu_{1.00}Ga_{1.00}Sn_{1.00}$	
	Single Crystal	Powder	Single Crystal	Powder	Single Crystal	Powder
a (Å)	4.1686(6)	4.1699(5)	4.2646(6)	4.2690(2)	4.5243(5)	4.5313(3)
c (Å)	4.5543(9)	4.5634(6)	18.041(5)	18.1237(2)	18.067(3)	18.0662(3)
c/*a* or 4*a*	1.0925	1.0944	1.0575	1.0613	0.9983	0.9967

Table S3. Anisotropic displacement parameters (Å^2) for EuGa*Tt* (*Tt* = Si, Ge, Sn). The exponent of the anisotropic displacement factor takes the form: $-2\pi^2[h^2a^{*2}U_{11} + \cdots + 2\,hka^*b^*U_{12}]$. For these space groups, U_{13} and $U_{23} = 0$.

Atom	$U_{11} = U_{22}$	U_{33}	U_{12}
	EuGaSi		
Eu	0.011(1)	0.009(1)	0.005(1)
Ga/Si	0.010(1)	0.032(1)	0.005(1)
	EuGaGe		
Eu(1)	0.009(1)	0.011(1)	0.005(1)
Eu(2)	0.009(1)	0.010(1)	0.005(1)
Ga	0.008(1)	0.026(1)	0.004(1)
Ge	0.008(1)	0.014(1)	0.004(1)
	EuGaSn		
Eu(1)	0.013(1)	0.013(1)	0.006(1)
Eu(2)	0.010(1)	0.011(1)	0.005(1)
Ga	0.009(1)	0.024(1)	0.005(1)
Sn	0.009(1)	0.013(1)	0.005(1)

Figure S4. Magnetization measurements as a function of external field (0-5.5 T) at 2 K for EuGa*Tt* (*Tt* = Si, Ge, Sn).

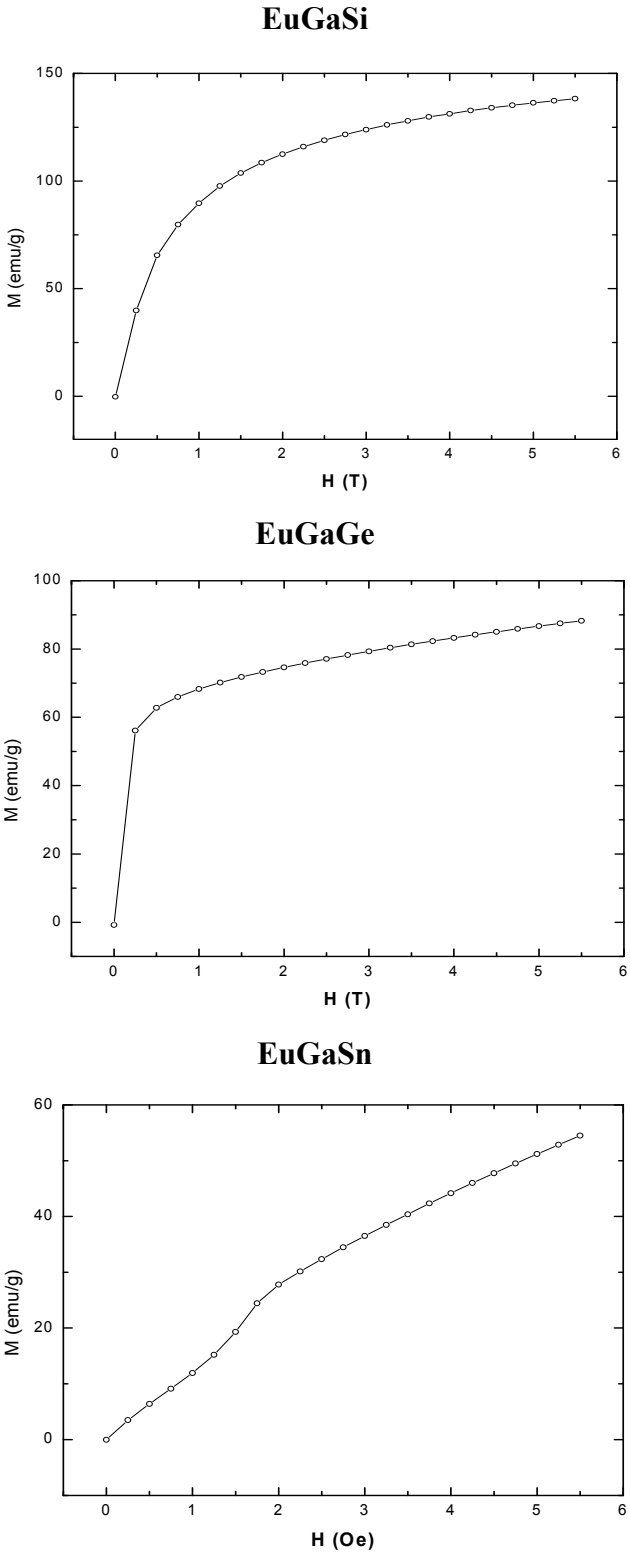

Figure S5. Electronic energy band structures of EuGaSi, model (1), with fatband contributions for p_x and p_y orbitals (top) and p_z orbitals (bottom) from Ga and Si, using the TB-LMTO-ASA method in the LSDA.

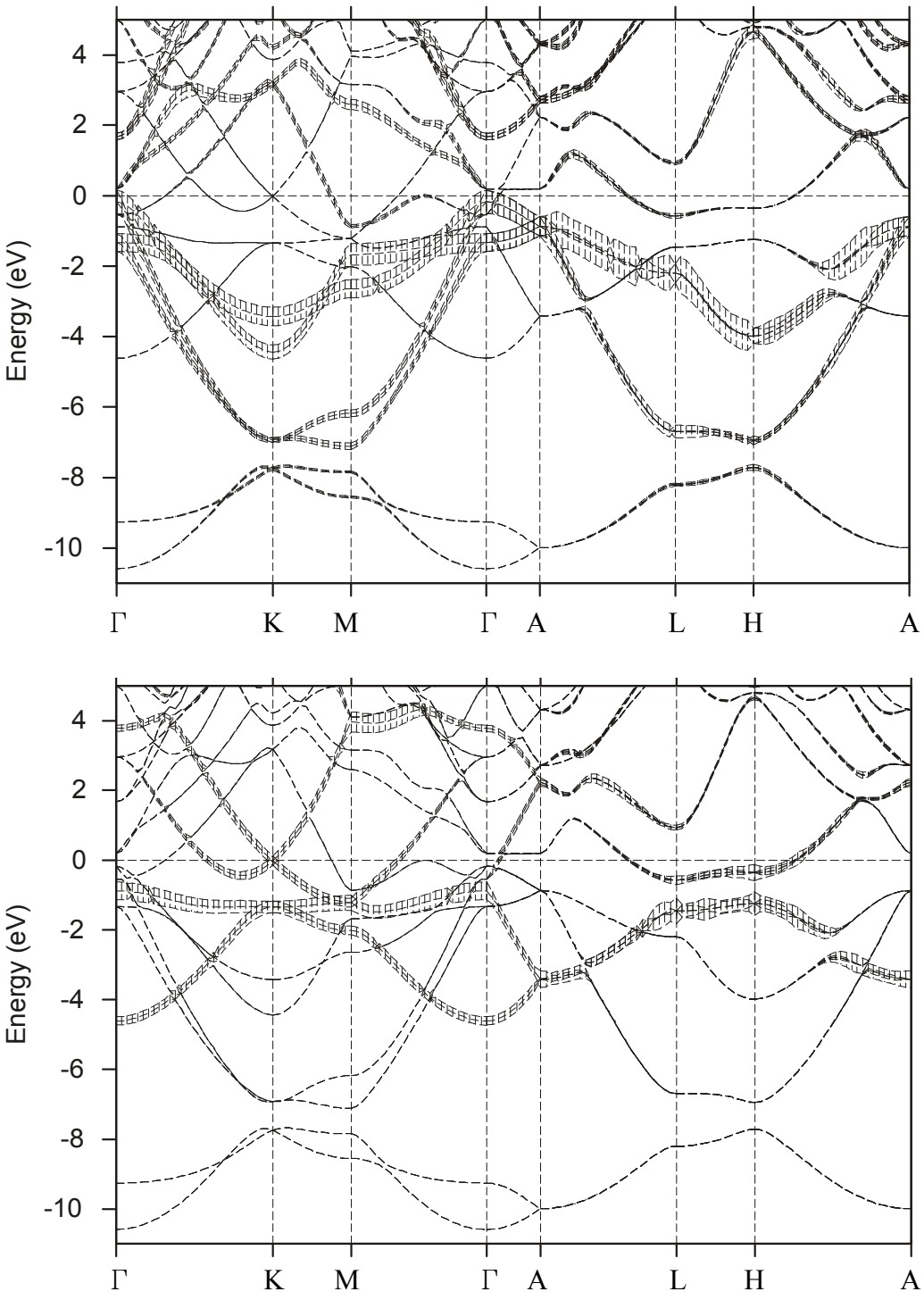

Figure S6. Electronic energy band structure of EuGaGe using the TB-LMTO-ASA method in the LSDA.

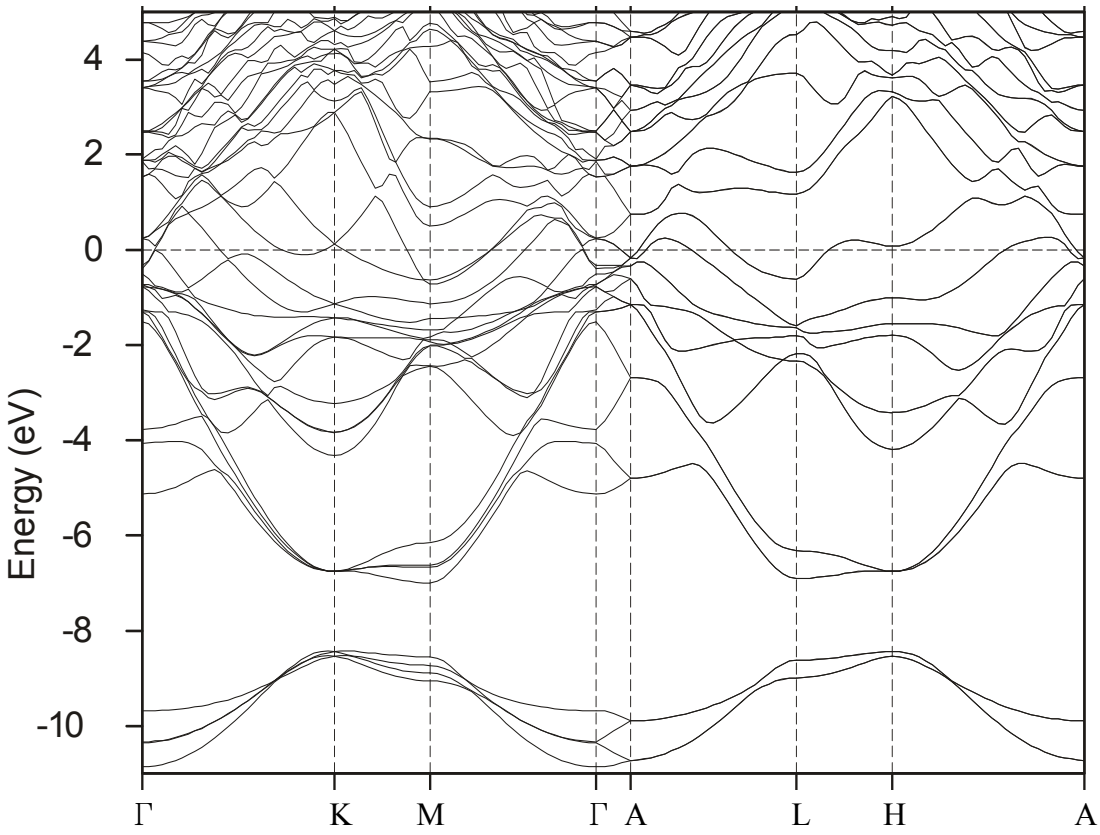

Figure S7. Electronic energy band structure of EuGaSn using the TB-LMTO-ASA method in the LSDA.

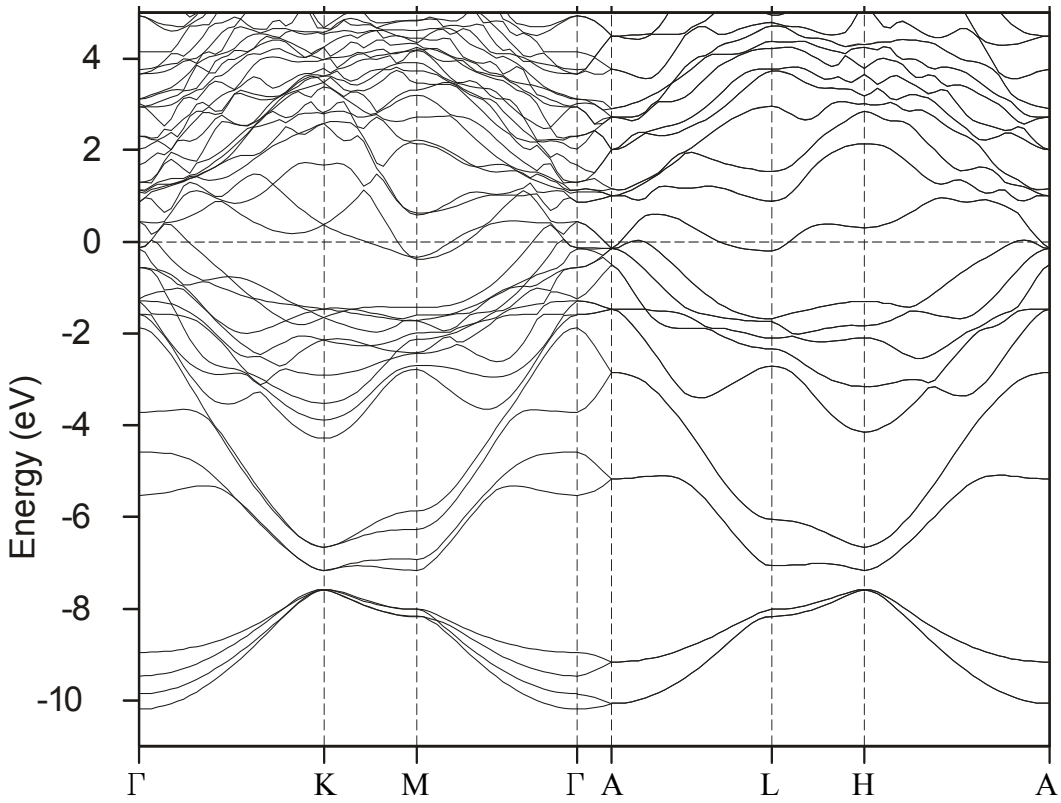

CHAPTER 3

To What Extent Does the Zintl-Klemm Formalism Work? The $Eu(Zn_{1-x}Ge_x)_2$ Series

A paper to be submitted to *Journal of the American Chemical Society*

Tae-Soo You,[1,2] and Gordon J. Miller[1,3]

3.1 Abstract

The series of ternary polar intermetallics $Eu(Zn_{1-x}Ge_x)_2$ ($0 \leq x \leq 1$) has been investigated and characterized by powder and single crystal X-ray diffraction as well as physical property measurements. For $0.50(2) \leq x \leq 0.75(2)$, this series shows a homogeneity width of hexagonal AlB_2-type phases (space group *P6/mmm*, Pearson symbol *hP*3) with Zn and Ge atoms statistically distributed in the planar polyanionic 6^3 nets. As the Ge content increases in this range, *a* decreases from 4.3631(6) Å to 4.2358(6) Å, while *c* increases from 4.3014(9) Å to 4.5759(9) Å, resulting in an increasing *c/a* ratio. Furthermore, the Zn−Ge bond distance within the hexagonal net drops significantly from 2.5190(3) Å to 2.4455(3) Å, but the anisotropy of the displacement ellipsoids significantly increases along the *c*-direction. At lower and higher values of *x*, respectively, orthorhombic KHg_2-type and trigonal $EuGe_2$-type phases are observed as one of the majority phases in corresponding product mixtures. Temperature-dependent magnetic susceptibility measurements for two AlB_2-type compounds show Curie−Weiss behavior above 40.0(2) K and 45.5(2) K with magnetic moments of 7.98(1) μ_B for $Eu(Zn_{0.48(2)}Ge_{0.52(2)})_2$ and 7.96(1) μ_B for $Eu(Zn_{0.30(2)}Ge_{0.70(2)})_2$, respectively,

---

[1] Graduate student and Professor, respectively, Department of Chemistry, Iowa State University

[2] Primary researcher and author

[3] Author for correspondence

indicating a $(4f)^7$ electronic configuration for Eu atoms (Eu^{2+}). The Zintl-Klemm formalism accounts for the lower limit of Ge content in the AlB_2-type phases, but does not identify the observed upper limit. In a companion paper, the intrinsic relationship among chemical structures, compositions, and electronic structures are analyzed by theoretical electronic structure calculations of several models of these phases and discussed to provide comprehensive interpretation of these structural results.

3.2 Introduction

Polar intermetallic compounds represent a growing collection of inorganic solids to investigate relationships among structure, physical properties and chemical bonding.[1] They involve combinations of electropositive elements, i.e., alkali-, alkaline-earth or rare-earth elements, with electronegative metals close to the Zintl line. The electronegative metals typically form networks that either conform to simple electron counting rules, such as the Zintl-Klemm formalism,[2–4] or give rise to an electronic structure characterized by a pseudogap in the electronic density of states curve and optimized orbital interactions at the Fermi level.[5] The electropositive metals formally act like cations, as in classical valence compounds (Zintl phases), by providing their valence electrons to influence the structure of the electronegative component. Their surroundings also involve large coordination numbers. However, unlike Zintl phases, these "active" metals do not transfer all valence electrons to the electronegative component, but are involved in "lattice covalency" through their valence orbitals.[6] The presence of the pseudogap at the Fermi level can lead to potentially interesting physical properties, especially if rare-earth metals serve as the active metal due to partially filled 4*f* bands.[7] In general, polar intermetallics can be considered as a compound class intermediate between classical intermetallic compounds, such as Hume-Rothery electron phases, and Zintl-Klemm compounds.[2–4]

During our systematic investigation of the $Eu(M_{1-x}M'_x)_2$ series (M, M′ = Group 12−14 elements) to study the correlation among atomic, electronic, and possible magnetic structures by varying atomic sizes and valence electron counts, we have observed a systematic structural variation within the $Eu(Zn_{1-x}Ge_x)_2$ system as x increases from the KHg_2-type to the AlB_2-type and, finally, the $EuGe_2$-type structure. These structure types differ in the networks

formed by the electronegative components: (a) the KHg_2-type shows a four-bonded, three-dimensional (4b-3D) net with locally distorted tetrahedral coordination; (b) the AlB_2-type contains three-bonded, two-dimensional (3b-2D) planes with trigonal planar coordination; and (c) the $EuGe_2$-type exhibits 3b-2D puckered nets with local trigonal pyramidal environments. The transition from planar to puckered three-connected nets has been discussed frequently in the literature,[8] and is clearly related to the concentration of valence *s* and *p* electrons. In a recent study of EuGaTt (Tt = Si, Ge, Sn),[9] atomic size also influences puckering of 3b-2D nets, which is further mediated by the role of valence orbitals at the active metal site by creating multi-centered interactions. In this paper, we have attempted to reduce the atomic size factor and to focus on valence electron count in the $Eu(Zn_{1-x}Ge_x)_2$ series. The $Eu(Zn_{1-x}Ge_x)_2$ compounds adopting the AlB_2-type phase are related to the superconducting AEAlSi (AE = Ca and Sr)[10–14], which are recently receiving attention for their similarity to superconducting MgB_2[15] with respect to their atomic structures and valence electrons counts.

3.3 Experimental Section

3.3.1 Synthesis and Chemical Analysis

Fifteen compositions along the $Eu(Zn_{1-x}Ge_x)_2$ series ($0 \leq x \leq 1$) were prepared using corresponding stoichiometric molar ratios of the pure elements (Eu: Ames Laboratory, 99.99%; Zn: Alfa, 99.999%; and Ge: Alfa, 99.999%) by induction-melting. Reactant mixtures were loaded into tantalum ampoules, which were sealed by arc-melting in an argon-filled glove box with the concentration of O_2 lower than 10 ppm. The tantalum ampoules were then sealed in evacuated silica jackets to prevent oxidation. $EuZn_2$,[16] $Eu(Zn_{1-x}Ge_x)_2$, and $EuGe_2$[17] were heated, respectively, to 880°C, 1100°C, and 1050°C, and held at these temperatures for 15 min. Then, all products were allowed to cool to room temperature, and no subsequent annealing process was needed for any of the products, according to powder X-ray diffraction. All products remain visibly stable upon exposure to both air and moisture over several weeks. Analysis by energy-dispersive X-ray spectroscopy (EDXS) was conducted on a Hitachi S-2460N variable-pressure scanning electron microscope (SEM),

equipped with Oxford Instruments Link Isis Model 200 X-ray analyzer. The corresponding pure elements were used as standards for intensity references.

3.3.2 Crystal Structure Determination

The $Eu(Zn_{1-x}Ge_x)_2$ series was characterized at room temperature by both powder and single crystal X-ray diffraction. Powder X-ray diffraction patterns were collected with a Huber G670 Guinier image-plate powder diffraction camera equipped with monochromatic Cu $K\alpha_1$ radiation (λ = 1.54059 Å). The step size was set at 0.005°, and the exposure time was 1-2 h. Data acquisition was controlled via the *in situ* program. The crystal systems and the lattice parameters were determined by Rietveld refinement using the program *Rietica*.[18] These powder X-ray diffraction patterns were used to check the number and identity of phases in product mixtures, as well as to compare lattice parameters with subsequent single crystal refinements. The two binary compounds, $EuZn_2$ and $EuGe_2$, as well as several multi-phase products were characterized solely by powder X-ray patterns.

For single crystal X-ray diffraction experiments of the AlB_2-type phases, several silvery lustrous crystals were selected from the cast of each product. The quality of each crystal was checked by a rapid scan on a Bruker SMART Apex CCD diffractometer with Mo Kα radiation (λ = 0.71073 Å). The best crystals were selected for further analysis, and then data were collected at 293(2) K using either a Bruker SMART Apex CCD diffractometer or a STOE IPDS diffractometer. On the Bruker SMART Apex CCD diffractometer, data were collected in a full sphere and harvested by taking three sets of 606 frames with 0.3° scans in ω and with an exposure time of 10 s per frame. On the STOE IPDS diffractometer, data from two sets of 180 frames were collected with an exposure time of 3 min for each frame. The angular range of 2θ was 9.0-70.0° for all compounds.

Intensities of the entire sets of reflections were extracted and corrected for Lorenz and polarization effects using the *SAINT* program,[19] and absorption was corrected empirically with the program *SADABS*.[19] The space group was determined by program *XPREP* in the *SHELXTL* software package.[20] All structures were solved by direct methods and refined on F^2 by full-matrix least-squares methods using the *SHELXTL* software package.[20] The entire sets of reflections of $Eu(Zn_{1-x}Ge_x)_2$ for $0.50(2) \leq x \leq 0.75(2)$ were matched with the

hexagonal crystal system. Further analysis led us to choose *P*6/*mmm* (AlB_2-type), in which Eu atoms are located at the origin (1*a* sites) of the hexagonal unit cells, and Zn and Ge atoms are statistically situated at $x = 1/3$, $y = 2/3$, and $z = 1/2$ (2*d* sites) with no preferred ordering. For the region below $x = 0.50(2)$, the hexagonal phase (AlB_2-type) coexisted with the orthorhombic phase $EuZn_2$. On the other hand, in the region above $x = 0.75(2)$, the trigonal phase $EuGe_2$ appeared as a secondary phase in product mixtures. Anisotropic displacement parameters of the Zn/Ge site along the *c*-axis are larger than those along *a*- and *b*-axis in Ge-rich composition of the AlB_2-type phases. This can indicate the tendency of puckering of anionic nets as previously observed by Pöttgen.[21] To check the possibility of puckering, space groups $P6_3mc$ and $P\bar{3}m1$ with a free atomic coordinate for the Zn/Ge atoms along the *c*-axis were used for structural refinements. However, these refinements located the Zn/Ge atoms at $z = 0.4994(7)$. Moreover, an electron density contour map in the *ac*-planes located at $x = 1/3$ and $x = 2/3$ showed just a single maximum at the Zn/Ge positions centered at $z = 1/2 \pm 0.0006(7)$ rather than two separated maxima. Therefore, *P*6/*mmm* is chosen to be the most appropriate space group for structural refinement. Given the similar scattering factors of Zn and Ge, these atoms cannot be differentiated in the X-ray diffraction experiment. Therefore, we assumed that Zn and Ge atoms were statistically distributed within the hexagonal net according to the stoichiometric ratio provided by EDXS analyses during the refinement processes.

3.3.3 Physical Property Measurements

Temperature-dependent magnetic susceptibility measurements for two compounds, $Eu(Zn_{0.48(2)}Ge_{0.52(2)})_2$ and $Eu(Zn_{0.30(2)}Ge_{0.70(2)})_2$, were conducted using a Quantum Design, MPMS-5 SQUID magnetometer. The measured temperature range was 1.8–300 K with a magnetic field of 0.1 T. Magnetic measurements were carried out on bulk samples (approximately 300 mg) from the same preparations as the one used for powder diffraction experiments. Temperature-dependent electrical resistivities of $Eu(Zn_{0.45(2)}Ge_{0.55(2)})_2$ and $Eu(Zn_{0.33(2)}Ge_{0.67(2)})_2$ were measured by the electrode-less "Q" method with the aid of a Hewlett-Packard 4342A Q-meter.[22] Approximately 110 mg of each sample ground with a grain diameter between 180 and 200 μm was mixed with chromatographic alumina and

sealed into a Pyrex tube. The measurement was conducted at 34 MHz over the temperature range of ca. 110–230 K.

3.4 Results and Discussion

Along the series $Eu(Zn_{1-x}Ge_x)_2$, we observed five distinct regions of phase behavior according to X-ray powder diffraction, shown in Figure 1. Three of these regions indicate single-phase behavior, while the other two regions exhibit two-phase features: (1) $x = 0$ in Figure 1a, i.e., $EuZn_2$, exhibits the orthorhombic KHg_2 structure type; (2) $0 < x < 0.50(2)$ patterns, as in Figure 1b, contain orthorhombic KHg_2-type and hexagonal AlB_2-type characteristics; (3) $0.50(2) \leq x \leq 0.75(2)$ in Figures 1c and 1d is a single phase region with patterns matching the AlB_2 structure type; (4) $0.75(2) < x < 1$ patterns as in Figure 1e, have hexagonal AlB_2-type and trigonal $EuGe_2$-type features; and (5) $x = 1$ in Figure 1f, i.e., $EuGe_2$, forms the trigonal $EuGe_2$ structure type. All Rietveld refinements of powder diffraction patterns produced lattice parameters in very good agreement with those obtained from single crystal X-ray diffraction experiments throughout the entire series, as listed in Table 1. The crystallographic results of four distinct single crystal specimens adopting the AlB_2-type structure are summarized in Tables 2 and 3.

3.4.1 Regions (1) and (2): $Eu(Zn_{1-x}Ge_x)_2$

For the $x = 0$ case, $EuZn_2$ crystallizes in the orthorhombic KHg_2-type structure (space group *Imma*) shown in Figure 2 (left) as originally proposed,[16] and the powder X-ray diffraction pattern is displayed in Figure 1a. The KHg_2-type structure is closely related to the hexagonal AlB_2-type structure because both structure types contain 6^3 anionic nets stacked in an eclipsed manner with larger atoms located between these nets.[23] The hexagonal nets in $EuZn_2$ are puckered in a manner to create Zn–Zn contacts between nets and a distorted tetrahedral environment at each Zn atom. This puckering is expected based on how closely these sheets approach each other along the stacking direction, i.e., the *b*-axis, which can be measured by the $b/2a$ ratio (these fall under the $(c/a)^*$ column in Table 1 as an analogy to the c/a ratios for the hexagonal and trigonal phases).[8]

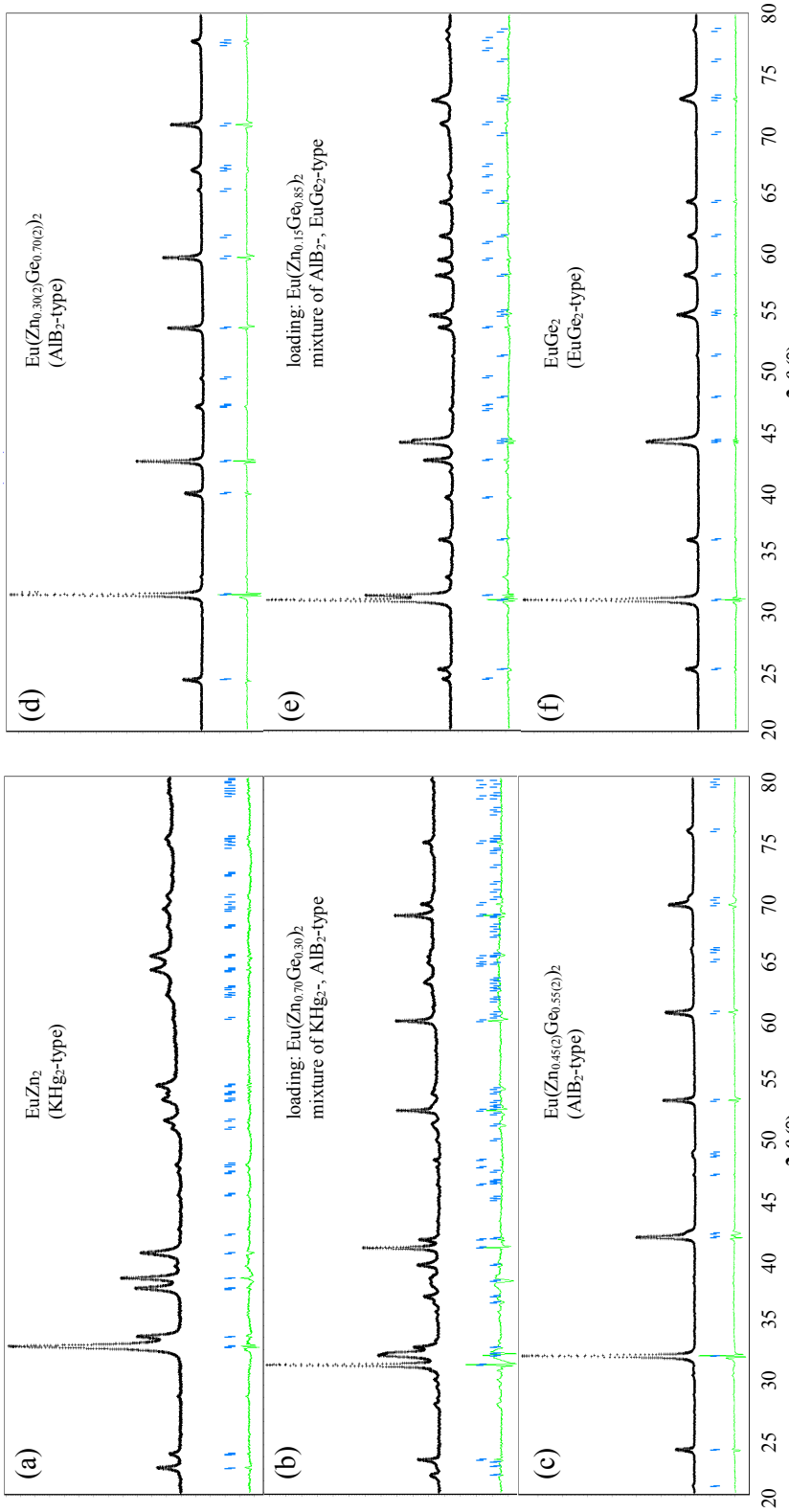

Figure 1. Powder X-ray diffraction patterns of selected samples from the $Eu(Zn_{1-x}Ge_x)_2$ series ($0 \leq x \leq 1$). Miller indices are also shown for two AlB_2-type phases, (c) and (d).

Table 1. Lattice Constants and Unit Cell Volumes as Determined by Single and Powder X-ray Diffraction for $Eu(Zn_{1-x}Ge_x)_2$ ($0 \le x \le 1$). V* = volume per formula unit; (c/a)* = c/a for hexagonal AlB_2-type and = $b/2a$ for orthorhombic KHg_2-type samples.

x (loaded)	x (EDXS)	Structure Type	Sample	a (Å)	b (Å)	c (Å)	(c/a)* (Å)	V* (Å^3)
0.00	0.00(2)	KHg_2	powder	4.7313(6)	7.6444(9)	7.6564(9)	0.808	69.23(2)
0.17		KHg_2	powder	4.6964(3)	7.6249(5)	7.7269(6)	0.812	69.18(1)
	0.49(2)	AlB_2	powder	4.3692(2)	4.3692(2)	4.3000(2)	0.985	71.090(5)
			single crystal	4.3649(6)	4.3649(6)	4.2955(8)	0.984	70.881(2)
0.30		KHg_2	powder	4.6770(2)	7.6346(4)	7.7604(4)	0.816	69.28(1)
	0.50(2)	AlB_2	powder	4.3670(2)	4.3670(2)	4.3098(1)	0.987	71.179(3)
			single crystal	4.3631(6)	4.3631(6)	4.3014(9)	0.986	70.913(2)
0.40		KHg_2	powder	4.6617(5)	7.6283(8)	7.7830(1)	0.818	69.19(2)
	0.50(2)	AlB_2	powder	4.3668(1)	4.3668(1)	4.3187(1)	0.989	71.32(1)
			single crystal	4.3635(4)	4.3635(4)	4.2981(5)	0.985	70.87(2)
0.45		KHg_2	powder	4.6443(1)	7.5996(1)	7.7438(1)	0.818	68.33(1)
	0.50(2)	AlB_2	powder	4.3549(3)	4.3549(3)	4.2998(3)	0.987	70.62(1)
0.50	0.52(2)	AlB_2	powder	4.3577(2)	4.3577(2)	4.3239(1)	0.992	71.108(4)
			single crystal	4.3552(8)	4.3552(8)	4.3187(1)	0.991	70.941(4)
0.55	0.55(2)	AlB_2	powder	4.3137(2)	4.3137(2)	4.4036(2)	1.021	70.961(1)
			single crystal	4.3116(6)	4.3116(6)	4.4179(1)	1.025	71.125(2)
0.60	0.60(2)	AlB_2	powder	4.3035(1)	4.3035(1)	4.4584(2)	1.036	71.51(1)
			single crystal	4.3031(5)	4.3031(5)	4.4407(8)	1.032	71.210(6)
0.65	0.67(2)	AlB_2	powder	4.2581(3)	4.2581(3)	4.5221(5)	1.062	71.01(0)
			single crystal	4.2554(4)	4.2554(4)	4.5154(3)	1.061	70.81(1)
0.69	0.70(2)	AlB_2	powder	4.2558(1)	4.2558(1)	4.5321(1)	1.065	71.087(3)
			single crystal	4.2514(4)	4.2514(4)	4.5363(6)	1.063	71.006(2)
0.73	0.75(2)	AlB_2	powder	4.2546(2)	4.2546(2)	4.5623(2)	1.072	71.520(4)
			single crystal	4.2358(5)	4.2358(5)	4.5759(6)	1.079	71.101(5)

0.78	0.76(2)	AlB_2	powder	4.2346(1)	4.2346(1)	4.5728(1)	1.080	71.01(0)
			single crystal	4.2324(6)	4.2324(6)	4.5710(9)	1.080	70.91(2)
		$EuGe_2$	powder	4.1040(1)	4.1040(1)	4.9983(1)	1.218	72.91(3)
0.80	0.76(2)	AlB_2	powder	4.2349(4)	4.2349(4)	4.5733(5)	1.080	71.030(1)
			single crystal	4.2343(6)	4.2343(6)	4.5746(1)	1.080	71.030(2)
		$EuGe_2$	powder	4.1045(2)	4.1045(2)	4.9950(1)	1.217	72.876(3)
0.85	0.75(2)	AlB_2	powder	4.2448(1)	4.2448(1)	4.5656(2)	1.076	71.242(4)
		$EuGe_2$	powder	4.1075(1)	4.1075(1)	4.9974(2)	1.217	73.017(3)
1.00	1.00(2)	$EuGe_2$	powder	4.1044(4)	4.1044(4)	4.9996(1)	1.218	72.940(2)

Table 2. Single Crystal Crystallographic Data for $Eu(Zn_{1-x}Ge_x)_2$ (x = 0.50(2), 0.55(2), 0.67(2), 0.75(2)).

	$Eu(Zn_{0.50(2)}Ge_{0.50(2)})_2$	$Eu(Zn_{0.45(2)}Ge_{0.55(2)})_2$	$Eu(Zn_{0.33(2)}Ge_{0.67(2)})_2$	$Eu(Zn_{0.25(2)}Ge_{0.75(2)})_2$
Formula Weight (g mol^{-1})	289.96	290.68	292.41	293.57
Unit Cell Parameters (Å)	a = 4.3631(6)	a = 4.3116(6)	a = 4.2554(4)	a = 4.2358(6)
	c = 4.3014(9)	c = 4.418(1)	c = 4.5154(3)	c = 4.5759(9)
V ($Å^3$)	70.91(2)	71.13(2)	70.81(1)	71.10(2)
Density, calcd. (g cm^{-3})	6.789	6.769	6.799	6.771
Diffractometer	STOE IPDS	SMART Apex	SMART Apex	STOE IPDS
Index Ranges	$-6 \le h \le 6$, $-6 \le k \le -7$, $-6 \le l \le 6$	$-6 \le h \le 6$, $-6 \le k \le -6$, $-7 \le l \le 7$	$-6 \le h \le 6$, $-6 \le k \le 6$, $-7 \le l \le 7$	$-6 \le h \le 6$, $-6 \le k \le 6$, $-6 \le l \le 7$
No. Reflections	1296	1052	1033	1328
Independent Reflns	87 [R_{init} = 0.0550]	88 [R_{init} = 0.0325]	87 [R_{init} = 0.0312]	90 [R_{init} = 0.1013]
Data/Parameters	87/6	88/5	86/6	90/5
GOF on F^2	1.231	1.067	1.204	1.160
R indices [$I > 2\sigma(I)$]	$R1$ = 0.0344, $wR2$ = 0.0769	$R1$ = 0.0154, $wR2$ = 0.0321	$R1$ = 0.0131, $wR2$ = 0.0305	$R1$ = 0.0296, $wR2$ = 0.0667
R indices (all data)	$R1$ = 0.0427, $wR2$ = 0.0791	$R1$ = 0.0164, $wR2$ = 0.0325	$R1$ = 0.0131, $wR2$ = 0.0305	$R1$ = 0.0302, $wR2$ = 0.0668
Diff. peak and hole ($e^-/Å^3$)	1.724/−2.549	1.490/−0.648	1.106/−0.641	1.309/−2.455

Table 3. Anisotropic Displacement Parameters (Å^2) of Eu($Zn_{1-x}Ge_x$)$_2$ (x = 0.50(2), 0.55(2), 0.67(2), 0.75(2)). The exponent of the anisotropic displacement factor takes the form: $-2\pi^2[h^2a^{*2}U_{11} + \cdots + 2\ hka^*b^*U_{12}\ ]$. For the space group $P6/mmm$, $U_{13} = U_{23} = 0$.

atom	$U_{11} = U_{22}$	U_{33}	U_{12}	U^{a}_{eq}
		Eu($Zn_{0.50(2)}Ge_{0.50(2)}$)$_2$		
Eu	0.013(1)	0.013(1)	0.007(1)	0.013(1)
Zn/Ge	0.011(1)	0.021(1)	0.005(1)	0.014(1)
		Eu($Zn_{0.45(2)}Ge_{0.55(2)}$)$_2$		
Eu	0.009(1)	0.012(1)	0.005(1)	0.010(1)
Zn/Ge	0.008(1)	0.027(1)	0.004(1)	0.014(1)
		Eu($Zn_{0.33(2)}Ge_{0.67(2)}$)$_2$		
Eu	0.011(1)	0.011(1)	0.006(1)	0.011(1)
Zn/Ge	0.009(1)	0.044(1)	0.004(1)	0.021(1)
		Eu($Zn_{0.25(2)}Ge_{0.75(2)}$)$_2$		
Eu	0.017(1)	0.016(1)	0.010(1)	0.017(1)
Zn/Ge	0.018(1)	0.127(3)	0.009(1)	0.054(1)

[a] U_{eq} is defined as one-third of the trace of the orthogonalized U_{ij} tensor.

The Zn–Zn distances between adjacent distorted 6^3 nets (parallel to the *b*-axis) are ca. 7% longer than those within the net. These distortions produce zigzag ribbons of rectangles formed by Zn atoms along the *a*-axis. The Eu atoms are symmetrically displaced along the *c*-axis away from these networks.

The KHg_2-type phase also occurs in the powder patterns of Eu($Zn_{1-x}Ge_x$)$_2$ samples for $x < 0.50(2)$. Refinements of lattice constants suggest that Ge atoms replace a small number of Zn atoms, but we have no further chemical analysis of this observation and have not identified the upper bound of a single-phase, KHg_2-type Eu($Zn_{1-x}Ge_x$)$_2$ region. Analysis of the theoretical electronic structure of $EuZn_2$ also suggests that the orthorhombic KHg_2 structure type is a stable structure for Ge substitution for a small number of Zn atoms.

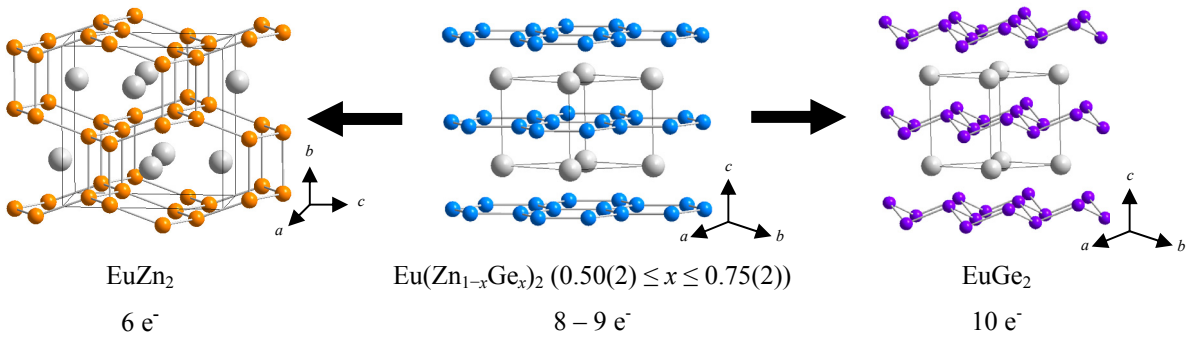

Figure 2. Crystal structures of $EuZn_2$ (KHg_2-type), $Eu(Zn_{1-x}Ge_x)_2$ ($0.50(2) \leq x \leq 0.75(2)$, AlB_2-type) and $EuGe_2$ ($EuGe_2$-type) with valence electron counts; Eu, gray; Zn, orange; Zn/Ge, blue; Ge, purple.

3.4.2 Region (3): $EuZn_{1-y}Ge_{1+y}$

As the amount of Ge increases in $Eu(Zn_{1-x}Ge_x)_2$, the AlB_2-type phase emerges in product mixtures, as shown in Figure 1b, and becomes single-phase when x reaches 0.50(2). This region remains single-phase up to $x = 0.75(2)$ suggesting a wide homogeneity range for this phase. Given this observation, we reformulate these ternary phases as $EuZn_{1-y}Ge_{1+y}$ ($0 \leq y \leq 0.5$). Furthermore, the extrapolation of measured resistivities show room-temperature values ca. 1.40×10^{-5} and 2.08×10^{-5} Ω·m, respectively, for $Eu(Zn_{0.45(2)}Ge_{0.55(2)})_2$ and $Eu(Zn_{0.33(2)}Ge_{0.67(2)})_2$, that decrease linearly over a temperature range from ca. 110-230 K which is indicative of either semiconducting or semimetallic behavior of these samples. Powder X-ray diffraction patterns of two AlB_2-type products are shown in Figure 1c and Figure 1d. Figure 3 shows how the lattice parameters, a and c, as well as the c/a ratio, vary with composition in these $EuZn_{1-y}Ge_{1+y}$ phase. As the Ge content increases from $EuZn_{1.00(2)}Ge_{1.00(2)}$ to $EuZn_{0.50(2)}Ge_{1.50(2)}$, a decreases from 4.3631(6) Å to 4.2358(6) Å, whereas c increases significantly from 4.3014(9) Å to 4.5759(9) Å, which results in monotonically increasing c/a ratios. Especially, for $y \leq 0.04$ ($x \leq 0.52$), $c/a < 1$, whereas for $y \geq 0.10$ ($x \geq 0.55$), $c/a > 1$. The crystal structures of these ternary compounds contains $^2_\infty[(Zn_{1-y}Ge_{1+y})_2]$ planar 6^3 net (Figure 2, middle) with both Zn and Ge atoms statistically distributed among the 2*d* sites.

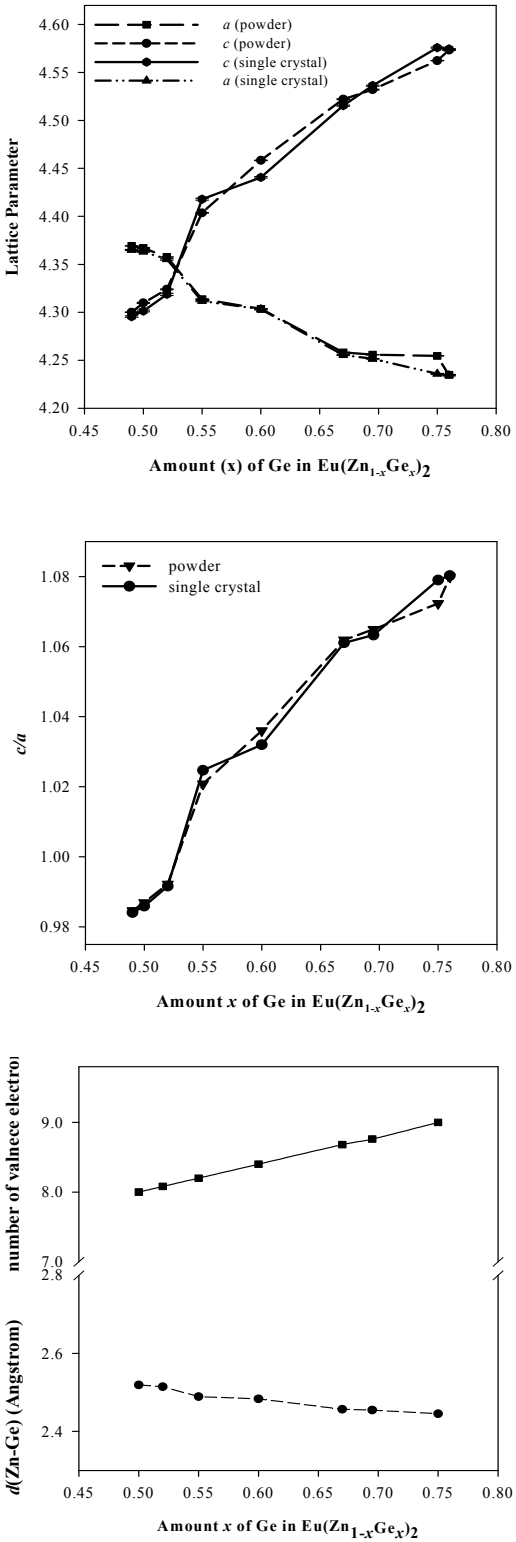

Figure 3. (Left) Lattice parameter *a, c*, (middle) *c/a* ratio and (right) the number of valence electron and Zn−Ge bond distance of the AlB_2-type phase of $Eu(Zn_{1-x}Ge_x)_2$ series as a function of the amount of Ge.

Eu atoms occupy the hexagonal prismatic voids between these nets. The experimentally observed Zn−Ge bond distances range from 2.5190(3) Å for $Eu(Zn_{0.50(2)}Ge_{0.50(2)})_2$ to 2.4455(3) Å for $Eu(Zn_{0.25(2)}Ge_{0.75(2)})_2$, a trend which is also illustrated in Figure 3. These bond distances are significantly shorter than the sum of the 12-coordinate, metallic radii of Zn and Ge (2.772 Å: *r*(Zn) = 1.394 Å, *r*(Ge) = 1.378 Å[24]), but are in excellent agreement with the sum of their covalent radii (2.47 Å: *r*(Zn) = 1.25 Å, *r*(Ge) = 1.22 Å[25]). We should note that the average Zn−Zn and Ge−Ge distances in $EuZn_2$ (2.699 Å)[16] and $EuGe_2$ (2.564(4) Å)[26] lie between the corresponding sums of metallic and covalent radii. In the ternary systems, therefore, the observed Zn−Ge bond distances indicate strong polar covalent interactions within the polyanionic nets, which will be further influenced by electron transfer from the electropositive Eu atoms to the electronegative Zn and Ge atoms. Aspects of the chemical bonding in these compounds have been carefully analyzed using electronic structure calculations, which can also account for the observed upper limit in Ge content in this homologous series, and will be discussed in a companion article.[27]

An additional significant result observed from the diffraction results of the $EuZn_{1-y}Ge_{1+y}$ phases is the substantial increase of U_{33}/U_{11} ratios of anisotropic displacement parameters as the Ge content increases. In $EuZn_{1.00(2)}Ge_{1.00(2)}$, this ratio is 1.9 and increases to 7.0 in $EuZn_{0.50(2)}Ge_{1.50(2)}$. As we mentioned earlier, all refinement attempts converge towards planar $^2_\infty[(Zn_{1-y}Ge_{1+y})_2]$ 6^3 nets, even when space groups are selected that allow the *z* parameter of the Zn and Ge sites to be free parameters. Nevertheless, the tendency to pucker the 6^3 nets increases steadily and significantly as the Ge content increases.[27]

3.4.3 Regions (4) and (5): $EuGe_2$

Beyond the experimentally observed upper limit of the single-phase region of the AlB_2-type structures in $Eu(Zn_{1-x}Ge_x)_2$, that is, $x > 0.75(2)$, the $EuGe_2$-type phase begins to appear as one of the majority phases in product mixtures as displayed in Figure 1e. However, lattice parameters determined from powder X-ray diffraction patterns of the two-phase products do not indicate significant Zn substitution for Ge in $EuGe_2$. At $x = 1$, the $EuGe_2$-type phase (Figure 2, right) crystallizes as a single-phase, binary compound and the powder X-ray diffraction pattern is shown in Figure 1f. The $EuGe_2$-type structure is derived from the

AlB_2-type structure by strong puckering of the hexagonal nets along the *c*-axis,[8,28] but unlike $EuZn_2$, there are no Ge−Ge contacts between the 6^3 nets.

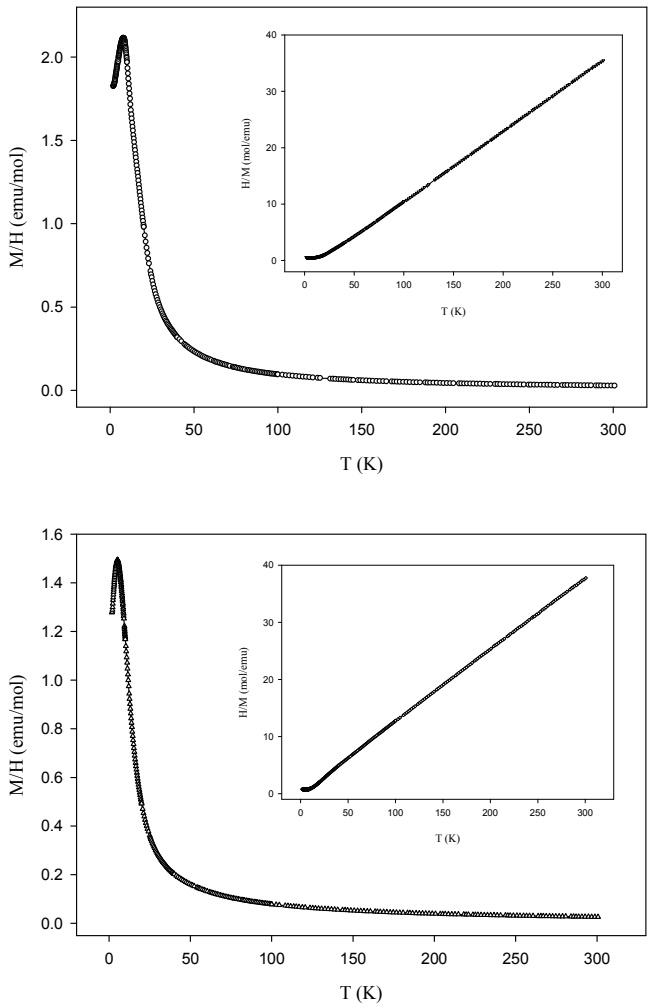

Figure 4. Temperature dependence of the magnetic susceptibilities and the reciprocal susceptibilities for $Eu(Zn_{0.48(2)}Ge_{0.52(2)})_2$ (left) and $Eu(Zn_{0.30(2)}Ge_{0.70(2)})_2$ (right).

3.4.4 Magnetic Susceptibilities

Temperature dependent magnetic susceptibilities and reciprocal susceptibilities are shown in Figure 4. The susceptibility behavior is dominated by the magnetic moment of Eu atoms and shows essentially Curie-Weiss behavior in the corresponding paramagnetic regions with antiferromagnetic (AFM) behavior for both $Eu(Zn_{0.48(2)}Ge_{0.52(2)})_2$ and

$Eu(Zn_{0.30(2)}Ge_{0.70(2)})_2$ at low temperatures. Effective magnetic moments for each compound, as calculated from the corresponding slopes of the $1/\chi$ vs. T plots and corrected for the temperature-independent diamagnetic terms, gave 7.98(1) μ_B for $Eu(Zn_{0.48(2)}Ge_{0.52(2)})_2$ and 7.96(1) μ_B for $Eu(Zn_{0.30(2)}Ge_{0.70(2)})_2$, both of which are very close to the value of the Eu^{2+} free ion, 7.94 μ_B, to indicate a $(4f)^7$ electronic configuration for Eu. $Eu(Zn_{0.48(2)}Ge_{0.52(2)})_2$ shows Curie-Weiss behavior at temperatures above 40.0(2) K, while below this temperature the susceptibility becomes dependent on the external magnetic field resulting in FM ordering with θ_p = +15.3(3) K. On the other hand, $Eu(Zn_{0.30(2)}Ge_{0.70(2)})_2$ displays Curie-Weiss paramagnetic above 45.0(2) K, but shows AFM ordering with $\theta_p = -1.95(3)$ K.

3.4.5 Structural Comparisons

The trends in phase behavior and crystal structures along the $Eu(Zn_{1-x}Ge_x)_2$ series can be attributed to the interplay among atomic sizes, valence electron counts, and types of chemical bonding, which can be estimated by the atomic electronegativities and their differences.[29] Common AB_2 structures for A coming from the alkaline earth elements and B coming from the tetrelides (Group 14), trielides (Group 13), and Zn group (Group 12) include the orthorhombic KHg_2-type, the trigonal $CaIn_2$-type, the hexagonal AlB_2-type, as well as the three Laves phase structure types: cubic $MgCu_2$-type and the hexagonal $MgZn_2$- and $MgNi_2$-types. A recent analysis of 6-electron and 8-electron AB_2 phases indicates that AlB_2-type structures are preferred for larger size ratios (V_A/V_B) and electronegativity differences ($\chi_B - \chi_A$), whereas the KHg_2-type structure becomes preferred as the corresponding electronegativity difference becomes smaller while the size ratio remains constant.[30] Laves phase structures dominate when these two parameters are smaller, which has been interpreted as effective packing of differently sized metal atoms.[31] The 12-coordinate metallic radius of Eu is 2.041 Å, which lies between that of Sr and Ba, and it is slightly more electronegative than these elements according to Pauling's scale. Therefore, for the $Eu(Zn_{1-x}Ge_x)_2$ series, we have a large size ratio ($V_{Eu}/V_{Zn/Ge}$) and an increasing electronegativity difference ($\chi_{Zn/Ge} - \chi_{Eu}$) as the Ge content increases, which implies a switch from orthorhombic KHg_2-type to hexagonal AlB_2-type phases.

The observed structural transformations along the $Eu(Zn_{1-x}Ge_x)_2$ series can be illustrated using the *Bärnighausen* tree[32-33] of group-subgroup relationships. As shown in Figure 5, the KHg_2-type structure derives from the ortho-hexagonal setting of the AlB_2-type structure (space group *C*2/*m*2/*m*2/*m*) via a *translationengleiche* transformation of index 3 (*t*3), followed by a *klassengleiche* transformation of index 2 (*k*2) to space group *Imma*. On the other hand, the trigonal $EuGe_2$-type structure arises by puckering of the hexagonal nets of the AlB_2-type structure. This symmetry reduction from AlB_2 to $EuGe_2$ occurs via a *translationengleiche* transformation of index 2 (*t*2) of *P*6/*m*2/*m*2/*m* to space group $P\bar{3}m1$.[29]

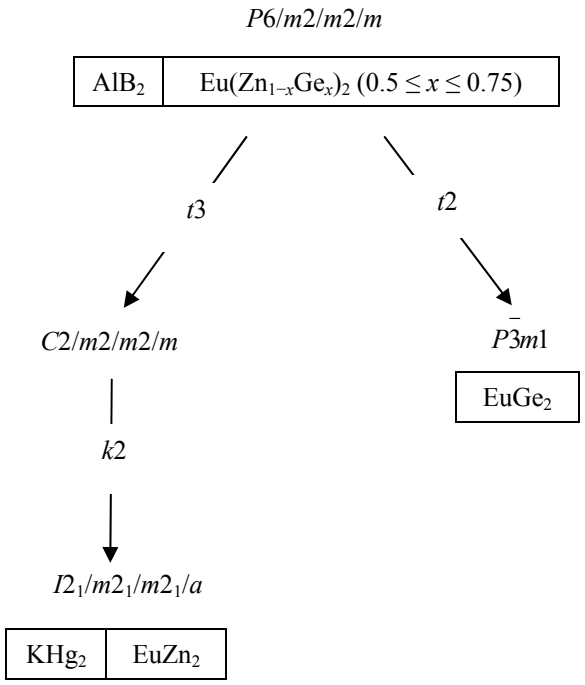

Figure 5. The *Bärnighausen* tree of group-subgroup relationship of the AlB_2 derivatives for KHg_2-type and $EuGe_2$-type structures.

A final structural consideration of the $Eu(Zn_{1-x}Ge_x)_2$ series is the monotonic increase of the $(c/a)^*$ ratios and unit cell volumes, which are listed in Table 1, as Ge content (x) increases, while the 6^3 nets vary from puckered in $EuZn_2$ to planar in $EuZn_{1-y}Ge_{1+y}$, and then to puckered in $EuGe_2$. The trend in unit cell volumes counters expectations based on the

relative sizes of Zn and Ge, whether 12-coordinate metallic or covalent radii are used. However, the increasing (c/a)* ratios suggest an increasing repulsion between adjacent $^{2}_{\infty}[(Zn_{1-x}Ge_x)_2]$ 6^3 nets. Both of these intriguing features will be addressed by analysis of electronic structure calculations in the companion paper.[27]

The relationship between the puckering of the 6^3 nets and the (c/a)* ratios also depends on the electronic structure.[8] At low (c/a)* ratios, puckering is driven by an increasing occupation of intra-plane π-antibonding orbitals through inter-plane p-p σ overlap. As the (c/a)* ratio increases, this σ overlap steadily decreases and the 6^3 network becomes planar, as in graphite. The puckering observed in $EuGe_2$, however, is attributed to the local electronic structure at Ge, which can be rationalized by the Zintl-Klemm concept.

3.4.6 The Zintl-Klemm Concept

At the Ge-rich end of the $Eu(Zn_{1-x}Ge_x)_2$ series, i.e., $EuGe_2$, the puckered, three-bonded $^{2}_{\infty}[Ge_2]$ net follows from the Zintl-Klemm formalism for $[Ge_2]^{2-}$, which is based on divalent Eu atoms. The five-electron Ge^-, which is isoelectronic with As, prefers a trigonal pyramidal coordination by using its valence electrons to form three two-center, two-electron σ-bonds and one lone pair. Implicit in this interpretation is an ionic formulation that follows the relative electronegativities: on the Pauling scale, χ(Eu) = 1.2 and χ(Ge) = 2.01. On the other hand, $EuZn_2$ is electron deficient, and does not satisfy the Zintl-Klemm formalism: the 4b-3D network of Zn atoms would require four valence electrons per Zn atom. Nevertheless, Zn is more electronegative than Eu: χ(Zn) = 1.65. Therefore, at some point along the $Eu(Zn_{1-x}Ge_x)_2$ series, this formalism, which relates local electronic structure and chemical bonding features, changes validity.

According to our results, this point occurs at "EuZnGe." For ternary Eu-Zn-Ge examples, the relative electronegativities suggest that Ge will attract electrons more strongly than Zn atoms. In light of our experimental results that the minimum Ge content is $EuZn_{1.00(2)}Ge_{1.00(2)}$ for the AlB_2-type phases, we can simply formulate this limiting composition as $Eu^{2+}Zn^{2+}Ge^{4-}$, which is a closed-shell compound. According to the Zintl-Klemm formalism, there will be no short Ge–Ge contacts within the planar 6^3 nets, so the

only solution is an alternant $^{2}_{\infty}[ZnGe]^{2-}$ net (see Figure 6a). As a corollary, there will be no short Zn–Zn contacts. Since X-ray diffraction could not distinguish Zn and Ge atoms, a completely random distribution of these two atoms does allow for homonuclear contacts, which will violate the Zintl-Klemm rules. Thus, we assume that each 6^3 net in $EuZn_{1.00(2)}Ge_{1.00(2)}$ is an alternant $^{2}_{\infty}[ZnGe]^{2-}$ net, but that they stack randomly along the *c*-axis. Furthermore, we express those $Eu(Zn_{1-x}Ge_x)_2$ phases for which the Zintl-Klemm formalism holds as $EuZn_{1-y}Ge_{1+y}$, for which $0 \le y \le 1$.

The Zintl-Klemm concept provides the relationship between the average formal charge and the average coordination for main group elements in a chemical structure. For example, in $EuZn_{1-y}Ge_{1+y}$, if we treat Eu and Zn as each donating two valence electrons to Ge, then the following relations hold:

$$\text{Average formal charge per Ge atom} = -\frac{4-2y}{1+y};$$

$$\text{Average valence electron count per Ge atoms} = 4+\frac{4-2y}{1+y} = \frac{8+2y}{1+y}; \text{ and}$$

$$\text{Average Ge–Ge connectivity} = 8-\frac{8+2y}{1+y} = \frac{6y}{1+y}.$$

These relationships are plotted in Figure 7. Therefore, for the $EuZn_{1-y}Ge_{1+y}$ series, the average formal charge at Ge can vary from –4 (EuZnGe) to –1 ($EuGe_2$), while the average number of Ge–Ge bonds per Ge atom change from 0 (EuZnGe) to 3 ($EuGe_2$). Integral formal charges at Ge also occur for $EuZn_{0.8}Ge_{1.2}$ (–3; 1-bonded Ge) and $EuZn_{0.5}Ge_{1.5}$ (–2; 2-bonded Ge). For a given chemical formula, however, there can be numerous structural solutions that will satisfy these predictions. According to our experimental results, the $EuZn_{1-y}Ge_{1+y}$ series adopts an AlB_2-type structure. Therefore, the Zintl-Klemm formalism should also be compatible with the structural constraints.

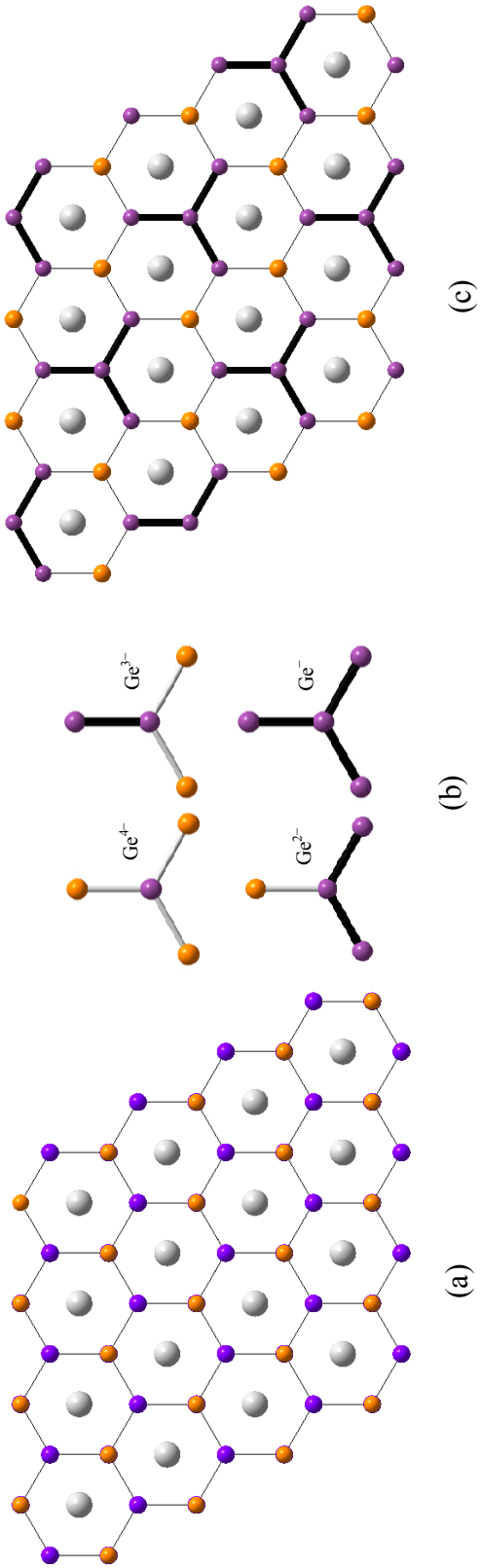

Figure 2. (a) Alternant 6^3 net of [ZnGe]; (b) the four different local coordination environments at Ge; and (c) the layer with $[Ge_4]$ stars. Eu, gray; Zn, orange; Ge, purple.

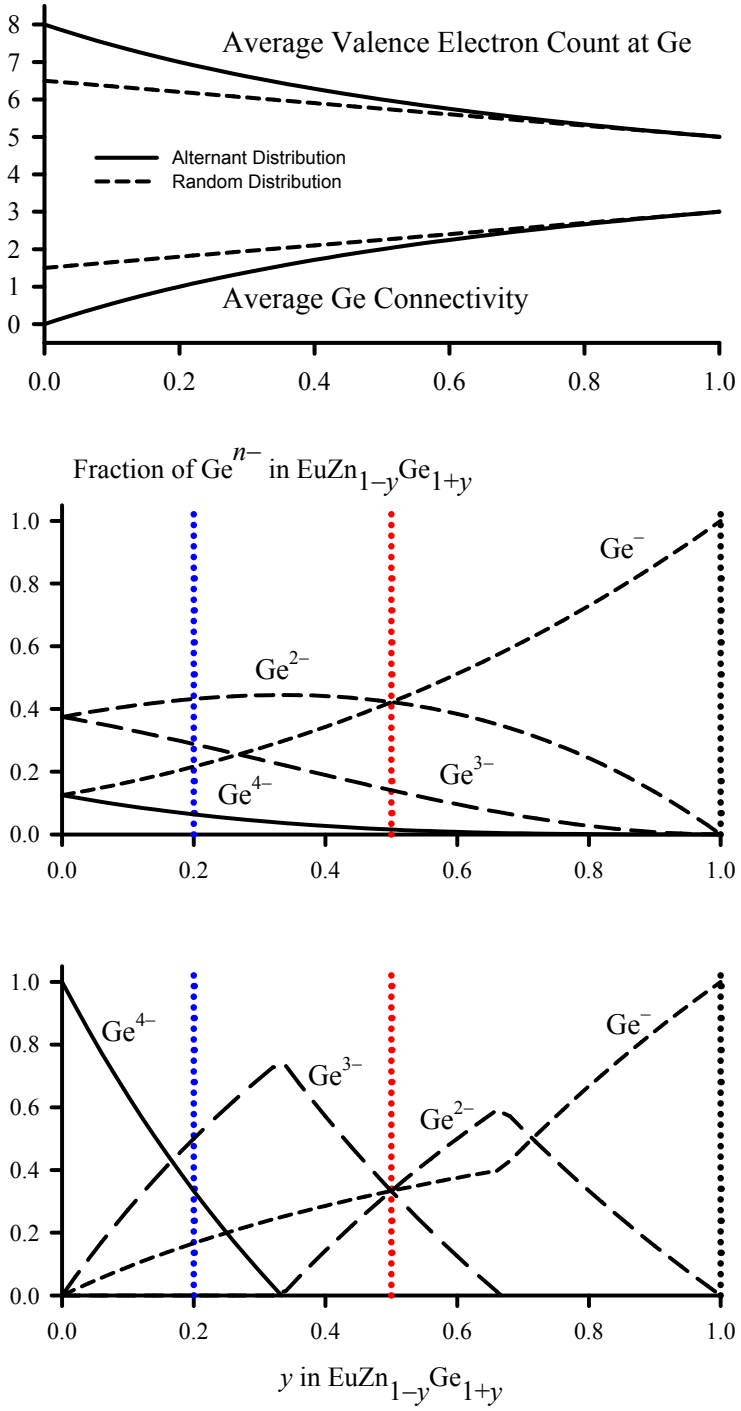

Figure 7. (Top) Average connectivity and valence electron count in $EuZn_{1-y}Ge_{1+y}$ for random and alternant 6^3 net. (Bottom) Concentrations of different Ge sites in random (middle) and alternant (bottom) in $EuZn_{1-y}Ge_{1+y}$.

In this regard, there are numerous potential solutions: we explore two specific cases here:

(1) Random *Distribution* of Zn and Ge Atoms in each 6^3 Net: In this model, the occupation of each atomic site of the honeycomb net is determined by the composition. The fraction of Zn atoms is $(1 - y)/2$; the fraction of Ge atoms is $(1 + y)/2$. Surrounding a Ge site, there will be a binomial distribution of (Zn_3), (Zn_2Ge), ($ZnGe_2$), and (Ge_3) coordination environments (shown in Figure 6b); each of these four concentrations are plotted as a function of y in Figure 7. If we use the Zintl-Klemm formalism for this random distribution and compare the average Ge valence electron count and Ge–Ge connectivity, there are significant deviations at low y values from the behavior anticipated by the equations above, which are derived just from the chemical formula. Specifically, for $y = 0$, i.e., EuZnGe, the random distribution of Zn and Ge atoms would predict an average formal charge at Ge of –2.5, which implies an average 1.5-bonded Ge atom. This evaluation of the local electronic structure at Ge, as well as Zn, contradicts expectations from electronegativity arguments.

(2) Random *Replacement* of Zn by Ge on the Alternant 6^3 Net: In this case, we start from the alternating $^2_\infty[ZnGe]^{2-}$ net anticipated for EuZnGe, and replace Zn by Ge atoms. This model guarantees keeping the Zn atoms widely separated so that there are no close Zn–Zn contacts. Furthermore, as the Ge content increases, the connectivity of Ge atoms steadily increases. At low concentrations, trigonal Ge_4 stars emerge. For these fragments to remain planar, we expect their formal charge to be –8: $[Ge_4]^{8-}$ would be isoelectronic to the planar CO_3^{2-} ion, and there are numerous examples of these ions.[34] On the other hand, simply from the Ge–Ge connectivity, the formal charge can be –10, but we could expect the central Ge atom to adopt a pyramidal local coordination. If we keep the Zn atoms most widely separated, Ge atoms will belong only to such Ge_4 stars in the limiting case, $Eu_3Zn_2Ge_4 = EuZn_{0.67}Ge_{1.33}$, which is illustrated in Figure 6c. Further replacement of Zn atoms by

Ge atoms creates larger Ge-based fragments that can grow continuously until $EuGe_2$ is achieved.

Thus, the Zintl-Klemm formalism provides a rationale for one end of the AlB_2-type $Eu(Zn_{1-x}Ge_x)_2$ phases, i.e., the Zn-rich end, but does not explain our experimental results at the Ge-rich end. Nevertheless, this electron counting rule eliminates a completely random distribution of Zn and Ge atoms within each 6^3 net as a viable solution that is compatible with both local geometrical structure and local electronic structure. Therefore, electronic structure theory is essential to provide an understanding of the relationship between chemical structure and electronic structure in these $Eu(Zn_{1-x}Ge_x)_2$ phases, theory which is the subject of the accompanying paper.[27]

3.5 Summary

We have prepared fifteen different compositions in the $Eu(Zn_{1-x}Ge_x)_2$ series ($0 \leq x \leq 1$) using induction melting and have characterized these products by powder and single crystal X-ray diffraction to study the influence of valence electron count on structural trends. As the Ge content increases, the $Eu(Zn_{1-x}Ge_x)_2$ series varies from the orthorhombic KHg_2-type to the hexagonal AlB_2-type, and finally to the trigonal $EuGe_2$-type, with two-phase regions between each of these three single-phase regions. $EuZn_2$ possibly allows restricted substitution of Zn by Ge atoms, whereas we do not observe Zn replacement for Ge in $EuGe_2$. The hexagonal AlB_2-type phases occur for a range of compositions from $EuZn_{1.00(2)}Ge_{1.00(2)}$ to $EuZn_{0.50(2)}Ge_{1.50(2)}$. Although structure solutions yield planar $^2_\infty[(Zn_{1-x}Ge_x)_2]\,6^3$ nets, the U_{33}/U_{11} ratios suggest increasing pyramidalization of these nets as the Ge content increases. Moreover, the diffraction results suggest that the distribution of Zn and Ge atoms in these nets is completely random along the *c*-axis, which also destroys possible superstructures in the *ab*-plane. The AlB_2-type phases show increasing separation between the 6^3 nets and unit cell volumes with increasing Ge content, which contrasts with the atomic size relationship between Zn and Ge. Magnetic susceptibility and temperature-dependent electrical resistivities indicate divalent Eu behavior as well as semiconducting or semimetallic

characteristics. Therefore, the Zintl-Klemm electron counting rule is an attractive formalism to account for the possible structural and physical behavior. However, the Zintl-Klemm formalism accounts for one end of the AlB_2-phases, i.e., $EuZn_{1.00(2)}Ge_{1.00(2)}$, but does not explain the upper bound in Ge content at $EuZn_{0.50(2)}Ge_{1.50(2)}$. To accomplish this, as well as to understand the structural and bonding features of the entire $Eu(Zn_{1-x}Ge_x)_2$ series, theoretical electronic structure calculations are imperative, and have been conducted and analyzed.[27]

Acknowledgements

This work was supported by NSF DMR 02−41092 and 06−05949. The authors are grateful to Dr. Warren Straszheim for the EDXS measurements at Iowa State University and to Dr. Walter Schnelle for magnetization measurements at Max−Planck−Institute for Chemical Physics of Solids in Dresden, Germany.

References

[1] Westbrook, J. H.; Fleisher, R. L., Ed.; *Intermetallic Compounds: Principle and Practice*s; Wiley, New York, **1995**.

[2] Nesper, R., *Prog. Solid State Chem*. **1990**, *20*, 1.

[3] Miller, G. J. In *Chemistry, Structure, and Bonding of Zintl Phases and Ions*; Kauzlarich, S. M., Ed.; VCH Publishers; New York, 1996; pp 1−59.

[4] Schäfer, H. *Ann. Rev. Mater. Sci.* **1985**, *5*, 1.

[5] Miller, G. J.; Lee, C.−S.; Choe, W. In *Highlights in Inorganic Chemistry*; Meyer, G., Ed.; Wiley−VCH; Heidelberg, **2002,** 21−54.

[6] Klem, M. T.; Vaughey, J. T.; Harp, J. G.; Corbett, J. D. *Inorg. Chem*. **2001**, *40*, 7020−7026.

Zintl, E.; Dullenkopf, W. *Z. Phy. Chem*. **1932**, *B12*, 183.

[7] Gout, D.; Benbow, E.; Gourdon, O.; Miller, G. J. *J. Solid State Chem*. **2003**, *176,* 538−548.

[8] Burdett, J. K.; Miller, G. J. *Chem. Mater*. **1990**, *2*, 12−26.

[9] You, T.−S.; Grin, Y.; Miller, G. J. *Inorg. Chem*. 2007, 46, 8801−8811.

[10] Huang, G. Q.; Liu, M.; Chen, L. F.; Xing, D. Y. *Physica C* **2005**, 423, 9−14.

[11] Imai, M.; Abe, E.; Ye, J.; Nishida, K.; Kimura, T.; Honma, K.; Abe, H,; Kitazawa, H. *Phys. Rev. Lett*. **2001**, *87*, 077003.

[12] Imai, M.; Nishida, K.; Kimura, T.; Abe, H. *Appl. Phys. Lett*. **2002**, *80*, 1019−1021.

[13] Imai, M.; Nishida, K.; Kimura, T.; Kitazawa, H.; Abe, H.; Kito, H.; Yoshii, K. *Physica C* **2002**, *382*, 361−366.

[14] Lorenz, B.; Lenzi, J.; Cmaidalka, J.; Meng, R. L.; Sun, Y. Y; Xue, Y. Y.; Chu, C. W. *Physica C* **2002**, *383*, 191−196.

[15] Nagamatsu. J.; Nakagawa, N.; Muranaka, T.; Zenitani, Y.; Akimitsu J. *Nature* **2001**, *410*, 63−64.

[16] Iandelli, A.; Palenzona, A. *Atti Accad. Naz. Lincei Rend. Sci. Fis. Mat. Natur*. **1964**, *37*, 165−168

[17] Hladyshevsky, E. I. *Dopov. Akad. Nauk.* **1964**, 2, 209−212

[18] Hunter, B. A.; Howard, C. J. *Rietica*; Australian Nuclear Science and Technology Organization: Menai, Australia, 2000.

[19] XRD single crystal software. Bruker Analytical X−ray System: Madison, WI, **2002**.

[20] *SHELXTL*, version 5.1; Bruker AXS Inc.: Madison, WI, **1998.**

[21] Pöttgen. R.; Johrendt. D., *Chem. Mater*. **2000**, *12,* 875−897

[22] Zhao, J. T.; Corbett, J. D. *Inorg. Chem*. **1995**, *34*, 378.

[23] Pöttgen, R.; Kotzyba, G.; Schappacher, F. M.; Mosel, B. D.; Eckert, H.; Grin. Y. *Z. Anorg. Allg. Chem*. **2001**, *627*, 1299−1304.

[24] Teatum, E.; Gshneidner, K. (Jr.); Waber, J.; *Radii of the Elements for CN12;* U. S. Department of Commerce; Washington, D. C., **1960**, LA−2345**.**

[25] Emsley, J. *The Elements*; Clarendon Press: Oxford, U. K., **1998**.

[26] Bobev, S.; Bauer, E. D.; Thompson, J. D.; Sarrao, J. L.; Miller, G. J.; Eck, B.; Dronskowski, R. *J. Solid State Chem*. **2004**, *177,* 3545−3552.

[27] You, T.−S.; Miller, G. J.A companion article proceeding.

[28] Pöttgen, R., *J. Alloys Compd.* **1996**, *243*, L1−L4.

[29] Hoffmann,R.; Pöttgen, R. *Z. Kristallogr*. **2001**, *216*, 127.

[30] Amerioun, S. *Phase and Structural Stability Principles of Polar Intermetallic AeE_4 and AeE_2 systems (Ae = Ca, Sr, Br; E = Al, Ga, In)*, Ph.D. thesis, Stockholm University, 2003.

[31] Johnston, R. L.; Hoffmann, R. *Z. Anorg. Allg. Chem*. **1992**, *616*, 105.

[32] Bärnighausen, H. *Common. Math. Chem*. **1989**, *9*, 139.

[33] Bärnighausen, H.; Müller, U. Symmetriebeziehungen zwischen den Raumgruooen als Hilfsmittel zur straffen Darstellung von Strukturzusammenhängen in der Kristallchemie. Universität Karlsruhe and Universität−Gh Kassel, Germany, **1996.**

[34] Eisenmann, B.; Klein, J; Somer, M. *Angew. Chem. Int. Ed. Engl*. **1990,** *29*, 87.

Supplementary Material 1

Figure S1. Temperature-dependent electrical resistivity of $Eu(Zn_{0.45(2)}Ge_{0.55(2)})_2$.

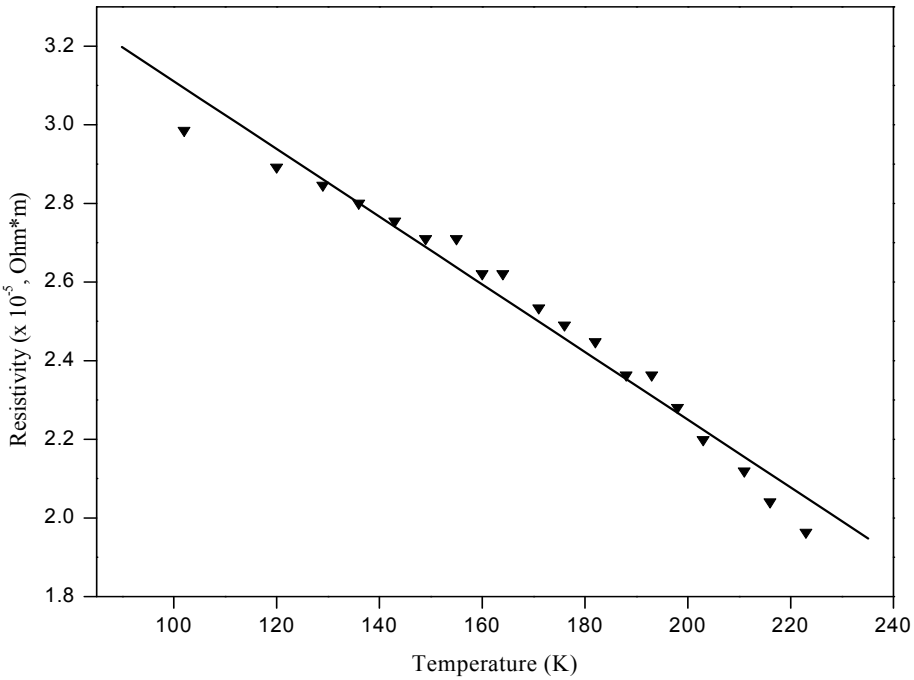

Figure S2. Temperature-dependent electrical resistivity of $Eu(Zn_{0.33(2)}Ge_{0.67(2)})_2$.

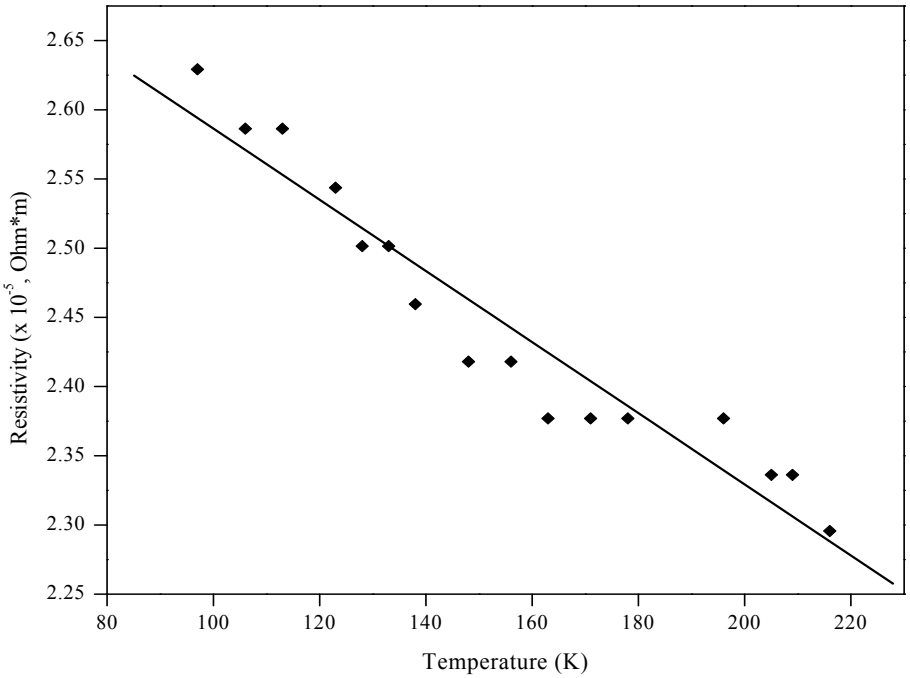

Supplementary Material 2

Incommensurately Modulated Peaks observed in $Eu(Zn_{0.25(2)}Ge_{0.75(2)})_2$

During the X-ray diffraction experiments, although we observed the increase of U_{33}/U_{11} ratios of anisotropic displacement parameters at the Zn/Ge site as the Ge content increases among the AlB_2-type phase, all refinement attempts converged towards planar $^2_\infty[(Zn_{1-y}Ge_{1+y})_2]$ 6^3 nets, even when space groups were selected that allowed the *z* parameter of the Zn and Ge sites to be free parameters. Nevertheless, the tendency to pucker the 6^3 nets increased steadily and significantly as the Ge content increased. Recently, we observed incommensurately modulated peaks along the *c*-axis from the Ge-rich end $Eu(Zn_{0.25(2)}Ge_{0.75(2)})_2$ using HRTEM. These peaks were also observed from a X-ray diffraction experiment using a STOE IPDS diffractometer with an exposure time of 10 min. We are currently attempting to solve this incommensurately modulated structure and to understand the difference from the AlB_2-type structure.

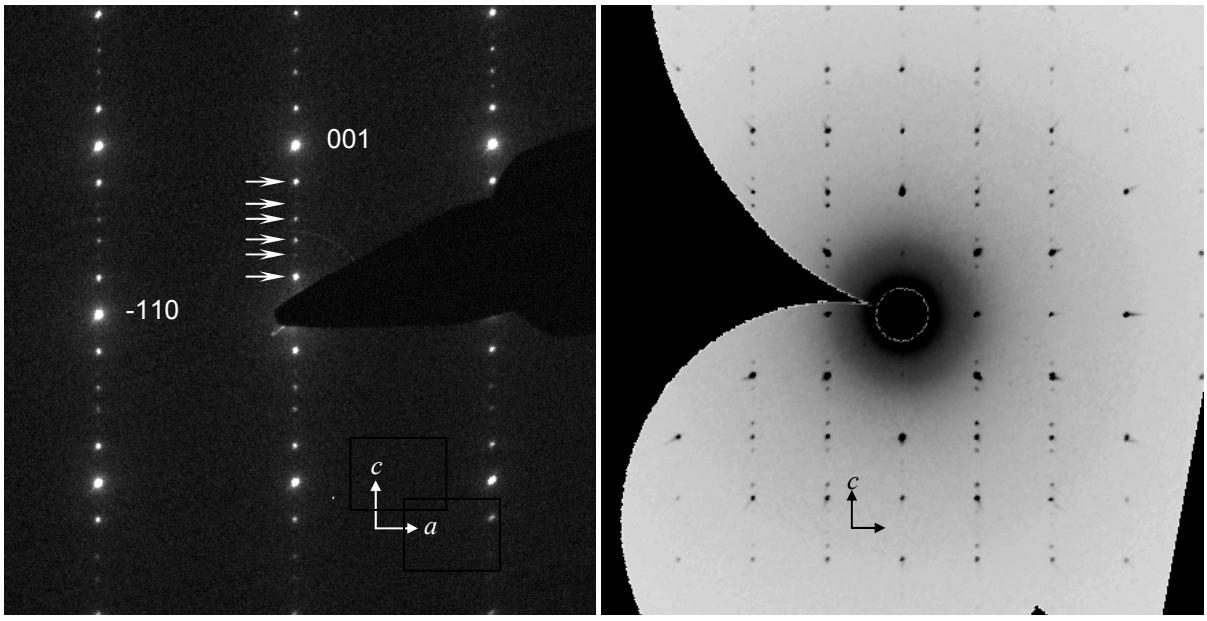

Figure 3. (Left) HRTEM of (1 1 0) plane, incommensurately modulated peaks are marked with arrows. (right) Reciprocal space displayed along the (1 1 0) plane.

CHAPTER 4

Theoretical Interpretation of the Structural Transition along the $Eu(Zn_{1-x}Ge_x)_2$ ($0 \leq x \leq 1$) Series

A paper to be submitted to *Journal of the American Chemical Society*

Tae-Soo You,[1,2] and Gordon J. Miller[1,3]

4.1 Abstract

The electronic structures of polar intermetallics $EuZn_2$, $Eu(Zn_{0.75}Ge_{0.25})_2$, $Eu(Zn_{0.5}Ge_{0.5})_2$, $Eu(Zn_{0.25}Ge_{0.75})_2$ and $EuGe_2$ have been investigated using the tight-binding, linear muffin-tin orbital (TB-LMTO) method to understand the structural preferences influenced by valence electron counts and to explain the observed homogeneity range of the AlB_2-type phase. The crystal orbital Hamilton population (COHP) curve for Zn−Zn contacts in $EuZn_2$ suggests the possibility of the homogeneity width of the KHg_2-type phase, which is observed from analysis of X-ray powder diffraction patterns. The density of states (DOS) and COHP analysis for a hypothetical Zn-rich compound, $Eu(Zn_{0.75}Ge_{0.25})_2$, indicates that keeping two distinct phases, $EuZn_2$ and $Eu(Zn_{1-x}Ge_x)_2$ ($0.5 \leq x \leq 0.75$) is more favorable than having a single Zn-rich composition adopting the AlB_2-type phase. Among ten structural models of the equiatomic compound $Eu(Zn_{0.5}Ge_{0.5})_2$, the one with heteroatomic Zn−Ge interactions both within and perpendicular to the 6^3 nets is energetically the most favorable structure. The experimentally observed Zn−Ge bond distance is attributed to the contribution of both σ- and π-bond interactions. Zn−Ge, Eu−Zn and Eu−Ge COHP curves that show

---

[1] Graduate student and Professor, respectively, Department of Chemistry, Iowa State University

[2] Primary researcher and author

[3] Author for correspondence

bonding character above the Fermi level explain the observed wide homogeneity width of the AlB_2-type phase. In particular, the theoretically predicted upper limit in composition is in excellent agreement with our experimental results. The Ge-rich structural model, $Eu(Zn_{0.25}Ge_{0.75})_2$, proves that 9 valence electrons are optimum for Zn−Ge bonding within these planar 6^3 nets of the AlB_2-type phase. The structure relaxation using VASP method revealed that the hexagonal layers tend to pucker rather than being planar. An Electron Localization Function (ELF) analysis for $Eu(Zn_{0.5}Ge_{0.5})_2$ reveals that there exists no two-center, two-electron bond or multi-centered interactions between interlayer Zn···Ge contacts.

4.2 Introduction

Polar intermetallic compounds represent a growing collection of inorganic solids to investigate relationships among structure, physical properties and chemical bonding.[1] They involve combinations of electropositive elements, i.e., alkali-, alkaline-earth or rare-earth elements, with electronegative metals close to the Zintl line. The electronegative metals typically form networks that either conform to simple electron counting rules, such as the Zintl−Klemm formalism,[2−4] or give rise to an electronic structure characterized by a pseudogap in the electronic density of states curve and optimized orbital interactions at the Fermi level.[5] The electropositive metals formally act like cations, as in classical valence compounds (Zintl phases), by providing their valence electrons to influence the structure of the electronegative component. Their surroundings also involve large coordination numbers. However, unlike Zintl phases, these "active" metals do not transfer all valence electrons to the electronegative component, but are involved in "lattice covalency" through their valence orbitals.[6] The presence of the pseudogap at the Fermi level can lead to potentially interesting physical properties, especially if rare-earth metals serve as the active metal due to partially filled 4*f* bands.[7] In general, polar intermetallics can be considered as a compound class intermediate between classical intermetallic compounds, such as Hume−Rothery electron phases, and Zintl−Klemm compounds.[2−4]

During our systematic investigation of the $Eu(M_{1-x}M'_x)_2$ series (M, M′ = Group 12−14 elements) to study the correlation among atomic, electronic, and possible magnetic structures

by varying atomic sizes and valence electron counts, we have observed a systematic structural variation within the $Eu(Zn_{1-x}Ge_x)_2$ system as x increases from the KHg_2-type to the AlB_2-type and, finally, the $EuGe_2$-type structure. These structure types differ in the networks formed by the electronegative components: (a) the KHg_2-type shows a four-bonded, three-dimensional (4b-3D) net with locally distorted tetrahedral coordination; (b) the AlB_2-type contains three-bonded, two-dimensional (3b-2D) planes with trigonal planar coordination; and (c) the $EuGe_2$-type exhibits 3b-2D puckered nets with local trigonal pyramidal environments. The transition from planar to puckered three-connected nets has been discussed frequently in the literature,[8,9] and is clearly related to the concentration of valence *s* and *p* electrons. In a recent study of EuGa*Tt* (*Tt* = Si, Ge, Sn),[9] atomic size also influences puckering of 3b-2D nets, which is further mediated by the role of valence orbitals at the active metal site by creating multi-center interactions. In this work, we explore the electronic structures of the $Eu(Zn_{1-x}Ge_x)_2$ ($0 \leq x \leq 1$) series by tight-binding, linear muffin-tin orbital calculation (TB-LMTO) to understand the influences of chemical bonding and valence electron count on the three observed structural types.

4.3 Electronic Structure Calculations

TB-LMTO calculations were carried out in the atomic sphere approximation (ASA) using the Stuttgart program.[11] Exchange and correlation were treated by the local spin density approximation (LSDA).[12] All relativistic effects except spin-orbit coupling were taken into account by using a scalar relativistic approximation.[13]

In the ASA method, space is filled with overlapping Wigner−Seitz (WS) spheres. The symmetry of the potential is considered spherical inside each WS sphere, and a combined correction is used to take into account the overlapping part.[14] The radii of WS spheres are obtained by requiring that the overlapping potential be the best possible approximation to the full potential, and were determined by an automatic procedure.[14] This overlap should not be too large because the error in kinetic energy introduced by the combined correction is proportional to the fourth power of the relative sphere overlap. No empty spheres (ES)[11] were necessary to fill the space of a unit cell. For our calculations on $EuZn_2$, $Eu(Zn_{0.75}Ge_{0.25})_2$, $Eu(Zn_{0.5}Ge_{0.5})_2$, and $Eu(Zn_{0.25}Ge_{0.75})_2$, the WS radii are: Eu, 2.241 Å; Zn, 1.351 Å; and Ge,

1.472 Å. For calculations on $EuGe_2$, they are: Eu, 2.241 Å; and Ge, 1.451 Å. The basis sets included 6*s*, 6*p* and 5*d* orbitals for Eu; 4*s*, 4*p* and 3*d* orbitals for Zn; 4*s*, 4*p* and 4*d* orbitals for Ge. The Eu 6*p* and Ge 4*d* orbitals were treated by the Löwdin downfolding technique[11–13] and the Eu 4*f* wavefunctions were treated as core functions occupied by 7 electrons. The crystal orbital Hamilton population (COHP) curves,[15] the integrated COHP values (ICOHPs) and electronic densities of states (DOS) were calculated to determine the relative influences of various interatomic orbital interactions. The ***k***-space integrations were performed by the tetrahedron method.[16] Self-consistent charge densities were obtained using a certain number of irreducible *k*-points in the Brillouin zone; these are 280-294 for ten hexagonal or orthorhombic structural models of $Eu(Zn_{0.5}Ge_{0.5})_2$; 118 for $EuZn_2$, $Eu(Zn_{0.75}Ge_{0.25})_2$ and $Eu(Zn_{0.25}Ge_{0.75})_2$; and 193 for $EuGe_2$. The contribution of the nonspherical part of the charge density to the potential was neglected.

Total energy calculations using VASP program[17-19] were also conducted for five different models of the $Eu(Zn_{0.25}Ge_{0.75})_2$ to find the most energetically favorable layered structure for the Ge-rich end composition. This program allows structure relaxations using pseudopotentials and a plane-wave basis set. The Kohn-Sham equations were solved self-consistently using an iterative matrix diagonalization method and an efficient Pulay mixing scheme of the charge density. In this system, we relaxed the free parameter of the atomic positions of Zn and Ge simultaneously with the *c*/*a* ratio for a set of constant volumes until forces converged to less than 0.005 eV/Å. The ultrasoft Vanderbilt-type pseudopotentials[20,21] were employed, and the actual valence electrons of the elements involved are indicated in the following configurations: Eu $5d^{10}6s^2$, Zn $3d^{10}4s^2$, and Ge $4s^24p^2$. Convergency was checked with respect to the plane-wave cutoff of 300 eV and the number of ***k***-points used in the summation over the Brillouin zone. These ***k***-points were obtained by the Monkhorst-Pack method[22] and sampled on a dense grid of 8 × 8 × 8.

The electron localization function[23] (ELF, η) was evaluated within the TB-LMTO-ASA Stuttgart program package[24] with an ELF module already implemented. To better understand features of local bonding environments for various compounds, a topological analysis of ELF was conducted with the program *Basin*.[25] The integrated electron density in each basin, which is defined by the surface of zero flux in the ELF gradient, analogous to the

procedure proposed by Bader for the electron density,[26] provides the basic information of electron counts for each basin, and additionally describes the bonding situation. The software *Amira*[27] was used to visualize ELF distributions of $Eu(Zn_{0.5}Ge_{0.5})_2$ and $EuGe_2$.

4.4 Results and Discussion

To understand the electronic structures and chemical bonding features that influence structural preferences for $Eu(Zn_{1-x}Ge_x)_2$ among three observed structural types, i.e., $EuZn_2$, $Eu(Zn_{1-x}Ge_x)_2$ ($0.50(2) \leq x \leq 0.75(2)$)[28] and $EuGe_2$, shown in Figure 1, electronic structure calculations were conducted on several structural models: (1) a binary, originally reported $EuZn_2$ structure[29] and a ternary derivative, $Eu(Zn_{0.75}Ge_{0.25})_2$, in the KHg_2-type structure, (2) ten ternary, equiatomic structural models, $Eu(Zn_{0.5}Ge_{0.5})_2$, with different atomic arrangements between Zn and Ge within or perpendicular to planar 6^3 nets and (3) two ternary, non-equiatomic structural models, i.e., a Zn-rich and a Ge-rich compound, with hypothetical atomic arrangements based on planar 6^3 nets of Zn and Ge atoms.

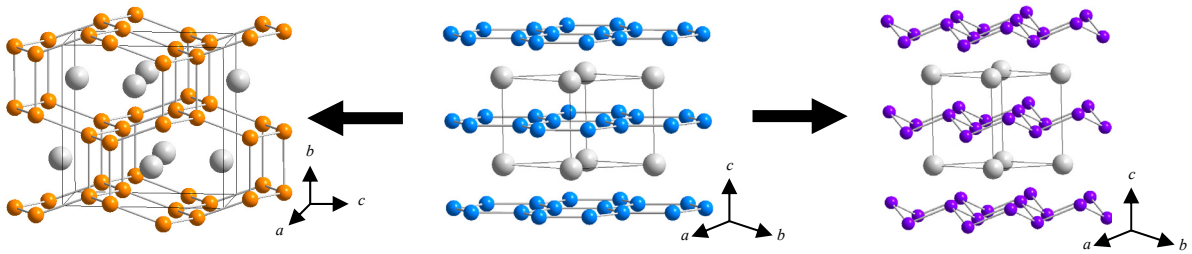

Figure 1. Crystal structures of $EuZn_2$ (KHg_2-type), $Eu(Zn_{1-x}Ge_x)_2$ ($0.50(2) \leq x \leq 0.75(2)$, AlB_2-type) and $EuGe_2$($EuGe_2$-type) with valence electron counts; Eu, gray; Zn, orange; Zn/Ge, blue; Ge, purple.

To create ten structural models of $Eu(Zn_{0.5}Ge_{0.5})_2$, both a hexagonal and orthorhombic unit cell were used. The orthorhombic unit cell is obtained by transforming the hexagonal AlB_2-type structure into an orthorhombic setting (*C* 2/*m* 2/*m* 2/*m*) via a *translationengleiche* transformation[30] of index 3 (*t*3) and followed by subsequent adjustments of the orthorhombic

unit cell depending upon the corresponding atomic arrangements. For the two non-equiatomic compounds, we selected two specific compositions to explain the behavior of Zn−Ge, Zn−Zn, and Ge−Ge orbital interactions: a hypothetical Zn-rich compound containing 7 valence electrons, $Eu(Zn_{0.75}Ge_{0.25})_2$; and a Ge-rich compound, which is the observed upper limit of the AlB_2-type structure containing 9 valence electrons, $Eu(Zn_{0.25}Ge_{0.75})_2$. To conduct electronic structure calculations for these specific compositions, we constructed two orthorhombic super cells (space group *Pcab*) of the hexagonal AlB_2-type cell with lattice parameters $2a_{hex} \times 2\sqrt{3}a_{hex} \times 2c_{hex}$. These parameters are a = 8.694 Å, b = 15.058 Å and c = 8.569 Å for $Eu(Zn_{0.75}Ge_{0.25})_2$; and a = 8.788 Å, b = 15.222 Å and c = 8.664 Å for $Eu(Zn_{0.25}Ge_{0.75})_2$ (see Figure 2). The unit cell volumes were obtained by summing the volumes of all WS spheres in the unit cell. More detailed structural information of these models are shown in Supplementary Material (Table S1).

In these cells, the hexagonal sheets are stacked alternately along the *c*-axis to maintain interlayer Zn···Ge contacts between planes because calculations on structural models of EuZnGe revealed interlayer Zn···Ge contacts to be energetically more stable than Zn···Zn and Ge···Ge contacts.

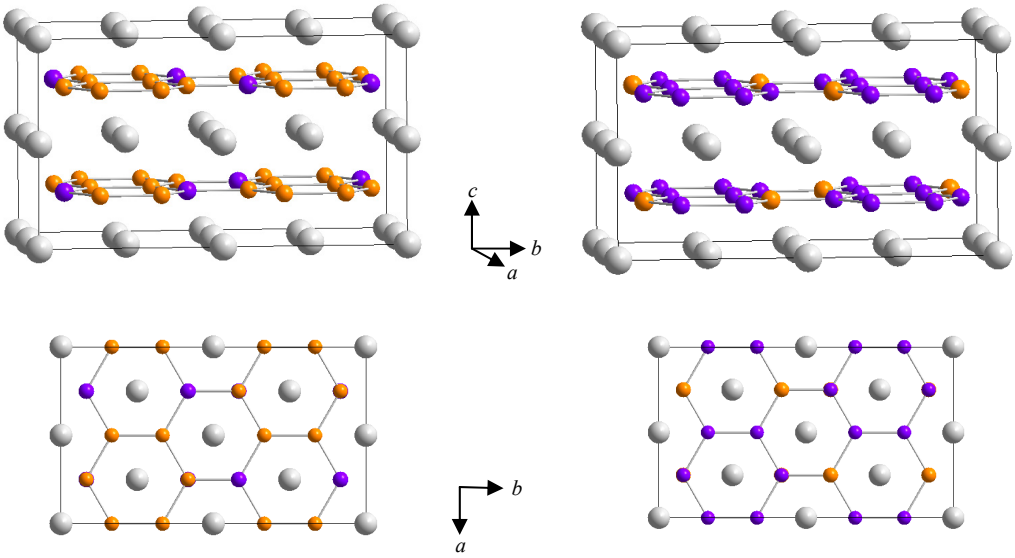

Figure 2. Two non-equiatomic structural models with Zn-rich (left) and Ge-rich (right) composition, respectively, in space group *Pcab*: Eu, gray; Zn, orange; Ge, purple.

4.4.1 $EuZn_2$

This compound adopts the orthorhombic KHg_2-type[29] structure with a 4b-3D anionic net of Zn atoms, each coordinated by a distorted tetrahedron, as shown in Figure 1. The 4b-3D net is constructed by puckered pseudo hexagonal 2D layers containing two slightly different Zn−Zn contacts of 2.688 Å and 2.699 Å. These puckered layers stack along the *c* direction to create interlayer Zn−Zn contacts of 2.907 Å, resulting in the 4b-3D net. Figure 3 displays its DOS and nearest neighbor Zn−Zn and Eu−Zn COHP curves; the Fermi level (E_F) is shown as a reference energy value in these curves. The total DOS (TDOS) curve up to ca. 2.8 eV below E_F contains more contribution from Zn valence orbitals. However, beyond this point, Eu 5*d* and 6*s* orbitals contribute more than Zn does to TDOS. The localized Zn 3*d* orbitals are observed between 7 and 8 eV below E_F. X-ray powder diffraction of Zn-rich $Eu(Zn_{1-x}Ge_x)_2$ phase suggests that Ge atoms can replace small amounts of Zn atoms in the KHg_2-type structure.[28] This observation can be understood from the COHP curve obtained from the combination of three types of Zn−Zn bonds, which shows significant bonding character in the 4b-3D net up to ca. 1.6 eV above E_F, where the curve switches its character from bonding to antibonding. This point corresponds to ca. 8 valence electrons and is located at local energy minimum of DOS curves. The Eu−Zn COHP curve also shows bonding character up to ca. 1.8 eV above E_F, then keeps nonbonding character up to ca. 3 eV above E_F which corresponds to ca. 10 valence electrons, where another local minimum appears in DOS curve. Thus, we conclude that the 4b-3D net in $EuZn_2$ can accept additional electrons provided by Ge substitution for Zn.

To verify this claim, we constructed a ternary structural model including Ge substitution for 25 % of Zn in $EuZn_2$ in the KHg_2-type structure, where substituting Ge atoms are isolated from one another (see Figure 4, top). More detailed structural information including atomic coordinates is displayed in Supplementary Material (Table S2). DOS and COHP curves are also shown in Figure 4 (bottom). In particular, Zn−Ge COHP is optimized at ca. 0.4 eV below E_F, which corresponds to 6.48 valence electrons and $Eu(Zn_{0.88}Ge_{0.12})_2$, and shows weak antibonding character up to E_F. This result supports that the KHg_2-type structure can hold up at least 6.48 valence electrons. Although Zn−Zn COHP curve maintains bonding character up to ca. 1 eV, which corresponds to 8 valence electrons as in $EuZn_2$, the

KHg_2-type structure would not bind these valence electrons since the Zn−Ge COHP curve has antibonding character beyond this count. In that sense, there is high possibility of existence of homogeneity width for the KHg_2-type phase according to the electronic structure of $EuZn_2$ and $Eu(Zn_{0.88}Ge_{0.12})_2$. However, we did not pursue any further analysis for this phase.

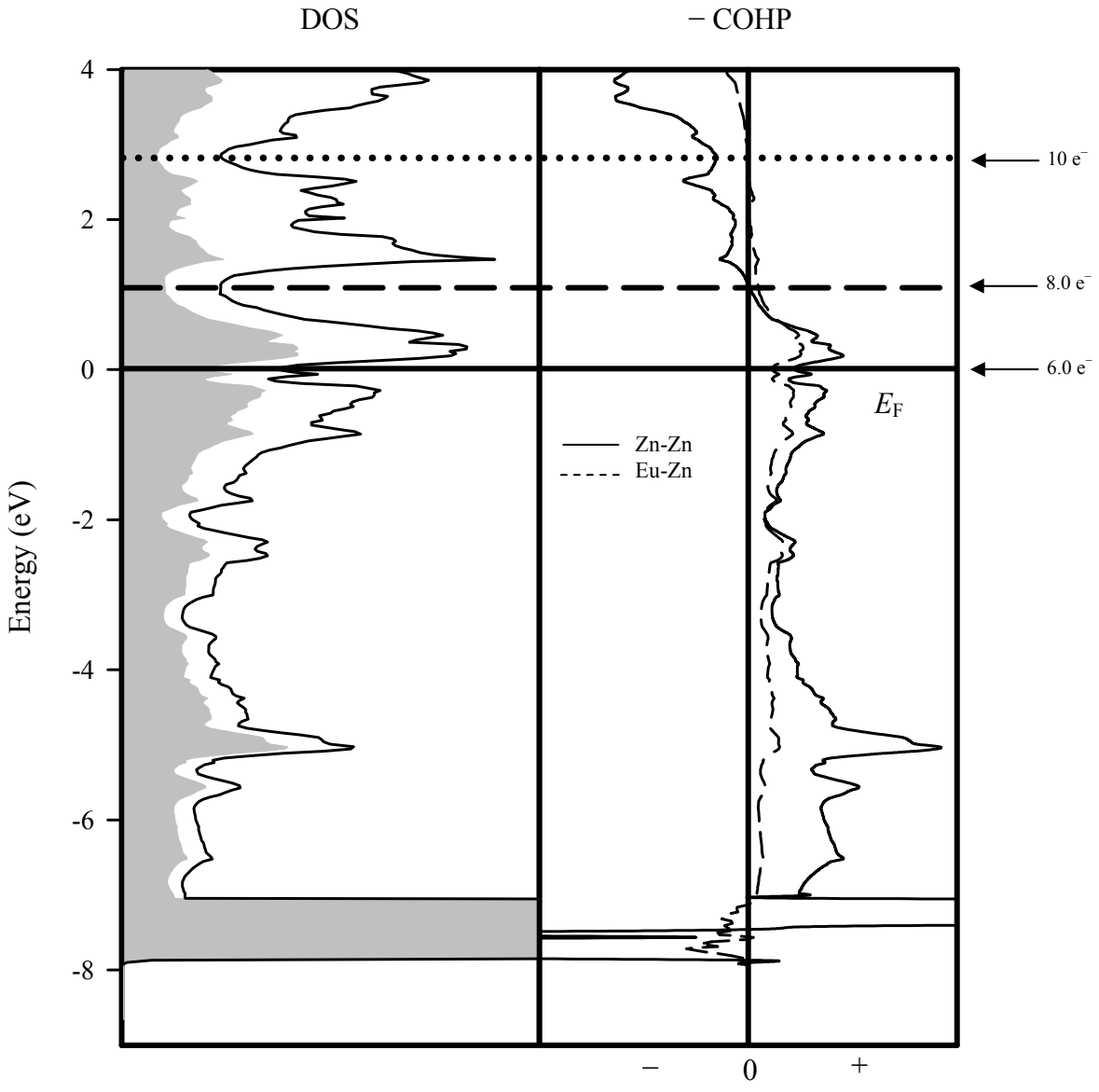

Figure 3. DOS and COHP curves for $EuZn_2$. (Left) Total DOS (solid line), Eu PDOS (white region), and Zn PDOS (gray region). (Right) Eu−Zn and Zn−Zn COHP curves. The Fermi level is indicated by the solid line and is the energetic reference (0 eV). The number of valence electrons, which corresponds to the Fermi level and the optima of COHP curves, are also shown.

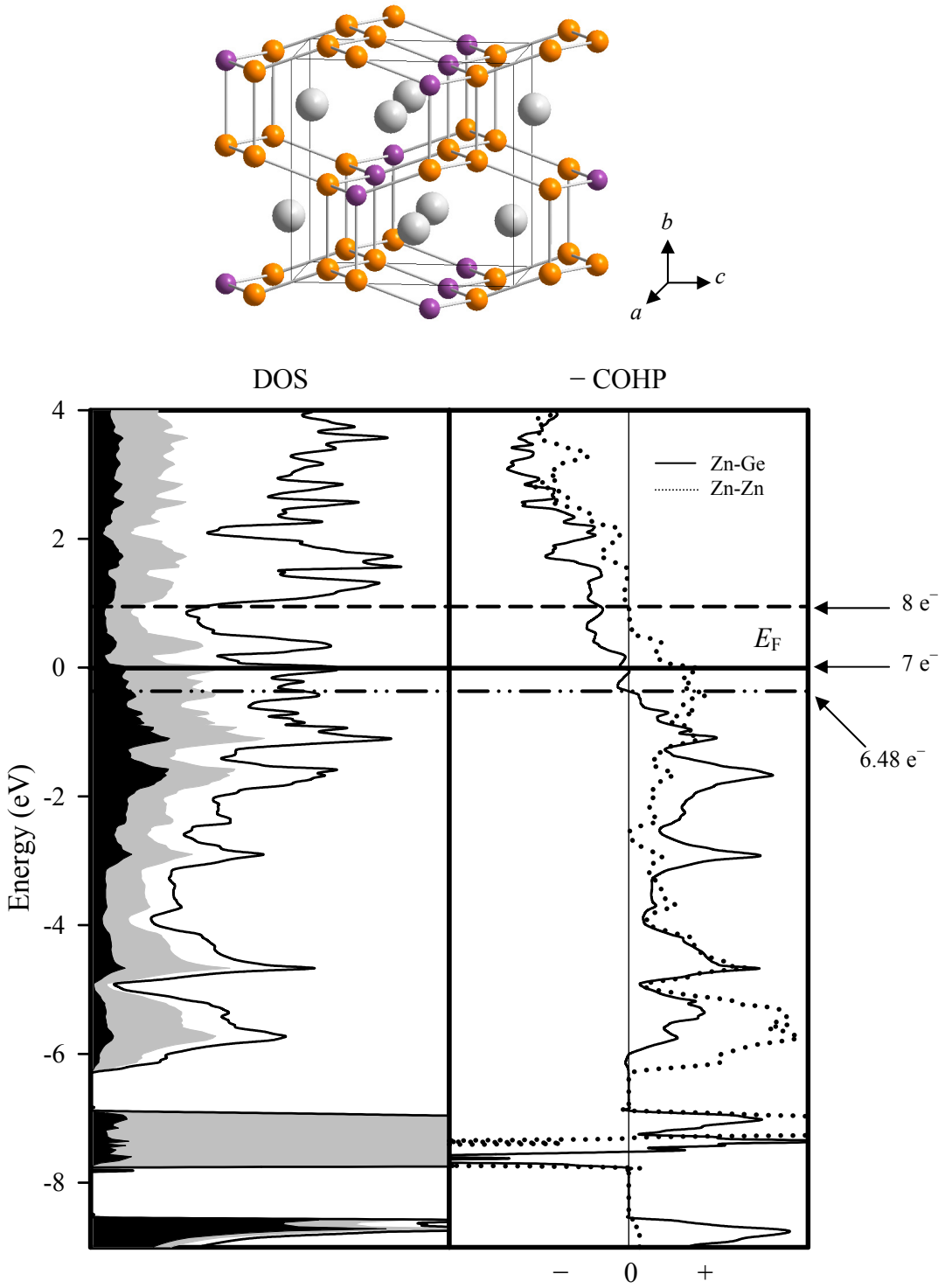

Figure 4. (Top) Crystal structure of $Eu(Zn_{0.75}Ge_{0.25})_2$ in the KHg_2-type structure: Eu, gray; Zn, orange; Ge, purple. (Bottom, left) Total DOS (solid line), Eu PDOS (white region), Zn PDOS (gray region) and Ge PDOS (black region). (Right) Zn−Ge (solid line) and Zn−Zn (dot line) COHP curves. The Fermi level is indicated by the solid line and is the energetic reference (0 eV). The numbers of valence electrons, which correspond to the Fermi level and optima of COHP curves, are also shown.

4.4.2 $EuZn_{1+x}Ge_{1-x}$

In a unit cell of a hypothetical Zn-rich compound with planar hexagonal nets, $Eu(Zn_{0.75}Ge_{0.25})_2$ containing 7.0 valence electrons, there must be Zn−Zn contacts, whereas no Ge−Ge contacts are expected since Ge atoms are most reduced with the highest negative formal charge (see Figure 2, left). The minimum number of valence electrons for an $Eu(Zn_{1-x}Ge_x)_2$ planar 6^3 net is 8 according to our experimental results.[28]

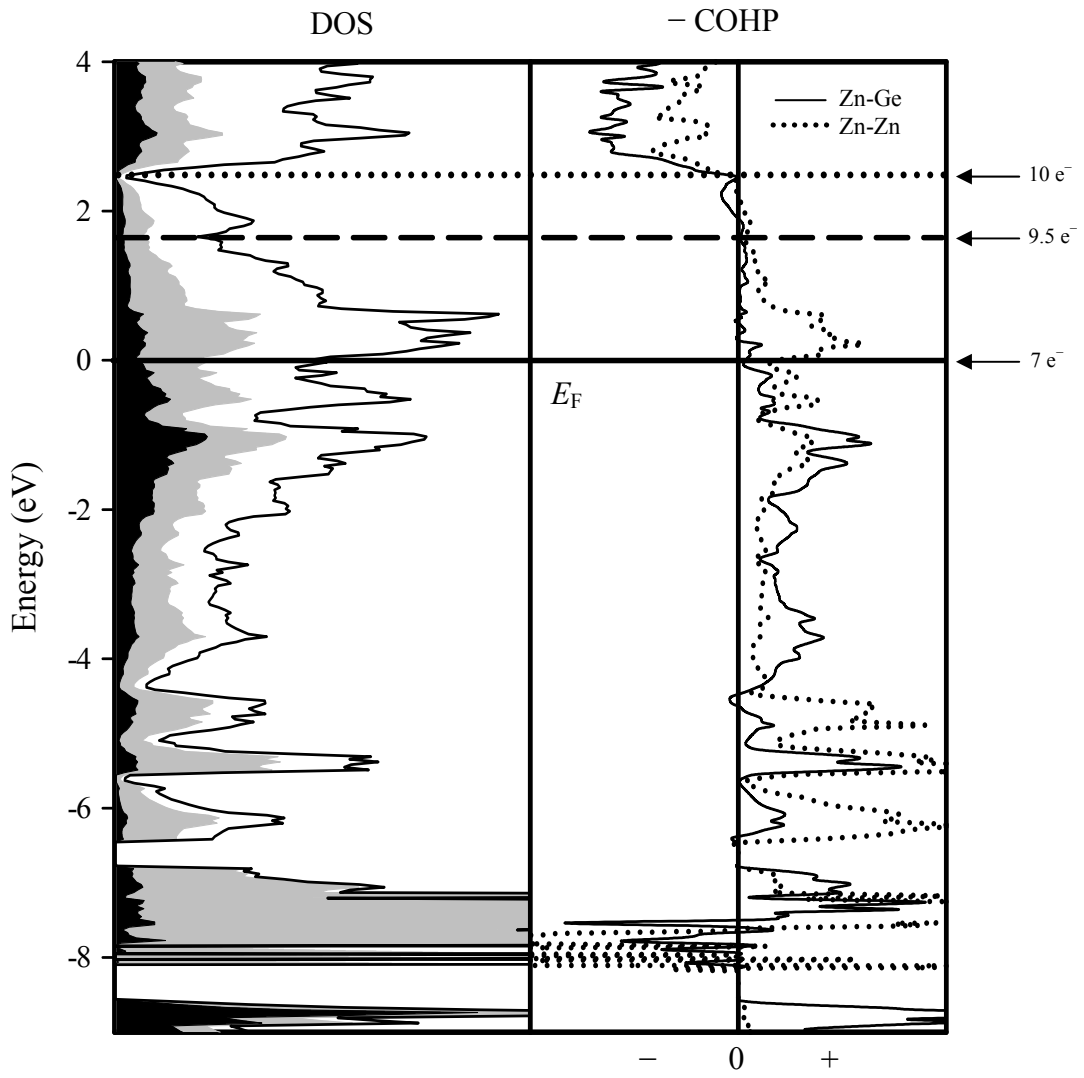

Figure 5. DOS and COHP curves for $Eu(Zn_{0.75}Ge_{0.25})_2$. (Left) Total DOS (solid line), Eu PDOS (white region), Zn PDOS (gray region), and Ge PDOS (black region). (Right) Zn−Ge (solid line) and Zn−Zn (dot line) COHP curves. The Fermi level is indicated by the solid line and is the energetic reference (0 eV). The numbers of valence electrons, which corresponds to the Fermi level, two optima of TDOS curve are also shown.

Since this model contains less than the required number of valence electrons for $Eu(Zn_{1-x}Ge_x)_2$ planar 6^3 net, the structure is purely hypothetical and constructed for calculating the electronic structures to understand orbital interactions in a Zn-rich unit cell. The DOS and nearest neighbor Zn−Zn and Zn−Ge COHP curves are illustrated in Figure 5. E_F (7 electrons) is the reference energy value. Zn 3*d* orbitals are localized around 7 eV below E_F and strong valence orbital mixing between Zn 4*s* and 4*p*, and Ge 4*s* and 4*p* are observed in the range between 6.5 eV below E_F and E_F itself. The Zn−Ge COHP curve is nearly optimized at E_F and maintains non-bonding character up to ca. 1.8 eV above E_F corresponding to 9.5 valence electrons. The Zn−Zn COHP curve shows strong bonding character at E_F and optimized at ca. 2.5 eV above E_F, which corresponds to 10 valence electrons, where a pseudogap is observed in a TDOS curve. In fact, this Zn−Zn COHP curve displays a very similar pattern to that of $EuZn_2$.

The total electronic energy of this Zn-rich compound was calculated and compared with the half of the summed total electronic energies of $EuZn_2$ and $Eu(Zn_{0.5}Ge_{0.5})_2$ (AlB_2-type) to find which structural type is preferred for a given composition. The radii of WS spheres of elements were kept constant to provide identical calculation condition. The result revealed that having two distinct phases of $EuZn_2$ and $Eu(Zn_{0.5}Ge_{0.5})_2$ is energetically more favorable than having one Zn-rich compound by 116.6 meV. This explains the reason that there is no Zn-rich compound observed for $Eu(Zn_{1-x}Ge_x)_2$ ($0 < x < 0.5$), but rather separated two phases exist.

4.4.3 $Eu(Zn_{0.5}Ge_{0.5})_2$

Due to the small difference between the X-ray scattering factors of Zn and Ge, no indication of long-range ordering of these two elements could be detected by X-ray diffraction experiments within or perpendicular to the 6^3 nets. However, a certain degree of short-range ordering can be considered between Zn and Ge atoms.[31−32] Thus, we constructed ten ternary structural models (see Figure 6) by differentiating Zn and Ge atomic arrangements within or perpendicular to the 6^3 nets. Total electronic energy of each structure was calculated and compared to find the energetically most favorable structure.

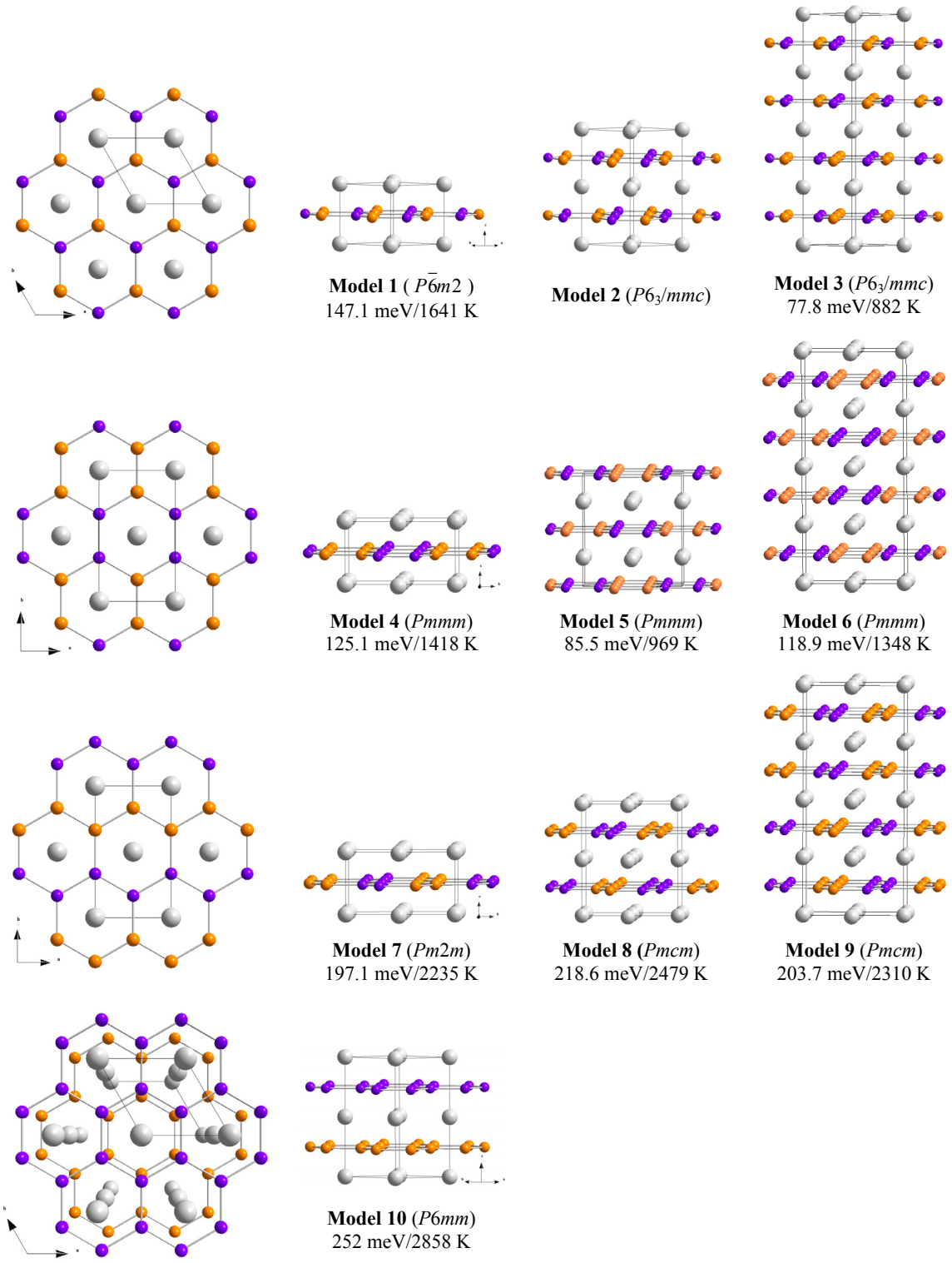

Figure 6. Ten ternary, equiatomic structural models of $Eu(Zn_{0.5}Ge_{0.5})_2$. See text for detail description: Eu, gray; Zn, orange; Ge, purple. Space groups and relative electronic energies per formula unit compare to Model 2 are also shown.

Models 1−3 contain alternating Zn and Ge atoms on the 6^3 sheets where each Zn/Ge atom is connected to three Ge/Zn atoms. However, these models differ from each other in such a way how the 6^3 sheets stack along the *c*-axis: (1) eclipsed to create Zn···Zn and Ge···Ge interactions between planes, space group $P\bar{6}m2$, Z = 1; (2) alternating to create Zn···Ge interactions between planes, space group $P6_3/mmc$, Z = 2; and (3) a 1:1 intergrowth of models 1 and 2 to create Zn···Ge, Zn···Zn, and Ge···Ge interactions between planes, space group $P6_3/mmc$, Z = 4. On the other hand, for models 4−10, homoatomic contacts occur within the 6^3 nets. For models 4−6, Zn and Ge atoms alternate along one-axis forming heteroatomic zigzag chains, whereas homoatomic Zn−Zn or Ge−Ge bonds exist along the orthogonal-axis. The stacking sequences of hexagonal sheets along *c*-axis for models 4−6 are also the same as those of models 1−3 and the unit cells are orthorhombic. For models 7−9, Zn/Ge atoms are connected to the same atoms along one-axis resulting in homoatomic zigzag chains, whereas heteroatomic Zn−Ge bonds exist along the orthogonal-axis. These three models differ from each other in stacking sequence of the hexagonal sheets along *c*-axis as for models 1−3. The corresponding unit cells are orthorhombic. Model 10 shows a hexagonal unit cell consisting of Zn-only and Ge-only hexagonal sheets alternating along the *c*-axis. All electronic structure calculations were conducted under identical conditions, where WS radii of elements are; r(Eu) = 2.241 Å, r(Zn) = 1.351 Å and r(Ge) = 1.472 Å, and irreducible *k*-points of in the Brillouin zone were kept between 280−294. More detailed structural information including atomic coordinates of each model is shown in Supplementary Material (Table S3).

On the basis of the number of the heteroatomic or homoatomic interactions on the 6^3 nets, ten structural models can be categorized into four groups: (1) models 1−3, three heteroatomic interactions; (2) models 4−6, two hetero- and one homoatomic interactions; (3) models 7−9, one hetero- and two homoatomic interactions; and (4) Model 10, three homoatomic interactions. As the 6^3 net contains more heteroatomic interactions, the structure is energetically more stable. Therefore, model 2 and 3 in group (1) are more stable than models in group (2). In the same sense, models in group (2) are more stable than models in group (3). Although model 1 in group (1) is exceptional from this trend, model 10 is indisputably the least stable. Among models in each group, interlayer atomic interactions

play an important role, which affects structural stability. However, because of the relatively longer interlayer atomic distances and intervention of Eu 5*d* orbitals locating between these layers, the number of heteroatomic interactions among models in the same group is not significantly as decisive as among different groups to reveal energetically most stable structure.

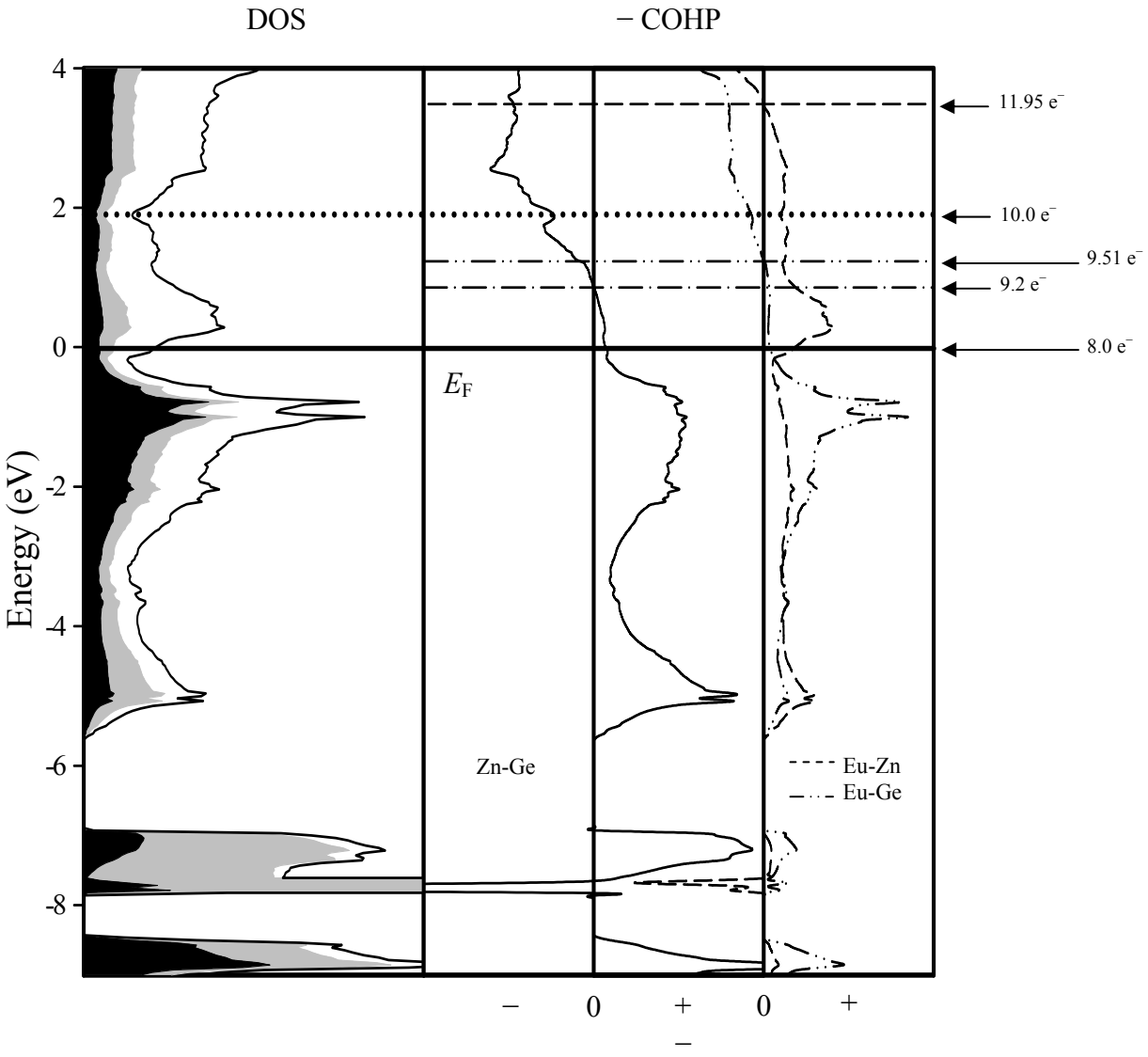

Figure 7. DOS and COHP curves for $Eu(Zn_{0.5}Ge_{0.5})_2$. (Left) Total DOS (solid line), Eu PDOS (white region), Zn PDOS (gray region), and Ge PDOS (black region). (Right) Zn−Ge, Eu−Zn and Eu−Ge COHP curves. The Fermi level is indicated by the solid line and is the energetic reference (0 eV). The numbers of valence electrons, which correspond to the Fermi level, the local minimum energies of TDOS curve, and the optima of COHP curves are also shown.

According to total electronic energies included in Figure 6, model 2 is energetically the most favorable structure, which contains only heteroatomic Zn−Ge interactions within and perpendicular to the hexagonal nets. Thus, although we cannot observe atomic ordering between Zn and Ge using X-ray diffractions, short-range in-plane and out-of-plane ordering should be considered. Therefore, all subsequent theoretical calculations for $Eu(Zn_{0.5}Ge_{0.5})_2$ are conducted using model 2. Figure 7 displays DOS and COHP curves of this equiatomic compound, where E_F is the reference energy value in these curves and is located slightly above a pseudogap in the DOS. These DOS and COHP curves are very similar to those of EuGaSi, which also adopts ternary version of the AlB_2-type structure.[10] Throughout the entire DOS curve, significant mixing between valence orbitals of Eu, Zn and Ge atoms are observed.

The region below E_F shows significant contributions from Ge 4*p* and Eu 5*d* orbitals with small contributions from Zn 4*p*, whereas the region above E_F is dominated by Eu 5*d* orbitals. Both DOS curves and electronic band structures (available in Supplementary Material, Figure S5 and S6) indicate that the majority of Ge 4*p* orbitals are located mostly within 5 eV below E_F, implying they are formally filled with electrons, whereas the majority of Zn 4*p* orbitals are centered far above E_F, between 7 and 15 eV above E_F, suggesting they are formally empty. Our experimental results revealed a Zn−Ge bond distance of 2.5190(3) Å[28] on the hexagonal nets, which is significantly shorter than the sum of 12-coordinated metallic radii of Zn and Ge (2.772 Å: *r*(Zn) = 1.394 Å, *r*(Ge) = 1.378 Å[33]), but are in excellent agreement with the sum of their covalent radii (2.47 Å: *r*(Zn) = 1.25 Å, *r*(Ge) = 1.22 Å[34]). Moreover, the average Zn−Zn and Ge−Ge distances in $EuZn_2$ (2.699 Å)[29] and $EuGe_2$ (2.564(4) Å)[35] lie between the corresponding sums of metallic and covalent radii. Therefore, the observed Zn−Ge bond distances indicate strong polar covalent interactions within the polyanionic nets. According to the fatband analyses shown in Supplementary Material (Figure S5 and S6), this Zn−Ge distance can be attributed to participation of both σ-bonding interactions, which corresponds to the bands spanning between ca. 6 and 0.2 eV below E_F, and π-bonding interactions, which corresponds to bands starting ca. 4.2 eV below E_F. Therefore, the 6^3 layer containing Zn and Ge atoms can be seen as graphite-like layers. In that sense, the chemical bonding of EuZnGe can be understood using Zintl−Klemm

concept,[2–4] and a formulation can be written $Eu^{2+}[ZnGe]^{2-}$ with divalent Eu atoms.[28] Thus, the $^{2}_{\infty}[ZnGe]^{2-}$ anionic net is isoelectronic with elemental graphite. Orbital interactions between $^{2}_{\infty}[ZnGe]$ planes along the *c*-axis occur via Eu 5*d* orbitals which drop below E_F (see Supplementary Material, Figure S5 and S6). Thus, Zn−Ge orbital interactions are predominantly 2-dimansional in character along the hexagonal nets.[10,36]

In the Zn−Ge COHP curve (Figure 7, right), bonding character changes to antibonding character at ca. 1.2 eV above E_F, which corresponds to 9.2 valence electrons. As discussed earlier for Zn−Zn contacts in the 4b-3D nets of $EuZn_2$, this implies that these hexagonal nets can accommodate additional valence electrons. Moreover, Eu−Ge and Eu−Zn COHP curves also show their bonding or nonbonding character up to this energy level. Therefore, the ternary AlB_2-type structure can accommodate more than 8.0 valence electrons and can adopt Ge-rich composition without building up any antibonding character within the nearest neighboring contacts, which is eventually influential to the phase separation into the AlB_2-type and the $EuGe_2$-type structure. Although Eu−Ge and Eu−Zn COHP curves maintain their bonding character, respectively, up to 1.5 and 3.5 eV above E_F, which corresponds to 9.51 and 11.95 valence electrons, we do not expect more than approximately 9.2 valence electrons for the Ge-rich system because the Zn−Ge COHP already begins to have antibonding character beyond this count. Therefore, on the basis of COHP curve analyses, we can expect that the experimentally obtainable upper limit in composition for the AlB_2-type phase would be approximately $Eu(Zn_{0.20}Ge_{0.80})_2$. According to our experimental results, that composition is $Eu(Zn_{0.25(2)}Ge_{0.75(2)})_2$, which contains 9.0 valence electron.[28] This is in excellent agreement with the results of theoretical calculations discussed in this article.

4.4.4 $EuZn_{1-x}Ge_{1+x}$

The unit cell of $Eu(Zn_{0.25}Ge_{0.75})_2$ with 9 valence electrons has the same atomic coordinates as those in Zn-rich structural model shown earlier, but with a larger unit cell volume and switched Zn and Ge positions. In a unit cell (see Figure 2, right), we arranged Zn and Ge atoms in such a way that Zn atoms are isolated from one another, whereas there are Ge−Ge contacts on hexagonal nets to create energetically the most stable structure for a

given composition. This atomic arrangement is proven to be most stable by the calculation results of ten structural models of equiatomic composition, which proves that if there are less homoatomic interactions on hexagonal nets, the structure would be energetically more stable.

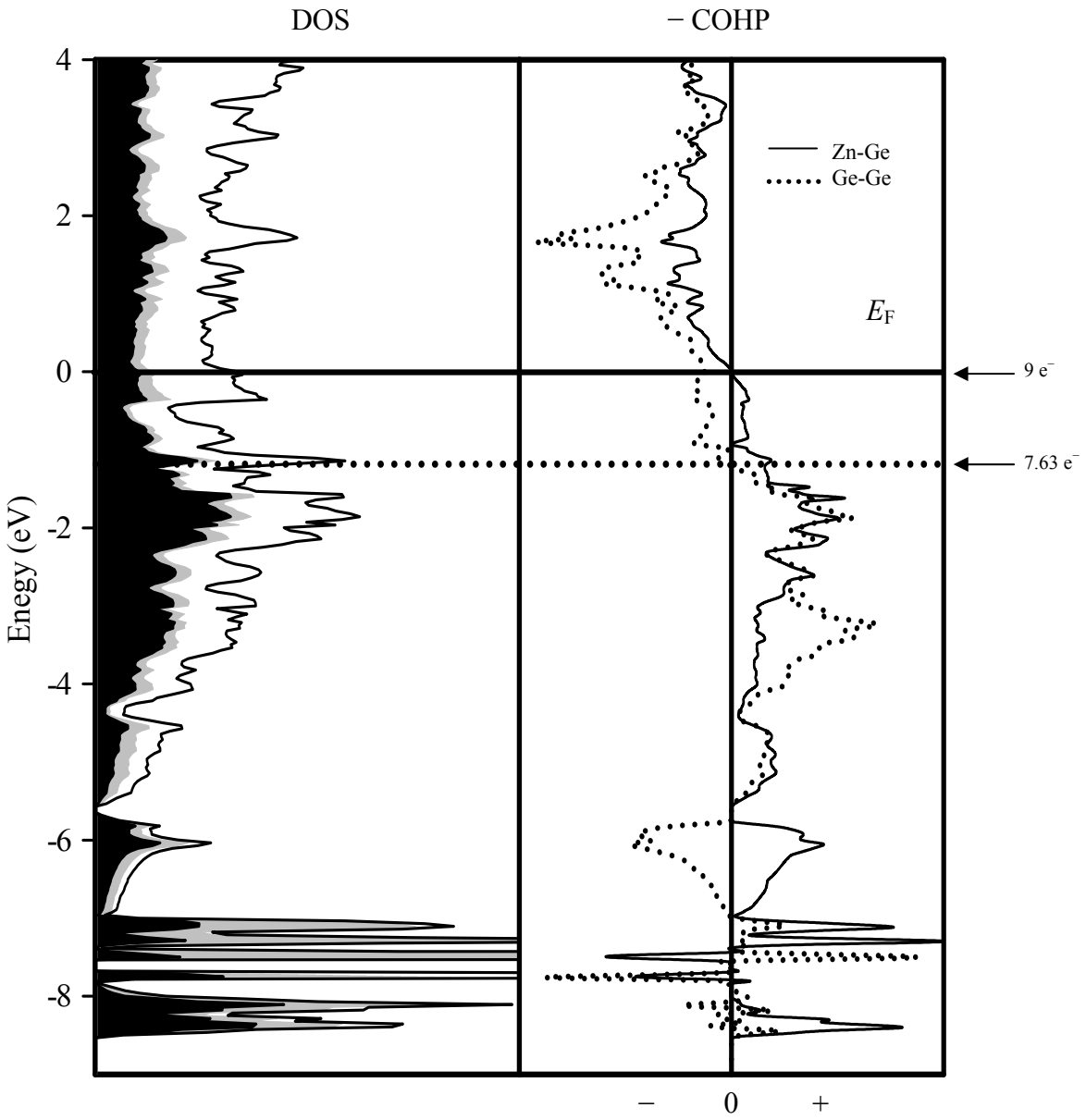

Figure 8. DOS and COHP curves for $Eu(Zn_{0.25}Ge_{0.75})_2$. (Left) Total DOS (solid line), Eu PDOS (white region), Ge PDOS (black region) and Zn PDOS (gray region). (Right) Zn−Ge and Ge−Ge COHP curves. The Fermi level is indicated by the solid line and is the energetic reference (0 eV). The number of valence electrons, which corresponds to the Fermi level and the optimum of Ge−Ge COHP curve are also shown.

Figure 8 illustrates DOS and nearest neighbor COHP curves for the Ge-rich model, where E_F is the reference energy value in these curves. Given the Ge-rich composition, Ge PDOS is more pronounced than Zn PDOS throughout the entire DOS curves. A pseudogap, which was clearly observed just below E_F in the DOS diagram of $Eu(Zn_{0.5}Ge_{0.5})_2$ (Figure 7, left) is no longer noticeable because of the more pronounce contribution from Eu 5*d* and Ge 4*p* orbitals near E_F. In Figure 8 (right), the Zn−Ge COHP curve is fully optimized at E_F. This indicates that 9.0 valence electrons are optimum for a Zn−Ge bond on planar hexagonal nets in the AlB_2-type structure, and this number of valence electrons is very close to the calculation result of Zn-Ge bond in $Eu(Zn_{0.5}Ge_{0.5})_2$, which is 9.2 valence electrons and also consistent with our experimental results.[28] However, the Ge−Ge COHP curve falls in the antibonding region, which indicates a Ge-Ge bond is energetically unfavorable. In fact, during the structure refinement, we observed an increase of thermal displacement parameters at the Zn and Ge positions as Ge content increases from X-ray diffraction experiments.[28] In particular, at the Ge-rich end of the AlB_2-type phases, i.e., $Eu(Zn_{0.25}Ge_{0.75})_2$, a large U_{33}/U_{11} value of ca. 7 was observed. Thus, we assumed that some displacements of the electronegative elements on the hexagonal layers occurred for the Ge-rich compositions, but they did not show long-range ordering because those puckered layers were not well ordered to show superstructure reflections.

To find out whether puckered hexagonal layers are energetically more favorable than planar layers for $Eu(Zn_{0.25}Ge_{0.75})_2$ as we speculated, and if so, which type of puckering would be the most favorable, we performed a series of calculations using the VASP code[17-19] for five different hypothetical models (Figure 9) of $Eu(Zn_{0.25}Ge_{0.75})_2$. In models 1-4, each hexagonal layer has a constant composition of $[Zn_{0.5}Ge_{1.5}]$ with identical lattice parameters. The only difference among these models is atomic positions of Zn and Ge along *c*-axis. Model 1 is identical to the model, which we previously used for LMTO calculations with planar hexagonal layers. Model 2 contains in-phase puckered layers, whereas model 3 has out-of-phase puckered layers, which form closer interlayer Zn···Ge and Zn···Zn interactions. Model 4 includes different types of out-of-phase puckered layers from model 3, in which Ge-sites have puckered environments as in model 3, whereas Zn-sites maintain locally planar environments as in model 1.

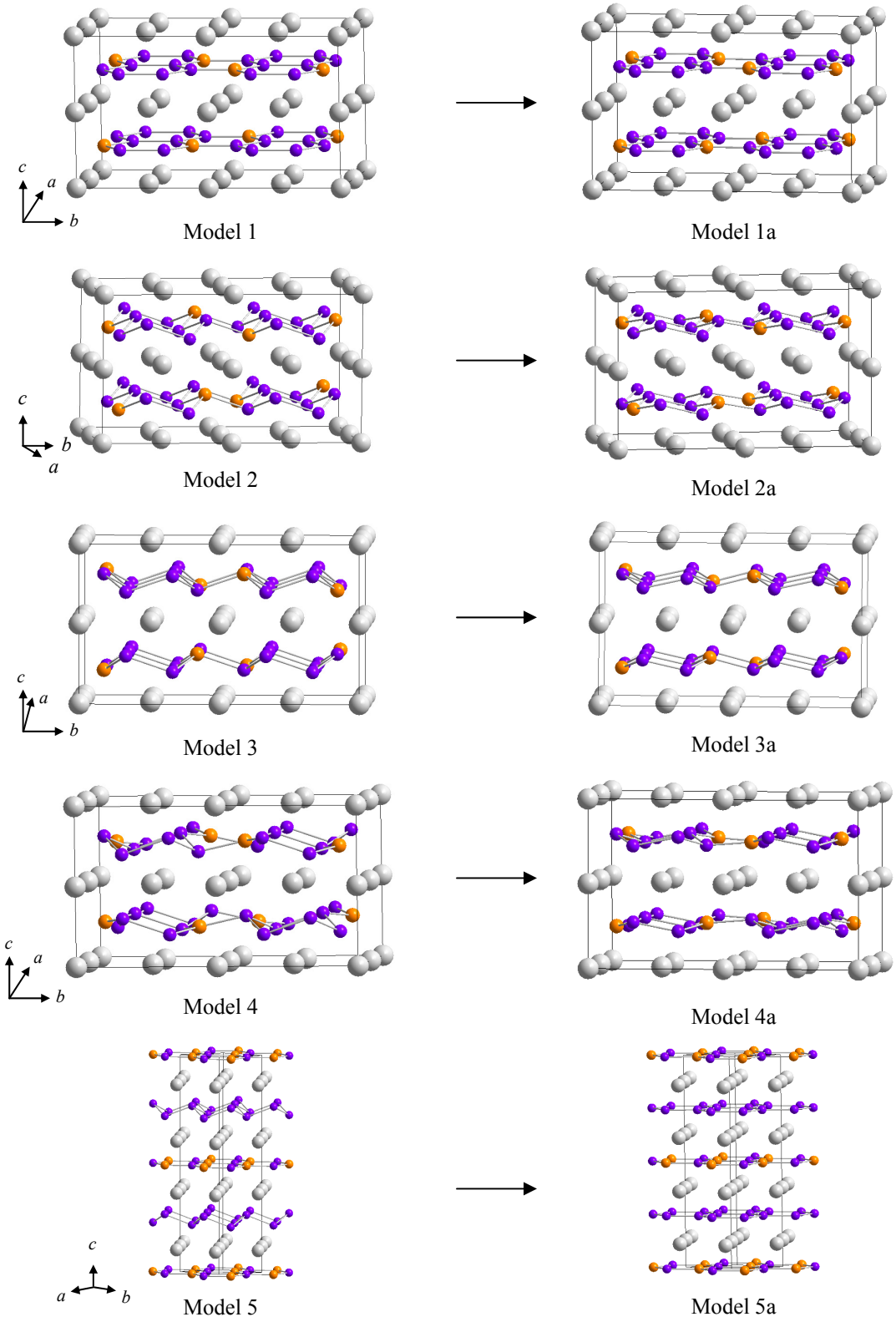

Figure 9. Five structure models of $Eu(Zn_{0.25}Ge_{0.75})_2$ before (left column) and after (right column) the structure relaxation using VASP code.

In model 5, equiatomic [ZnGe] planar hexagonal layers alternate with puckered Ge-only layers. Since Zn and Ge atoms cannot be easily differentiated by X-ray diffraction, we utilized results of TB-LMTO-ASA calculations which indicated that Zn atoms tended to avoid nearest neighbor contacts with each other on the hexagonal nets.

The relative total energies of the original and relaxed models are compared in Table 1. All relaxed models displayed lower energy than their original models, and among those, model 3a turned out to be the energetically most favorable structure.

Table 1. Energy comparison of five structure models of $Eu(Zn_{0.25}Ge_{0.75})_2$ using VASP code.

Model	$E-E_0$ (meV/f.u.)	Model	$E-E_0$ (meV/f.u.)
3a	0 (E_0)	3	+ 159.8
2a	+ 5.2	2	+ 184.9
4a	+ 18.3	4	+ 195.3
1a	+ 38.5	5a	+ 362.2
1	+ 68.3	5	+ 384.6

In model 3, the original angular deficiency from 360° of each atomic site, which indicates a tendency of pyramidalization at a given site, was 29.76° for both the Zn and Ge-sites. However, the deficiency decreased after structural relaxation to 16.2° for the Zn-site, 17.72° for the Ge1-site, and 15.36° for the Ge2-site. In addition, we also observed ca. 10 % increase of the *c*/*a* ratio after structural relaxation. Therefore, these calculation results proved that the hexagonal layers tend to pucker rather than being planar. Detailed crystallographic information of each model are included in Supplementary Material (Table S4).

4.5 Bonding Analysis by the Electron Localization Function (ELF)

The elements of chemical bonding are consequently derived by employing the topological features of the bonding-detector function, for example, the Electron Localization Function (ELF)[23] which is related to the motion of electron pairs in a chemical system. The directed interaction between atoms in a chemical structure can be distinguished in real space. Maxima of the ELF in the valence region (valence shells)[37] provide signatures for directed (covalent) bonding. This analysis of the topology of ELF can be combined with the consecutive integration of the electron density in "basins," which are bound by zero-flux surfaces in the ELF gradient field.[25] This procedure, similar to the one proposed for electron density,[26] allows assignment of an electron count for each basin, revealing basic information about chemical bonding.

The ELF can be illustrated in two distinct ways: (1) as surfaces corresponding to a single ELF value ("isosurfaces"); and (2) as a slice through the structure. To achieve further insights into the valence region of $Eu(Zn_{0.5}Ge_{0.5})_2$, especially whether there exists any interlayer interaction between 6^3 sheets, e.g., two-center, two-electron bonds between interlayer Zn···Ge contact or multi-centered interactions involving Zn/Ge and Eu atoms, as observed in EuGaSn,[10] ELF was analyzed carefully. To have reference systems for comparison, the ELF analyses on $EuZn_2$ and $EuGe_2$ were also conducted. The ELF contribution of $Eu(Zn_{0.5}Ge_{0.5})_2$ and $EuGe_2$ are illustrated using both "isosurfaces" and a slice, whereas that of $EuZn_2$ is displayed using slices of different planes.

4.5.1 $EuZn_2$

ELF analysis indicates that four bond attractors, which are defined as local maxima of the ELF values, exist around each Zn atom. As shown in Figure 10, each Zn atom forming 4b-3D nets with locally distorted tetrahedral coordination is connected to two other Zn atoms, respectively, along *b* direction creating 2D chains with bond distances of 2.688 Å – 2.907 Å and along *a* direction forming 2D zigzag chains with a bond distance of 2.699 Å. Since there exists only homoatomic bonds between Zn atoms, bond attractors are observed in the midst of two neighboring Zn atoms.

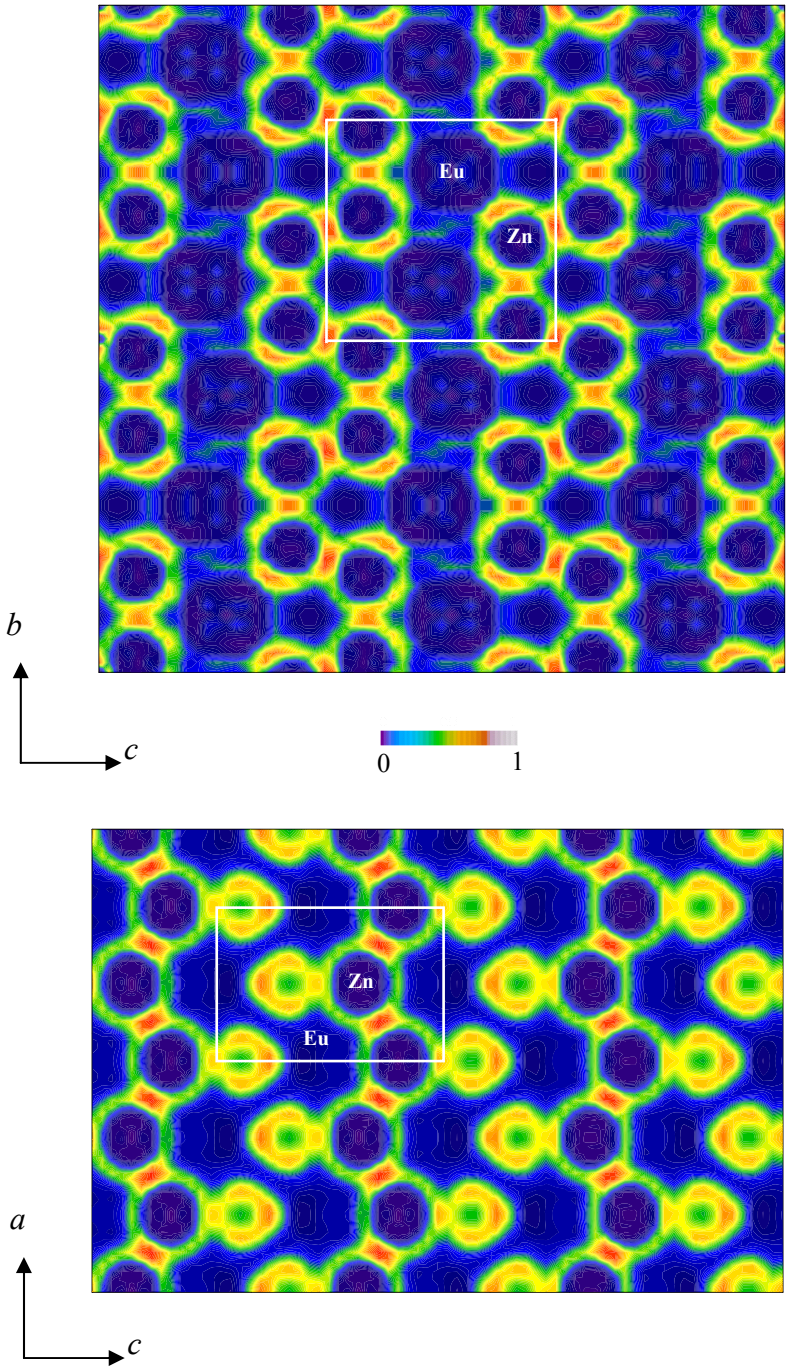

Figure 10. ELF distribution, depicted as filled contour slices for $EuZn_2$. Left: (1 0 0) slice, $a = 0$; Right: (0 1 0) slice, $b = 0.06$ are shown.

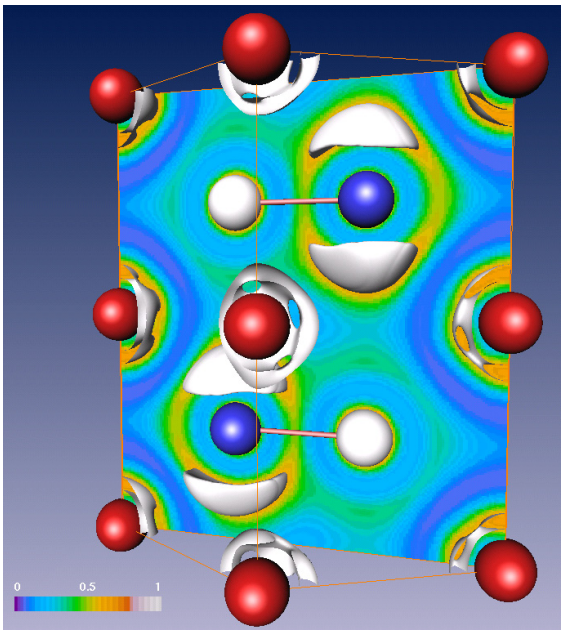

$\eta = 0.58$

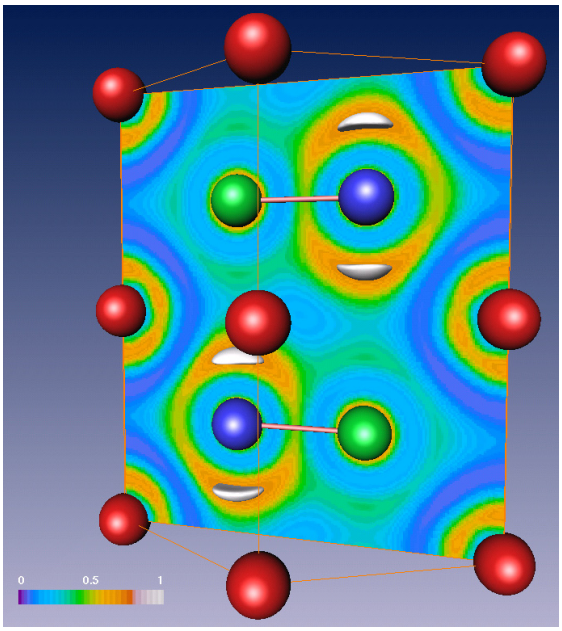

$\eta = 0.68$

Figure 11. ELF distribution (color scale indicated) in $Eu(Zn_{0.5}Ge_{0.5})_2$: Eu sites, red spheres; Zn sites, green spheres; Ge sites, blue spheres. ELF isosurfaces (η = 0.58 and 0.68), colored in white, produce attractors associated with Zn and Ge atoms. A (110) ELF slice is also illustrated.

4.5.2 $Eu(Zn_{0.5}Ge_{0.5})_2$

Two types of ELF attractors are located around the 3b-2D Zn and Ge atoms showing trigonal planar coordination on the 6^3 sheets. In Figure 11, lone pair-like attractors are detected symmetrically above and below Ge atoms along [001] together with bond attractors on Ga−Si bonds on the 6^3 sheets. Because of the different electronegativity of Zn and Ge: (Pauling scale, χ(Zn) = 1.65 and χ(Ge) = 2.01),[28] electrons are more localized around Ge than Zn. This electron localization is significantly more pronounced than those observed for Ga−Si bonds in EuGaSi or for Ga−Sn bonds in EuGaSn.[10] However, no attractor is detected between interlayer Zn···Ge contacts. This implies that the alternating stacking patterns of the 6^3 sheets along *c*-axis is not caused by an attractive interaction between Zn···Ge contacts, but rather caused by a repulsive interaction between interlayer Ge atoms containing localized electrons around. Integration of the total electron density within each basin gives values of 2.31 electrons for the valence shell basins of Zn and 5.84 electrons for the valence shell basins of Ge for a formulation of $Eu^{2.15+}[Zn^{0.31-}Ge^{1.84-}]$ with roughly divalent Eu atoms.

4.5.3 $EuGe_2$

The topological analysis of ELF reveals four attractors around each Ge atom creating 3b-2D puckered hexagonal nets with local trigonal pyramidal environments as shown in Figure 12. One lone pair-like attractor is located above (or below) Ge atoms along [001] and three other attractors are symmetrically located in the midst of Ge−Ge contacts. Integration of the total electron density within each basin gives the valence electron counts of 2.49 electrons for the lone pair-like attractor and 1.76 electrons for the Ge−Ge bond attractors. Thus, the total valence electron count for valence shell basin sets is 5.13 electrons per Ge atom (= 2.49 e^- ("lone pair") + 3 × 1.76 e^- / 2 ("bond pairs")), which can be written as $Ge^{1.13-}$. As a result, the bonding situation in $EuGe_2$ can be described as $Eu^{2.26+}[Ge^{1.13-}]_2$, which agrees reasonably well with a Zintl-Klemm representation as $Eu^{2+}[Ge^-]_2$.

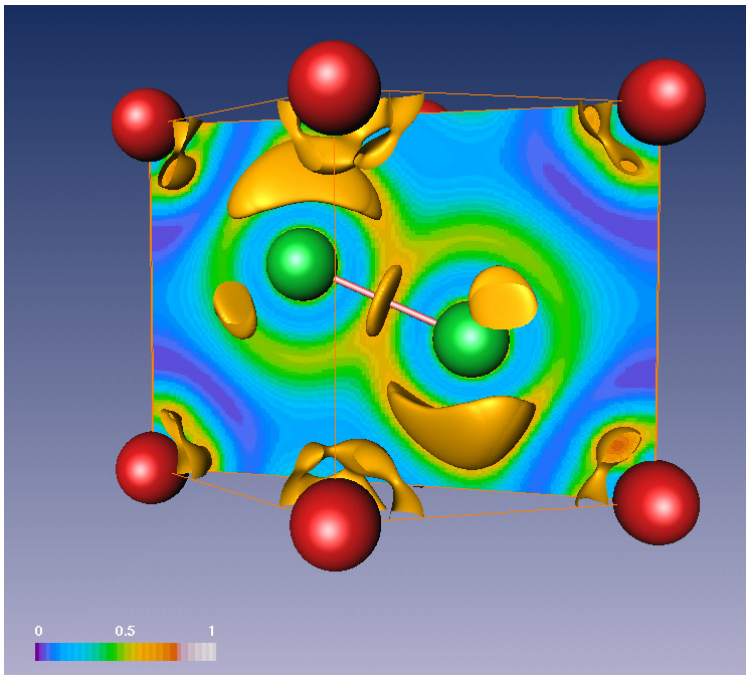

$\eta = 0.59$

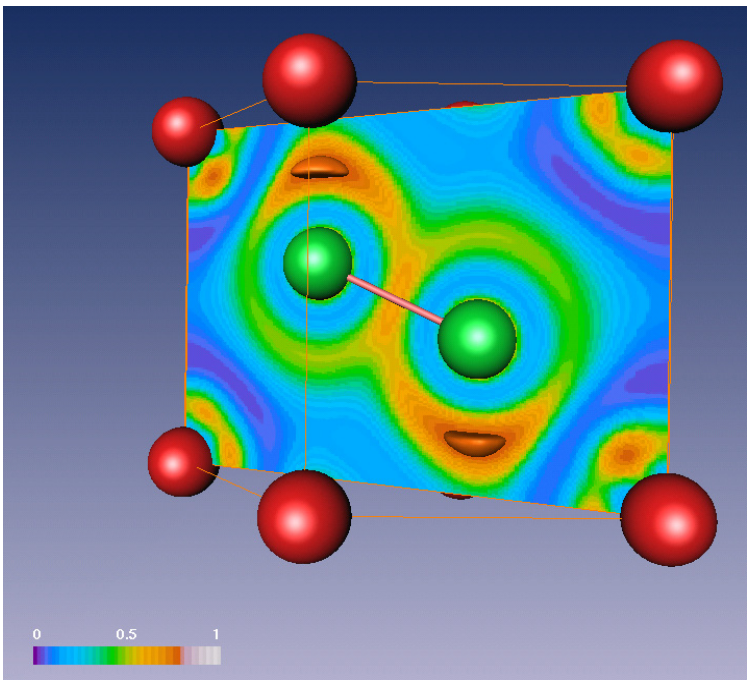

$\eta = 0.77$

Figure 12. ELF distribution (color scale indicated) in $EuGe_2$: Eu sites, red spheres; Ge sites, green spheres. ELF isosurfaces (η = 0.59 and 0.77), colored in yellow, produce attractors associated with Ge lone-pairs and a Ge−Ge bond. A (110) ELF slice is also illustrated.

4.6 Summary

We have conducted a series of electronic structure calculations for the observed and hypothetical structural models of $Eu(Zn_{1-x}Ge_x)_2$ ($0 \leq x \leq 1$) system using both TB-LMTO-ASA and VASP methods. The experimentally observed homogeneity width of $EuZn_2$ phase can be understood from Zn−Zn COHP curve showing significant bonding character at E_F. The DOS and COHP analyses for the hypothetical Zn-rich compound prove that the compound should prefer to exist as two distinct phases rather than to keep Zn-rich composition in the AlB_2-type structure. Total electronic energy comparison for ten possible equiatomic models indicates that the more heteroatomic interactions exist in a unit cell, the more energetically favorable structure it is. DOS curves and band structures show that the observed bond distance between Zn and Ge on the hexagonal nets can be attributed to both σ- and π-bond interactions. The observed homogeneity width of the AlB_2-type structure can be explained using COHP of Zn−Ge, Eu−Ge and Eu−Zn which maintains bonding character beyond the E_F, and the theoretically expected upper limit in composition is in very good agreements with our experimental results. The calculations on the Ge-rich composition model conclude that 9 valence electrons are optimum for Zn−Ge bonding on planar hexagonal nets in the AlB_2-type structure, and the structure relaxation using VASP method revealed that hexagonal layers tend to pucker rather than being planar. ELF analysis for the equiatomic compound indicates that the alternating stacking patterns of 6^3 sheets along *c*-axis is not caused by an attractive interaction between Zn···Ge contacts, but rather caused by repulsive interaction between interlayer Ge atoms containing localized electrons around.

Acknowledgement

This work was supported by NSF DMR 02−41092 and 06−05949. T.-S You is grateful to Dr. Warren Straszheim for the EDXS measurements at Iowa State University.

References

[1] Westbrook, J. H.; Fleisher, R. L., Ed.; *Intermetallic Compounds: Principle and Practices*; Wiley, New York, **1995**.

[2] Nesper, R., *Prog. Solid State Chem*. **1990**, *20*, 1.

[3] Miller, G. J. In *Chemistry, Structure, and Bonding of Zintl Phases and Ions*; Kauzlarich, S. M., Ed.; VCH Publishers; New York, 1996; pp 1.

[4] Schäfer, H. *Ann. Rev. Mater. Sci.* **1985**, *5*, 1.

[5] Miller, G. J.; Lee, C.−S.; Choe, W. In *Highlights in Inorganic Chemistry*; Meyer, G., Ed.; Wiley−VCH; Heidelberg, **2002,** 21.

[6] Klem, M. T.; Vaughy, J. T.; Harp, J. G.; Corbett, J. D. *Inorg. Chem*. **2001**, *40*, 7020. Zintl, E.; Dullenkopf, W. *Z. Phy. Chem*. **1932**, *B12*, 183.

[7] Gout, D.; Benbow, E.; Gourdon, O.; Miller, G. J. *J. Solid State Chem*. **2003**, *176,* 538.

[8] Burdett, J. K.; Miller, G. J. *Chem. Mater*. **1990**, *2*, 12.

[9] Hoffman, R.-D.; Pöttgen, R., *Z. Kristallogr.* **2001**, 216, 127.

[10] You, T.−S.; Grin, Y.; Miller, G. J. *Inorg. Chem*. **2007**, *46*, 8801.

[11] Anderson, O. K. *Phys. Rev. B* **1986**, *34*, 2439.

[12] Anderson, O. K.; Jepsen, O. *Phys. Rev. Lett.* **1984***, 53*, 2571.

[13] Andersen, O. K.; Jepsen, O.; Glötzel, D. In *Highlights of condensed matter theory*; F. Bassani, F. Fumi, M.Tosi, Eds.; New York, North−Holland, Lambrecht, W. R. L., **1985.**

[14] Jepsen, O.; Anderson, O. K.; *Z. Phys. B* **1995**, *97*, 35.

[15] Dronskowski, R.; Blochl, P. *J. Phys. Chem*. **1993**, *97*, 8617.

[16] Blöchl, P. E.; Jepsen, O.; Anderson, O. K. *Phys. Rev. B* **1994**, *49*, 16223.

[17] Kresse, G.; Hafner, J. *Phys. Rev.* **1993**, *B47*, RC 558.

[18] Kresse, G.; Furthmüller, J. *Phys. Rev.* **1996**, 11169.

[19] Kresse, G.; Furthmüller, J. *Comput. Mater. Sci.* **1996**, 6, 15.

[20] Vanderbilt, D. *Phys. Rev.* **1990**, *B41*, 7892.

[21] Kresse, G.; Hafner, J. *J. Phys.: Condens. Matter.* **1994**, 6, 824.

[22] Monkhurst, H. J.; Pack, J. D. *Phys. Rev.* **1973**, *B13*, 518.

[23] Savin, A.; Flad, H. J.; Preuss, H.; von Schnering, H. G. *Angew. Chem.* **1992**, *104*, 185; *Angew. Chem., Int. Ed. Engl.* **1992**, *31*, 185.

[24] Jepsen, O.; Burkhardt, A.; Andersen, O. K. *The TB-LMTO-ASA Program*, version 4.7; Max-Planck-Institut für Festkörperforschung: Stuttgart, Germany, 1999.

[25] Kohout, M. *BASIN*, version 2.3; Max-Planck-Institut für Chemische Physik fester Stoffe: Dresden, Germany, 2001.

[26] Bader, R. F. W. *Atoms in molecules: a quantum theory*; Oxford University Press: Oxford, 1999.

[27] *Amira* visualization software; Konrad-Zuse-Zentrum für Informationstechnik Berlin (ZIB): Berlin, Germany, 2003.

[28] You, T. −S; Miller, G. J. A companion article proceeding.

[29] Iandelli, A.; Palenzona, A. *Atti Accad. Naz. Lincei Rend. Sci. Fis. Mat. Natur*. **1964**, *37*, 165.

[30] Bärnighausen, H.; *Match-Commun. Math. Co*. **1980**, 9, 139.

[31] Pöttgen, R. *Z. Kristallogr*. **1995**, *210*, 924.

[32] Buschow, K. H. J.; Schobinger−Paramatellos, P.; Fischer, P.; *J. Less−Common Met*. **1988**, *39*, 221.

[33] Teatum, E.; Gshneidner, K. (Jr.); Waber, J.; *Radii of the Elements for CN12;* U. S. Department of Commerce; Washington, D. C., **1960**, LA−2345**.**

[34] Emsley, J. *The Elements*; Clarendon press: Oxford, **1998.**

[35] Bobev, S.; Bauer, E. D.; Thompson, J. D.; Sarrao, J. L.; Miller, G. J.; Eck, B.; Dronskowski, R. *J. Solid State Chem*. **2004**, *177,* 3545.

[36] Pöttgen, R. *J. Alloys. Comp.* **1996**, *243*, L1.

[37] Kohout, M.; Wagner, F. R.; Grin, Yu. *Theor. Chem. Acc.* **2002**, 108, 150.

Supplementary Material

Table S1. Structural information of $Eu(Zn_{0.75}Ge_{0.25})_2$ and $Eu(Zn_{0.25}Ge_{0.75})_2$ in *Pcab* displayed in Figure 2.

Model	Lattice Parameter (Å)			Atomic Coordinate			
	a	***b***	***c***	**atom**	***x***	***y***	***z***
$Eu(Zn_{0.75}Ge_{0.25})_2$	8.694	15.058	8.569	Eu1	0	0	0
				Eu2	1/2	0	0
				Eu3	0	1/2	0
				Eu4	1/2	1/2	0
				Eu5	0	0	1/2
				Eu6	1/2	0	1/2
				Eu7	1/4	1/4	0
				Eu8	1/4	1/4	1/2
				Eu9	0	1/2	1/2
				Eu10	1/2	1/2	1/2
				Zn1	0	1/6	1/4
				Zn2	1/4	1/12	1/4
				Zn3	1/2	1/6	1/4
				Zn4	0	1/3	1/4
				Zn5	1/4	0.41667	1/4
				Zn6	1/2	1/3	1/4
				Ge1	3/4	1/12	1/4
				Ge2	3/4	0.41667	1/4
$Eu(Zn_{0.25}Ge_{0.75})_2$	8.788	15.222	8.664	Eu1	0	0	0
				Eu2	1/2	0	0
				Eu3	0	1/2	0
				Eu4	1/2	1/2	0
				Eu5	0	0	1/2
				Eu6	1/2	0	1/2
				Eu7	1/4	1/4	0
				Eu8	1/4	1/4	1/2
				Eu9	0	1/2	1/2
				Eu10	1/2	1/2	1/2
				Ge1	0	1/6	1/4
				Ge2	1/4	1/12	1/4
				Ge3	1/2	1/6	1/4
				Ge4	0	1/3	1/4
				Ge5	1/4	0.41667	1/4
				Ge6	1/2	1/3	1/4
				Zn1	3/4	1/12	1/4
				Zn2	3/4	0.41667	1/4

Table S2. Structural information of $Eu(Zn_{0.75}Ge_{0.25})_2$ in the KHg_2-type shown in Figure 4.

Model	Space group	Lattice Parameter (Å)			Atomic Coordinate			
		a	***b***	***c***	**atom**	***x***	***y***	***z***
$Eu(Zn_{0.75}Ge_{0.25})_2$	*P*1*m*1	7.650	4.728	7.655	Eu1	3/4	1/2	0.052
					Eu2	3/4	0	0.448
					Eu3	1/4	0	0.552
					Eu4	1/4	1/2	0.948
					Zn1	0.060	0	0.165
					Zn2	0.440	0	0.165
					Zn3	0.060	1/2	0.335
					Zn4	0.56	1/2	0.665
					Zn5	0.56	0	0.835
					Zn6	0.94	0	0.835
					Ge1	0.44	1/2	0.335
					Ge2	0.94	1/2	0.665

Table S3. Structural information of ten $Eu(Zn_{0.5}Ge_{0.5})_2$ models shown in Figure 6.

Model	Space Group	Lattice Parameter (Å)			Atomic Coordinate			
		a	*b*	*c*	atom	*x*	*y*	*z*
1	$P\bar{6}m2$ [187]	4.3631	4.3631	4.3014	Eu Zn Ge	0 1/3 2/3	0 2/3 1/3	0 1/2 1/2
2	$P6_3/mmc$ [194]	4.3631	4.3631	8.6028	Eu Zn Ge	0 1/2 1/3	0 2/3 2/3	0 1/4 3/4
3	$P6_3/mmc$ [194]	4.3631	4.3631	17.2056	Eu1 Eu2 Zn Ge	0 0 1/3 2/3	0 0 2/3 1/3	0 1/4 1/8 1/8
4	*Pm*2*m* [25]	4.3631	7.5571	4.3014	Eu1 Eu2 Zn1 Zn2 Ge1 Ge2	0 1/2 0 1/2 0 1/2	0 1/2 2/3 5/6 1/3 1/6	0 0 1/2 1/2 1/2 1/2
5	*Pmcm* [51]	4.3631	7.5571	8.6028	Eu1 Eu2 Zn1 Zn2 Ge1 Ge2	0 1/2 0 1/2 0 1/2	0 1/2 2/3 5/6 1/3 1/6	0 0 1/4 1/4 1/4 1/4
6	*Pmcm* [51]	4.3631	7.5571	17.2056	Eu1 Eu2 Eu3 Eu4 Zn1 Zn2 Ge1 Ge2	0 1/2 0 1/2 0 1/2 0 1/2	0 1/2 0 1/2 2/3 5/6 1/3 1/6	0 0 1/4 1/4 1/8 1/8 1/8 1/8
7	*Pmmm* [47]	4.3631	7.5571	4.3014	Eu1 Eu2 Zn1 Ge1	0 1/2 0 1/2	0 1/2 1/3 1/6	0 0 1/2 1/2
8	*Pmmm* [47]	4.3631	7.5571	8.6028	Eu1 Eu2 Zn1 Zn2 Ge1 Ge2	1/2 0 0 1/2 1/2 0	1/2 0 1/3 1/6 1/6 1/3	1/4 1/4 0 1/2 0 1/2
9	*Pmmm* [47]	4.3631	7.5571	17.2056	Eu1 Eu2 Eu3 Eu4 Eu5 Eu6 Ge1 Ge2 Zn1 Zn2	0 1/2 0 1/2 0 1/2 1/2 0 0 1/2	0 1/2 0 1/2 0 1/2 1/6 1/3 1/3 1/6	0 0 1/4 1/4 1/2 1/2 1/8 3/8 1/8 3/8
10	*P6mm* [183]	4.3631	4.3631	8.6028	Eu1 Eu2 Zn Ge	0 0 1/3 1/3	0 0 2/3 2/3	0 1/2 1/4 3/4

Table S4. Structural information of five $Eu(Zn_{0.25}Ge_{0.75})_2$ models shown in Figure 9.

Model	Space Group	Lattice Parameter (Å)			Atomic Coordinate			
		a	*b*	*c*	atom	*x*	*y*	*z*
1	*P*222 [16]	8.788	15.222	8.664	Eu1	0	0	0
					Eu2	1/2	0	0
					Eu3	0	1/2	0
					Eu4	1/2	1/2	0
					Eu5	0	0	1/2
					Eu6	1/2	0	1/2
					Eu7	1/4	1/4	0
					Eu8	1/4	1/4	1/2
					Eu9	0	1/2	1/2
					Eu10	1/2	1/2	1/2
					Ge1	0	1/6	1/4
					Ge2	1/4	1/12	1/4
					Ge3	1/2	1/6	1/4
					Ge4	0	1/3	1/4
					Ge5	1/4	0.41667	1/4
					Ge6	1/2	1/3	1/4
					Zn1	3/4	1/12	1/4
					Zn2	3/4	0.41667	1/4
2	*P*121 [3]	15.222	8.788 $\beta = 90°$	8.664	Eu1	0	0	0
					Eu2	1/2	0	0
					Eu3	0	1/2	0
					Eu4	1/2	1/2	0
					Eu5	0	0	1/2
					Eu6	1/2	0	1/2
					Eu7	1/4	1/4	0
					Eu8	1/4	1/4	1/2
					Eu9	0	1/2	1/2
					Eu10	1/2	1/2	1/2
					Ge1	0	1/6	0.3
					Ge2	1/4	1/12	0.2
					Ge3	1/2	1/6	0.3
					Ge4	0	1/3	0.2
					Ge5	1/4	0.41667	0.3
					Ge6	1/2	1/3	0.2
					Ge7	0	2/3	0.3
					Ge8	1/2	2/3	0.3
					Ge9	3/4	0.5833	0.2
					Ge10	0	5/6	0.2
					Ge11	1/2	5/6	0.2
					Ge12	3/4	0.9167	0.3
					Zn1	3/4	1/12	0.2
					Zn2	3/4	0.41667	0.3
					Zn3	1/4	0.5833	0.2
					Zn4	1/4	0.9167	0.3
3	*P*121 [3]	8.788	15.222 $\beta = 90°$	8.6028	Eu1	0	0	0
					Eu2	1/2	0	0
					Eu3	0	1/2	0
					Eu4	1/2	1/2	0
					Eu5	0	0	1/2
					Eu6	1/2	0	1/2
					Eu7	1/4	1/4	0
					Eu8	1/4	1/4	1/2
					Eu9	0	1/2	1/2
					Eu10	1/2	1/2	1/2

					Ge1	0	1/6	0.3
					Ge2	1/4	1/12	0.2
					Ge3	1/2	1/6	0.3
					Ge4	0	1/3	0.2
					Ge5	1/4	0.41667	0.3
					Ge6	1/2	1/3	0.2
					Ge7	0	2/3	0.3
					Ge8	1/2	2/3	0.3
					Ge9	3/4	0.5833	0.2
					Ge10	0	5/6	0.2
					Ge11	1/2	5/6	0.2
					Ge12	3/4	0.9167	0.3
					Zn1	3/4	1/12	0.2
					Zn2	3/4	0.41667	0.3
					Zn3	1/4	0.5833	0.2
					Zn4	1/4	0.9167	0.3
4	*P*222 [16]	8.788	15.222	8.6028	Eu1	0	0	0
					Eu2	1/2	0	0
					Eu3	0	1/2	0
					Eu4	1/2	1/2	0
					Eu5	0	0	1/2
					Eu6	1/2	0	1/2
					Eu7	1/4	1/4	0
					Eu8	1/4	1/4	1/2
					Eu9	0	1/2	1/2
					Eu10	1/2	1/2	1/2
					Ge1	0	0.16667	0.3
					Ge2	1/4	1/12	0.2
					Ge3	1/2	1/6	0.3
					Ge4	0	1/3	0.2
					Ge5	1/4	0.41667	0.3
					Ge6	1/2	1/3	0.2
					Zn1	3/4	1/12	0.2667
					Zn2	3/4	0.41667	0.2333
5	*P-6m2* [187]	4.2358	4.2358	29.1318	Eu1	0	0	0.0785
					Eu2	0	0	1/4
					Eu3	0	0	0.4215
					Zn1	2/3	1/3	0
					Zn2	1/3	2/3	1/2
					Ge1	1/3	2/3	0
					Ge2	1/3	2/3	0.1801
					Ge3	2/3	1/3	0.1485
					Ge4	1/3	2/3	0.3515
					Ge5	2/3	1/3	0.3199
					Ge6	2/3	1/3	1/2

Figure S5. Electronic energy band structures of $Eu(Zn_{0.5}Ge_{0.5})_2$ with fatband contributions for p_x and p_y orbitals (top) and p_z orbitals (bottom) from Ge, using the TB-LMTO-ASA method in the LSDA.

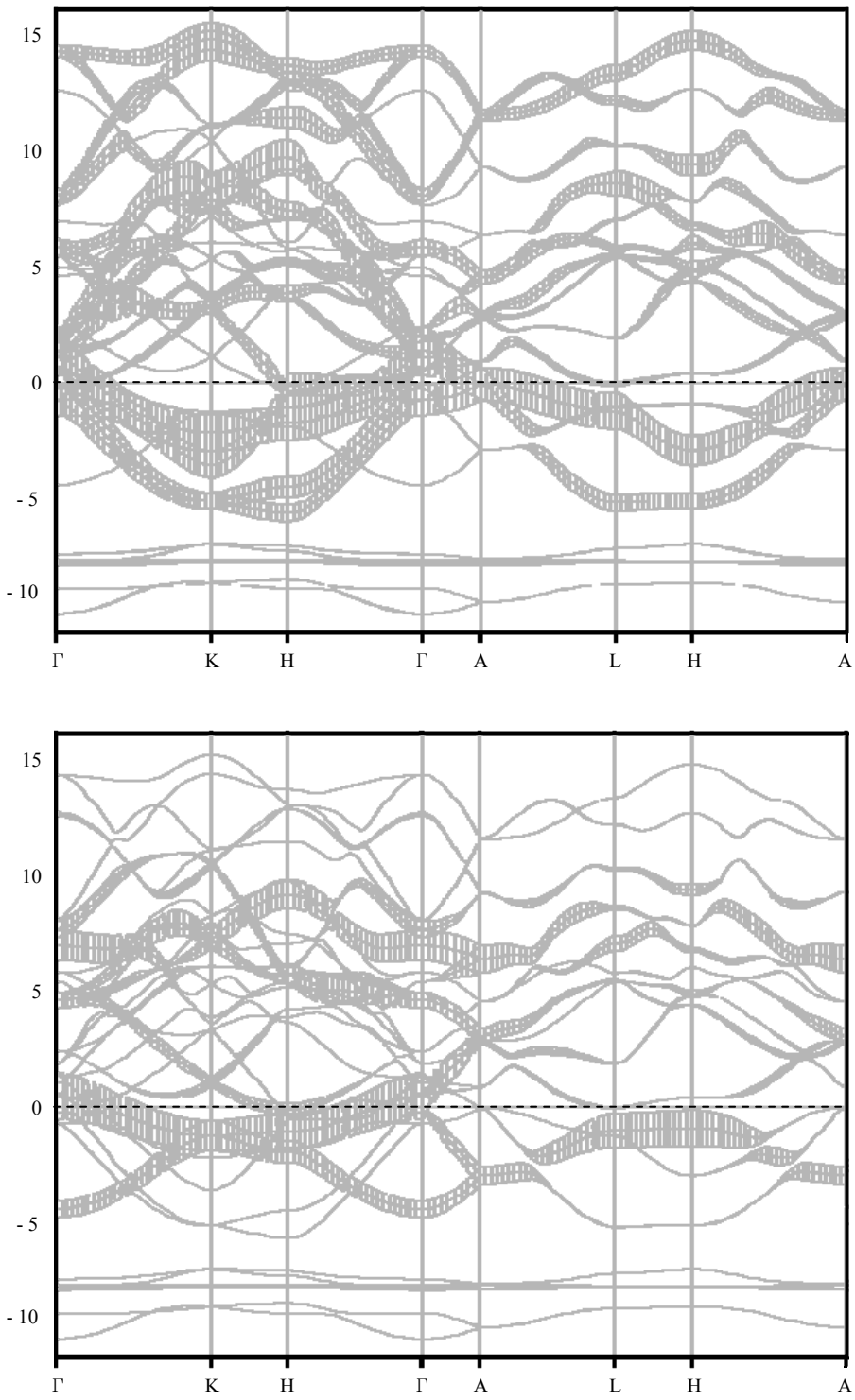

Figure S6. Electronic energy band structures of $Eu(Zn_{0.5}Ge_{0.5})_2$ with fatband contributions for p_x and p_y orbitals (top) and p_z orbitals (bottom) from Zn, using the TB-LMTO-ASA method in the LSDA.

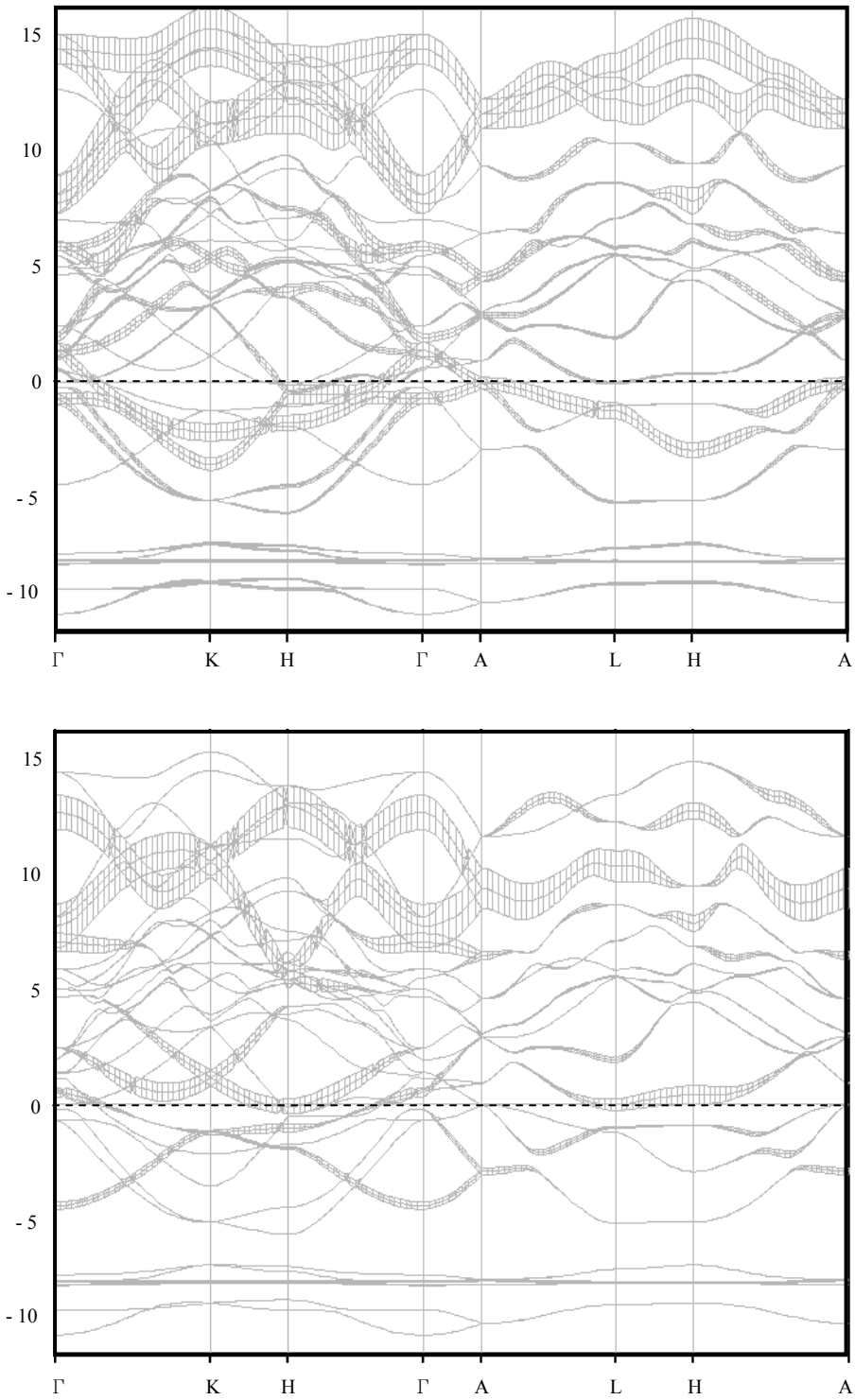

CHAPTER 5

Structure-Composition Sensitivity in "Metallic" Zintl Phases: A Study of $Eu(Ga_{1-x}Tt_x)_2$ (Tt = Si, Ge, $0 \le x \le 1$)

A paper to be submitted to *Chemistry of Materials*

Tae−Soo You,[1,2] Jing-Tai Zhao,[3] Rainer Pöttgen,[4] Yuri Grin,[5] and Gordon J. Miller[1,6]

5.1 Abstract

The series of two isoelectronic polar intermetallic $Eu(Ga_{1-x}Tt_x)_2$ (Tt = Si, Ge, $0 \le x \le 1$) series has been synthesized and characterized by powder and single crystal X-ray diffraction, physical property measurements, and theoretical calculations. In the $Eu(Ga_{1-x}Si_x)_2$ series, structural variation ranges from the KHg_2-type at low x values to the AlB_2-type and, finally, the $ThSi_2$-type structure as x approaches 1. The hexagonal AlB_2-type structure (space group *P6/mmm*, Pearson symbol *hP*3) occurs only for ternary compositions with a phase width in which $0.22\ (6) \le x \le 0.82(2)$, and Ga and Si atoms are statistically distributed in the planar polyanionic 6^3 nets. As smaller Si atoms replace Ge atoms, the lattice parameters a and c, as well as the unit cell volumes decrease significantly. In addition, the Ga-Si distances decreases from 2.440(2) Å for $Eu(Ga_{0.71(2)}Si_{0.28(2)})_2$ to 2.3750(2) Å for $Eu(Ga_{0.32(2)}Si_{0.68(2)})_2$ as the number of valence electrons increases by ca. 1.0. On the other

---

[1] Graduate student and Professor, respectively, Department of Chemistry, Iowa State University

[2] Primary researcher and author

[3] Shanghai Institute of Ceramics, Chinese Academy of Sciences, 1295 Dingxi Road, Shanghai, 200050 China

[4] Institut für Anorganische und Analytische Chemie, Universität Münster, Münster, Germany

[5] Max-Planck-Institut für Chemische Physik fester Stoffe, Nöthnitzer Straße 40, 01187 Dresden, Germany

[6] Author for correspondence

hand, in $Eu(Ga_{1-x}Ge_x)_2$ series, six different structural types exist as x increases. Besides two binary compounds, the KHg_2-type for $EuGa_2$ (in the space group *Imma*) and its own type for $EuGe_2$ (in the space group $P\bar{3}m1$), ternary compositions adopt four different structures derived from the AlB_2- and the YPtAs-like motifs: the AlB_2-type structure for Ga-rich compositions, the YPtAs-type structure for the equiatomic composition, and two new structures for Ge-rich compositions. Observed two Ge-rich phases include: 1) $Eu(Ga_{0.45(2)}Ge_{0.55(2)})_2$ containing nine puckered 6^3 nets stacked along the *c*-axis with a Ge-only hexagonal layer in the midst of a crystallographic unit cell, and 2) $Eu(Ga_{0.40(2)}Ge_{0.60(2)})_2$ containing five puckered 6^3 nets stacked along *c*-axis with a split site at $x = 2/3$, $y = 1/3$ and $z = 0.4798(2)$ with ca. 50 % site occupancies. Temperature-dependent magnetic susceptibility measurements of three $Eu(Ga_{1-x}Ge_x)_2$ compounds display Curie−Weiss behavior above ca. 100(2) K, and show effective magnetic moments of, respectively, $7.98(1)\mu_B$ for $Eu(Ga_{0.50(2)}Ge_{0.50(2)})_2$, $7.96(1)\mu_B$ for $Eu(Ga_{0.45(2)}Ge_{0.55(2)})_2$, and $7.99(1)\mu_B$ for $Eu(Ga_{0.40(2)}Ge_{0.60(2)})_2$, all of which indicates a $4f^7$ electronic configuration for Eu. X-ray absorption spectra (XAS) are also consistent with these magnetic properties. Electronic structure calculations supplemented by density of states (DOS) and crystal orbital Hamilton population (COHP) analyses rationalize the observed homogeneity width of the AlB_2-type phase in both systems and the structural variations as a function of Tt content.

5.2 Introduction

Polar intermetallic compounds represent an interesting class of inorganic solids to study relationships among crystal structure, physical property, and chemical composition.[1] This class of compounds consists of electropositive elements (i.e., alkali-, alkaline-earth or rare-earth metals) and electronegative elements close to the Zintl border. The electronegative elements form structural fragments that often conform to simple electron counting rules, such as the Zintl−Klemm formalism,[2–4] and give rise to an electronic structure characterized by a pseudogap in the electronic density of states (DOS) curve and optimized orbital interactions at the Fermi level.[5] These orbital interactions are evaluated by a population analysis of the

DOS curve.[6,7] On the other hand, the electropositive metals act like cations, which simply donate valence electrons to the electronegative components as in classical valence compounds or Zintl phases. However, in polar intermetallic compounds these cationic metals do not transfer all valence electrons to the electronegative component, but are involved in "lattice covalency" through their valence orbitals,[8] and, thus form polar-covalent interaction with the electronegative metals. The presence of the pseudogap at the Fermi level can lead to potentially interesting physical properties, especially if rare-earth metals serve as the active metal because of partially filled 4f bands.[9] In general, polar intermetallics can be considered as a compound class intermediate between classical intermetallic compounds, such as, e.g., Hume−Rothery electron phases, and Zintl phases.[2−4]

During our systematic investigation of the Eu($M_{1-x}M'_x$)$_2$ phases (M, M' = Group 12−14 elements) to study the correlation among atomic, electronic, and possible magnetic structures by varying atomic sizes and valence electron counts, we have observed, to date, different structural trends for two isoelectronic Eu($Ga_{1-x}Tt_x$)$_2$ (Tt = Si, Ge) systems as x varies. In the Eu($Ga_{1-x}Si_x$)$_2$ series, structural variation ranges from the KHg_2-type at low x values to the AlB_2-type and, finally, the $ThSi_2$-type structure as x approaches 1. The AlB_2-type structure occurs only for ternary compositions. The ternary compounds adopting the AlB_2-type phase are related to the superconducting AEAlSi (AE = Ca and Sr) phases,[10−14] which are receiving recent attention for their similarity to superconducting MgB_2[15] with respect to their atomic structures and valence electrons counts. In Eu($Ga_{1-x}Ge_x$)$_2$, however, six different structural types exist as x increases. Besides two binary compounds, the KHg_2-type for $EuGa_2$ and its own type for $EuGe_2$, ternary compositions adopt four different structures derived from the AlB_2- and the YPtAs-like motifs. In our previous investigations, we have characterized and analyzed the influence of the atomic size factor[16] and valence electron count[17] on the anionic networks causing the transition from planar to puckered three-connected nets, respectively, for EuGaTt (Tt = Si, Ge, Sn)[16] and Eu($Zn_{1-x}Ge_x$)$_2$ ($0 \le x \le 1$).[17] In this work, we examine the influence of these two factors simultaneously for the Eu($Ga_{1-x}Tt_x$)$_2$ (Tt = Si, Ge, $0 \le x \le 1$) series.

5.3 Experimental

5.3.1 Synthesis and Chemical Analysis

The $Eu(Ga_{1-x}Tt_x)_2$ (*Tt* = Si, Ge, $0 \leq x \leq 1$) series were synthesized from the pure elements, Eu (Ames Laboratory, rod, 99.99%), Ga (Ames Laboratory, ingot, 99.99%), Si (Aldrich, piece, 99.999%) and Ge (Alfa, piece, 99.999%) in various molar ratios.

$Eu(Ga_{1-x}Si_x)_2$. Eight different mixtures targeting $Eu(Ga_{1-x}Si_x)_2$ ($0 \leq x \leq 1$) and each weighing 1.0 ± 0.2 g were arc-melted under a high purity argon atmosphere on a water-cooled copper hearth. Each pellet was remelted six times after turning to ensure homogeneity. As discussed previously,[16] although we observed weight losses of ca. 0.4-0.7 wt % during arc-melting, these losses did not affect the final targeted compositions. Moreover, samples prepared using either a radio-frequency (RF) induction-furnace or a conventional tube furnace yielded identical products, but crystals extracted from these products were less suitable for subsequent diffraction experiments. Further details about the synthetic methods and characterization of these products are described in an earlier article.[16] $EuGa_2$ was easily synthesized using arc-melting without any subsequent low temperature annealing procedure unlike original reports[18–19] but in agreement with a later publication.[20] On the basis of the powder X-ray diffraction patterns along the series, all samples showed proper crystallinities to pursue subsequent single-crystal X-ray experiments without any further annealing.

$Eu(Ga_{1-x}Ge_x)_2$. Eight samples of $Eu(Ga_{1-x}Ge_x)_2$ ($0 \leq x \leq 1$) were prepared using RF induction melting at 1300 °C with a holding time of 15 min. Reactant mixtures were loaded into tantalum ampoules, which were sealed by arc-melting in an argon-filled glove box with the concentration of O_2 lower than 10 ppm. Each tantalum ampoule was then sealed in an evacuated silica jacket to prevent oxidation. According to the powder X-ray diffraction patterns, no annealing was necessary for these products to improve crystallinity except the equiatomic composition $Eu(Ga_{0.50(2)}Ge_{0.50(2)})_2$. Thus, one-half of the $Eu(Ga_{0.50(2)}Ge_{0.50(2)})_2$ product was wrapped with tantalum foil and annealed at 350 ºC in an evacuated fused silica jacket for one week. After heating, the furnace was turned off and allowed to cool to room temperature.

All sixteen products of the $Eu(Ga_{1-x}Tt_x)_2$ series (Tt = Si, Ge, $0 \leq x \leq 1$) appeared to be stable to exposure to both air and moisture over several weeks. Analysis by energy-dispersive X-ray spectroscopy (EDXS) was conducted on Hitachi S-2460N variable-pressure scanning electron microscope (SEM) equipped with an Oxford Instruments Link Isis Model 200 X-ray analyzer. The corresponding pure elements were used as standards for intensity references.

5.3.2 Crystal Structure Determination

The $Eu(Ga_{1-x}Tt_x)_2$ (Tt = Si, Ge, $0 \leq x \leq 1$) series was characterized at room temperature by both powder and single-crystal X-ray diffraction. Phase analysis and lattice parameters were determined on a Huber 670 image-plate powder diffraction camera (Cu $K\alpha_1$ radiation, λ = 1.54059 Å) with a step size of 0.005° and exposure time of 1-2 hours. Data acquisition was controlled via the *in situ* program. The crystal system and the lattice parameters were obtained from Rietveld refinement using program *Rietica*.[21]

For single crystal X-ray diffraction experiments, several silvery block- or plate-shaped crystals were selected from the cast of each product. The quality of each crystal was checked by a rapid scan on a Bruker SMART Apex CCD diffractometer with Mo $K\alpha_1$ radiation (λ = 0.71073 Å), and then the best crystals were chosen for further data collection. Diffraction data were harvested from three sets of 606 frames on a full sphere with 0.3° scans in ω and with an exposure time of 10 sec per frame. For experiments conducted on a STOE IPDS diffractometer, data were harvested from two sets of 180 frames with an exposure time of 1 min per frame. Data collection on the STOE STADI 4 machine was done in usual $\theta/2\theta$ mode. Relevant parameters of data collection are given in Table 1.

Intensities were extracted and then corrected for Lorentz and polarization effects using the *SAINT* program.[22] The program *SADABS*[22] was used for empirical absorption correction. Numerical absorption corrections were applied using the X-RED/X-SHAPE program.[23] The space group was determined by program *XPREP* in the *SHELXTL* software package.[24] The structures were solved by direct methods and refined on F^2 by full-matrix least-squares methods using the *SHELXTL*[24] or WinCSD[25] software packages. The entire sets of reflections for the ternary $Eu(Ga_{1-x}Tt_x)_2$ (Tt = Si, Ge, $0 \leq x \leq 1$) series were matched with hexagonal or trigonal crystal systems. Further analysis led us to choose *P6/mmm* (AlB_2-type) for

$Eu(Ga_{1-x}Si_x)_2$ ($0.22(6) \leq x \leq 0.82(2)$). During refinements of $Eu(Ga_{1-x}Ge_x)_2$ ($0.25 \leq x \leq 0.60$), the Ga and Ge atoms could not be distinguished given the X-ray scattering factors for Ga and Ge atoms which differ by at most 3.1%. Moreover, interatomic distances within a unit cell were also not useful to distinguish Ga and Ge atoms due to their similar covalent radii: r(Ga) = 1.25 Å and r(Ge) = 1.22 Å.[26] However, as we reported in our earlier investigation,[16] electronic structure calculations performed on several structural models of EuGaGe provided a clear energetic minimum, which agreed with structural characterization of EuGaSn. Thus, we utilized similar calculations to address these structures and their compositions. Furthermore, the chemical composition of all compounds obtained from EDXS analysis very well matched the loading composition.

5.3.3 X-ray Absorption Spectroscopy (XAS)

XAS measurements on the Eu L_{III} edge of three $Eu(Ga_{1-x}Ge_x)_2$ (x = 0.50(2), 0.55(2), 0.60(2)) samples were examined at the EXAFS beam-line A1 of HASYLAB at DESY (Hamburg, Germany). Each sample was ground together with dry B_4C powder before the measurement. Wavelength selection was realized by means of a double-crystal Si(111) monochromator of four crystal modes with digitally stabilized components. Resolution was about 2 eV (fwhm) at the Eu L_{III} edge of 6977 eV. Eu_2O_3 was used as a reference during the measurement.

5.3.4 Magnetic Susceptibility Measurements

Temperature dependent magnetic susceptibility of $Eu(Ga_{1-x}Ge_x)_2$ (x = 0.50(2), 0.55(2), 0.60(2)) samples were measured using a Quantum Design, MPMS XL-7 SQUID magnetometer. The measured temperature range was 1.8-400 K in a magnetic field of 0.1 T. The bulk samples (ca. 200 mg) from the same preparation as the one used for powder diffraction experiments were exploited for the magnetic measurements.

5.3.5 Computational Details

Tight-binding, linear muffin-tin orbital (TB-LMTO) calculations were carried out in the atomic sphere approximation (ASA) using the Stuttgart program.[27] Exchange and

correlation were treated by the local spin density approximation (LSDA).[28] All relativistic effects except spin-orbit coupling were taken into account by using a scalar relativistic approximation.[29]

In the ASA method, space is filled with overlapping Wigner-Seitz (WS) atomic spheres. The symmetry of the potential is considered spherical inside each WS sphere, and a combined correction is used to take into account the overlapping part.[30] The radii of WS spheres were obtained by requiring that the overlapping potential be the best possible approximation to the full potential, and were determined by an automatic procedure.[30] This overlap should not be too large because the error in kinetic energy introduced by the combined correction is proportional to the fourth power of the relative sphere overlap. No empty spheres (ES)[27] were used, but the overlapping maximum was adjusted to fill up the interstitial space. The WS radii for the various elements covered the following ranges: Eu, 2.09-2.26 Å; Ga, 1.30-1.52 Å; Si = 1.33 Å; Ge = 1.46-1.51 Å. More details are shown in Supplementary material (see Table S1). The basis sets included 6*s*, 6*p*, and 5*d* orbitals for Eu; 4*s*, 4*p*, and 4*d* orbitals for Ga; 3*s*, 3*p*, and 3*d* orbitals for Si; 4*s*, 4*p*, and 4*d* orbitals for Ge. The Eu 6*p*, Ga 4*d*, Si 3*d*, and Ge 4*d* orbitals were treated by the Löwdin downfolding technique,[27–29] and the Eu 4*f* wave functions were treated as core functions occupied by 7 electrons. The crystal orbital Hamilton population (COHP) curves[6] and the integrated COHP values (ICOHPs) were calculated to determine the relative influences of various interatomic orbital interactions. The *k*-space integrations were performed by the tetrahedron method.[31] The self-consistent charge density was obtained using 296 irreducible *k*-points in the Brillouin zone for the hexagonal cell. The contribution of the nonspherical part of the charge density to the potential was neglected.

5.4 Results and Discussion

5.4.1 Crystal Structures

$Eu(Ga_{1-x}Si_x)_2$ ($0.22(6) \leq x \leq 0.82(2)$) adopt only the AlB_2-type structure (space group *P*6/*mmm*) with a wide homogeneity width, whereas $Eu(Ga_{1-x}Ge_x)_2$ ($0.25(2) \leq x \leq 0.60(2)$) crystallize in four different structure types, all of which can be described as derivatives of the

AlB_2-typ structure. Important crystallographic data for $Eu(Ga_{1-x}Si_x)_2$ (x = 0.29(1), 0.33(1), 0.50(2), 0.69(1)) and $Eu(Ga_{1-x}Ge_x)_2$ (x = 0.25(2), 0.35(2), 0.45(5), 0.50(2), 0.55(2), 0.60(2)) are summarized in Tables 1-2 (also see Supplementary materials Table S2 and S3).

Table 1. Single Crystal Crystallographic Data for $Eu(Ga_{1-x}Si_x)_2$

Loaded composition	$Eu(Ga_{0.74}Si_{0.26})_2$	$Eu(Ga_{0.70}Si_{0.30})_2$	$Eu(Ga_{0.50}Si_{0.50})_2$	$Eu(Ga_{0.33}Si_{0.67})_2$
Empirical formula	$Eu(Ga_{0.71(1)}Si_{0.29(1)})_2$	$Eu(Ga_{0.67(1)}Si_{0.33(1)})_2$	$Eu(Ga_{0.50(1)}Si_{0.50(1)})_2$	$Eu(Ga_{0.31(1)}Si_{0.69(1)})_2$
Formula weight ($g\ mol^{-1}$)	267.18	263.91	249.77	233.95
Lattice params (Å)	a = 4.2431(6)	a = 4.2267(3)	a = 4.1698(2)	a = 4.1087(6)
	c = 4.5829(9)	c = 4.5846(5)	c = 4.5592(4)	c = 4.5384(9)
Vol ($Å^3$)	71.46(2)	70.93(1)	68.651(8)	66.35(2)
Density calcd. ($g\ cm^{-3}$)	5.804	5.847	6.041	5.897
Diffractometer	STOE IPDS	SMART Apex	STOE IPDS	STOE IPDS
2θ range (deg)	8.90−68.4	8.9−70.04	8.94−69.72	8.98−69.44
Index ranges	$-6 \le h \le 6$, $-6 \le k \le 6$, $-6 \le l \le 7$	$-6 \le h \le 6$, $-6 \le k \le 6$, $-7 \le l \le 7$	$-6 \le h \le 6$, $-6 \le k \le 6$, $-7 \le l \le 7$	$-6 \le h \le 5$, $-6 \le k \le 6$, $-7 \le l \le 6$
Reflns collected	1263	1020	1030	1312
Independent reflns	86 [R_{init} = 0.0493]	89 [R_{init} = 0.0208]	87 [R_{init} = 0.0172]	84 [R_{init} = 0.0659]
Data/refined params	86/6	89/6	87/6	84/6
GOF on F^2	1.192	1.146	1.190	1.173
R indices [$I > 2\sigma(I)$]	R1 = 0.0212, wR2 = 0.0594	R1 = 0.0097, wR2 = 0.0235	R1 = 0.0085, wR2 = 0.0216	R1 = 0.0125, wR2 = 0.0320
R indices (all data)	R1 = 0.0212, wR2 = 0.0594	R1 = 0.0097, wR2 = 0.0235	R1 = 0.0085, wR2 = 0.0216	R1 = 0.0125, wR2 = 0.0320
Largest diff. peak and hole ($e^-/Å^3$)	1.569/−1.806	0.483/−0.630	0.672/−0.414	0.439/−0.780

Table 2. Crystallographic Data for Single Crystals of $Eu(Ga_{1-x}Ge_x)_2$

$Eu(Ga_{0.75(2)}Ge_{0.25(2)})_2$	$Eu(Ga_{0.65(2)}Ge_{0.35(2)})_2$	$Eu(Ga_{0.55(5)}Ge_{0.45(5)})_2$	$Eu(Ga_{0.50(2)}Ge_{0.50(2)})_2$	$Eu(Ga_{0.45(2)}Ge_{0.55(2)})_2$	$Eu(Ga_{0.40(2)}Ge_{0.60(2)})_2$
293.20	293.40	293.60	294.27	294.56	294.85
*P*6/*mmm* (no.191)	*P*6/*mmm* (no.191)	*P*6/*mmm*(no.191)	$P6_3/mmc$ (no.194)	$P\bar{3}m1$ (no.164)	$P\bar{6}m2$ (no.187)
$a = 4.2812(6)$	$a = 4.2614(8)$	$a = 4.241(1)$	$a = 4.2646(6)$	$a = 4.2484(6)$	$a = 4.232(1)$
$c = 4.6031(9)$	$c = 4.582(1)$	$c = 4.555(1)$	$c = 18.041(5)$	$c = 40.852(8)$	$c = 23.02(1)$
73.07(2)	72.06(3)	70.95(5)	284.15(9) Å^3	638.54(18)	357.0(2)
1	1	1	4	9	5
6.688	6.781	6.688	6.879	6.887	6.844
STOE IPDS	SMART Apex	STOE STADI 4	SMART Apex	SMART Apex	SMART Apex
11.00−70.60	8.9−69.88	8.95-64.78	4.48−55.94	2.00−56.61	1.76−55.84
$-6 \le h \le 6$, $-6 \le k \le 6$, $-5 \le l \le 7$	$-6 \le h \le 6$, $-6 \le k \le 6$, $-7 \le l \le 7$	$-6 \le h \le 5$, $0 \le k \le 6$, $-6 \le l \le 6$	$-5 \le h \le 5$, $-5 \le k \le 5$, $-23 \le l \le 23$	$-5 \le h \le 5$, $-5 \le k \le 5$, $-53 \le l \le 52$	$-5 \le h \le 5$, $-5 \le k \le 5$, $-30 \le l \le 29$
1377	712	573	2203	5647	3075
92 [$R_{init} = 0.1219$]	82 [$R_{init} = 0.0937$]	75	169 [$R_{init} = 0.0428$]	734 [$R_{init} = 0.0369$]	419 [$R_{init} = 0.0246$]
92/6	86/6	71/11	169/12	734/43	419/27
1.192	1.073	0.85	1.259	1.144	1.125
R1 = 0.0305, wR2 = 0.0629 R1 = 0.0348, wR2 = 0.0641	R1 = 0.0343 wR2 = 0.0727 R1 = 0.0346 wR2 = 0.0729	R1 = 0.0239, wR2 = 0.0359 R1 = 0.0279, wR2 = 0.0367	R1 = 0.0245, wR2 = 0.0504 R1 = 0.0322, wR2 = 0.0530	R1 = 0.0565, wR2 = 0.1204 R1 = 0.0787, wR2 = 0.1357	R1 = 0.0278, wR2 = 0.0518 R1 = 0.0382, wR2 = 0.0556
2.38/–1.55	2.23/–2.75	0.24/-0.45	0.80/–0.97	4.21/–5.75	0.94/–1.14

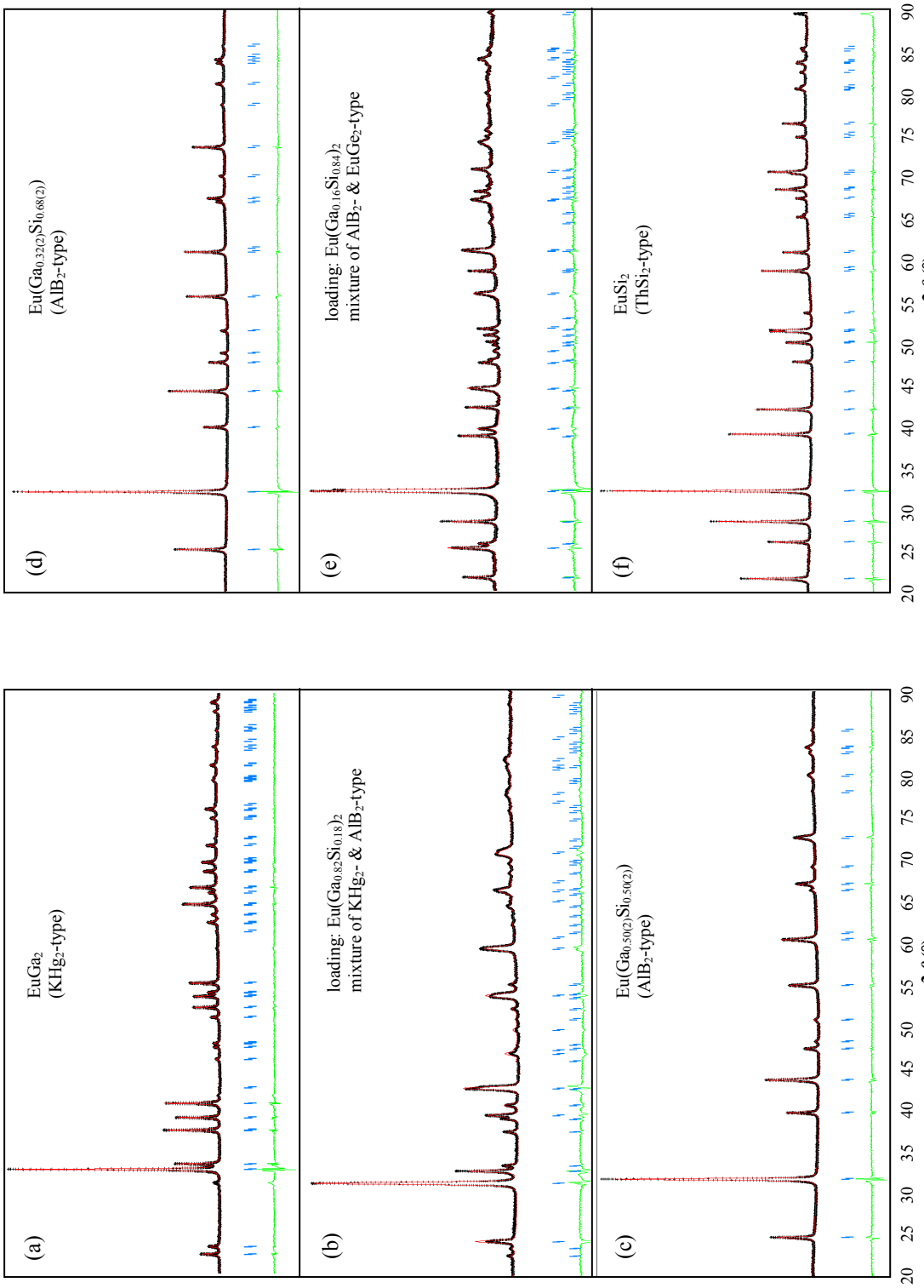

Figure 4. Powder X-ray diffraction patterns of selected samples of the $Eu(Ga_{1-x}Si_x)_2$ ($0 \leq x \leq 1$) series

$Eu(Ga_{1-x}Si_x)_2$. Along the entire $Eu(Ga_{1-x}Si_x)_2$ series, three different structure types are observed as clearly seen in powder X-ray diffraction patterns (Figure 1). Single-phase products adopting the AlB_2-type structure appear in the region of $0.22(6) \leq x \leq 0.82(2)$. Two two-phase regions, where diffraction patterns from two boundary phases are detected, surround this single-phase region. All Rietveld refinements of powder diffraction patterns produced lattice parameters in excellent agreement with those obtained from single crystal X-ray diffraction throughout the series. The three observed crystal structures are illustrated in Figure 2.

$EuGa_2$ adopts the orthorhombic KHg_2-type structure in the space group *Imma*, which is closely related to the AlB_2-type structure since both structural types contain hexagonal anionic networks stacked in an eclipsed manner with larger atoms located between these networks. Ga atoms form a 3-dimensional 4-connected (3D4C) net based on six-membered chair-shaped rings which lie directly above/below each other in an alternating way[32] and create a distorted tetrahedral environment at each Ga atom[20]. Two Ga−Ga bond distances are observed within pseudo hexagonal nets: 2.654(1) Å and 2.6916(9) Å; a slightly larger distance of 2.812(1) Å was found between these layers[20]. Larger Eu atoms fill the voids within these chair-shaped networks, and are symmetrically displaced along the *y*-axis away from these networks.

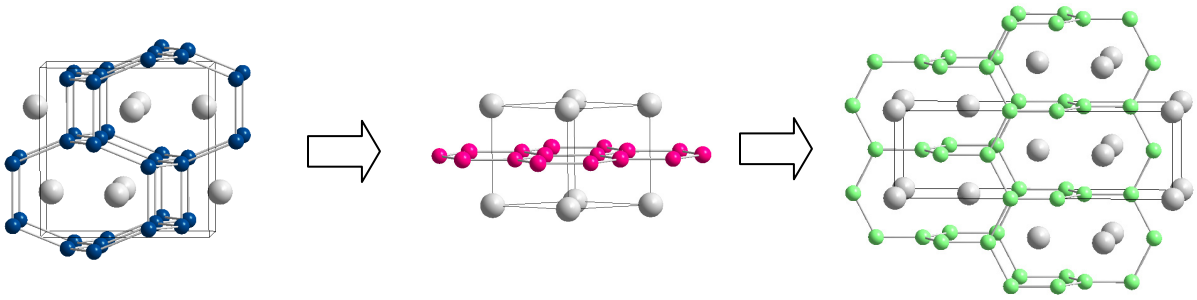

$EuGa_2$ (KHg_2-type, 8 e^-)

$Eu(Ga_{1-x}Si_x)_2$ ($0.22(6) \leq x \leq 0.82(2)$) ($AlB_2$-type, 8.44(12) – 9.64(4) e^-)

$EuSi_2$ ($ThSi_2$-type, 10 e^-)

Figure 2. Three observed crystal structures of the $Eu(Ga_{1-x}Si_x)_2$ $(0 \leq x \leq 1)$ series

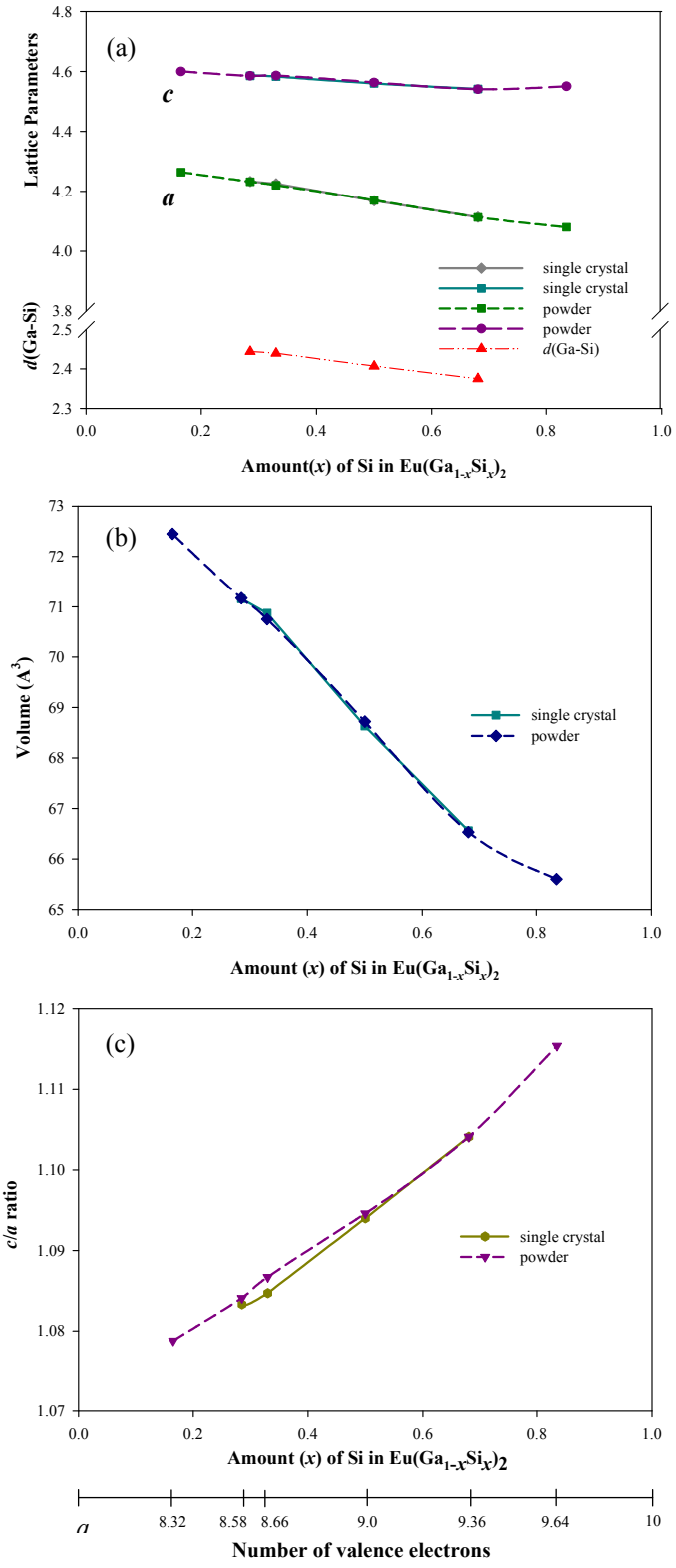

Figure 3. Lattice parameter *a*, *c* and *d*(Ga−Si) (a),unit cell volume (b), and *c*/*a* ratio and the corresponding number of valence electrons (c) of the AlB_2-type phase of $Eu(Ga_{1-x}Si_x)_2$ as a function of Si amounts.

As Si atoms replace Ga atoms in $EuGa_2$, a mixture of KHg_2-type and AlB_2-type structures occurs, as seen in the powder X-ray diffraction patterns in Figure 1(b). As the Si content increases, the patterns indicate single-phase, AlB_2-type phases. Refinements of single crystal diffraction data indicate that Ga and Si atoms are statistically distributed on the 2*d* sites and form honeycomb-like $^{2}_{\infty}[(Ga_{1-x}Si_x)_2]$ planar nets, while Eu atoms are located in the hexagonal prismatic voids between these nets.[33] Refinements and chemical analyses of $Eu(Ga_{1-x}Si_x)_2$ samples containing AlB_2-type structures indicate the lower boundary of composition lies between $x = 0.16(2)$ and 0.28(2), while the upper boundary extends up to at least $x = 0.82(2)$. Therefore, the observed range of composition, $0.22(6) \leq x \leq 0.82(2)$, corresponds to 8.44(12)-9.64(4) valence electrons per formula unit.

As illustrated in Figure 3 plots the lattice parameters *a* and *c*, as well as the unit cell volumes decrease significantly as smaller Si atoms replace Ga atoms (covalent radii: *r*(Si) = 1.17 Å, *r*(Ga) = 1.25 Å).[26] Moreover, *a* drops faster than *c*, so the *c*/*a* ratios increase. In addition to the size effect, however, the number of valence electrons increases by ca. 1.0 electron, and the Ga−Si distances decrease from 2.440(2) Å for $Eu(Ga_{0.71(2)}Si_{0.28(2)})_2$ to 2.3750(2) Å for $Eu(Ga_{0.32(2)}Si_{0.68(2)})_2$.

Beyond the experimentally observed homogeneity range of the AlB_2-type phase, i.e., $x \geq 0.82(2)$, products begin to contain the $ThSi_2$-type phase (space group $I4_1/amd$) in addition to an AlB_2-type phase, as shown in Figure 1(e). Refinement of the powder X-ray diffraction patterns also suggest that Ga substitutes for a small amount of Si atoms in $EuSi_2$, but we did not pursue any further analysis. At $x = 1$, the $ThSi_2$-type, $EuSi_2$ phase (see Figure 2(right)) crystallizes as a single-phase product, see Figure 1(f).

$Eu(Ga_{1-x}Ge_x)_2$. Two binary end compounds of this series, $EuGa_2$ and $EuGe_2$, adopt, respectively, the KHg_2-type (in the space group *Imma*)[18,19] and the $EuGe_2$-type (in the space group $P\bar{3}m1$).[33] For ternary compositions, we have found four distinct, but structurally related compounds: the AlB_2-type structure for Ga-rich compositions, the YPtAs-type structure for the equiatomic composition, and two new structures for Ge-rich compositions. The crystal structures for $x \geq 0.50$ are based on puckered 6^3 nets of Ga/Ge atoms stacked in an eclipsed fashion along the *c*-axis. The powder X-ray diffraction patterns are illustrated in

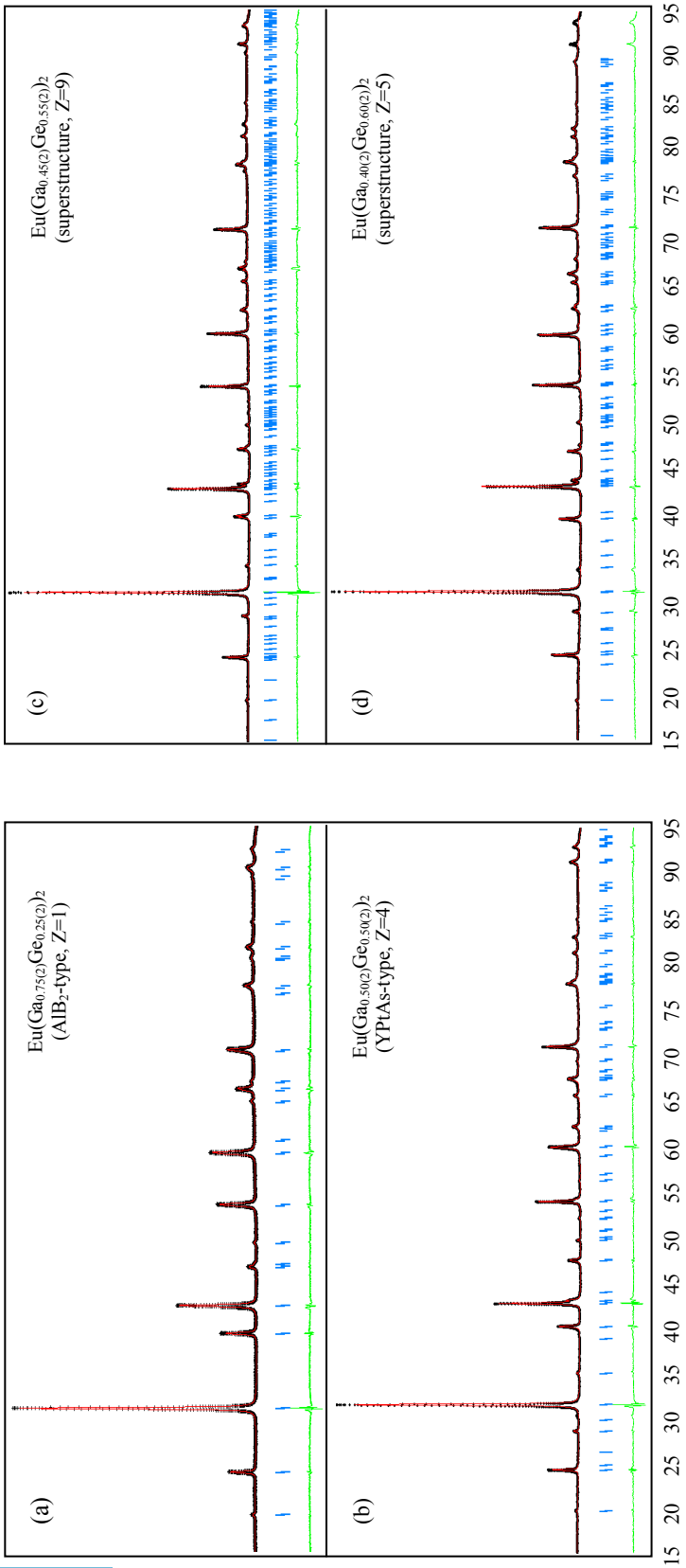

Figure 4. Powder X-ray diffraction patterns of $Eu(Ga_{1-x}Ge_x)_2$ (x = 0.25(2), 0.50(2), 0.55(2), 0.60(2))

Figure 4, and all lattice parameters obtained from powder X-ray diffraction are in good agreement to those from single crystal X-ray diffractions.

Two Ga-rich compounds, $Eu(Ga_{0.75(2)}Ge_{0.25(2)})_2$ and $Eu(Ga_{0.65(2)}Ge_{0.35(2)})_2$, crystallize in the AlB_2-type structure (Figure 5); the powder patterns of $Eu(Ga_{0.75(2)}Ge_{0.25(2)})_2$ is shown in Figure 4(a). As in the $Eu(Ga_{1-x}Si_x)_2$ phases, the Ga and Ge atoms are statistically distributed at the 2*d* site. Furthermore, there is no evidence to suggest any in-plane or out-of-plane ordering of Ga and Ge atoms throughout the structure.

As the composition reaches an equiatomic ratio EuGaGe, the YPtAs-type structure forms (see Figure 5), which can be described as a puckered derivative of the AlB_2-type structure yielding a quadrupled lattice parameter *c* because of the stacking sequence of 6^3 nets.[16] Ga and Ge atoms form puckered three-bonded, alternating hexagonal layers, and this observed puckering mode locates Ga atoms closer to and Ge atoms farther from each other between adjacent layers. Furthermore, there are two distinct coordination environments at the Eu sites: Eu(1) is surrounded by an octahedron of Ge atoms, whereas Eu(2) is surrounded by a trigonal prism of Ga atoms. Assigning the positions for Ga and Ge atoms could be obtained by (1) differentiation between Ga and Sn in isostructural EuGaSn; (2) total energy comparisons obtained from electronic structure calculations on different atomic arrangements; and (3) the differential isotropic thermal displacement parameters (U_{11}) at the two 4*f* sites.[16] In Figure 4(b), the diffraction peaks generated by this quadrupled unit cell are clearly detected at 2θ = 28.62°, 34.33°, and 62.03° among strong diffraction peaks which exist for $Eu(Ga_{0.75(2)}Ge_{0.25(2)})_2$.

Two Ge-rich phases in $Eu(Ga_{1-x}Ge_x)_2$, x = 0.55 and 0.60, adopt two complex structures, which also can be described as puckered derivatives of the AlB_2-type structure. $Eu(Ga_{0.45(2)}Ge_{0.55(2)})_2$ contains nine puckered 6^3 nets stacked along the *c*-axis (see Figure 5). During refinement, we adopted the manner in which Ga and Ge atoms are distributed in $Eu(Ga_{0.50(2)}Ge_{0.50(2)})_2$, with Ga atoms located closer to and Ge atoms located farther away from each other between adjacent layers. During this process, we identified a single hexagonal layer in the unit cell that should contain only Ge atoms because the atoms on this layer are located away from atoms both above and below this layer. Furthermore, by assigning Ge atoms to these sites, we agree with the loaded chemical composition, which is

also confirmed by EDXS measurements. This structure type is a combination of two YPtAs-type EuGaGe unit cells with one $EuGe_2$ unit cell.

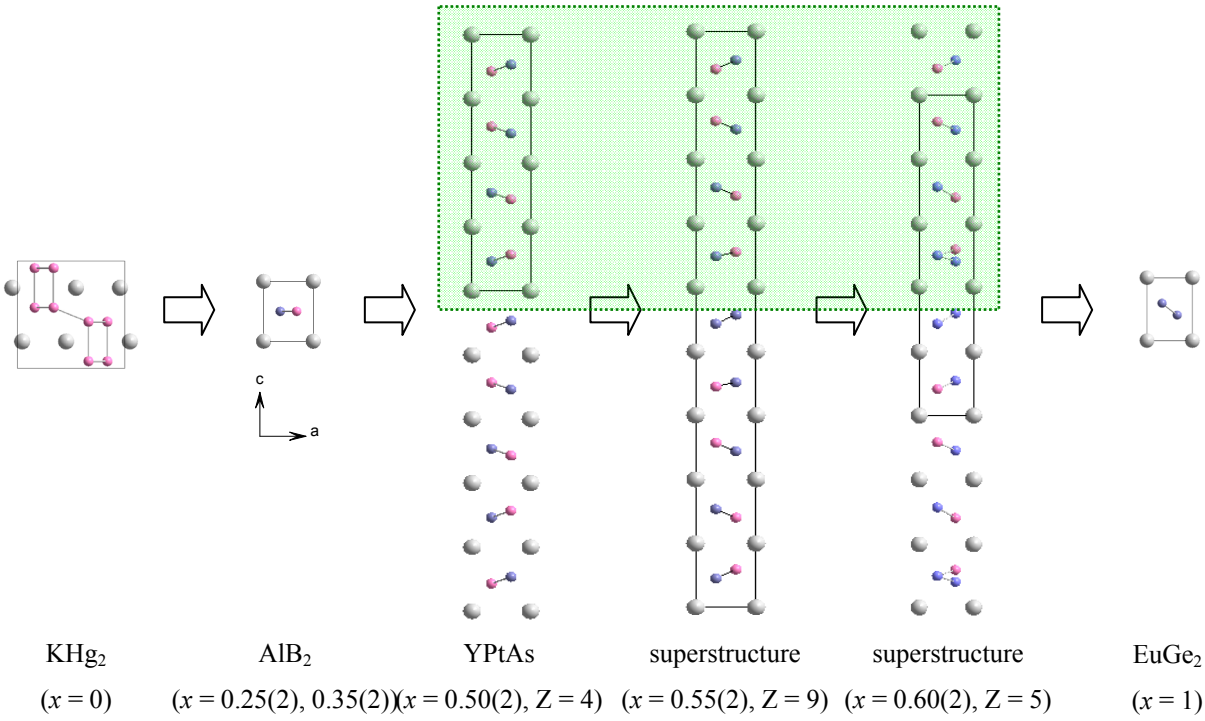

Figure 5. Six Crystal Structures of $Eu(Ga_{1-x}Ge_x)_2$ ($0 \leq x \leq 1$) series.

A second phase, $Eu(Ga_{0.40(2)}Ge_{0.60(2)})_2$, contains five puckered 6^3 nets stacked along *c*-axis in the crystallographic unit cell. During refinement, we observed an anomalously large thermal parameter (U_{33}) for one 1*f* site at $x = 2/3$, $y = 1/3$, and $z = 1/2$. Thus, we refined this site as a split site, in which two symmetrically identical 2*i* sites with ca. 50 % site occupancies at $x = 2/3$, $y = 1/3$, and $z = 0.4798(2)$ are chosen over one 1*f* site located on a mirror plane. We assigned Ga and Ge atoms as for $Eu(Ga_{0.50(2)}Ge_{0.50(2)})_2$ and $Eu(Ga_{0.45(2)}Ge_{0.55(2)})_2$. To achieve agreement with the chemical composition confirmed by EDXS, we assign Ga to one of two split-sites.

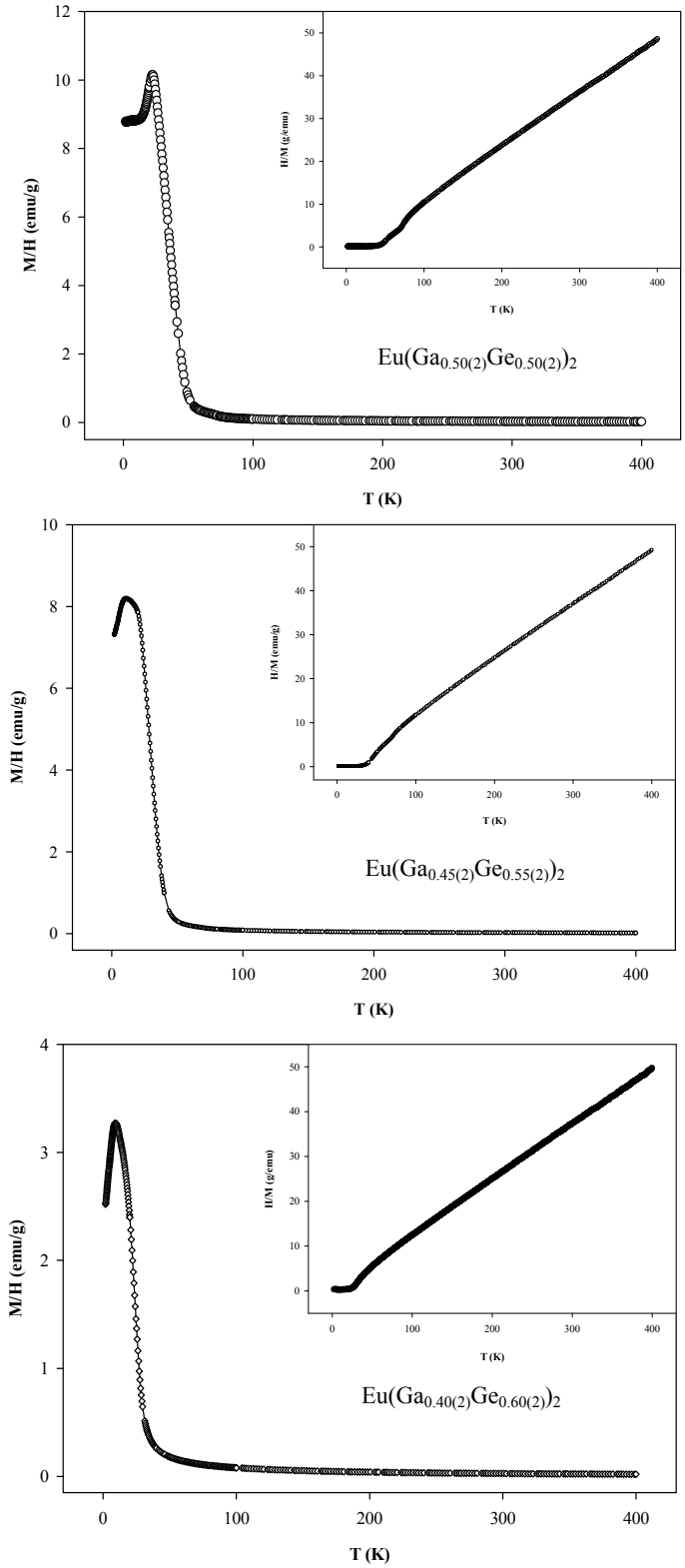

Figure 6. Temperature dependence of the magnetic susceptibilities and the reciprocal susceptibilities for $Eu(Ga_{1-x}Ge_x)_2$ (x = 0.50(2), 0.55(2), 0.60(2)).

5.4.2 Magnetic Susceptibilities

Temperature dependent magnetic susceptibilities and reciprocal susceptibilities of three $Eu(Ga_{1-x}Ge_x)_2$ compounds (x = 0.50(2), 0.55(2), 0.60(2)) were measured at 0.1 T, and shown in Figure 6. All three compounds show Curie-Weiss behavior at temperature above, 130(1) K for $Eu(Ga_{0.50(2)}Ge_{0.50(2)})_2$; 140(1) K for $Eu(Ga_{0.45(2)}Ge_{0.55(2)})_2$; 100(1) K for $Eu(Ga_{0.40(2)}Ge_{0.60(2)})_2$. However, below these temperatures, the susceptibilities become dependent on the external magnetic field and present antiferromagnetic ordering, respectively, with θ_p = +14.45(5) K for $Eu(Ga_{0.50(2)}Ge_{0.50(2)})_2$, +6.74(4) K for $Eu(Ga_{0.45(2)}Ge_{0.55(2)})_2$, and +4.81(5) for $Eu(Ga_{0.40(2)}Ge_{0.60(2)})_2$. Fitting the linear $1/\chi$ versus T curves above ca. 130 K give effective magnetic moments to be 7.98(1)μ_B for $Eu(Ga_{0.50(2)}Ge_{0.50(2)})_2$, 7.96(1)$\mu_B$ for $Eu(Ga_{0.45(2)}Ge_{0.55(2)})_2$, and 7.99(1)$\mu_B$ for $Eu(Ga_{0.40(2)}Ge_{0.60(2)})_2$, measurements all of which are very close to the value of the Eu^{2+} free ion, 7.94 μ_B, to indicate a $4f^7$ electronic configuration for Eu.

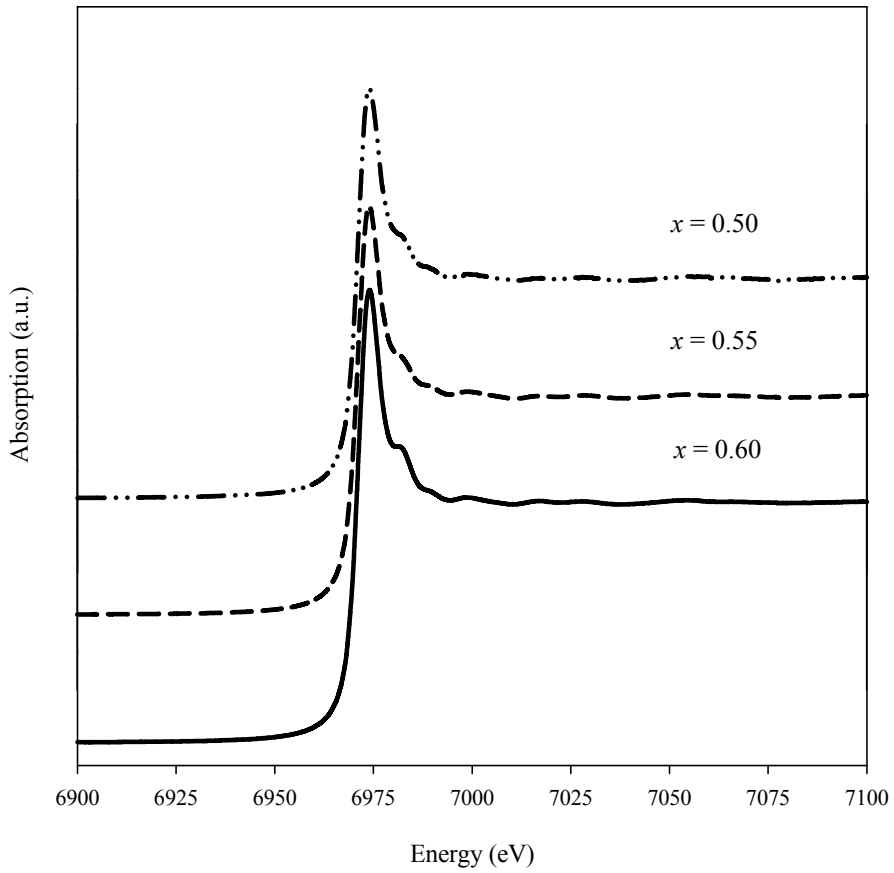

Figure 7. XAS spectra of $Eu(Ga_{1-x}Ge_x)_2$ (x = 0.50(2), 0.55(2), 0.60(2))

5.4.3 Eu L_{III} XAS Measurements

In Figure 7, sharp absorption maxima are observed at ca. 6977 eV for three $Eu(Ga_{1-x}Ge_x)_2$ (x = 0.50(2), 0.55(2), 0.60(2)) samples, which further indicates a $4f^7$ electronic configuration at the Eu atoms. Small shoulders are observed in these spectra at ca. 10 eV higher than the main absorption peak, which are assigned to small traces of Eu_2O_3 (electronic configuration $4f^6$, Eu^{3+}) in all three samples.

5.4.4 Electronic Structure Calculations

To investigate the electronic structure and chemical bonding features that contribute to the structural trends and atomic distributions in $Eu(Ga_{1-x}Tt_x)_2$ (Tt = Si, Ge, $0 \leq x \leq 1$), TB-LMTO-ASA electronic structure calculations were carried out on observed and hypothetical models of the crystal structures. In particular, DOS and COHP curves were carefully analyzed to understand the observed homogeneity range of the AlB_2-type phase of $Eu(Ga_{1-x}Tt_x)_2$. For all systems, the DOS curves for the majority and minority spin states differed only slightly, so subsequent DOS curves illustrate their superpositions.

$EuGa_2$. The DOS and two Ga−Ga COHP curves are illustrated in Figure 8, with the Fermi level (E_F) shown as the reference energy value. The Ga 4p bands dominate the total DOS in the region below E_F, which occurs near a pseudogap. Eu 5d and 6s bands show significant contributions to the total DOS above E_F. This decomposition of the total DOS curve of $EuGa_2$ is indicative of a polar intermetallic compound.[5] Two COHP curves correspond to two types of Ga−Ga bonds: (1) shorter bonds (2.654(1) Å and 2.6916(9) Å) within the 2-dimensional (2D) hexagonal nets; and (2) a longer bond (2.812(1) Å) connecting these 2D nets to create the 3D network. The COHP curves for the longer and shorter Ga−Ga contact are nearly optimized at E_F. Since $EuGa_2$ adopts the same KHg_2-type structure as $EuZn_2$ which we studied in our earlier work,[17] DOS and COHP curves of these two compounds can be compared, and, in fact, are very similar to each other. In our work for $Eu(Zn_{1-x}Ge_x)_2$,[17] we suggested that a small amount of Ge substitution for Zn in $EuZn_2$ might exist on the basis of the observed lattice constant changes detected from powder X-ray patterns. This suggestion could be supported by the Zn−Zn COHP curve: E_F fell among bonding states and the DOS

remained Zn−Zn bonding up to ca. 1.3 eV above E_F. $EuGa_2$ contains two more valence electrons than $EuZn_2$, and Ga−Ga COHP curve is, indeed, nearly optimized at E_F.

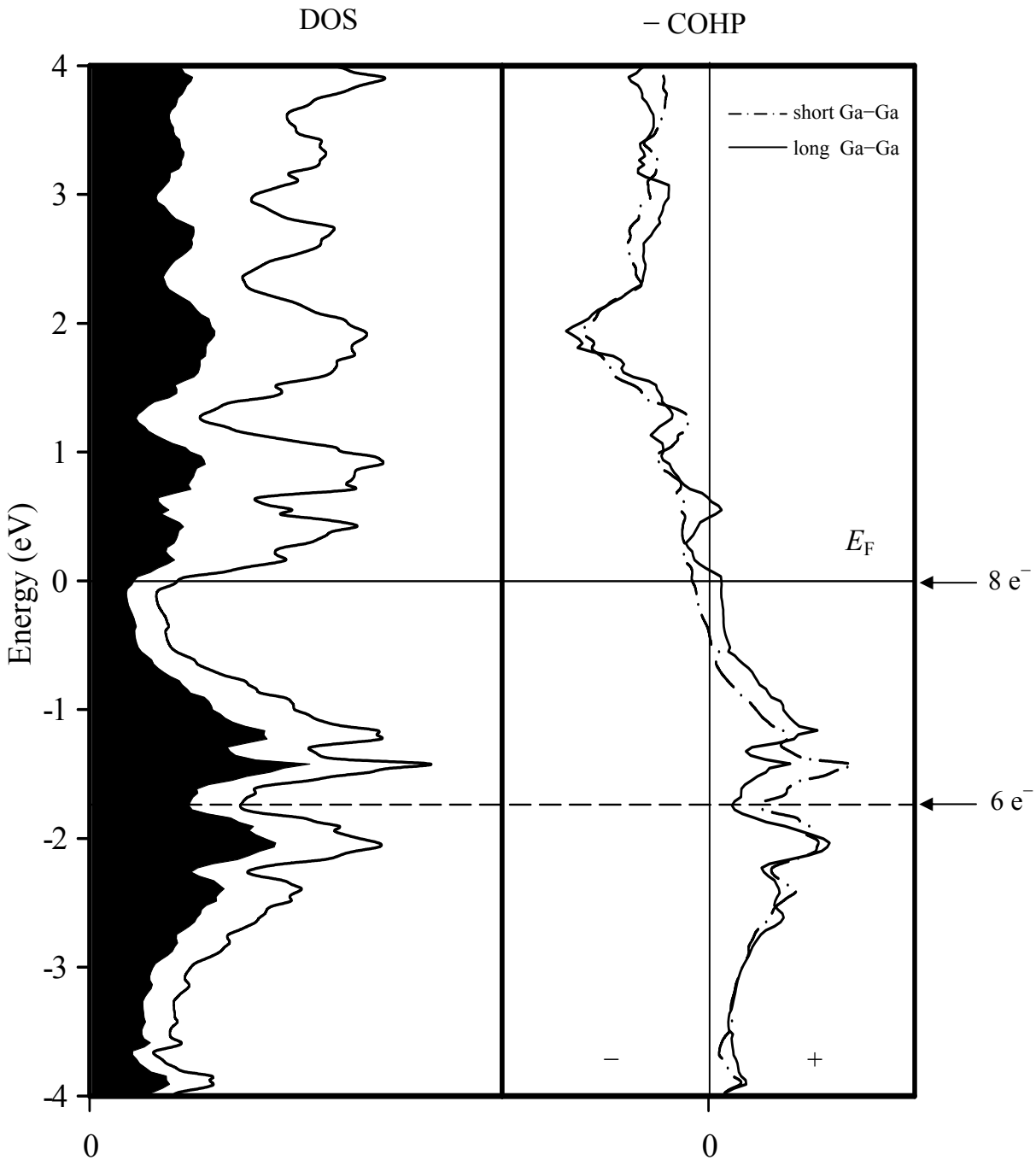

Figure 8. DOS and COHP curves for $EuGa_2$. (Left) Total DOS (solid line), Eu PDOS (white region) and Ga PDOS (black region). (Right) Two types of Ga−Ga COHP curves. The Fermi level is indicated by the long solid line and is the energetic reference (0 eV).

Therefore, analysis of COHP curves proves that there exists the homogeneity range for the $Eu(Zn_{1-x}Ge_x)_2$ series in the KHg_2-type structure, which corresponds to a maximum of 8 valence electrons per formula unit.

$Eu(Ga_{1-x}Si_x)_2$ (AlB_2-type). Ternary silicide compounds for $0.22(6) \leq x \leq 0.82(2)$ crystallized in the AlB_2-type structure, and X-ray diffraction concluded the complete absence of ordering of Ga and Si. However, we considered a local short-range ordering between Ga and Si for theoretical calculations. Thus, we constructed three ordered, model structures of $Eu(Ga_{0.50(2)}Si_{0.50(2)})_2$ for TB-LMTO calculations. All models contain planar $^2_\infty[GaSi]$ layers with only Ga−Si contacts (an alternant 6^3 sheet), but differ from each other in how these 6^3 nets stack along *c*-axis. Detailed descriptions of model structures and calculation methods can be found in a previous article.[16] These calculations concluded that an ordered structure, which contains 6^3 sheets alternating along the *c*-axis to create Ga···Si interactions between planes in the space group $P6_3/mmc$ (Figure 9, top) is the most stable structure. Thus, we utilized this model structure for subsequent DOS and COHP analysis.

Figure 9 (bottom) displays DOS and COHP curves, where E_F is the reference energy value in these curves. Throughout the entire DOS curve, significant mixing between valence orbitals of Eu and Ga/Si atoms are observed. In particular, the region below ca. −1.0 eV shows significant contributions from Ga and Si atoms, whereas the region above −1.0 eV is dominated by valence orbitals at Eu. A pseudogap at ca. −1.0 eV in the DOS curve corresponds to a valence band filling of 8 valence electrons per formula unit, which nearly matches the top of the Ga-Si bonding states shown in the adjacent COHP curve. In fact, E_F of EuGaSi falls nearly in essentially nonbonding states of the Ga-Si COHP curve. These nonbonding states extend ca. ±0.5 eV around E_F, indicating that a certain amount of additional electrons could be introduced above E_F without filling any significant Ga-Si antibonding states. Moreover, Eu-Ga and Eu-Si COHP curves stay in bonding states around this region. Although the Eu-Si and Eu-Ga COHP curves remain among bonding states, respectively, up to ca. 1 eV and ca. 2 eV above E_F, additional electrons should not exceed ca. 0.5 eV above E_F because it would introduce significant antibonding states to the Ga-Si COHP curve.

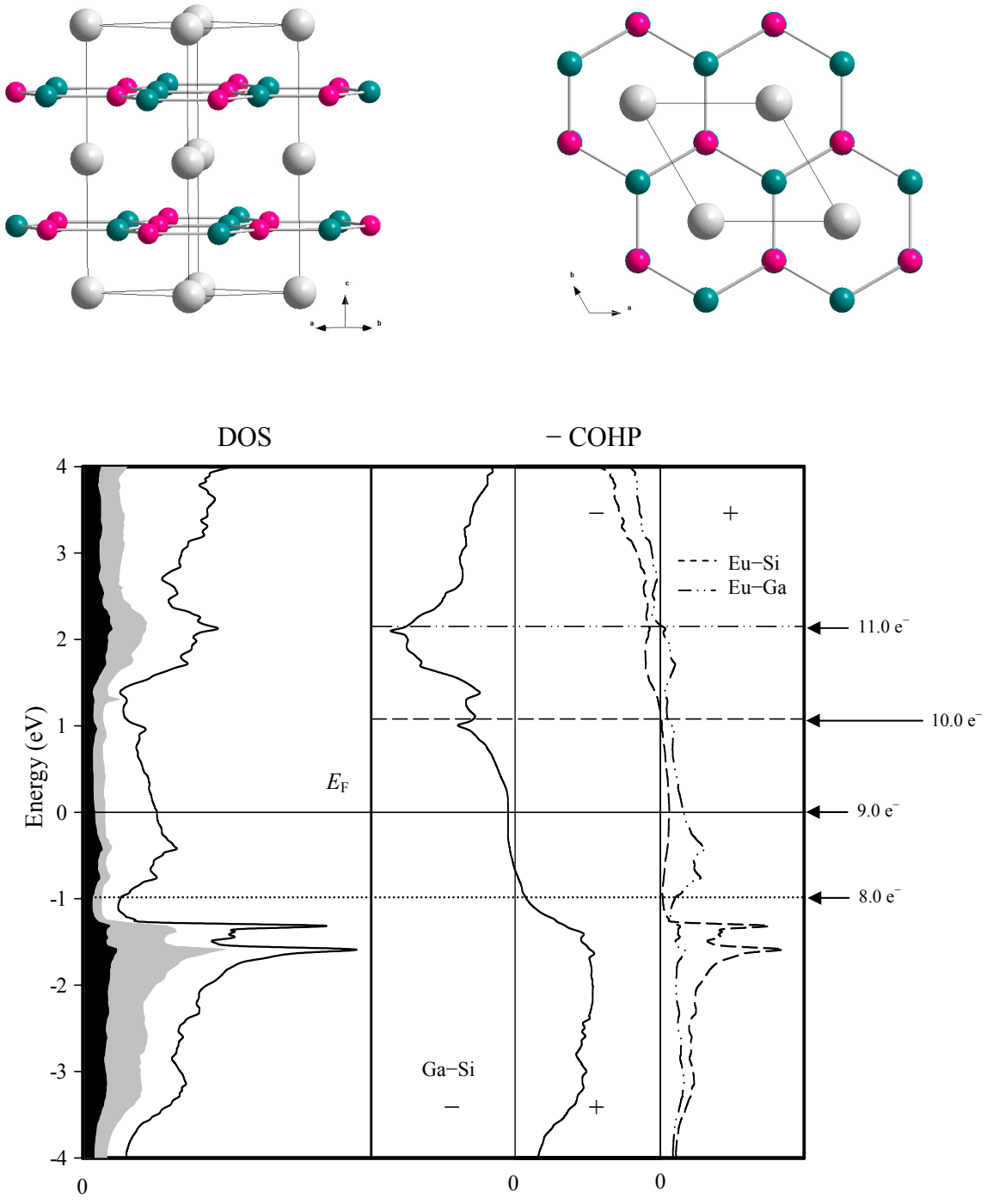

Figure 9. (Top) Structural model of $Eu(Ga_{0.50}Si_{0.50})_2$. See text for detailed descriptions. Eu: gray; Ga: red; Si: green. (Bottom) DOS and COHP curves for $Eu(Ga_{0.50}Si_{0.50})_2$. (Left) Total DOS (solid line), Eu PDOS (white region) and Si PDOS (gray region), and Ga PDOS (black region). (Right) Ga−Si, Eu−Si, and Eu−Ga COHP curves. The Fermi level is indicated by the long solid line and is the energetic reference (0 eV).

Therefore, we can consider the energy window for the AlB_2-type structure to lie within ±0.5 eV of E_F for EuGaSi, which corresponds to ca. 8.5-9.5 valence electrons. This theoretically obtained homogeneity range agrees well with the experimentally observed homogeneity range from ca. 8.44 e^- for $Eu(Ga_{0.78}Si_{0.22})_2$ to 9.64 e^- for $Eu(Ga_{0.18}Si_{0.82})_2$.

$Eu(Ga_{1-x}Ge_x)_2$ (AlB_2-type). Two experimentally obtained Ga-rich compounds for x = 0.25 and 0.35 adopt the AlB_2-type structure in the space group *P6/mmm*. Although we did not attempt to determine the precise upper or lower boundaries of this phase, we are certain that a homogeneity width exists for Ga-rich compositions with x between 0.25 and 0.35. We were not able to differentiate Ga and Ge atoms using X-ray diffraction, but we considered a local short-range ordering between Ga and Ge for theoretical calculations as we considered previously for Ga and Si in the isostructural $Eu(Ga_{1-x}Si_x)_2$.

DOS and COHP curves are illustrated in Figure 10. Most of the features of these curves are very similar to those of $Eu(Ga_{1-x}Si_x)_2$ in the AlB_2-type phase, including Eu-Ga and Eu-Ge COHP curves which are optimized, respectively, at ca. 1 eV and ca. 2 eV above E_F. A noticeable difference between the two compounds comes from the Ga-Ge COHP curve. Whereas the Ga-Si COHP curve of $Eu(Ga_{1-x}Si_x)_2$ shows essentially nonbonding states within ±0.5 eV of E_F for EuGaSi, the Ga-Ge COHP curve of "EuGaGe" is optimized at ca. 0.65 eV below E_F and sharply changes into antibonding states above this point. On the other hand, the Eu-Ga and Eu-Ge COHP curves for EuGaGe closely resemble those for EuGaSi. Therefore, on the basis of COHP analyses, we can expect that the upper limit of the homogeneity range for $Eu(Ga_{1-x}Ge_x)_2$ cannot exceed that of $Eu(Ga_{0.50(2)}Si_{0.50(2)})_2$, and can extend to lower valence electron counts. The energy window for the homogeneity range of $Eu(Ga_{1-x}Ge_x)_2$ with the AlB_2-type structure can occur between the optimum point of Ga-Ge COHP curve (ca. 0.65 eV below E_F corresponding to 8.25 e^-) and E_F. This can provide the reason that the AlB_2-type structure is observed only in Ga-rich compositions corresponding to less than 9 valence electrons for $Eu(Ga_{1-x}Ge_x)_2$ series. In fact, two experimentally observed compounds adopting the AlB_2-type structures have, respectively, 8.5 and 8.7 valence electrons, and these correspond to −0.42 and −0.25 eV below E_F.

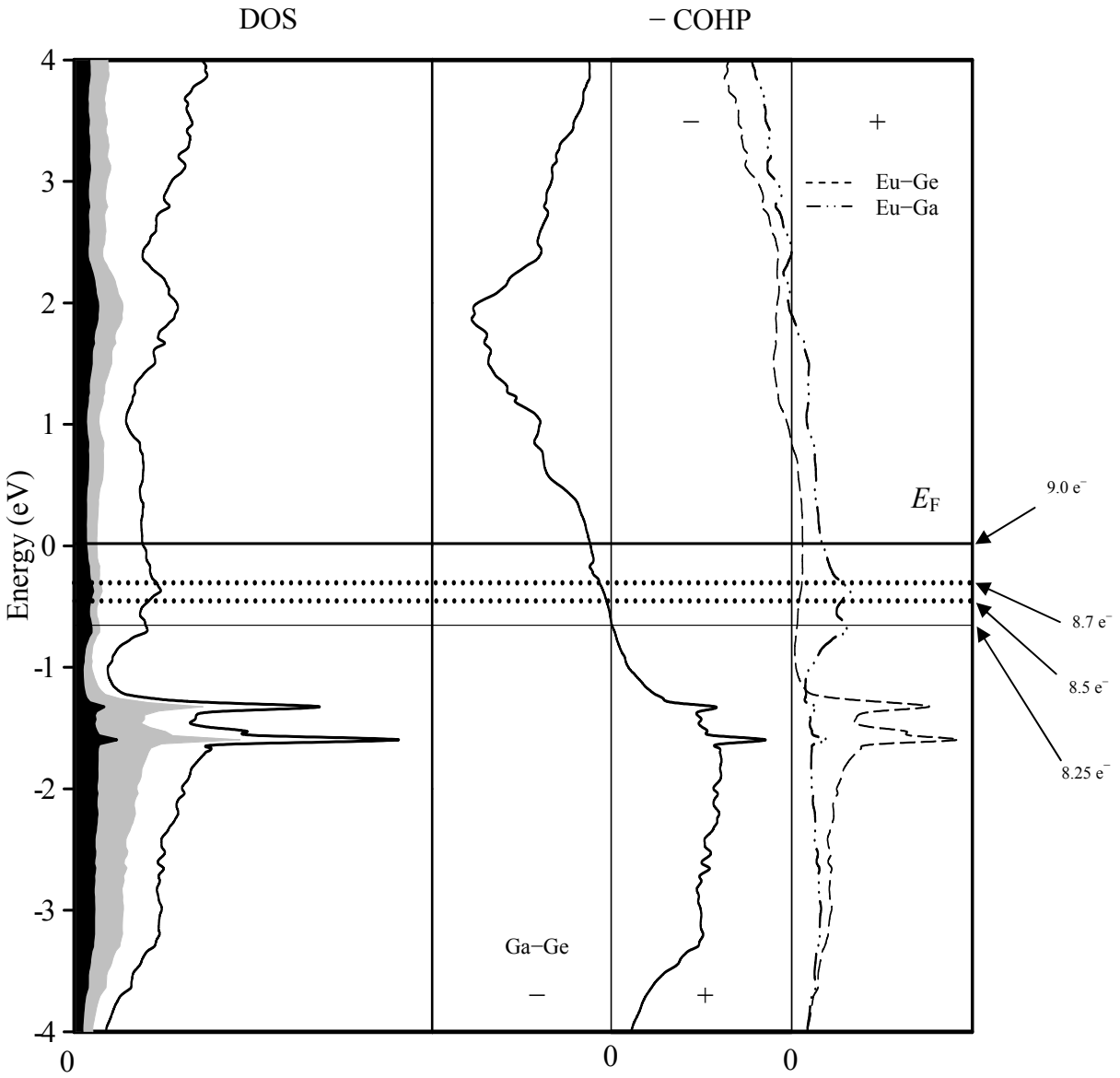

Figure 10. DOS and COHP curves for $Eu(Ga_{1-x}Ge_x)_2$ ($0.25 \leq x \leq 0.35$, AlB_2-type). (Left) Total DOS (solid line), Eu PDOS (white region), Ge PDOS (gray region), and Ga PDOS (black region). (Right) Ga−Ge, Eu−Ge, and Eu−Ga COHP curves. The Fermi level is indicated by the long solid line and is the energetic reference (0 eV)

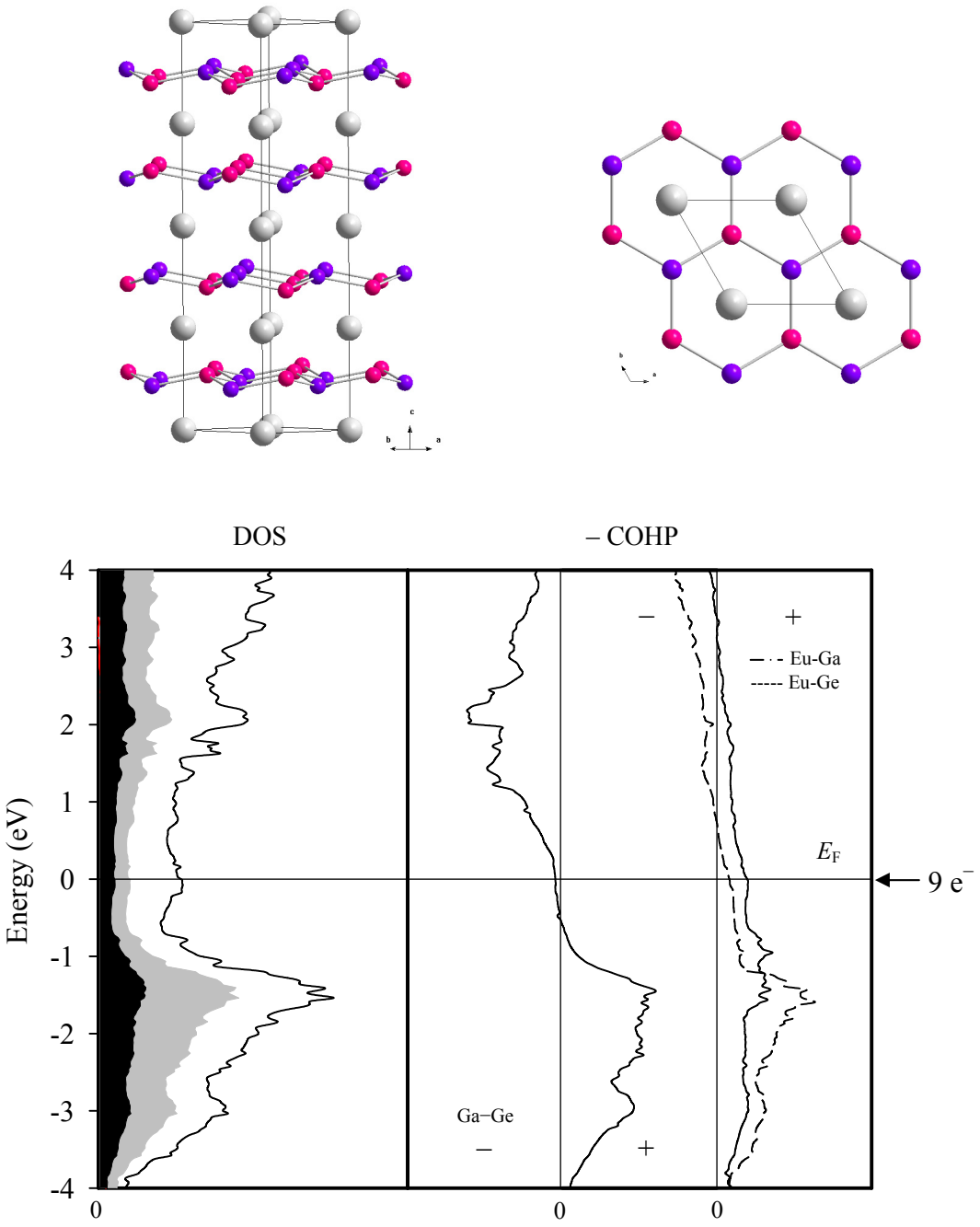

Figure 11. (Top) Structural model of $Eu(Ga_{0.50}Ge_{0.50})_2$. See text for detailed descriptions. Eu: gray; Ga: red; Ge: purple. (Bottom) DOS and COHP curves for $Eu(Ga_{0.50}Ge_{0.50})_2$ (YPtAs-type). (Left) Total DOS (solid line), Eu PDOS (white region), Ge PDOS (gray region), and Ga PDOS (black region). (Right) Ga–Ge, Eu–Ga, and Eu–Ge COHP curves. The Fermi level is indicated by the long solid line and is the energetic reference (0 eV).

$Eu(Ga_{0.50}Ge_{0.50})_2$. EuGaGe crystallizes in the YPtAs-type structure instead of the AlB_2-type structure with puckered $^2_\infty[GaGe]$ layers and interlayer Ga···Ga contacts at 3.726(1) Å (Figure 11, top). According to electronic structure calculations,[16] the observed arrangement of Ga and Ge atoms with closer Ga···Ga contacts between $^2_\infty[GaGe]$ sheets was the most favorable structure.

The corresponding DOS and Ga−Ge, Eu−Ga, and Eu−Ge COHP curves are also displayed in Figure 11 (bottom). These curves are qualitatively similar to those of the Ga-rich composition in the AlB_2-type structure including the sharp maxima observed at ca. 1.7 eV below E_F, which consists primarily of valence p_x and p_y orbitals of the anionic elements. The Eu−Ga and Eu−Ge COHP curves are optimized, respectively, at ca. 1 eV and ca. 2 eV above E_F. However, there are also subtle differences in the DOS curves for the AlB_2-type and YPtAs-type structures: (i) decreased intensity of the maximum valence peak and (ii) diminished deep minimum caused by filling the Eu 5*d* band (see Supplementary materials Figure S1). Ga−Ge COHP curves in each structure are quite different. Ga−Ga COHP curve of the YPtAs-type structure is nearly optimized at E_F for the YPtAs-type structure, but falls in the relatively deep antibonding state at E_F for the AlB_2-type structure. This difference of Ga−Ge COHP curve can solely be attributed to the different layered structure of $^2_\infty[GaGe]$ sheets (planar versus puckered), and explain the structural preference of the equiatomic composition toward YPtAs-type structure.

$Eu(Ga_{0.45}Ge_{0.55})_2$. The Ge-rich composition $Eu(Ga_{0.45(2)}Ge_{0.55(2)})_2$ adopts a 2:1 intergrowth, respectively, of the YPtAs-type structure and the $EuGe_2$-type structure. Given the correlation of the crystal structure to YPtAs-type substructure, DOS curves (Figure 12) are very similar to those of previously discussed equiatomic composition. The sharp maximum peak is observed at ca. 1.7 eV below E_F, but a small minimum observed just below E_F in $Eu(Ga_{0.50(2)}Ge_{0.50(2)})_2$ is now completely disappears. There is more Ge *p* band contribution to total DOS than Eu *d* orbitals or Ga *p* orbitals below E_F because of the given Ge-rich composition, while Eu *d* orbitals contribution becomes greater above E_F. Ga−Ge COHP curve falls in the nonbonding state at E_F, which is quite similar to that of $Eu(Ga_{0.50(2)}Ge_{0.50(2)})_2$. However, unlike the equiatomic composition, there is a puckered

hexagonal layer consisting of entirely Ge atoms, and its COHP curve is also shown in Figure 12. This Ge−Ge COHP curve is optimized at ca. 1.5 eV below E_F, and shows antibonding state at E_F.[34] This Ge-only layer can be compared with Ge layers in $EuGe_2$, where Ge−Ge COHP curve is nearly optimized at E_F with 10 valence electrons. The difference of COHP curve can be understood from different local environments above or below this Ge layer. This Ge layer cannot pucker as much as it need to stabilize the layered structure with respect to the given number of valence electrons because of the spatial restriction caused by puckered 6^3 Ga/Ge layers located above and below. As a result, the shorter Ge−Ge bond distance is observed in this structure: 2.527 Å in $Eu(Ga_{0.45}Ge_{0.55})_2$ and 2.552 Å in $EuGe_2$,[30] and can explain the antibonding state of Ge−Ge COHP at E_F.

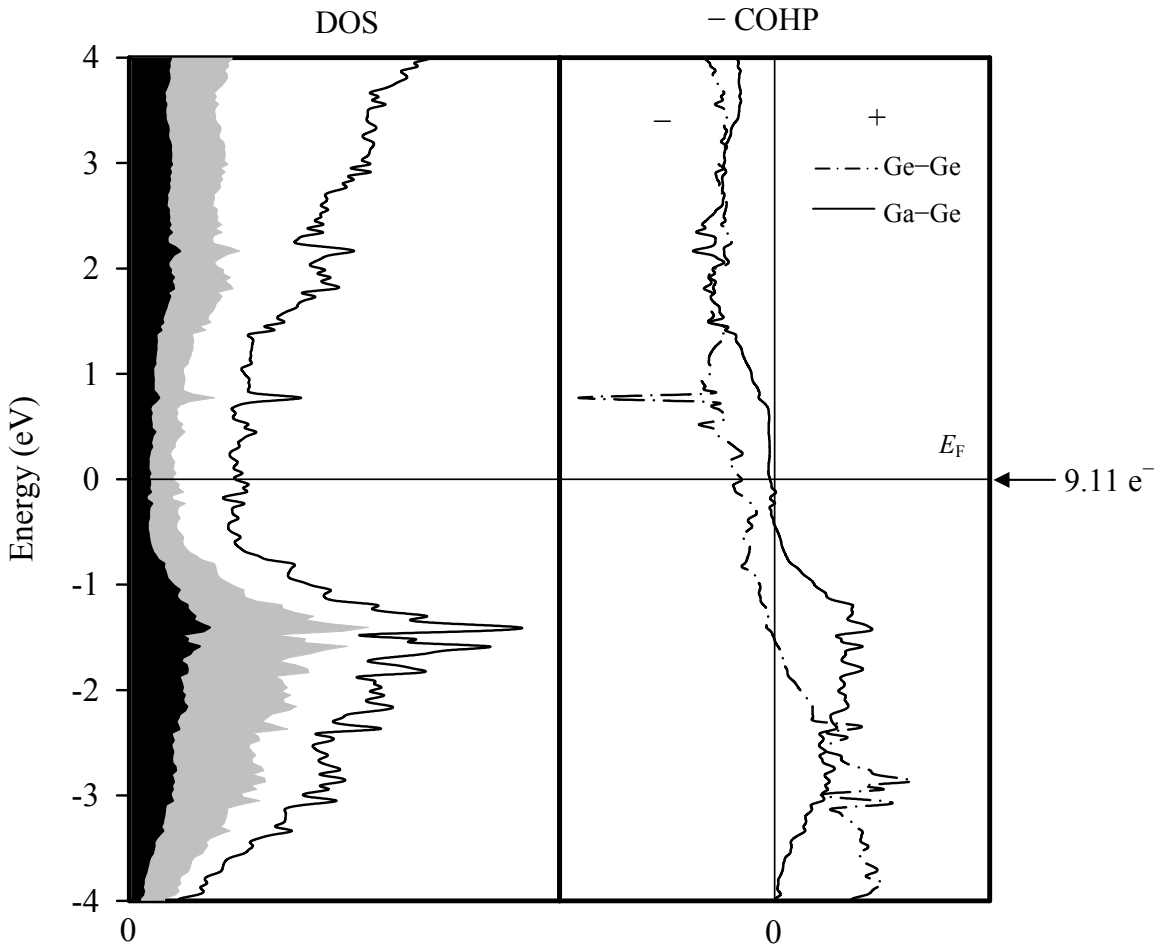

Figure 12. DOS and COHP curves for $Eu(Ga_{0.45}Ge_{0.55})_2$. (Left) Total DOS (solid line), Eu PDOS (white region), Ge PDOS (gray region), and Ga PDOS (black region). (Right) Ga−Ge, Eu−Ga, and Eu−Ge COHP curves. The Fermi level is indicated by the long solid line and is the energetic reference (0 eV).

5.5 Summary

Total sixteen samples of $Eu(Ga_{1-x}Tt_x)_2$ compounds (Tt = Si, Ge, $0 \leq x \leq 1$) were synthesized using high temperature method and characterized using powder and single crystal X-ray diffraction. $Eu(Ga_{1-x}Si_x)_2$ series crystallized in three different structural types depending upon the given composition including two binary compounds structures (KHg_2-type and $ThSi_2$-type) and one ternary compounds structure (AlB_2-type) with wide homogeneity range. On the other hand, $Eu(Ga_{1-x}Ge_x)_2$ series adopts six distinct structural types depending upon the Ge amount. The homogeneity range of the AlB_2-type structure was also observed for ternary Ga-rich compounds, but the range was smaller than that of $Eu(Ga_{1-x}Si_x)_2$. Two ternary Ge-rich compounds showed two distinct complex superstructures, and contained Ge-only hexagonal layer in a unit cell. Electronic structures of each compound were influential to the observed structural trends and local environments of atomic distributions.

Acknowledgement

This work was supported by NSF DMR 02−41092 and 06−05949. The authors are grateful to Dr. Warren Straszheim for the EDXS measurements at Iowa State University, to Dr. Ulrich Burkhardt for XAS measurements, and to Dr. Walter Schnelle for magnetization measurements at Max−Planck−Institute for Chemical Physics of Solids in Dresden, Germany.

References

[1] Westbrook, J. H.; Fleisher, R. L., Ed.; *Intermetallic Compounds: Principle and Practices*; Wiley, New York, **1995**.

[2] Nesper, R., *Prog. Solid State Chem*. **1990**, *20*, 1.

[3] Miller, G. J. In *Chemistry, Structure, and Bonding of Zintl Phases and Ions*; Kauzlarich, S. M., Ed.; VCH Publishers; New York, 1996; pp 1.

[4] Schäfer, H. *Ann. Rev. Mater. Sci.* **1985**, *5*, 1.

[5] Miller, G. J.; Lee, C.−S.; Choe, W. In *Highlights in Inorganic Chemistry*; Meyer, G., Ed.; Wiley−VCH; Heidelberg, **2002,** 21.

[6] Dronskowski, R.; Blochl, P. *J. Phys. Chem*. **1993**, *97*, 8617.

[7] Hughbanks, R; Hoffmann, R. J. Am. Chem. Soc. **1983**, 105, 3528.

[8] Klem, M. T.; Vaughy, J. T.; Harp, J. G.; Corbett, J. D. *Inorg. Chem*. **2001**, *40*, 7020.

[9] Gout, D.; Benbow, E.; Gourdon, O.; Miller, G. J. *J. Solid State Chem*. **2003**, *176,* 538.

[10] Huang, G. Q.; Liu, M.; Chen, L. F.; Xing, D. Y. *Physica C* **2005**, 423, 9.

[11] Imai, M.; Abe, E.; Ye, J.; Nishida, K.; Kimura, T.; Honma, K.; Abe, H,; Kitazawa, H. *Phys. Rev. Lett*. **2001**, *87*, 077003.

[12] Imai, M.; Nishida, K.; Kimura, T.; Abe, H. *Appl. Phys. Lett*. **2002**, *80*, 1019.

[13] Imai, M.; Nishida, K.; Kimura, T.; Kitazawa, H.; Abe, H.; Kito, H.; Yoshii, K. *Physica C* **2002**, *382*, 361.

[14] Lorenz, B.; Lenzi, J.; Cmaidalka, J.; Meng, R. L.; Sun, Y. Y; Xue, Y. Y.; Chu, C. W. *Physica C* **2002**, *383*, 191.

[15] Nagamatsu. J.; Nakagawa, N.; Muranaka, T.; Zenitani, Y.; Akimitsu J. *Nature* **2001**, *410*, 63.

[16] You, T.−S.; Grin, Yu., Miller, G. J. *Inorg. Chem*. **2007**, *46*, 8801.

[17] You, T.−S. ; Miller, G. J. to be published.

[18] Buschow, K. H. J.; Mooij, D. B. *J. Less−Common Met*. **1984**, *97*, L5.

[19] Miedema, A. R. *J. Less−Common Met*. **1976**, *46*, 167.

[20] Sichevych, O.; Cardoso-Gil, R.; Grin, Yu. *Z. Kristallogr. - NCS* **2006,** *221,* 261.

[21] Hunter, B. A.; Howard, C. J. *Rietica*; Australian Nuclear Science and Technology Organization: Menai, Australia, 2000.

[22] XRD single crystal software. Bruker Analytical X-ray System: Madison, WI, **2002**.

[23] *X-SHAPE*, *Program for numeric absorption*, version 1.03; Stoe & Cie: Darmstadt, Germany, 1998

[24] *SHELXTL*, version 5.1; Bruker AXS Inc.: Madison, WI, **1998.**

[25] Akselrud, L.G.; Zavalii, P. Yu.; Grin, Yu.; Pecharski, V. K.; Baumgartner, B., Wölfel, E. *Mat. Sci. Forum* **1993**, *133-136*, 335.

[26] Emsley, J. *The Elements*; Clarendon press: Oxford, **1998.**

[27] Anderson, O. K. *Phys. Rev. B* **1986**, *34*, 2439.

[28] Anderson, O. K.; Jepsen, O. *Phys. Rev. Lett.* **1984***, 53*, 2571.

[29] Andersen, O. K.; Jepsen, O.; Glötzel, D. In *Highlights of condensed matter theory*; F. Bassani, F. Fumi, M.Tosi, Eds.; New York, North−Holland, Lambrecht, W. R. L., **1985.**

[30] Jepsen, O.; Anderson, O. K.; *Z. Phys. B* **1995**, *97*, 35.

[31] Blöchl, P. E.; Jepsen, O.; Anderson, O. K. *Phys. Rev. B* **1994**, *49*, 16223−16233.

[32] Hoffmann, R.; Pöttgen, R. *Z. Kristallogr*. **2001**, *216*, 127−145.

[33] Hladyshevsky, E. I. *Dopl. Akad. Nauk Ukr. RSR* **1964**, *2*, 209−212.

[34] Bobev, S.; Bauer, E. D.; Thompson, J. D.; Sarrao, J. L.; Miller, G. J.; Eck, B.; Dronskow-ski, R. *J. Solid State Chem*. **2004**, *177,* 3545−3552.

Supplementary Material

Table S1. Wigner-Seitz (WS) atomic sphere radii of elements used in LMTO calculations.

compound	Eu	Ga	Si	Ge
$EuGa_2$	2.09	1.52	.....	.....
EuGaSi	2.28	1.30	1.33	.....
EuGaGe (AlB_2-type)	2.23	1.42	.....	1.47
EuGaGe (YPtAs-type)	1) 2.26 2) 2.19	1.42	.....	1.47
$Eu(Ga_{0.45}Ge_{0.55})_2$	1) 2.24 2) 2.15 3) 2.20 4) 2.16 5) 2.23	1) 1.46 2) 1.46 3) 1.47 4) 1.42	.....	1) 1.51 2) 1.46 3) 1.51 4) 1.50 5) 1.48

Table S2. Lattice Parameters and Unit Cell Volumes as Determined by Powder and Single Crystal X-ray Diffraction for the $Eu(Ga_{1-x}Si_x)_2$ ($0 \leq x \leq 1$) series.

x (loaded)	x (EDS)	structural type	sample	a (Å)	b (Å)	c (Å)	c/a	V (Å^3)
0	0.00(2)	KHg_2	powder	4.6449(9)	7.628(2)	7.638(2)	------	270.61(9)
0.18	0.16(2)	KHg_2	powder	4.6524(5)	7.6461(9)	7.6464(8)	------	272.00(5)
		AlB_2	powder	4.2640(2)		4.6000(2)	1.0788	72.45(5)
0.26	0.29(2)	AlB_2	powder	4.2324(3)		4.5885(4)	1.0841	71.17(1)

0.30	0.33(2)	AlB_2	powder	4.2204(2)	4.5863(2)	1.0867	70.75(1)
0.50	0.50(2)	AlB_2	powder	4.1699(5)	4.5634(6)	1.0946	68.72(2)
0.67	0.68(2)	AlB_2	powder	4.1132(3)	4.5412(4)	1.1041	66.53(1)
0.84	0.82(2)	AlB_2	powder	4.0821(1)	4.5538(3)	1.1156	65.72(3)
		$ThSi_2$	powder	4.2989(4)	13.864(2)	------	256.22(1)
1.00	1.00(2)	$ThSi_2$	powder	4.3065(4)	13.683(1)	------	253.76(4)

Table S3 Atomic coordinates and equivalent displacement parameters for $Eu(Ga_{1-x}Ge_x)_2$ (x = 0.25(2), 0.35(2), 0.45(5) 0.50(2), 0.55(2), 0.60(2))

Atom	Wyckoff position	x	y	z	U_{eq}[a]
		$Eu(Ga_{0.75(2)}Ge_{0.25(2)})_2$			
Eu	1*a*	0	0	0	0.014(1)
Ga/Ge	2*d*	1/3	2/3	1/2	0.020(1)
		$Eu(Ga_{0.65(2)}Ge_{0.35(2)})_2$			
Eu	1*a*	0	0	0	0.011(1)
Ga/Ge	2*d*	1/3	2/3	1/2	0.021(1)
		$Eu(Ga_{0.65(2)}Ge_{0.35(2)})_2$			
Eu	1*a*	0	0	0	0.0170(3)
0.301(5) Ga/Ge	2*d*	1/3	2/3	1/2	0.015(1)
0.356(6) Ga/Ge	4*h*	1/3	2/3	0.5871(8)	0.011(1)
		$Eu(Ga_{0.50(2)}Ge_{0.50(2)})_2$			
Eu(1)	2*a*	0	0	0	0.013(1)

Eu(2)	2*b*	0	0	1/4	0.010(1)
Ga	4*f*	2/3	1/3	0.1620(1)	0.014(1)
Ge	4*f*	1/3	2/3	0.1168(1)	0.011(1)
		$Eu(Ga_{0.45(2)}Ge_{0.55(2)})_2$			
Eu(1)	1*a*	0	0	0	0.004(1)
Eu(2)	2*c*	0	0	0.1114(1)	0.005(1)
Eu(3)	2*c*	0	0	0.2217(1)	0.009(1)
Eu(4)	2*c*	0	0	0.3335(1)	0.017(1)
Eu(5)	2*c*	0	0	0.4442(1)	0.012(1)
Ga(1)	2*d*	1/3	2/3	0.0651(1)	0.010(1)
Ga(2)	2*d*	1/3	2/3	0.1560(1)	0.010(1)
Ge(1)	2*d*	1/3	2/3	0.2706(1)	0.010(1)
Ge(2)	2*d*	1/3	2/3	0.3900(2)	0.024(1)
Ge(3)	2*d*	2/3	1/3	0.0505(1)	0.007(1)
Ge(4)	2*d*	2/3	1/3	0.1706(1)	0.004(1)
Ga(3)	2*d*	2/3	1/3	0.2871(1)	0.007(1)
Ga(4)	2*d*	2/3	1/3	0.3867(4)	0.092(3)
Ge(5)	2*d*	2/3	1/3	0.4920(1)	0.022(1)
		$Eu(Ga_{0.40(2)}Ge_{0.60(2)})_2$			
Eu(1)	1*a*	0	0	0	0.009(1)
Eu(2)	2*g*	0	0	0.1994(1)	0.009(1)
Eu(3)	2*g*	0	0	0.4009(1)	0.014(1)
Ge(1)	1*d*	1/3	2/3	0.5000(1)	0.009(1)
Ga(1)	2*h*	1/3	2/3	0.0843(2)	0.019(1)
Ge(2)	2*h*	1/3	2/3	0.2870(1)	0.010(1)
Ge(3)	2*i*	2/3	1/3	0.1095(2)	0.018(1)
Ga(2)	2*i*	2/3	1/3	0.3197(1)	0.012(1)
Ga(3)	2*i*	2/3	1/3	0.4798(2)	0.016(2)

[a] U_{eq} is defined as one third of the trace of the orthogonalized U_{ij} tensor.

Figure S1. Band Structure of $Eu(Ga_{0.5}Ge_{0.5})_2$ with fatband contributions of Eu 5*d* orbitals.

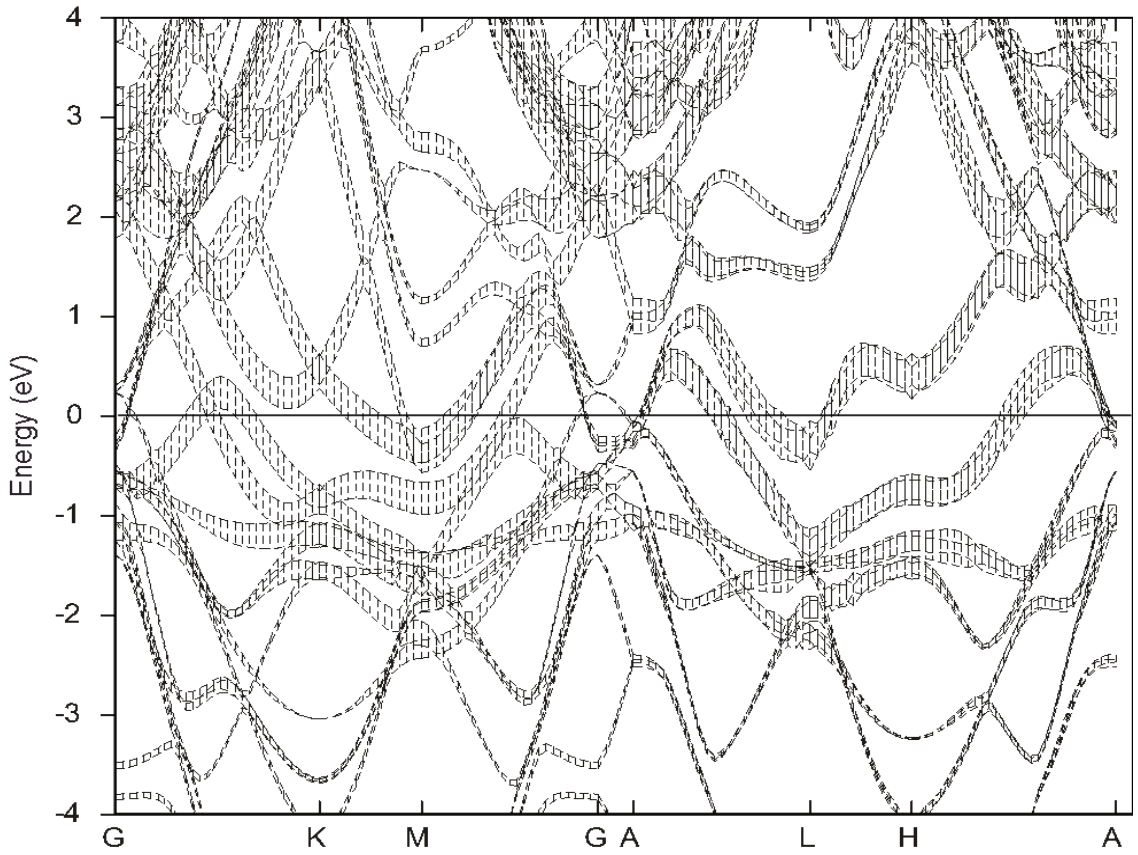

Chapter 6

On the "Coloring Problem" in YMgZn and Related Phases

Modified from a paper published in *Inorganica Chimica Acta*

Tae-Soo You,[2,4] Mi-Kyung Han,[3] and Gordon J. Miller[2,5]

6.1 Abstract

During exploration in the Y-Mg-Zn system for quasicrystal approximants, three new phases, $YMg_{1-x}Zn_{1+x}$ ($0 \le x \le 0.17$) adopting the hexagonal ZrNiAl structure type, have been discovered. In these structures, the elements are completely ordered to minimize both the site energies and the bond energies as calculated by tight-binding calculations. Evaluation of the electron density in YMgZn suggests that Mg–Zn and Y–Zn bonding coupled with maximizing the Zn···Zn separations is the main factor influencing the atomic arrangements. Analysis of the electronic density of states of YMgZn indicates an optimized bonding situation for 8 valence electrons per formula unit, e.g., as in YMgGa. Subsequently, YMgAl, YMgGa, and YMgIn were successfully prepared and structurally characterized. Their structures show relationships to both densely packed structures common for intermetallics as well as three-dimensional networks common for valence compounds.

6.2 Introduction

One significant chemical issue concerning intermetallic compounds is an understanding of how the different elements distribute themselves in a structure. This aspect

---

[1] Reproduced with permission from *Inorganica Chimica Acta*, 2008, 361, 3053-3062.

[2] Graduate student and Professor, respectively, Department of Chemistry, Iowa State University

[3] Postdoctoral Associate, Department of Chemistry, Northwest University

[4] Primary researcher and author

[5] Author for correspondence

of structural chemistry is called the *coloring problem*.[1] For molecules, Gimarc introduced the phrase, "topological charge stabilization" to address the site preference problem for multi-component molecules.[2] For example, in the linear molecule N_2O, the O atom occupies a terminal position rather than the central position due to electronegativities.[3] Also, in the isostructural molecules S_4N_4 and As_4S_4, the S atoms occupy three-bonded sites in S_4N_4 but the two-bonded sites in As_4S_4, an observation which is also attributed to the relative electronegativities of As, S, and N.[3] For extended solids, Franzen developed the concept "differential fractional site occupancy," which addresses the problem of incompletely disordered arrangements of transition metals in ternary metal-rich sulfides and phosphides.[4] One example of this phenomenon occurs in $Ta_{1+x}Nb_{1-x}S$, a structure consisting of $[M_4S_2]$ slabs constructed by four planes of metal (Ta, Nb) atoms sandwiched by two planes of S atoms.[5] In this structure, Ta atoms segregate toward the two interior planes (farther from the sulfur atoms) while the Nb atoms segregate toward the two exterior planes (closer to the sulfur atoms). Franzen and coworkers attributed this atomic distribution to optimizing metal-metal bonding in this structure. Therefore, these two distinctive concepts, "topological charge stabilization" and "differential fractional site occupancy," address the coloring problem from two different viewpoints, i.e., respectively, atomic electronegativities and interatomic bonding.

These two concepts can be combined into a single model arising from a reformulation of the total valence electronic energy as determined from tight-binding (linear combination of atomic orbitals) approach by decomposing this total energy into a *site-energy* term and a *bond-energy* term.[1] The site energy is evaluated as the sum of the products of the atomic orbital occupation numbers with the corresponding atomic orbital energies. The bond energy is the overlap population[3] weighted by the corresponding resonance integrals[3] between pairs of atoms showing significant orbital overlaps. The observed atomic distribution in a solid will minimize the total energy, and this distribution typically emphasizes one term or the other. For example, in the elements themselves, the optimum chemical structure seeks to optimize (minimize) the bond-energy term. In compounds with significant differences in electronegativities between the component elements, i.e., ionic salts, the site-energy term dominates the atomic distribution. But, in intermetallic compounds, which involve elements

with small electronegativity differences and variable composition, the final solution can be a compromise between the best site-energy solution and the best bond-energy solution to achieve the overall lowest total electronic energy.[6]

In this communication, we explore the *coloring problem* for a new compound YMgZn, which involves three hexagonally close packed metals with three very different atomic characteristics and examine how they are distributed in its crystal structure. We compare our experimental results with results of theoretical calculations, and successfully prepare the isostructural compounds, YMgAl, YMgGa,[7] and YMgIn.[8]

6.3 Experimental

6.3.1 Synthesis

The $YMg_{1-x}Zn_{1+x}$ series and YMgAl, YMgGa, and YMgIn were synthesized from the pure elements, Y (Ames Laboratory, rod, 99.99%), Mg (Alfa, ribbon, 99.95%), Zn (Alfa, piece, 99.99%), Al (Alfa, piece, 99.98%), Ga (Ames Laboratory, ingot, 99.99%), and In (Aldrich, shot, 99.99%). Several different Mg:Zn molar ratios, both Mg-rich and Zn-rich, as well as the three stoichiometric triel (triel = Al, Ga, In, symbolized generally as *Tr*) compounds were prepared using either a high frequency (HF) induction furnace at 1100°C with a holding time of 15 min and followed by annealing at 450°C for one hour or a conventional tube furnace at 1100°C for three days followed by annealing at 450°C for one week. Reactant mixtures were loaded into tantalum ampoules, which were then sealed at both ends by arc-melting in an argon-filled glove box with the concentration of O_2 lower than 10 ppm. The tantalum ampoules were placed in evacuated sealed silica jackets to prevent oxidation. Analysis by energy-dispersive X-ray spectroscopy (EDS) was conducted on a Hitachi S-2460N variable-pressure scanning electron microscope (SEM) with an Oxford Instruments Link Isis Model 200 X-ray analyzer. The corresponding pure elements were used as standards for intensity references.

6.3.2 Crystal Structure Determination

$YMg_{1-x}Zn_{1+x}$, YMgAl, YMgGa, and YMgIn were characterized by both powder and single crystal X-ray diffraction. Phase purity and lattice parameters were determined using a

Huber G670 Guinier image-plate powder diffraction camera with monochromatic Cu $K\alpha_1$ radiation (λ = 1.54059 Å). The step size was set at 0.005°, and the exposure time was 2 hours. Data acquisition was controlled via the *in situ* program. The lattice parameters obtained from Rietveld refinements of the X-ray patterns using program *Rietica*[9] were in very good agreement to the results of single crystal X-ray diffraction.

For single crystal X-ray diffraction experiments, several silvery crystals were selected from crushed samples. The crystals were checked for crystal quality by a rapid scan on a Bruker SMART Apex CCD diffractometer with Mo $K\alpha$ radiation (λ = 0.71073 Å), and then the best crystals were selected for further data collection at 293(2) K. Single crystal X-ray diffraction data were collected from three sets of 606 frames on a full sphere with 0.3° scans in ω and with an exposure time of 10 sec per frame. The angular range of 2θ was ca. 6-56°.

Intensities were extracted and then corrected for Lorentz and polarization effects using the *SAINT* program.[10] The program *SADABS* was used for empirical absorption correction.[10] The entire sets of reflections of the six compounds were matched with the hexagonal crystal system. After further analysis, the space group $P\bar{6}2m$ was chosen for all structures with three formula units per unit cell. All structures were solved by direct methods and refined on F^2 by full-matrix least-squares methods using the *SHELXTL* software package.[11] During the refinement process of YMgAl, the Mg and Al atoms could not be distinguished because their X-ray scattering factors differ by at most 7.7%, but atomic positions were refined based on results for the isostructural YMgGa and YMgIn. The chemical compositions of all compounds obtained from EDS analysis very well matched the refined compositions from single crystal X-ray diffraction experiments.

6.3.3 Computational Details

Tight-binding, linear muffin-tin orbital (TB-LMTO)[12-13] calculations were carried out for YMgZn in the atomic sphere approximation (ASA) using the Stuttgart program.[14] Exchange and correlation were treated by the local density approximation (LDA). All relativistic effects except spin-orbit coupling were taken into account by using a scalar relativistic approximation.[15]

In the ASA method, space is filled with overlapping Wigner-Seitz (WS) atomic spheres. The symmetry of the potential is considered spherical inside each WS sphere, and a combined correction is used to take into account the overlapping part. The radii of WS spheres were obtained by requiring that the overlapping potential be the best possible approximation to the full potential, and were determined by an automatic procedure.[16] This overlap should not be too large because the error in kinetic energy introduced by the combined correction is proportional to the fourth power of the relative sphere overlap. No empty spheres (ES) were needed. The WS radii are as follows: Y = 1.98 Å, Mg = 1.76 Å and Zn = 1.51 Å. The basis sets included 5*s*, 5*p* and 4*d* orbitals for Y; 3*s* and 3*p* orbitals for Mg; 4*s*, 4*p* and 3*d* orbitals for Zn. The Y 4*f* orbitals were treated by the Löwdin downfolding technique.[12,13] Crystal orbital Hamilton populations (COHP) curves[17] and the integrated COHP values (ICOHPs) were calculated to determine the relative influences of various interatomic orbital interactions. The *k*-space integrations were performed by the tetrahedron method.[18] The self-consistent charge density was obtained using 217 irreducible *k*-points in the Brillouin zone for the hexagonal cell.

6.4 Results and Discussion

6.4.1 $YMg_{1-x}Zn_{1+x}$

Structural Results

According to the powder X-ray diffraction patterns shown in Figure 1 for loaded compositions $YMg_{0.6}Zn_{1.4}$, $YMg_{0.8}Zn_{1.2}$, $YMg_{1.0}Zn_{1.0}$, $YMg_{1.2}Zn_{0.8}$, and $YMg_{1.4}Zn_{0.6}$, the major phase in all cases is the hexagonal ZrNiAl-type structure, space group $P\bar{6}2m$, which displays sharp intense peaks that can be indexed by the Rietveld method. All patterns also show some less intense peaks from minor phases, such as YMg_2 or YZn. Furthermore, the major phase in the Zn-rich products shows variation in the scattering angles to indicate different lattice constants and variable Zn content. On the other hand, the major phase in all Mg-rich products gives identical diffraction patterns with YMgZn. Thus, according to our synthetic approach, this hexagonal phase displays a homogeneity width for Zn-rich compositions, $YMg_{1-x}Zn_{1+x}$, but not for Mg-rich compositions.

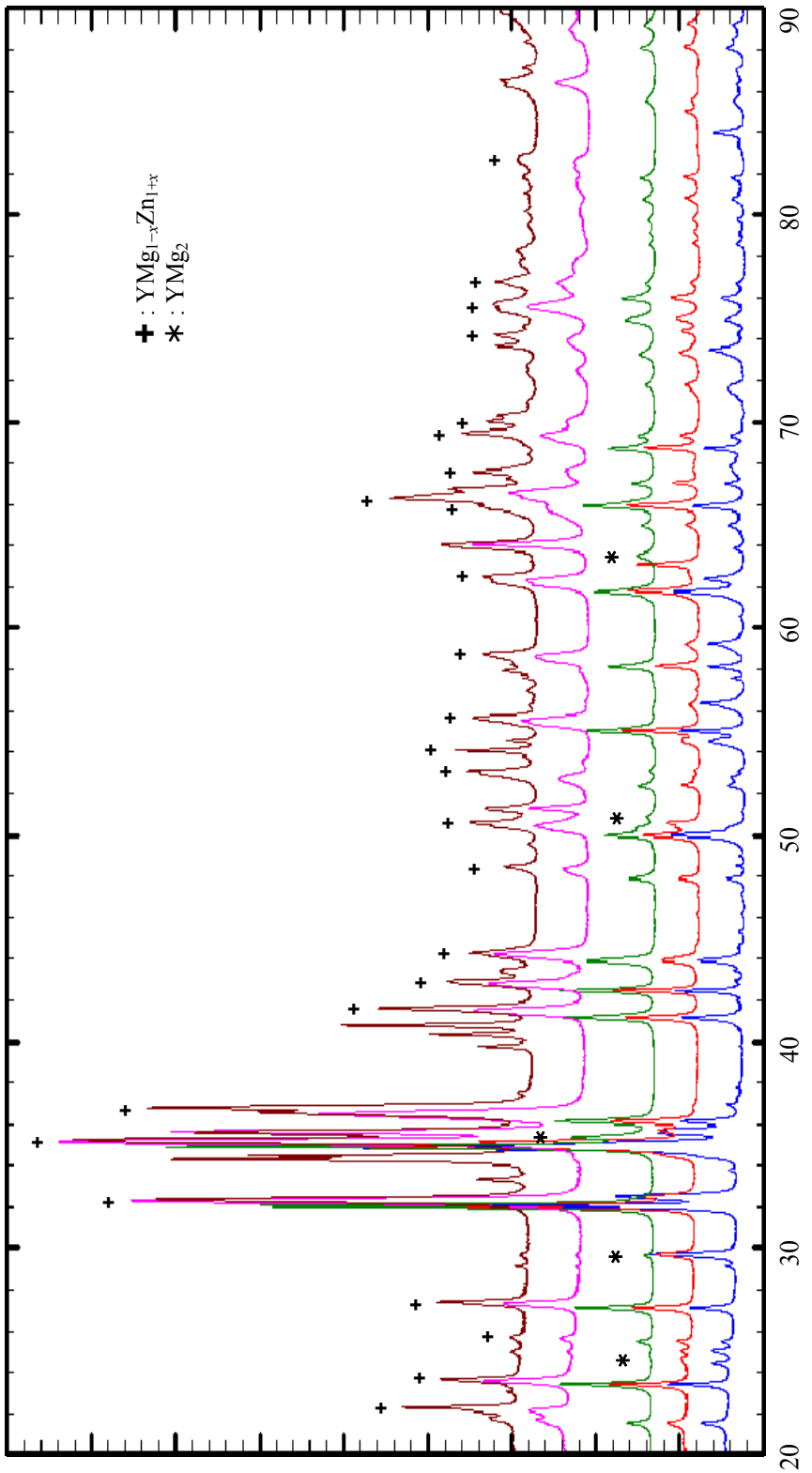

Figure 5. Powder X-ray diffraction patterns of $YMg_{1-x}Zn_{1+x}$ for loaded compositions $x = -0.4$, -0.2, 0.0, +0.2, and +0.4.

To investigate the upper limit of Zn composition, crystals suitable for single crystal X-ray diffraction studies were extracted from the Zn-rich products. In general, products synthesized in a conventional tube furnace were suitable for such experiments, whereas those synthesized in a HF induction furnace showed poor crystallinity. Important crystallographic data, atomic positions, site occupancy factors and isotropic temperature factors, as well as selected interatomic distances for $YMg_{1-x}Zn_{1+x}$ are summarized in Tables 1-3.

Table 1. Crystallographic Data for $YMg_{1-x}Zn_{1+x}$.

	$YMg_{0.83(1)}Zn_{1.17(1)}$	$YMg_{0.94(1)}Zn_{1.06(1)}$	YMgZn
Formula weight	185.59	181.07	178.60
Lattice parameters			
a (Å)	7.5267(8)	7.582(1)	7.579(2)
c (Å)	4.1083(5)	4.1138(2)	4.1159(9)
Volume (Å^3)	201.53(4)	204.79(2)	204.75(2)
D_{calc} (g cm^{-3})	4.439	4.348	4.341
Index ranges	$-9 \le h \le 9$, $-9 \le k \le 9$, $-5 \le l \le 5$	$-9 \le h \le 9$, $-9 \le k \le 9$, $-5 \le l \le 5$	$-9 \le h \le 10$, $-9 \le k \le 10$, $-5 \le l \le 5$
Reflections collected	1712	1748	1800
Independent reflections	206 [R_{int} = 0.0618]	207 [R_{int} = 0.0548]	215 [R_{int} = 0.0737]
Data/refined parameters	206/14	207/14	215/13
Goodness-of-fit on F^2	0.963	0.803	0.969
Final R indices [$I > 2\sigma(I)$]	R_1 = 0.0222, wR_2 = 0.0351	R_1 = 0.017, wR_2 = 0.0302	R_1 = 0.0272, wR_2 = 0.0393
R indices (all data)	R_1 = 0.0314, wR_2 = 0.0387	R_1 = 0.0184, wR_2 = 0.0305	R_1 = 0.0334, wR_2 = 0.0401
Largest difference in peak and hole (e$^-$/Å^3)	1.399 / –1.060	0.338/ –0.505	0.655 / –0.776

Table 2. Atomic Coordinates, Occupancy, and Equivalent Displacement Parameters for $YMg_{1-x}Zn_{1+x}$.

atom	Wyckoff Position	occupancy	*x*	*y*	*z*	U_{eq} [a]
			$YMg_{0.83(1)}Zn_{1.17(1)}$			
Y	3*f*	1	0.5859(2)	0	0	0.015(1)
Mg/Zn	3*g*	0.83(1)/0.17(1)	0.2489(3)	0	1/2	0.014(1)
Zn1	2*d*	1	1/3	2/3	1/2	0.014(1)
Zn2	1*a*	1	0	0	0	0.020(1)
			$YMg_{0.94(1)}Zn_{1.06(1)}$			
Y	3*f*	1	0.5865(1)	0	0	0.013(1)
Mg/Zn1	3*g*	0.94(1)/0.06(1)	0.2479(3)	0	1/2	0.014(1)
Zn1	2*d*	1	1/3	2/3	1/2	0.013(1)
Zn2	1*a*	1	0	0	0	0.016(1)
			YMgZn			
Y	3*f*	1	0.5866(2)	0	0	0.014(1)
Mg	3*g*	1	0.2477(4)	0	1/2	0.009(1)
Zn1	2*d*	1	1/3	2/3	1/2	0.015(1)
Zn2	1*a*	1	0	0	0	0.016(1)

Table 3. Selected Interatomic Distance (Å) for $YMg_{1-x}Zn_{1+x}$.

	$YMg_{0.83(1)}Zn_{1.17(1)}$	$YMg_{0.94(1)}Zn_{1.06(1)}$	YMgZn
Y−Mg [i]	3.259(1)	3.289(2)	3.293(3)
Y−Mg [ii]	3.400(1)	3.4199(7)	3.421(1)
Y−T1	3.0540(7)	3.0740(4)	3.0759(7)
Y−T2	3.109(1)	3.1324(9)	3.134(1)
Mg−T1	2.8734(2)	2.903(1)	2.906(2)
Mg−T2	2.776(2)	2.787(1)	2.787(2)
Mg−Mg	3.237(4)	3.253(3)	3.251(5)

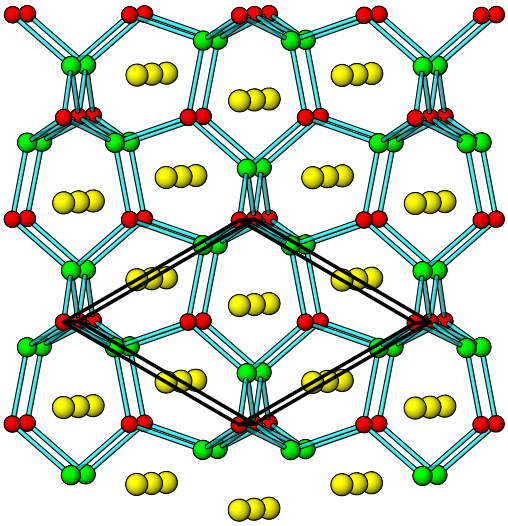

001): Mg-Zn Contacts

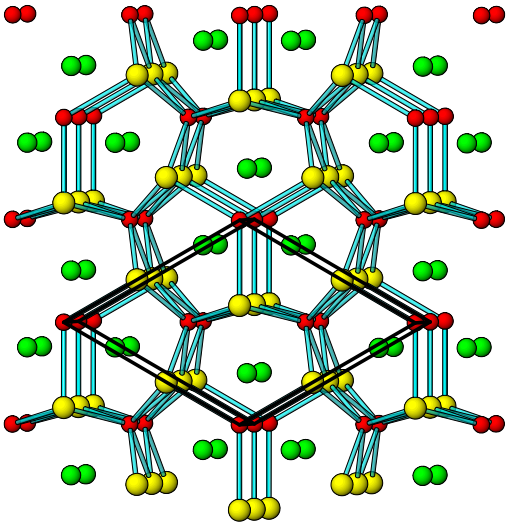

(001): Y-Zn Contacts

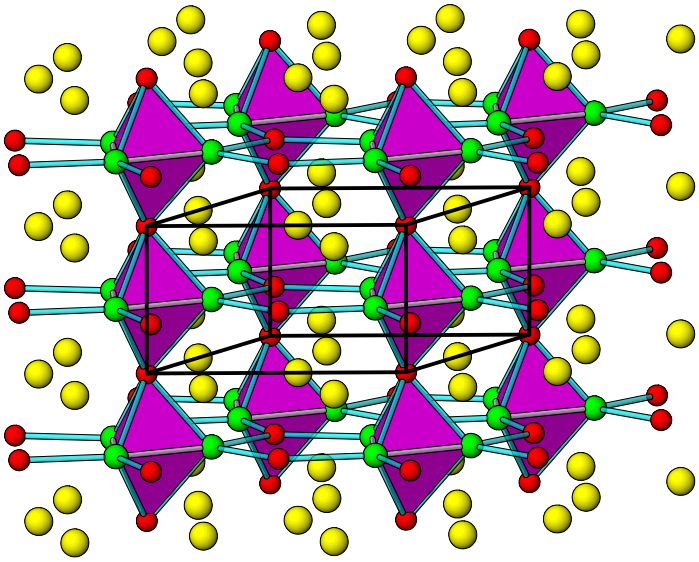

(100) Clinographic Projection

Figure 2. (Top) (001) Projections of YMgZn emphasizing (left) Mg-Zn and (right) Y-Zn contacts; (Bottom) (100) Clinographic projection emphasizing the $[Mg_3Zn_2]$ trigonal bipyramids. Red spheres, Zn; green spheres, Mg; yellow spheres, Y.

Refinements of several single crystals indicated a maximum Zn content of 1.17(3), i.e., $YMg_{0.83(3)}Zn_{1.17(3)}$. As the Zn content increases, the lattice parameters *a* and *c* decrease, which is consistent with the sizes of Mg and Zn based on their 12-coordinate metallic radii (r(Zn) = 1.34 Å and r(Mg) = 1.60 Å).[19]

Figure 2 illustrates the structure of $YMg_{1-x}Zn_{1+x}$ using three different perspectives. Two projections along the *c*-axis highlight, respectively, Mg–Zn and Y–Zn contacts. Clearly, we see Mg atoms tetrahedrally coordinated by Zn atoms with Mg–Zn distances of ca. 2.77-2.90 Å; and Y atoms sitting within square pyramids of Zn atoms with Y–Zn distances of ca. 3.05-3.10 Å. Closer examination of the interatomic distances reveals the axial Y–Zn distance to be slightly longer (ca. 0.05 Å) than the four equatorial Y–Zn distances. Zn1 and Zn2 sites both have local D_{3h} point symmetry and are coordinated by tricapped trigonal prisms: Zn1 is surrounded by a trigonal prism of Y atoms with three Mg atoms along the waist; Zn2 shows the inverse, a trigonal prism of Mg atoms with three Y atoms along the waist. The clinographic projection orthogonal to the *c*-axis reveals columns of trans-vertex sharing [Mg_3Zn_2] trigonal bipyramids linked by Zn1 atoms. The Mg–Mg distances in the equatorial planes of the trigonal bipyramids are ca. 3.2 Å, distances which are similar to Mg–Mg distances in hcp Mg.

Electronic Structure and Bonding

An understanding of the chemical bonding in intermetallics, like YMgZn et al., relies on accurate electronic structure calculations of the periodic solid-state structure. Figure 3 illustrates the total density of states (DOS) curve, calculated by the TB-LMTO-ASA method, with the components from the individual atoms, Y, Mg, and Zn, indicated. The Zn 3*d* states occur in a very narrow band of essentially localized, soft-core orbitals at ca. 8 eV below the Fermi level (E_F) for YMgZn. The occupied bands in the DOS curve show three distinctive regions: (i) three bands between 4 and 7 eV below E_F are mostly Zn 4*s* states, with some contributions from Mg and Y valence orbitals; (ii) ca. two bands between 2 and 4 eV below E_F show nearly equal contributions from Zn, Mg and Y orbitals – band structure analysis reveals these bands to originate largely from $4p_x$ and $4p_y$ orbitals on the Zn1 sites that form

σ-bonding orbitals with Mg 3*s* and 3*p* orbitals; and (iii) ca. seven bands between 2 eV below and 0.5 eV above E_F constitute another strong mixture of Zn, Mg, and Y valence orbitals. The unoccupied bands lying 0.5 eV above E_F for YMgZn have their greatest contribution from Y 5*s* and 4*d* orbitals. E_F for YMgZn falls near a peak in the DOS curve, a feature that typically identifies an electronic instability toward some type of geometrical or electronic distortion.[20] However, we did not observe any structural distortions at room temperature and further, low-temperature diffraction studies are warranted. At 0.5 eV above E_F for YMgZn, a deep pseudogap is found in the DOS curve, which corresponds to filling twelve bands. This occupation level is exactly satisfied by YMgGa. Analysis of the pairwise orbital interactions in the DOS curve by Crystal Orbital Hamilton Population (COHP) curves,[17] also illustrated in Figure 3, clearly indicate that Mg–Ga and Y–Ga interactions would be optimized: Mg–Ga and Y–Ga bonding orbitals are completely filled while their corresponding antibonding orbitals remain completely empty for this hexagonal structure.

In YMgZn, with one less electron per formula unit (three fewer valence electrons in the unit cell), these interactions are not optimized. Furthermore, for both YMgZn and YMgGa, Y–Mg and Mg–Mg interactions give lower COHP values and are not optimized for either case. Thus, this bonding analysis strongly suggests stability of the hexagonal ZrNiAl-structure type for YMgGa and isoelectronic analogues. Therefore, we proceeded to prepare YMgAl, YMgGa,[7] and YMgIn.[8] Although YMgGa and YMgIn have been reported,[7-8] we decided to repeat their characterization to obtain structural information from the same instrument as well as to further investigate the distribution of elements.

6.4.2 YMg*Tr* (*Tr* = Al, Ga, In)

The three triel examples, YMgAl, YMgGa, and YMgIn, were all successfully prepared and produced specimens suitable for single crystal X-ray diffraction experiments. Tables 4-6 summarize the important crystallographic data, atomic positions and isotropic temperature factors, and selected interatomic distances in these hexagonal structures. Although Mg and Al could not be unequivocally differentiated during refinements, Al sites were assigned based on the results for YMgGa and YMgIn. In these trielides, Al, Ga, or In

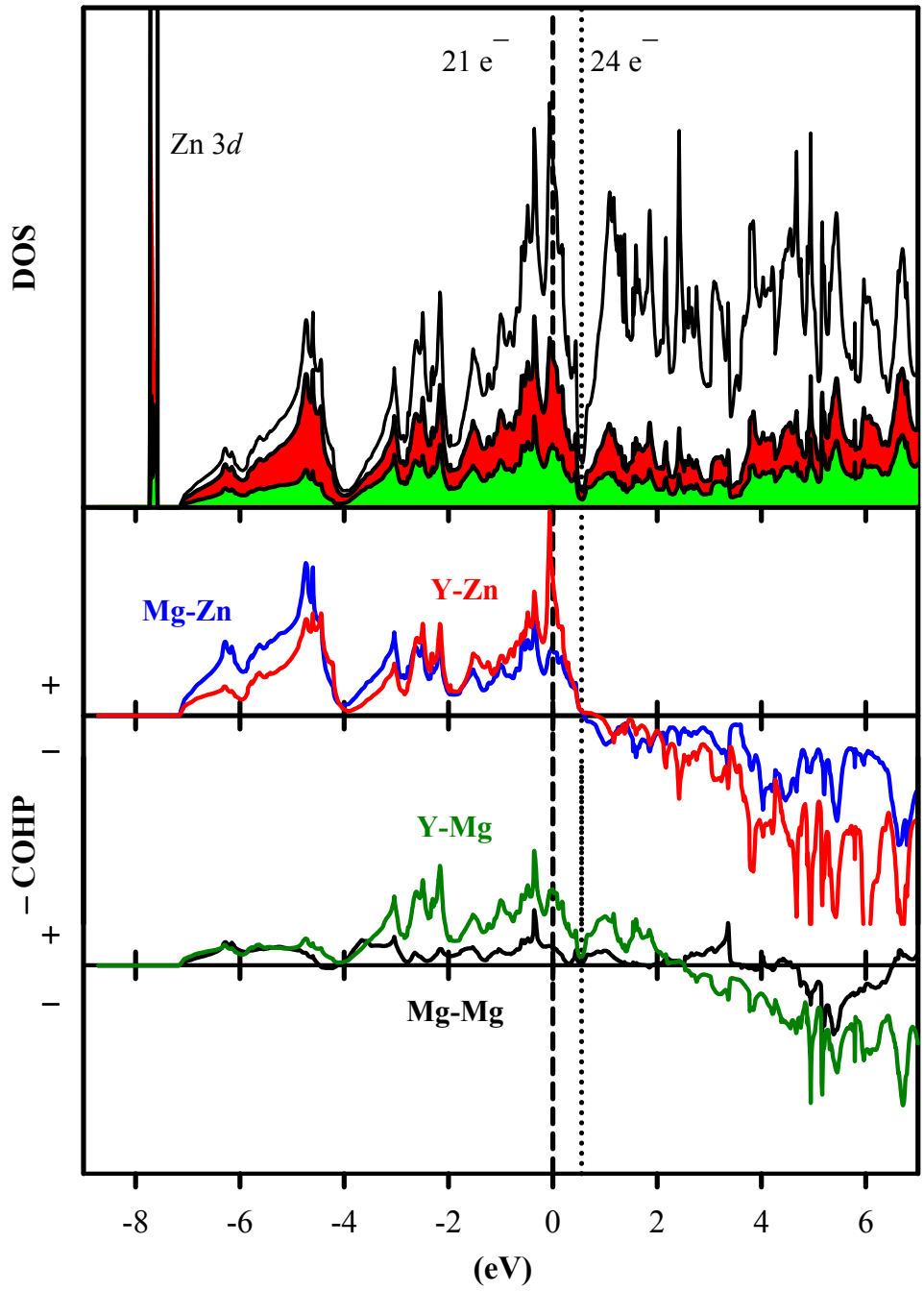

Figure 3. DOS and COHP curves for YMgZn. In DOS curve, Mg (green) and Zn (red) and Y (yellow) orbital contributions are indicated. The Fermi level for YMgZn (21 e^-) is marked by the dashed line (and is the reference energy, 0 eV); the Fermi level calculated for YMgGa (24 e^-)is marked by the dotted line. In the COHP curves, + values are bonding interactions; – values are antibonding interactions.

atoms occupy the Zn sites in YMgZn. The unit cell volume for YMgGa is smaller than that for YMgZn, which is consistent with the COHP analysis above, but counters a size argument given that the atomic radius of Ga atoms (1.40 Å) is larger than that of Zn atoms (1.34 Å).[19]

Table 4. Crystallographic Data for YMg*Tr* (*Tr* = Al, Ga, In).

	YMgAl	YMgGa	YMgIn
Formula weight	140.19	182.93	228.04
Lattice parameters			
a (Å)	7.345(1)	7.2732(1)	7.5145(1)
c (Å)	4.5913(8)	4.4359(1)	4.6593(1)
Volume (Å^3)	214.55(7)	203.32(1)	227.85(1)
D_{calc} (g cm^{-3})	3.275	4.494	4.948
Reflections collected	1768	1783	1706
Independent reflections	217 [R_{int} = 0.0289]	211 [R_{int} = 0.0288]	230 [R_{int} = 0.0600]
Data/refined parameters	217/14	211/15	230/14
Goodness-of-fit on F^2	0.869	1.139	1.040
Final *R* indices [$I > 2\sigma(I)$]	R_1 = 0.0127, wR_2 = 0.0263	R_1 = 0.0124, wR_2 = 0.0251	R_1 = 0.0277, wR_2 = 0.0561
R indices (all data)	R_1 = 0.0138, wR_2 = 0.0265	R_1 = 0.0126, wR_2 = 0.0251	R_1 = 0.0288, wR_2 = 0.0565
Largest difference in peak and hole (e$^-$/Å^3)	0.491 / –0.473	0.317/ –0.422	1.321/ –0.827

Table 5. Atomic Coordinates, Occupancy, and Equivalent Displacement Parameters for YMg*Tr* (*Tr* = Al, Ga, In).

atom	Wyckoff Position	occupancy	*x*	*y*	*z*	U_{eq} [a]
			YMgAl			
Y	3*f*	1	0.5664(1)	0	0	0.010(1)
Mg	3*g*	1	0.2417(2)	0	1/2	0.012(1)
Al1	2*d*	1	1/3	2/3	1/2	0.010(1)
Al2	1*a*	1	0	0	0	0.013(1)
			YMgGa			
Y	3*f*	1	0.5732(1)	0	0	0.008(1)
Mg	3*g*	1	0.2440(1)	0	1/2	0.010(1)
Ga1	2*d*	1	1/3	2/3	1/2	0.008(1)
Ga2	1*a*	1	0	0	0	0.010(1)
			YMgIn			
Y	3*f*	1	0.5662(2)	0	0	0.011(1)
Mg	3*g*	1	0.2425(5)	0	1/2	0.009(1)
In1	2*d*	1	1/3	2/3	1/2	0.011(1)
In2	1*a*	1	0	0	0	0.014(1)

[a] U_{eq} is defined as one-third of the trace of the orthogonalized U_{ij} tensor.

Table 6. Selected Interatomic Distance (Å) for YMg*Tr* (*Tr* = Al, Ga, In).

	YMgAl	YMgGa	YMgIn
Y−Mg [i]	3.2981)	3.259(2)	3.377(3)
Y−Mg [ii]	3.5835(4)	3.4900(6)	3.675(3)
Y−T1	3.1497(2)	3.0964(3)	3.231(3)
Y−T2	3.1916(5)	3.106(1)	3.267(3)
Mg−T1	2.8867(9)	2.838(2)	2.966(4)
Mg−T2	2.851(1)	2.806(2)	2.913(3)
Mg−Mg	3.081(2)	3.077(5)	3.163(7)

Moreover, YMgGa shows the minimum unit cell volume along the triel series YMgAl-YMgGa-YMgIn, which is consistent with size arguments (r(Al) = 1.43 Å; r(Ga) = 1.40 Å; r(In) = 1.58 Å),[19] but could also point toward the importance of orbital interactions in these intermetallic compounds. In particular, Ga atoms differ from Al atoms by providing a filled 3*d* set of "soft core" orbitals, which would be located below the occupied valence band and could interact favorably with the empty 4*d* orbitals of Y; these interactions are not available in YMgAl. This conjecture is under further theoretical scrutiny to examine the influence of such filled *d*-empty *d* orbital interactions in related intermetallics and will be the subject of a future paper.

6.5 The Coloring Problem in YMgZn

Tight-binding analysis of the coloring problem involves calculating the site energy and bond energy terms for different colorings.[1] For YMgZn, we examined the alternative where the Zn1 and Zn2 sites are switched against the Mg sites, i.e., the hypothetical "YZnMg." The total electronic energy favors the observed structure over the hypothetical one by 0.885 eV; the tight-binding analysis indicates that the observed structure is preferred with respect to both the site energy and bond energy terms, results of which are summarized in Table 7.

The DOS curve for the alternative structure "YZnMg," which is illustrated in Figure 4, provides some clues to this result: (a) the energy of the Zn 3*d* band is ca. 0.5 eV higher relative to E_F in "YZnMg" than in YMgZn and is ca. twice as broad; (b) the structure of the occupied valence bands is less evident in "YZnMg"; (c) the pseudogap corresponding to 8 valence electrons per formula unit still occurs, but the DOS value is ca 50% larger as for the observed coloring. These qualitative features in the DOS curve point toward minimizing (or even eliminating) close Zn···Zn contacts in the structure. COHP analysis of the DOS curve further indicates that the "short" Y–Mg orbital interactions are not optimized, even for "YGaMg." However, due to screening effects[22] arising from the inherent metallic character of YMgZn, there is no effective charge transfer among the various elements, but, rather, a redistribution of atomic orbital occupations.[23] The bond energy is influenced by maximizing the number of close Y–Zn contacts.

Table 7. Results of tight-binding analysis of site and bond energy terms in YMgZn and "YZnMg." E_{TOT} = total (core + valence) electronic energy; E_{BAND} = total valence electronic energy from energy band filling; Site Energy = sum of site energies for Y, Mg, and Zn; Bond Energy = sum of bond energies (COHP analysis) for the four significant interactions listed. Site + Bond Energy = sum of Site Energy and Bond Energy. E_{TOT} and E_{BAND} are given relative to YMgZn (the observed structure).

	YMgZn		"YZnMg"
E_{TOT}	0.00 eV		0.885 eV
E_{Band}	0.00 eV		0.436 eV
	Site Energies		
Y	+0.184 eV		+0.214 eV
Mg	–0.177 eV		–0.178 eV
Zn	–7.396 eV		–7.116 eV
Total	–7.389 eV		–7.080 eV
	Bond Energies		
Mg–Zn (4×)	–0.241 eV	Mg–Zn (4×)	–0.241 eV
Mg–Mg (3×)	–0.041 eV	Zn–Zn (3×)	–0.031 eV
Y–Zn (5×)	–0.233 eV	Y–Mg (5×)	–0.205 eV
Y–Mg (6×)	–0.276 eV	Y–Zn (6×)	–0.287 eV
Total	–3.908 eV		–3.804 eV
	Site + Bond Energies		
	–11.297 eV		–10.884 eV
Relative Total	0.00		0.413 eV

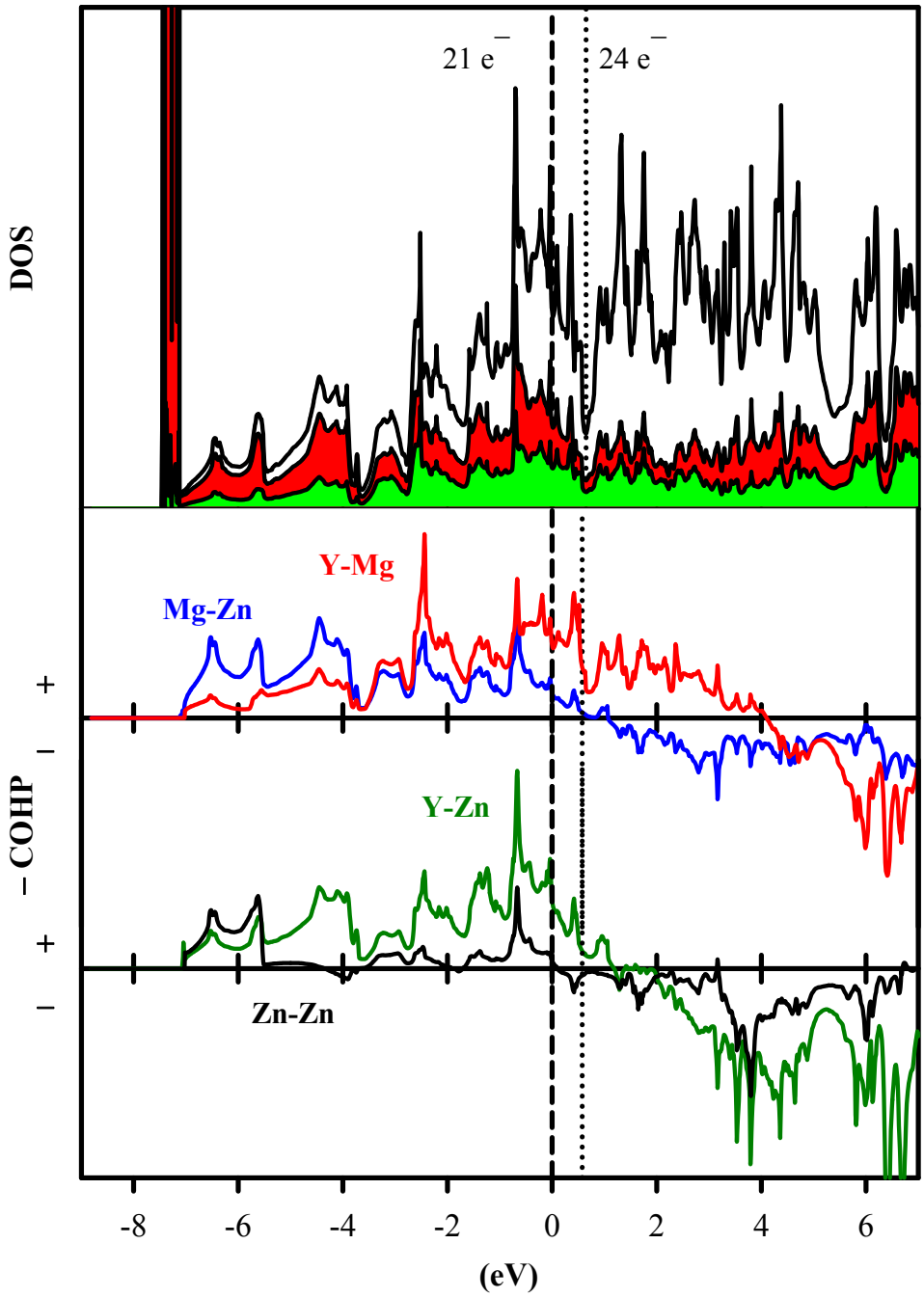

Figure 4. DOS and COHP curves for "YZnMg." In DOS curve, Mg (green) and Zn (red) and Y (yellow) orbital contributions are indicated. The Fermi level for "YZnMg" (21 e^-) is marked by the dashed line (and is the reference energy, 0 eV); the Fermi level calculated for "YGaMg" (24 e^-)is marked by the dotted line. In the COHP curves, + values are bonding interactions; – values are antibonding interactions.

The greatest influence on the site energy comes from minimizing (eliminating) close Zn···Zn contacts in the structure, which can be attributed to both a filled 3*d* subshell as well as the low energy 4*s* atomic orbitals. A comparison of the atomic orbital energies[21] for Y, Mg, and Zn (see Scheme **1**) indicate that Zn will show a tendency toward "anionic" behavior in this intermetallic system because its filled 3*d* and 4*s* atomic orbitals are lowest in energy. There is a better energetic match between Y 4*d* and Zn 4*p* orbitals than between Y 4*d* and Mg 3*p* orbitals (see also Scheme **1**; the strength of orbital interactions, $\Delta E \propto S^2/\Delta E^{(0)}$ is proportional to the square of the spatial overlap and is inversely proportional to the energies of the noninteracting orbitlals[3]).

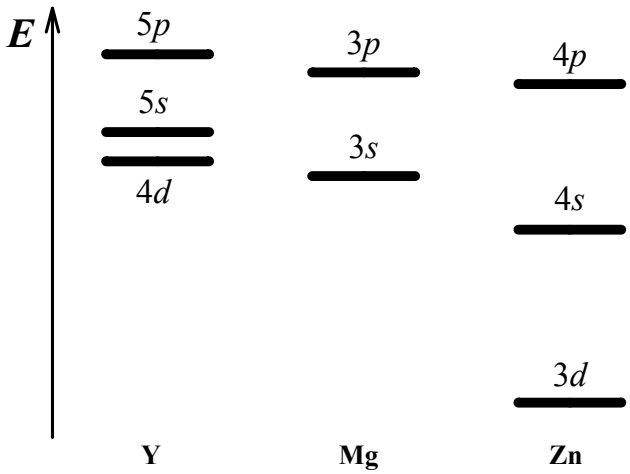

1

Plots of electron density and electron localization functions (ELF)[24] in YMgZn further confirm this analysis. Figure 5 illustrates these projections as filled contour plots with respect to the (001) and (100) planes. Maxima in the valence electron density in YMgZn occur at each atomic site, and there is some electron density building up within triangles of Y atoms in the $z = 0$ planes. In the $z = 1/2$ planes, valence electron density around the Zn1 sites deforms slightly toward the neighboring Mg atoms, and a similar distortion is observed in the (100) planes between Mg and Zn2 sites.

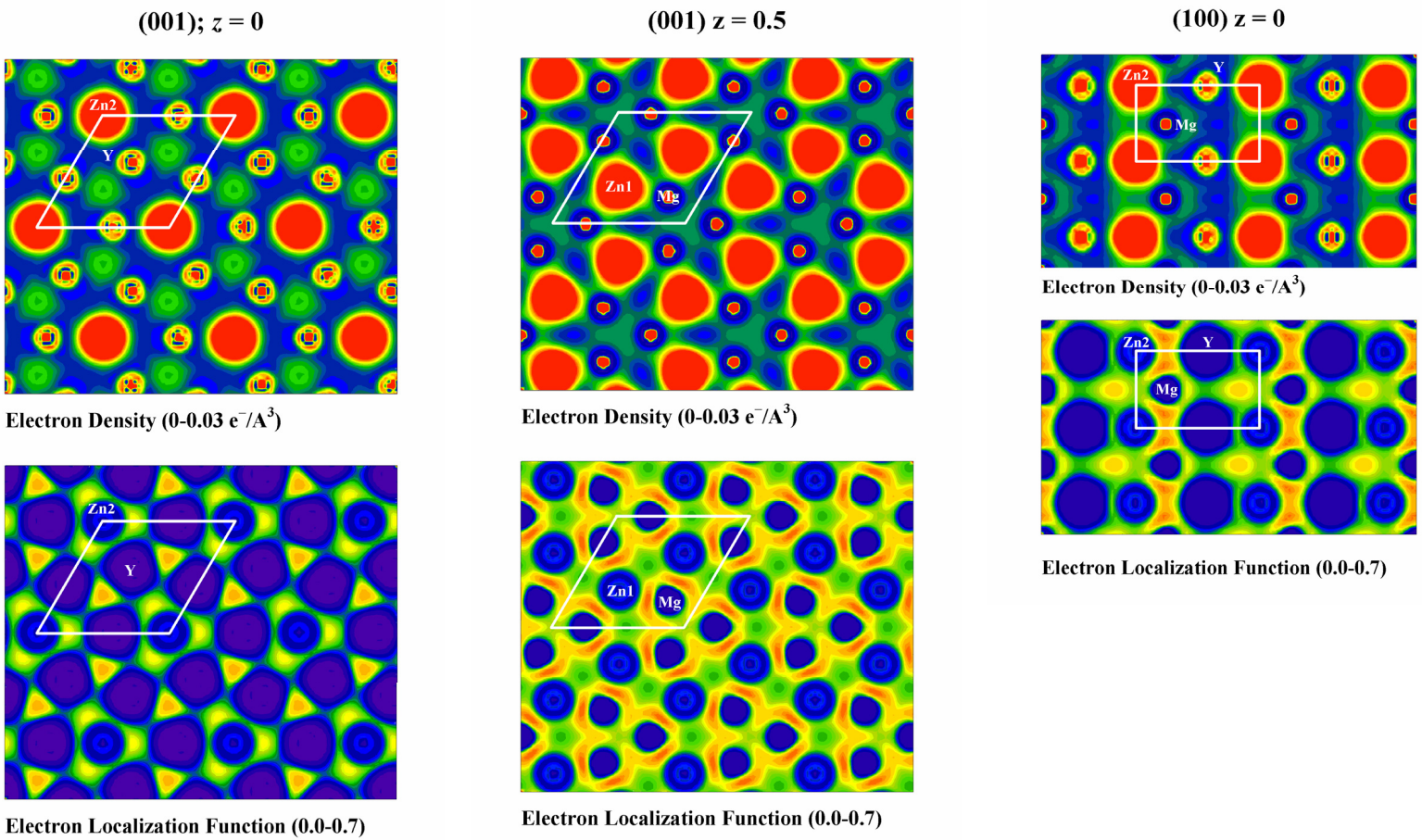

Figure 6. Valence electron densities and electron localization functions (ELF), depicted as filled contour plots, in various projections for YMgZn. Valence electron density color scheme (top) range from blue-red (0.0-0.03 $e^{-}/Å^{3}$); electron localization function color scheme (bottom) range from blue-orange (0.0-0.7). Values of (ELF) exceeding 0.5 identify

ELF maxima are noteworthy between Mg and Zn sites as well as within the triangles of Y atoms in the z = 0 planes, triangles which are located near Zn atoms above and below these sites at z = 1/2. Analysis of the coloring problem in YMgZn also provides some insights about the observed variation in Zn composition, which occurs only on the Zn-rich side of composition. The preferred distribution of Mg and Zn atoms maximizes the number of Y–Zn contacts over the number of Y–Mg contacts. As we have mentioned, an orbital picture for this preference is through significant Y 4*d*-Zn 4*s*, 4*p* interactions that can be enhanced via filled 3*d*-empty 4*d* interactions. Such enhancements are the focus of on-going theoretical efforts.

6.6 Structural Relationships

The electronic structure, atomic structure, and chemical bonding of the elements Y, Mg, and Zn have been well described by nearly-free-electron and pseudopotential theory. All three elements adopt the hexagonally closest packed arrangement of atoms as their ground state structures.[19] Theory has even accounted for the unusually large *c/a* ratio of the unit cell parameters in Zn.[25] YMgZn, from the perspective of orbital interactions and electron density analysis, form two interpenetrating networks that involve Zn atoms: (a) the Mg-Zn framework with tetrahedrally coordinated Mg atoms; and (b) the Y-Zn framework with square pyramidally coordinated Y atoms. There are two other structure types with identical local coordination modes that can compete with this structure type: the tetragonal Cu_2Sb and the orthorhombic Co_2Si structures types.[26] Electronic structure calculations of relative total energies rank the observed, hexagonal ZrNiAl-type as the minimum energy structure for YMgZn.

The different environments for Y and Mg can be attributed to size as well as electronic factors; if the size is not an issue, then electronic factors can play a significant role as observed in ZrNbP and ZrMoP.[27] Zn's influence on the structure and the arrangement of atoms is further confirmed in Figure 6, which plots the trends in average atomic volumes and valence electron densities for the known binary phases in the Y/Mg, Y/Zn, and Mg/Zn systems. These phases exist for valence electron *concentrations* of 2.0-2.5 e^-/atom. Linear regression fits of the valence electron densities ($e^-/Å^3$) show nearly identical behavior for the

Mg/Zn and the Y/Zn systems. When the average atomic volume and valence electron density of YMgZn are added to the graph, the volume is in line with the trends in Y-Zn and Mg-Zn binary phases, whereas the electron density is lower than the Zn-phases, but greater than the Y-Mg phases. Since all of the binary phases are densely packed, metallic structures, YMgZn conforms to this behavior. On the other hand, the valence electron density is lower than expected based exclusively on Y-Zn and Mg-Zn phases, which suggests that the Zn atoms are involved in a covalently-bonded network that involves Mg–Zn and Y–Zn interactions.

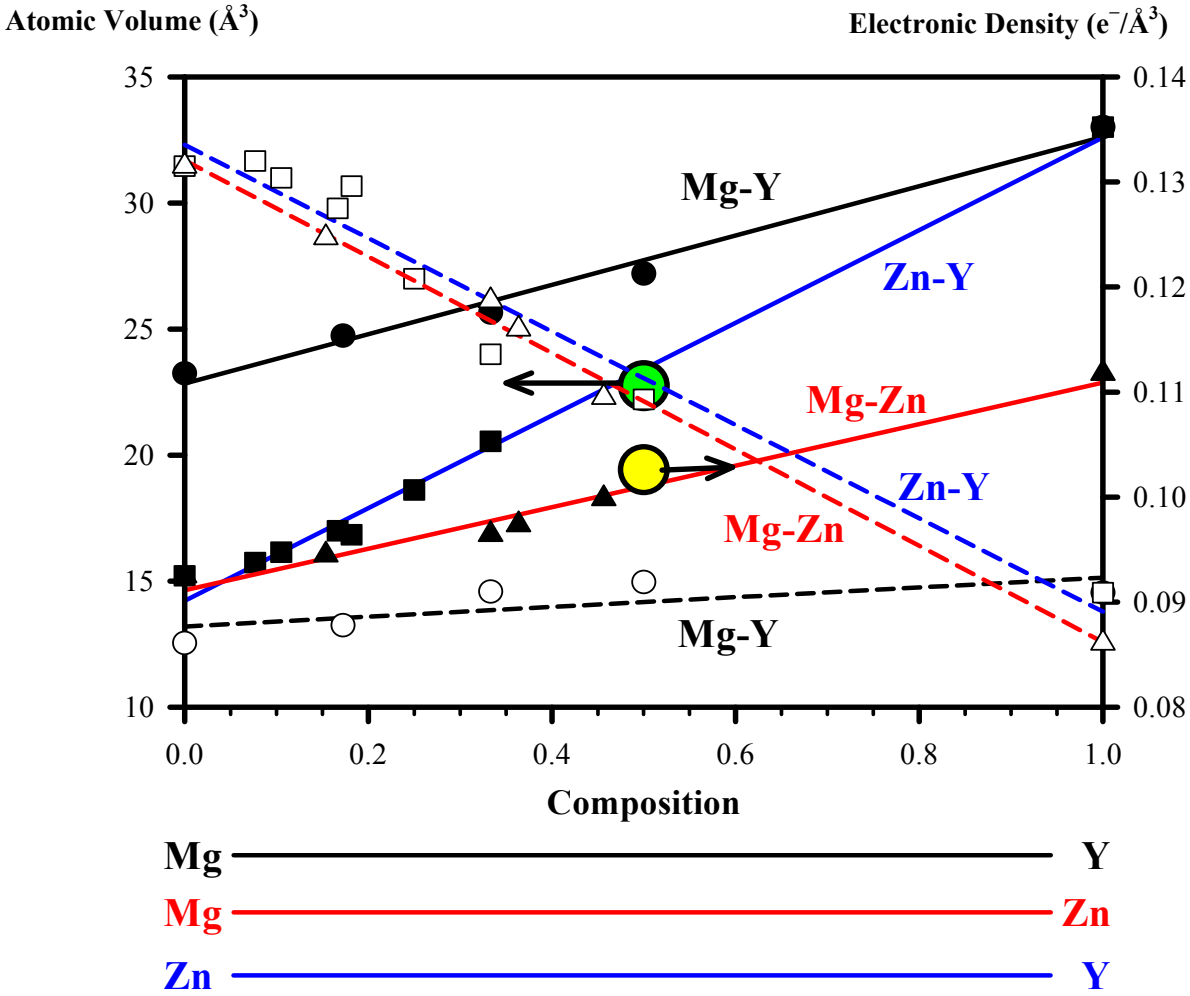

Figure 6. Variations in atomic volumes (solid lines, filled points) and valence electron densities (dashed lines, open points) vs. composition for binary Mg-Zn, Y-Zn, and Y-Mg

Thus, this simple graphical analysis based on unit cell volumes and electron counting corroborate the electronic structure analysis: the Mg–Zn and Y–Zn interactions dictate the structural chemical nature of this series. The Y–Mg interactions are less influential.

Finally, the isoelectronic compounds YCuAl[28] and YNiSi[29] are also known and consist of elements closely related to YMgZn. YCuAl is isostructural with YMgZn with Al occupying the Mg sites and Cu occupying the Zn sites. Unlike our refinements, the authors report some degree of mixed occupancy for Cu and Al among the three crystallographic sites in the unit cell.[28] YNiSi, however, adopts the related, orthorhombic Co_2Si structure type. We are investigating the theoretical electronic structures of these systems to provide a more general picture of the influence of relative atomic orbital energies and interatomic orbital overlap over these complex intermetallic phases.

6.7 Summary

The new phases, $YMg_{1-x}Zn_{1+x}$, form in the hexagonal ZrNiAl structure type with a specific ordering of the three elements so as to minimize Zn···Zn interactions while maximizing Y–Zn and Mg–Zn interactions. The structure and atomic arrangement can be described as two interpenetrating three-dimensional networks involving Mg-Zn and Y-Zn contacts. Among these three elements, the occupied valence atomic orbitals of Zn are lowest in energy, which gives it pseudo-anionic behavior in these intermetallics. The phase can accommodate some excess Zn atoms replacing Mg atoms. Bonding analysis of the electronic DOS of YMgZn indicated stability of YMgGa, YMgAl, and YMgIn, which were successfully prepared and structurally characterized to show similar site preferences as in YMgZn. Other phases isoelectronic with YMgZn show similar atomic distributions or related structures, and further theoretical investigations are underway.

Acknowledgements

This work was supported by NSF DMR 02-41092 and 06-05949. G.J.M. wishes to thank MPI-CPFS in Dresden, Germany for providing resources for part of this research during an academic sabbatical leave.

References

[1] Miller, G.J. *Eur. J. Inorg. Chem.***1998**, 523.

[2] Gimarc, B. M. *J. Am. Chem. Soc.* **1983**, *105*, 1979.

[3] Albright, T. A.; Burdett, J. K.; Whangbo, M.-H. *Orbital Interactions in Chemistry*; Wiley-Interscience: New York, 1985.

[4] Franzen, H.F.; Köckerling, M. *Prog. Solid State Chem.* **1995**, *23*, 265.

[5] Yao, X.; Miller, G. J.; Franzen, H. F. *J. Alloys and Compounds* **1992**, *183*, 7.

[6] Miller, G. J.; Lee, C.-S.; Choe, W. In *Inorganic Chemistry Highlights*; Meyer, G., Naumann, D., Wesemann, L., Ed.; Wiley-VCH: Berlin, 2002.

[7] Kraft,R.; Valldor, M.; Pöttgen, R. *Z. Naturforsch. B* **2003**, *58*, 827.

[8] Kraft,R.; Valldor, M.; Kurowski, D.; Hoffmann, R.-D.; Pöttgen, R. *Z. Naturforsch. B* **2004**, *59*, 513.

[9] Hunter, B. A.; Howard, C. J. *Rietica*; Australian Nuclear Science and Technology Organization: Menai, Australia, 2000.

[10] XRD single crystal software; Bruker Analytical X-ray System: Madison, WI, 2002.

[11] *SHELXTL*, version 5.1; Bruker AXS Inc.: Madison, WI, 1998.

[12] Jepsen, O.; Burkhardt, A.; Andersen, O. K. *The TB-LMTO-ASA Program*, version 4.7; Max-Planck-Institut für Festkörperforschung: Stuttgart, Germany, 1999.

[13] Anderson, O. K. *Phys. Rev. B* **1986**, *34*, 2439.

[14] Anderson, O. K.; Jepsen, O. *Phys. Rev. Lett.* **1984***, 53*, 2571−2574.

[15] Andersen, O. K.; Jepsen, O.; Glötzel, D. In *Highlights of condensed matter theory*; Bassani, F.; Fumi, F.; Tosi, M. Ed.; North-Holland: New York, 1985.

[16] Jepsen, O.; Anderson, O. K. *Z. Phys. B* **1995**, *97*, 35.

[17] Dronskowski, R.; Blochl, P. *J. Phys. Chem*. **1993**, *97*, 8617−8624.

[18] Blöchl, P. E.; Jepsen, O.; Anderson, O. K. *Phys. Rev. B* **1994**, *49*, 16223−16233.

[19] Emsley, J. *The Elements*; Clarendon Press: Oxford, U. K., 1998.

[20] Dronskowski, R. *Adv. Solid State Phys*. **2002**, *42*, 433.

[21] Dronskowski, R. *Computational Chemistry of Solid State Materials*; Wiley-VCH: Weinheim, Germany, 2005.

[22] Pettifor, D. *Bonding and Structure of Molecules and Solids*; Clarendon Press: Oxford, 1995.

[23] Gourdon, O.; Gout, D.; Miller, G. J. In *Encyclopedia of Condensed Matter Physics*, Ed. Bassani, G.; Liedl, G.; Wyder, P. Ed.; Elsevier: Amsterdam, Netherlands, 2005, pp. 409-422.

[24] (a) Savin, A.; Flad, H. J.; Preuss, H.; von Schnering, H. G. *Angew. Chem.* **1992**, *104*, 185; *Angew. Chem., Int. Ed. Engl.* **1992**, *31*, 185; (b) Kohout, M. *Int. J. Quantum Chem.* **2004,** *97*, 651; (c) Kohout, M.; Wagner, F. R.; Grin, Yu. *Theor. Chem. Acc.* **2002**, *108*, 150; (d) Gatti, C. *Z. Kristallogr.* **2005**, *220***,** 399.

[25] Häussermann, U.; Simak, S. I. *Phys. Rev. B* **2001**, *64*, 245114.

[26] Villars, P.; Calvert, L. D. *Pearson's Handbook of Crystallographic Data for Intermetallic Phases*; American Society for Metals: Metals Park, OH, 1985.

[27] Miller, G. J.; Cheng, J. *Inorg. Chem.* **1995**, *34*, 2962.

[28] Krachan, T.; Stel'makhovich, B.M.; Kuz'ma, Yu.B. *J. Alloys Compd.*, **2003**, *349*, 134.

[29] Hovestreydt, E.; Engel, N.; Klepp, K.O.; Chabot, B.; Parthe, E. *J. Less-Common Met.*, **1982**, *85*, 247.

Chapter 7

Phase Width and Site Preferences in the $EuMg_xGa_{4-x}$ Series

Modified from a paper in press for *Zeitschrift für Anorganische und Allgemeine Chemie*

Tae-Soo You,[2,3] and Gordon J. Miller[2,4]

7.1 Abstract

A series of $EuMg_xGa_{4-x}$ compounds were synthesized using high temperature, solid-state methods and characterized by both powder and single crystal X-ray diffraction. All compounds crystallize in the tetragonal $BaAl_4$-type structure (space group $I4/mmm$, $Z = 2$, Pearson symbol $tI10$) with full occupancy of Ga at the apical atom ($4e$) site and mixed-occupancy of Mg and Ga at the basal atom ($4d$) site. Six compositions were analyzed by single crystal X-ray diffraction: $EuMg_{0.21(1)}Ga_{3.79(1)}$, $EuMg_{0.91(1)}Ga_{3.09(1)}$, $EuMg_{1.22(1)}Ga_{2.78(1)}$, $EuMg_{1.78(1)}Ga_{2.22(1)}$, $EuMg_{1.84(1)}$-$Ga_{2.16(1)}$, and $EuMg_{1.94(1)}Ga_{2.06(1)}$. As the larger Mg atoms increasingly replace Ga atoms at the basal site in $EuMg_xGa_{4-x}$, the a-axis lengths at first decrease and then increase, while the c-axis lengths increase monotonically along the series. The phase width of the $BaAl_4$-type $EuMg_xGa_{4-x}$ series is identified to be $0 \leq x \leq 1.94(1)$, a range which corresponds to 12.06(1)-14 valence electrons per formula unit, and can be understood by their electronic structures using density of states (DOS) curves calculated by tight-binding calculations. Mg substitution for Ga at the basal site is consistent with the site preferences for mixed metals on the three-dimensional framework of the $BaAl_4$-structure based on both electronegativities and sizes, and provides the rationale for the unusual

---

[1] Reproduced with permission from *Z. Anorg. Allg. Chem.,* in press. Unpublished work copyright 2008 Wiley-VCH.

[2] Graduate student and Professor, respectively, Department of Chemistry, Iowa State University

[3] Primary researcher and author

[4] Author for correspondence

behavior in lattice parameters. The observed site preference was also rationalized by total electronic energies calculated for two different coloring schemes.

7.2 Introduction

Polar intermetallic compounds represent a class of inorganic solids that provide numerous opportunities to study relationships among crystal structure, physical properties, chemical bonding and chemical composition [1-3]. They can be considered as intermediate between classical intermetallic compounds on the one hand, such as Hume-Rothery phases [2] and valence compounds, i. e., Zintl-Klemm compounds on the other, [4, 5] because they involve combinations of electropositive active metals with electronegative late transition/post-transition metals in definite compositions but over a range of valence electron concentrations [3]. The electropositive elements formally donate valence electrons to the electronegative components, whereas electronegative elements form networks that either conform to simple electron counting rules, such as the Zintl−Klemm formalism [4, 5], or give rise to an electronic structure characterized by a pseudogap in the electronic density of states curve and optimized orbital interactions at the Fermi level [6].

During our investigation of various polyanionic networks in polar intermetallic compounds to study the correlation among valence electron count, atomic size and crystal structure, we crystallized the electron-deficient $EuMg_xGa_{4-x}$ series ($0.21(1) \leq x \leq 1.94(1)$) in the $BaAl_4$-type structure, where electron poorer Mg atoms replace Ga atoms in the aristotype $EuGa_4$. This crystal structure features a body-centered tetragonal unit cell (space group *I*4/*mmm*), which contains two distinct "anionic" sites forming an 18-vertex Fedorov polyhedron [7] with one "cationic" site at the center of the polyhedron. Among the rare-earth tetragallides, only $EuGa_4$ and $YbGa_4$ form: $EuGa_4$ adopts the tetragonal $BaAl_4$-type structure [8, 9], whereas $YbGa_4$ forms a distorted variant of the $BaAl_4$-type structure [10, 11]. Although $BaAl_4$-type intermetallics have been extensively investigated [1, 12-14], the complete phase-width of the $EuMg_xGa_{4-x}$ series remains unreported: the only reported ternary compound is $EuMg_{0.55}Ga_{3.45}$ [15]. In this communication, we report the experimentally identified phase-width and observed site preference between Mg and Ga atom in the $EuMg_xGa_{4-x}$ series including their synthesis and structural characterization.

7.3 Experimental Section

7.3.1 Sample Preparation and Chemical Analysis

Eight compositions of the $EuMg_xGa_{4-x}$ series (loaded values of x include 0.2, 1.0, 1.2, 1.6, 1.8, 1.9, 2.0, and 2.2) were synthesized using pure elements (Eu: Ames Laboratory, rod, 99.99%; Mg: Ames Laboratory, bar, 99.99%; and Ga: Ames Laboratory, ingot, 99.99%) by conventional, high-temperature methods. Mixtures of each reactant were loaded into tantalum ampoules, which were sealed by arc-melting in an argon-filled glove box with the concentration of O_2 lower than 10 ppm. These ampoules were then sealed in evacuated silica jackets to prevent oxidation. All compounds were heated to 1173 K and held at this temperature for 24 hr followed by annealing at 873 K for one week in a tube furnace. Then, samples were allowed to cool naturally to room temperature. All products appeared to be visibly stable upon exposure to both air and moisture over several weeks.

Analysis by energy-dispersive X-ray spectroscopy (EDS) was conducted on a Hitachi S-2460N variable-pressure scanning electron microscope (SEM), equipped with Oxford Instruments Link Isis Model 200 X-ray analyzer. For these measurements, ca. three pieces of each sample were selected from the same specimens that were used for powder X-ray diffraction experiments. Samples were mounted on carbon sample holders and polished using an alumina slurry to expose flat surfaces for measurement. The corresponding pure elements were used as standards for intensity references.

7.3.2 Crystal Structure Determination

$EuMg_xGa_{4-x}$ specimens were characterized by both powder and single crystal X-ray diffraction at 293(2) K. Phase purity and lattice parameters were examined for all eight samples on a Huber G670 Guinier image-plate powder diffraction camera applying monochromatic Cu $K\alpha_1$ radiation (λ = 1.54059 Å). The step size was set at 0.005°, and the exposure time was 1-2 h. Data acquisition was controlled via the *in situ* program. The lattice parameters and the crystal system were determined by Rietveld refinement using program *Rietica* [16] and Si powder (NIST; a = 5.430940 ± 0.000035 Å) as a calibration standard; these were in good agreement with the results from single crystal X-ray diffraction.

For single crystal X-ray diffraction experiments, several silvery, block-shaped crystals were extracted from each batch of gently crushed samples. The crystals were checked for crystal quality by a rapid scan on a Bruker SMART Apex CCD diffractometer with Mo Kα radiation (λ = 0.71073 Å), and then the best crystals were chosen for further data collection at 293(2) K. Such samples were extracted from specimens loaded as "$EuMg_{0.2}Ga_{3.8}$," "$EuMg_{1.0}Ga_{3.0}$," "$EuMg_{1.2}Ga_{2.8}$," "$EuMg_{1.8}Ga_{2.2}$," "$EuMg_{1.9}Ga_{2.1}$," and "$EuMg_{2.2}Ga_{1.8}$." Because of the poor crystallinity of the two samples, "$EuMg_{1.6}Ga_{2.4}$" and "$EuMg_{2.0}Ga_{2.0}$," no further investigations on these samples using single crystals were pursued. Single crystal X-ray diffraction data on specimens of "$EuMg_{0.2}Ga_{3.8}$," "$EuMg_{1.0}Ga_{3.0}$," "$EuMg_{1.2}Ga_{2.8}$," and "$EuMg_{1.9}Ga_{2.1}$" were collected using the SMART Apex CCD diffractometer from three sets of 606 frames on a full sphere with 0.3° scans in ω and with an exposure time of 10 sec per frame. Single crystal X-ray diffraction data of "$EuMg_{1.8}Ga_{2.2}$" and "$EuMg_{2.2}Ga_{1.8}$" were collected on a STOE IPDS diffractometer from two sets of 180 frames with an exposure time of 1 min for each frame. Further investigations were conducted for "$EuMg_{1.2}Ga_{2.8}$" and "$EuMg_{1.9}Ga_{2.1}$" using a STOE IPDS diffractometer with an exposure time of 2.5 min for each frame to see whether there were any satellites or diffuse reflections, which would suggest a possible superstructure. However, no evidence for a superstructure emerged.

Intensities were extracted and then corrected for Lorentz and polarization effects using the *SAINT* program [17]. The program *SADABS* [18] was used for empirical absorption correction. The entire sets of reflections of the three compounds were matched with the tetragonal crystal system. After further analysis, the space group *I*4/*mmm* was chosen for these products. The structures were solved by direct methods and refined on F^2 by full-matrix least-squares methods using the *SHELXTL* software package [18].

7.3.3 Electronic Structure Calculations

Tight-binding, linear muffin-tin orbital (TB-LMTO) calculations [19] were carried out in the atomic sphere approximation (ASA) using the Stuttgart program [20]. Exchange and correlation were treated by the local density approximation (LDA) [21]. All relativistic effects except spin-orbit coupling were taken into account by using a scalar relativistic

approximation [22]. In the ASA method, space is filled with overlapping Wigner-Seitz (WS) atomic spheres. The symmetry of the potential is considered spherical inside each WS sphere, and a combined correction is used to take into account the overlapping part [23]. The radii of WS spheres were obtained by requiring that the overlapping potential be the best possible approximation to the full potential, and were determined by an automatic procedure [23]. This overlap should not be too large because the error in kinetic energy introduced by the combined correction is proportional to the fourth power of the relative sphere overlap. No empty spheres [19] were necessary. The WS radii are as follows: Eu = 2.34 Å, Mg = 1.73 Å and Ga = 1.37 Å. The basis sets included 6*s*, 6*p*, and 5*d* orbitals for Eu; 3*s*, 3*p* and 3*d* orbitals for Mg; 4*s*, 4*p* and 4*d* orbitals for Ga. The Eu 6*p*, Mg 3*d* and Ga 4*d* orbitals were treated by the Löwdin downfolding technique [19, 21, 22], and the Eu 4*f* wavefunctions were treated as core functions occupied by 7 electrons. The *k*-space integrations were performed by the tetrahedron method [24]. The self-consistent charge density was obtained using 436 irreducible *k*-points in the Brillouin zone for the tetragonal cell.

7.4 Results and Discussion

Figure 1 shows the powder X-ray diffraction patterns of the $EuMg_xGa_{4-x}$ series (x = 0.2, 1.0, 1.2, 1.6, 1.8, 1.9, 2.0, and 2.2). Intense peaks originate from the major phase, which is the tetragonal $BaAl_4$-type phase, and can be indexed by the Rietveld method. As the larger Mg atoms increasingly replace Ga atoms in $EuMg_xGa_{4-x}$ (metallic radii (*CN* 12): Mg = 1.598 Å; Ga = 1.404 Å [25]), the unit cell volumes monotonically increase (see Table 1). Several less intense peaks from minor phases, e. g., $EuGa_2$ and $EuMg_2$, and other impurities are also observed. In particular, peaks from $EuGa_2$ can be clearly identified for the patterns with loaded x = 1.8, 1.9, 2.0 and 2.2, and show decreasing intensity and peak-shifting toward larger scattering angle as the loaded x value increases. This could indicate Mg substitution for a small number of Ga atoms in $EuGa_2$, which results in an orthorhombic KHg_2-type $EuMg_xGa_{2-x}$ phase. However, further chemical analysis of this observation was not pursued,

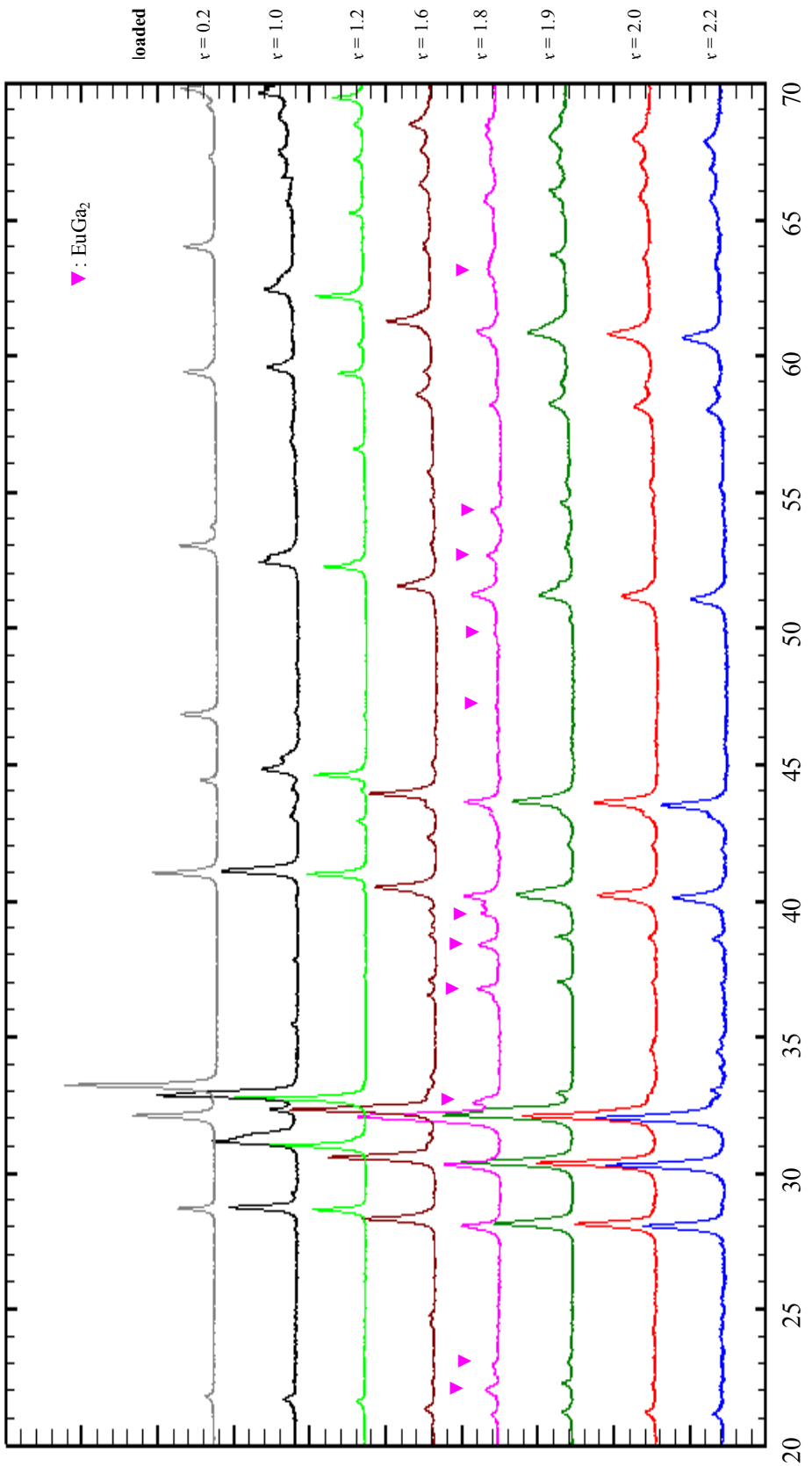

Figure 7. Powder X-ray diffraction patterns of $EuMg_xGa_{4-x}$ for loaded compositions $x = 0.2$, 1.0, 1.2, 1.6, 1.8, 1.9, 2.0 and 2.2.

nor was an upper bound for this phase region identified. Major peaks from trace amounts of $EuMg_2$ were also observed at 2θ = ca. 35º for patterns with loaded x = 2.0 and 2.2.

Three to five crystals were selected from each product for single crystal X-ray diffraction experiments. At least two crystals for each product were utilized for data collections, and consistency of refinement results was confirmed. Important crystallographic data, atomic coordinates, equivalent displacement parameters and selected interatomic distances of six phases (x = 0.21(1), 0.91(1), 1.22(1), 1.78(1), 1.84(1) and 1.94(1)) are summarized in Tables 1-3. Table 1 also includes a comparison of the refined, loaded, and EDS-measured chemical compositions, all of which are in close agreement with each other. Thus, our synthetic approach did not lead to any significant changes in Mg content on cooling, and corresponding quenching procedures from the annealing temperature were not carried out. Furthermore, although we loaded an equal or excess amounts of Mg as compared to Ga, i.e., atomic ratios of Eu:Mg:Ga = 1:2:2 or 1.0:2.2:1.8, the refined maximum Mg content is 1.94(1) per formula unit. Therefore, we conclude that the upper limit of Mg content results in $EuMg_{1.94(1)}Ga_{2.06(1)}$, which corresponds to 12.06(1) valence electrons.

Moreover, the phase width of the $EuMg_xGa_{4-x}$ series adopting the $BaAl_4$-type structure can be identified as $0 \leq x \leq 1.94(1)$ based, in part, on our experimental results, which cover $0.21(1) \leq x \leq 1.94(1)$, and literature precedents, which reported $EuGa_4$ [8, 9] and $EuMg_{0.55}Ga_{3.45}$ [15] as also adopting the $BaAl_4$-type.

Given the poor crystal qualities of two samples with loaded compositions x = 1.6 and 2.0, we were unable to pursue single crystal X-ray diffraction experiments even after we tested twenty crystals for each product. EDS analyses were conducted for all eight compounds and these compositions agreed well with compositions refined by single crystal X-ray diffraction results for six samples (x = 0.21(1), 0.91(1), 1.22(1), 1.78(1), 1.84(1) and 1.94(1)). These are also listed in Table 1. For the two compounds with poor crystal quality (loaded x = 1.6 and 2.0), EDS analysis yielded their chemical compositions, respectively, to be $Eu_{1.03(3)}Mg_{1.46(3)}Ga_{2.51(3)}$ and $Eu_{1.00(3)}Mg_{1.91(3)}Ga_{2.09(3)}$.

Figure 2 illustrates the crystal structure of $EuMg_xGa_{4-x}$. Each example crystallizes in the $BaAl_4$-type structure (space group $I4/mmm$, Z = 2, Pearson symbol $tI10$), which is one of the most widely adopted crystal structures among intermetallics [26, 27].

Table 2. Crystallographic data for $EuMg_xGa_{4-x}$ (x = 0.21(1), 0.91(1), 1.22(1), 1.78(1), 1.84(1) and 1.94(1)).

Loaded Composition	$EuMg_{0.20}Ga_{3.80}$	$EuMg_{1.00}Ga_{3.00}$	$EuMg_{1.20}Ga_{2.80}$	$EuMg_{1.80}Ga_{2.20}$	$EuMg_{2.00}Ga_{2.00}$	$EuMg_{2.20}Ga_{1.80}$
Empirical formula	$EuMg_{0.21(1)}Ga_{3.79(1)}$	$EuMg_{0.91(1)}Ga_{3.09(1)}$	$EuMg_{1.22(1)}Ga_{2.78(1)}$	$EuMg_{1.78(1)}Ga_{2.22(1)}$	$EuMg_{1.84(1)}Ga_{2.16(1)}$	$EuMg_{1.94(1)}Ga_{2.06(1)}$
EDS analysis	$Eu_{1.03(3)}Mg_{0.17(3)}Ga_{3.80(3)}$	$Eu_{1.02(3)}Mg_{0.88(3)}Ga_{3.10(3)}$	$Eu_{1.00(3)}Mg_{1.25(3)}Ga_{2.75(3)}$	$Eu_{1.02(3)}Mg_{1.73(3)}Ga_{2.25(3)}$	$Eu_{1.00(3)}Mg_{1.81(3)}Ga_{2.19(3)})$	$Eu_{1.00(3)}Mg_{1.90(3)}Ga_{2.10(3)}$
Molar mass (g mol^{-1})	421.32	389.53	375.45	350.01	347.29	342.75
Unit cell dimensions (Å)	a = 4.399(2)	a = 4.394(2)	a = 4.4071(5)	a = 4.4679(6)	a = 4.4770(7)	a = 4.4971(6)
	c = 10.796(6)	c = 11.275(6)	c = 11.452(2)	c = 11.657(2)	c = 11.673(3)	c = 11.733(2)
Volume ($Å^3$)	208.9(2)	217.7(2)	222.43(5)	232.69(6)	233.97(7)	237.28(6)
Calculated density (g cm^{-3})	5.865	5.628	5.509	5.266	4.826	4.759
Diffractometer	SMART APEX	SMART APEX	SMART APEX	STOE IPDS	SMART Apex	STOE IPDS
2θ range (°)	7.54-56.12	7.22-55.18	7.12-55.22	7.00-55.94	6.98-56.38	9.70-68.48
Index ranges	$-5 \le h \le 5$, $-5 \le k \le 5$, $-14 \le l \le 13$	$-5 \le h \le 5$, $-5 \le k \le 5$, $-14 \le l \le 14$	$-5 \le h \le 5$, $-5 \le k \le 5$, $-14 \le l \le 14$	$-5 \le h \le 5$, $-5 \le k \le 5$, $-15 \le l \le 15$	$-5 \le h \le 5$, $-5 \le k \le 5$, $-14 \le l \le 15$	$-7 \le h \le 7$, $-7 \le k \le 7$, $-14 \le l \le 18$
Total no. reflections	883	930	980	1149	1004	2005
Independent reflections	99 [R_{init} = 0.0228]	99 [R_{init} = 0.0331]	101 [R_{init} = 0.0310]	109 [R_{init} = 0.157]	110 [R_{init} = 0.024]	179 [R_{init} = 0.078]
Data/Refined parameters	99/10	99/9	101/10	109/10	110/9	179/9
Goodness-of-fit on F^2	1.213	1.166	1.146	0.958	1.252	1.159
Final R indices [$I > 2\sigma(I)$]	R_1 = 0.017, wR_2 = 0.033	R_1 = 0.016, wR_2 = 0.035	R_1 = 0.016, wR_2 = 0.035	R_1 = 0.027, wR_2 = 0.026	R_1 = 0.013, wR_2 = 0.029	R_1 = 0.028, wR_2 = 0.030
R indices (all data)	R_1 = 0.017, wR_2 = 0.033	R_1 = 0.017, wR_2 = 0.035	R_1 = 0.017, wR_2 = 0.036	R_1 = 0.039, wR_2 = 0.029	R_1 = 0.014, wR_2 = 0.029	R_1 = 0.038, wR_2 = 0.031
Largest diff. peak and hole ($e^-/Å^3$)	1.021 / –0.972	1.066 / –0.896	0.623 / –1.375	0.722 / –1.545	0.949 / –0.859	1.577 / –1.249

Table 2. Atomic coordinates and equivalent displacement parameters for $EuMg_xGa_{4-x}$ (x = 0.21(1), 0.91(1), 1.22(1), 1.78(1), 1.84(1) and 1.94(1)).

Atom	Wyckoff position	Occupancy	x	y	z	U_{eq} [a)]
			$EuMg_{0.21(1)}Ga_{3.79(1)}$			
Eu	2*a*	1	0	0	0	0.015(1)
Ga	4*e*	1	0	0	0.3844(1)	0.016(1)
Mg/Ga	4*d*	0.105(6)/0.895(6)	0	1/2	1/4	0.015(1)
			$EuMg_{0.91(1)}Ga_{3.09(1)}$			
Eu	2*a*	1	0	0	0	0.016(1)
Ga	4*e*	1	0	0	0.3885(1)	0.018(1)
Mg/Ga	4*d*	0.456(7))/0.544(7)	0	1/2	1/4	0.016(1)
			$EuMg_{1.22(1)}Ga_{2.78(1)}$			
Eu	2*a*	1	0	0	0	0.014(1)
Ga	4*e*	1	0	0	0.3905(1)	0.016(1)
Mg/Ga	4*d*	0.611(7)/0.389(7)	0	1/2	1/4	0.015(1)
			$EuMg_{1.78(1)}Ga_{2.22(1)}$			
Eu	2*a*	1	0	0	0	0.016(1)
Ga	4*e*	1	0	0	0.3931(1)	0.018(1)
Mg/Ga	4*d*	0.890(7)/0.110(7)	0	1/2	1/4	0.017(1)
			$EuMg_{1.84(1)}Ga_{2.16(1)}$			
Eu	2*a*	1	0	0	0	0.013(1)
Ga	4*e*	1	0	0	0.3935(1)	0.014(1)
Mg/Ga	4*d*	0.922(6)/0.078(6)	0	1/2	1/4	0.014(1)
			$EuMg_{1.94(1)}Ga_{2.06(1)}$			
Eu	2*a*	1	0	0	0	0.011(1)
Ga	4*e*	1	0	0	0.3939(1)	0.016(1)
Mg/Ga	4*d*	0.968(7)/0.032(7)	0	1/2	1/4	0.015(1)

[a)] U_{eq} is defined as one third of the trace of the orthogonalized U_{ij} tensor.

Table 3. Selected interatomic distances for $EuMg_xGa_{4-x}$ (x = 0.21(1), 0.91(1), 1.22(1), 1.78(1), 1.84(1) and 1.94(1)).

Compound	*d*(Eu-Ga)	*d*(Eu-Mg/Ga)	*d*(Ga-Ga)	*d*(Mg/Ga-Mg/Ga)	*d*(Ga-Mg/Ga)
$EuMg_{0.21(1)}Ga_{3.79(1)}$	3.352(1)	3.482(1)	2.495(2)	3.111(1)	2.635(1)
$EuMg_{0.91(1)}Ga_{3.09(1)}$	3.352(1)	3.574(1)	2.514(2)	3.107(1)	2.696(1)
$EuMg_{1.22(1)}Ga_{2.78(1)}$	3.3594(5)	3.6129(4)	2.509(2)	3.1163(4)	2.7282(6)
$EuMg_{1.78(1)}Ga_{2.22(1)}$	3.396(1)	3.672(0)	2.492(2)	3.159(0)	2.788(1)
$EuMg_{1.84(1)}Ga_{2.16(1)}$	3.401(0)	3.678(1)	2.487(1)	3.166(0)	2.796(1)
$EuMg_{1.94(1)}Ga_{2.06(1)}$	3.415(0)	3.696(0)	2.489(1)	3.180(0)	2.812(1)

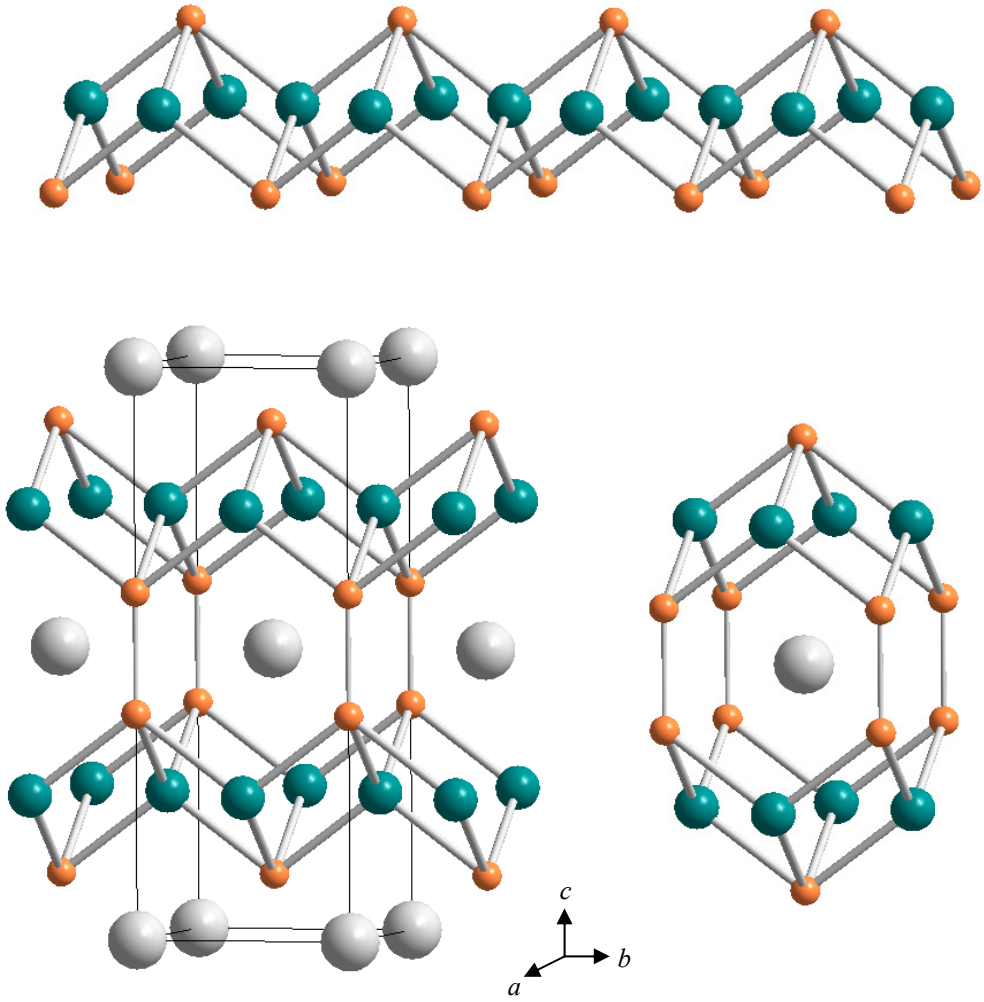

Figure 2. Crystal Structure of $EuMg_xGa_{4-x}$ ($0 \leq x \leq 1.94(1)$). (Top) a layer of 2D square pyramids; (bottom, left) a unit cell of the $BaAl_4$-type phase; (bottom, right) an 18-vertex Fedorov polyhedron. Grey sphere, Eu; green sphere, Mg/Ga mixed site; orange sphere, Ga.

A body-centered tetragonal unit cell contains one Eu site at the Wyckoff site 2*a* (0, 0, 0), one Ga site at the Wyckoff site 4*e* (0, 0, *z*) and one Mg/Ga mixed-site at Wyckoff site 4*d* (0, 1/2, 1/4). The two sites occupied by the main group metals can be differentiated as the apical (4*e*) site and the basal (4*d*) site, where the basal Mg/Ga atoms form two-dimensional (2D) square nets and the apical Ga atoms alternately cap above and below the planar square nets creating layers of square pyramids (Fig. 2, top) [28]. These 2D layers are connected to each other along the *c*-axis via two apical Ga atoms resulting in the 3D net

$^{3}_{\infty}[Mg_xGa_{4-x}]^{2-}$ (Fig. 2, bottom, left). In terms of local coordination within this 3D net, the basal (4*d*) sites are surrounded by a distorted tetrahedron of apical (4*e*) sites; the apical sites are coordinated by a square pyramid formed by 4 basal sites and 1 apical site. The coordination environment of the Eu atom is an 18-vertex Fedorov polyhedron [7] (Fig. 2, bottom, right), formed by 8 basal Mg/Ga atoms and 10 apical Ga atoms. According to our results (see Table 1) and references 9 and 15, the *c*-axis lengths increase as the Mg content in $EuMg_xGa_{4-x}$ increases across the entire series. On the other hand, the *a*-axis lengths decrease in the region of $0 \leq x \leq 0.55$, and then increase for greater Mg content. Since the expansion of the *c*-axis is more significant (by ca. 0.94 Å) than changes along the *a*- and *b*-axes (by ca. 0.12 Å), the unit cell volumes increase nearly linearly in a range of 206.5(9)- 237.28(6) Å^3 (for $x = 0$* [9] to 1.94(1)).

This change in a unit cell volume clearly follows Zen's law [31]. The expansion along the *c*-axis can be attributed to the increasing *d*(Ga-Mg/Ga) and *d*(Eu-Mg/Ga) values (see Table 3) as well as the apical-basal-apical atom angles surrounding each basal (Mg/Ga) site, angles which increase from 107.7º to 111.1º as *x* increases. On the other hand, the apical Ga–apical Ga distance decreases slightly from 2.514(2) Å to 2.487(1) Å as the Mg content increases. These Ga–Ga distances are significantly shorter than the doubled metallic radius of Ga, which is 2.808 Å (r_{CN12}(Ga) = 1.404 Å [25]), as well as other Ga–Ga bond lengths found in intermetallics such as $EuGa_2$ (2.72 Å) [32], $BaGa_4$ (2.66 Å) [1] and $SmGaSb_2$ (2.539(2) Å) [33]. However, these apical-apical distances are not sufficiently short to consider multiple bonding character between Ga atoms because Ga–Ga multiple bonds have been reported for reduced organogallium species with distances as short as 2.3-2.4 Å [34-36] as well as in Ga-cluster compounds, e.g., $Na_{22}Ga_{39}$, with a Ga–Ga distance of 2.435(7) Å [37] (see also Table 4). Nevertheless, the apical-apical distances of 2.487(1)-2.514(2) Å are consistent with the double covalent radius of Ga, which is ca. 2.52 Å (r_{cov}(Ga) = 1.26 Å [38]), but this radius has been determined from polar-covalent molecules in which Ga is a Lewis acid, such that electron density is shifted away from the Ga atom in the polar-covalent bonds. In this $EuMg_xGa_{4-x}$ series, Ga has a "reducing" environment, surrounded by the

* Among four reports of the crystal structure of $EuGa_4$ [8, 9, 29, 30], we selected the result [9] from the sample that had been prepared in a manner similar to our $EuMg_xGa_{4-x}$ phases.

electropositive Eu and Mg atoms. We return to this feature in a subsequent paragraph. Therefore, we conclude that apical Ga-apical Ga dimers found in this series have single bonded, covalent character.

Table 4. Ga-Ga distances observed in organometallic and intermetallics.

Organometallics	**bond length (Å)**	**description**
$Trip_2Ga{-}GaTrip_2$ [32]	2.515(3)	single bond
$\{GaPh\}_2^{2-}$ [33]	2.461	
$Na\{GaC_6H_3{-}2,6{-}Ph_2\}_2$ [33]	2.362	
$[Trip_2Ga{-}GaTrip_2]^-$ [32]	2.343(2)	1.5 bond
$Na[Mes^*_2C_6H_3{-}Ga{\equiv}Ga{-}C_6H_3Mes^*_2]$ [34]	2.319(3)	triple bond
Intermetallics	**bond length (Å)**	**description**
$EuGa_2$ [30]	2.72	average value
CaGa [36]	2.66	zigzag Ga chain
$BaGa_4$ [1]	2.66	
$Na_2Ga_3Sb_3$ [37]	2.541(3)	
Na_7Ga_{13} [35]	2.54	Ga_{15} cluster
$SmGaSb_2$ [31]	2.539(2)	
$LaGa_2$ [38]	2.494	planar 6^3 net
$CaGa_4$ [1]	2.47	
$LaGaBi_2$ [39]	2.466(2)	planar Ga_6 ring
$Na_{22}Ga_{39}$ [35]	2.435(7)	Ga_{15} cluster
$La_{13}Ga_8Sb_{21}$ [40]	2.422(5)	slightly puckered Ga_6 ring

Mg atoms occupy only the basal (4*d*) sites, as previously observed in other examples, such as $EuMg_{0.55}Ga_{3.45}$ [15] and $AEMg_xIn_{4-x}$ (AE = Sr, $0.85 \leq x \leq 1.53$; AE = Ba, $0 \leq x \leq 1.79$) [28]. However, no ordering between Mg and Ga atoms is observed within these basal sites for any of these compounds. The observed site preference for Mg atoms does provide a rationale for the unusual trend in *a*-axis lengths in $EuMg_xGa_{4-x}$ with Mg content: at low Mg levels, the first- and second-nearest neighbor basal (4*d*) sites surrounding a Mg (4*d*) position in the square net will be almost entirely Ga; when x reaches 0.5, i.e., $EuMg_{0.5}Ga_{3.5}$, then one-

fourth of these neighbors becomes Mg atoms; and for Mg content above $x = 0.5$, the number of (4*d*)···(4*d*) nearest neighbor Mg···Mg contacts increases rapidly. If we consider these Mg···Mg interactions to be repulsive and the corresponding Mg···Ga interactions to be attractive, then the *a*-axis lengths will go through a minimum value close to $EuMg_{0.5}Ga_{3.5}$, which is indeed observed by experiment.

Although the site preference problem in these phases appears complex [1, 12, 13], there are two major factors influencing the outcome: relative electronegativities and atomic sizes between the component elements. According to theoretical studies conducted by Häussemann et al. [1], elements with greater electronegativity prefer the apical (4*e*) site, e.g., Ga atoms in $SrMg_{1.7(1)}Ga_{2.3(1)}$ and $BaMg_{1.7(1)}Ga_{2.3(1)}$ [1]. The same tendency is also observed in other examples, such as Zn atoms in $REZn_2Al_2$ (*RE* = La, Ce) [39, 40] and $REZn_{1.66}Al_{2.34}$ (*RE* = Yb, Nd) [41] and In atoms in $AEMg_xIn_{4-x}$ (*AE* = Sr, $0.85 \leq x \leq 1.53$; *AE* = Ba, $0 \leq x \leq 1.79$) [28]. Our experimental results are consistent with these observations, where Ga atoms with greater electronegativity (Pauling values: Mg = 1.31; Ga = 1.81 [38]) occupy the apical (4*e*) sites, whereas Mg atoms are located only among the basal (4*d*) sites.

To get a better understanding of the chemical bonding in these polyanionic networks and the coloring problem related to a site preference between Mg and Ga in $EuMg_xGa_{4-x}$, TB-LMTO-ASA calculations [19] were conducted for two different coloring schemes. We restricted computational focus to two hypothetical models of $EuMg_2Ga_2$: one coloring scheme placed Mg atoms solely at the basal (4*d*) sites, i.e., "$EuMg_2Ga_2$;" the alternative scheme placed Mg atoms at the apical (4*e*) sites, i.e., "$EuGa_2Mg_2$." The lattice parameters and atomic positions were based on the crystallographic data of the $EuMg_{1.94(1)}Ga_{2.06(1)}$ (see Table 1, 2), which has the closest composition to Eu:Mg:Ga = 1:2:2. The calculated total energies favor the placement of Mg atoms in the 4*d* sites over the alternative by 1.966 eV/formula unit, i.e., 0.983 eV/Mg atom. If we consider mixing of Mg and Ga atoms among all the apical (4*e*) and basal (4*d*) sites, the free energy calculation taking into account the resulting configurational entropy, (8 ln 2)*R*, predicts that the completely disordered arrangement achieves a lower free energy at temperatures exceeding ca. 2057 K, which is well above the temperatures used in the preparation of the $EuMg_xGa_{4-x}$ phases.

Among the various contributions to the total energy, the band energy is the most influential contributing to this structural preference. The tight-binding approach allows the band energy to be decomposed into a "site-energy" term and a "bond-energy" term [42]. In TB-LMTO, the "site-energy" term is calculated for each distinct site in the asymmetric unit by summing the products of occupation numbers and band centers for each atomic orbital. The "bond-energy" term is evaluated by the integrated COHP values. Table 5 summarizes the results of this analysis for "$EuMg_2Ga_2$" and "$EuGa_2Mg_2$" based on the significant interatomic interactions: the observed distribution of Mg and Ga atoms is more favorable with respect to both the site-energy and bond-energy terms. Favorable site-energy contributions arise from the Eu and Mg atoms, whereas the Ga site preference is dictated more by bond-energy issues, by forming Ga–Ga dimers between adjacent apical sites.

Table 5. Results of tight-binding analysis of site-energy and bond-energy terms in $EuMg_2Ga_2$ and "$EuGa_2Mg_2$".

	$EuMg_2Ga_2$		"$EuGa_2Mg_2$"
E_{TOT} (eV)	0.000		1.966
E_{Band} (eV)	0.000		8.146
Site energies (eV)			
Eu	−0.687		1.908
Mg (2x)	−16.976		1.221
Ga (2x)	−1.504		−19.164
Total	−19.167		−16.035
Bond energies (eV)			
Ga−Ga (1×)	−2.416	Mg−Mg (1×)	−0.940
Ga−Mg (8×)	−11.124	Ga−Mg (8×)	− 10.722
Mg−Mg (4×)	−2.708	Ga−Ga (4×)	−1.869
Eu−Ga (4×)	−2.506	Eu−Mg (4×)	−1.577
Eu−Mg (4×)	−1.454	Eu−Ga (4×)	−1.680
Total	−20.208		−16.788
Site + bond energies (eV)	−39.375		−32.823
Relative total	0.000		6.552

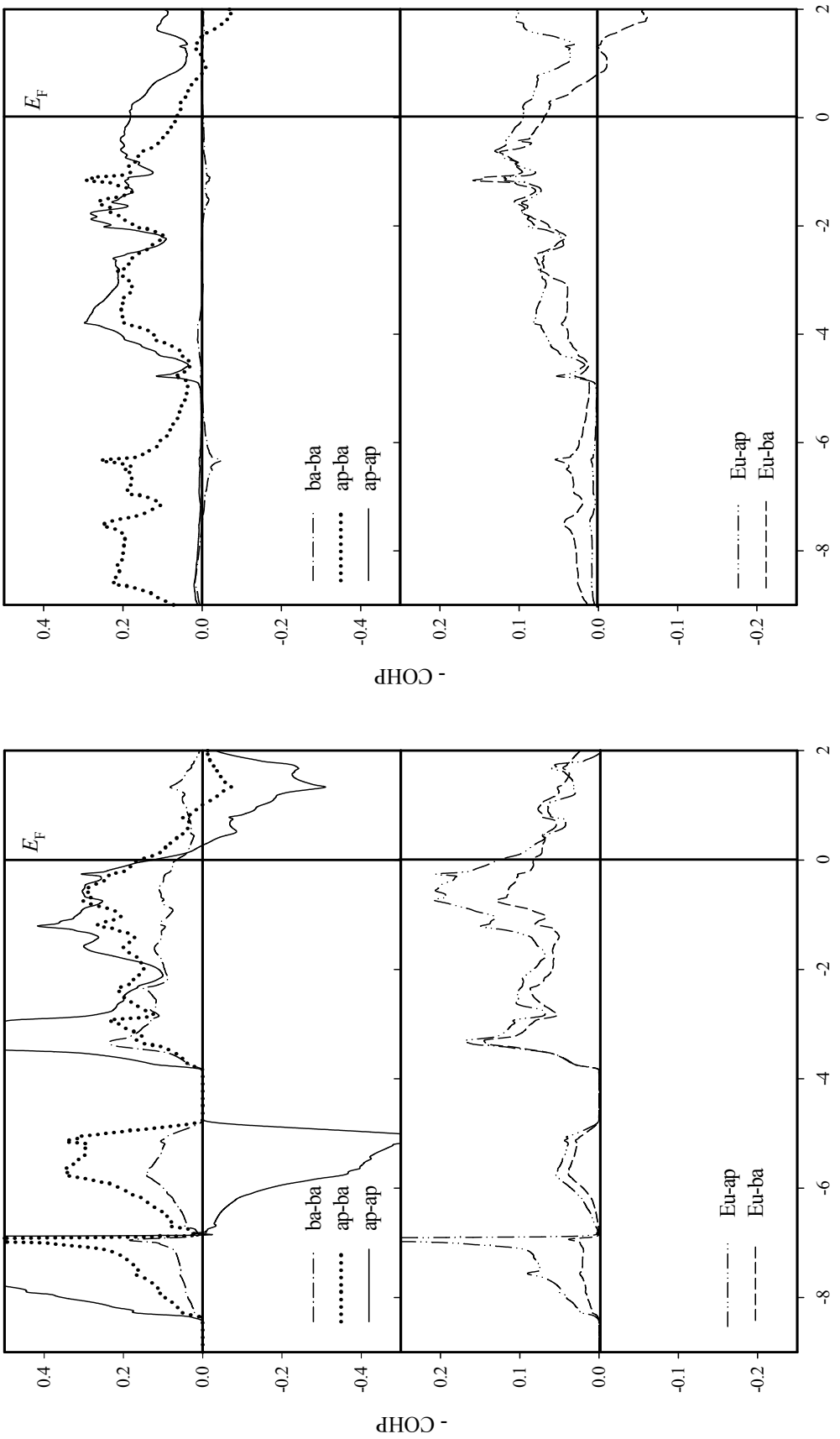

Figure 3. COHP curves of "$EuMg_2Ga_2$" (left) and "$EuGa_2Mg_2$" (right). The Fermi level is indicated by the bold line and is the energetic reference (0 eV)

A COHP analysis of the basal-basal interactions in "$EuGa_2Mg_2$", which are the shortest Ga-Ga contacts in this model, shows much smaller integrated values throughout the occupied states than those for the apical-apical (Ga-Ga) interactions in "$EuMg_2Ga_2$". These COHP curves for "$EuMg_2Ga_2$" and "$EuGa_2Mg_2$" are illustrated in Figure 3. As a final outcome of this analysis, if we sum up the various site-energy and bond-energy terms for each structural alternative, the difference approximates the total difference in calculated band energies between them. The discrepancy between the actual and estimated values arises because not all interatomic interactions are included in the bond-energy term.

The density of states (DOS) curve for the preferred coloring of $EuMg_2Ga_2$ is illustrated in Figure 4, a curve which shows significant mixing among the valence orbitals of Eu, Mg and Ga atoms throughout most of the occupied region. The DOS curve below the Fermi level (E_F) displays three distinctive segments: (1) a region between –7 and –8.5 eV, integrating as a single crystal orbital, is primarily Ga 4*s* states, with small contributions from Mg and Eu valence orbitals; (2) a region between –5 and –7 eV, also integrating as a single crystal orbital, involves a significant mixture of Ga 4*s* and Mg 3*s* orbitals with small contributions from Eu wavefunctions; and (3) a region between 0 and –4 eV, holding 8 electrons, consists of strong orbital mixing of Ga 4*p,* Mg 3*s* and 3*p* levels with Eu 5*d* states.

A distinct ca. 0.7 eV gap separates regions (2) and (3). The decomposition of the total DOS curve precludes the ionic formulation $Eu^{2+}(Mg^{2+})_2(Ga_2)^{6-}$, which would conclude a 12-electron Ga-Ga dimer. This dimer would be isoelectronic with O_2 and exhibit double-bond character. However, the observed Ga-Ga distances ca. 2.50 Å and the strong contributions from valence orbitals from both Mg and Eu atoms reinforce the concept of multi-center orbitals interactions in this polar intermetallic system [1].

In the DOS of $EuMg_2Ga_2$, the Fermi level (E_F), which corresponds to 12 valence electrons, is situated ca. 0.4 eV above a large peak and ca. 0.7 eV below a local minimum ("pseudogap"). Again, the COHP analysis (see Figure 3) shows significant bonding character above the calculated Fermi level for Eu-Mg, Eu-Ga, basal-basal (Mg-Mg), and basal-apical (Mg-Ga) interactions, but the apical-apical (Ga-Ga) contact quickly changes to antibonding states above E_F. Furthermore, the slopes of these COHP curves at the 12-electron Fermi level are quite large. Therefore, the COHP analysis of $EuMg_2Ga_2$ suggests

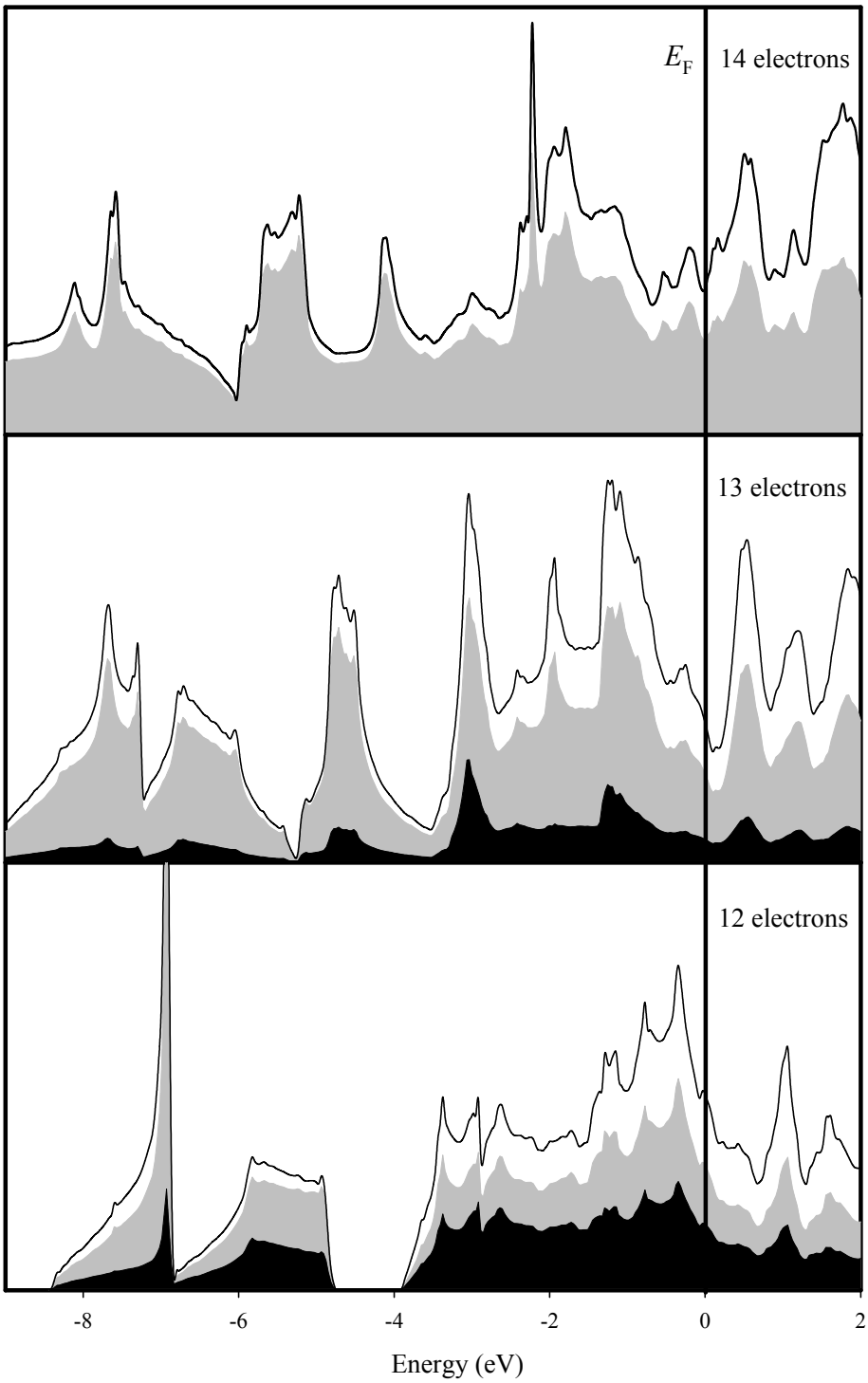

Figure 4 Density of states curves (DOS) for EuGa4, $EuMgGa_3$ and $EuMg_2Ga_2$. Total DOS (solid line), Eu partial DOS (PDOS) (white region), Ga PDOS (gray region) and Mg PDOS (black region). The Fermi level is indicated by the dashed line and is the energetic reference (0 eV).

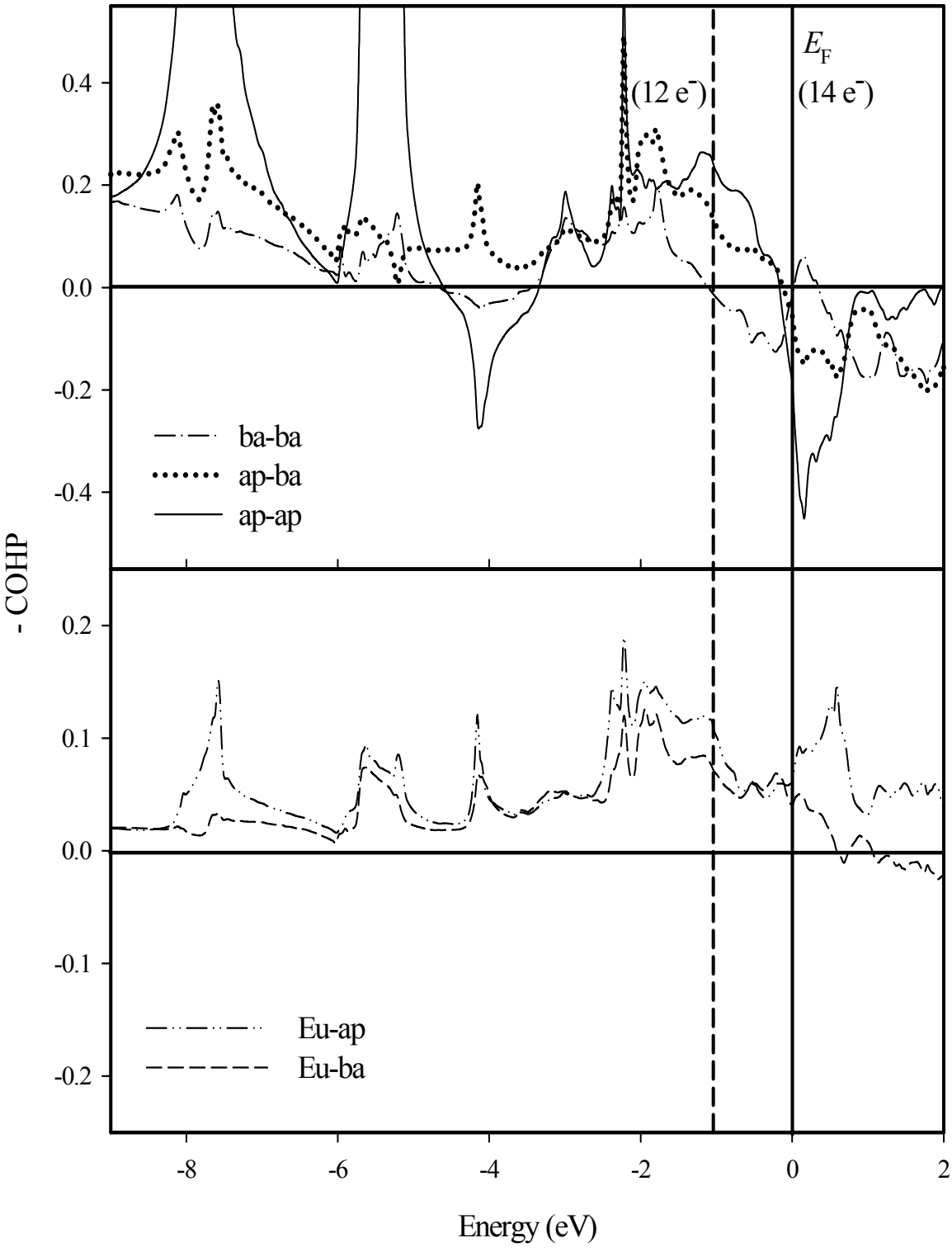

Figure 5.1. COHP curves of $EuGa_4$. The Fermi level is indicated by the bold line and is the energetic reference (0 eV). The numbers of valence electrons, which correspond to the Fermi level, are also shown

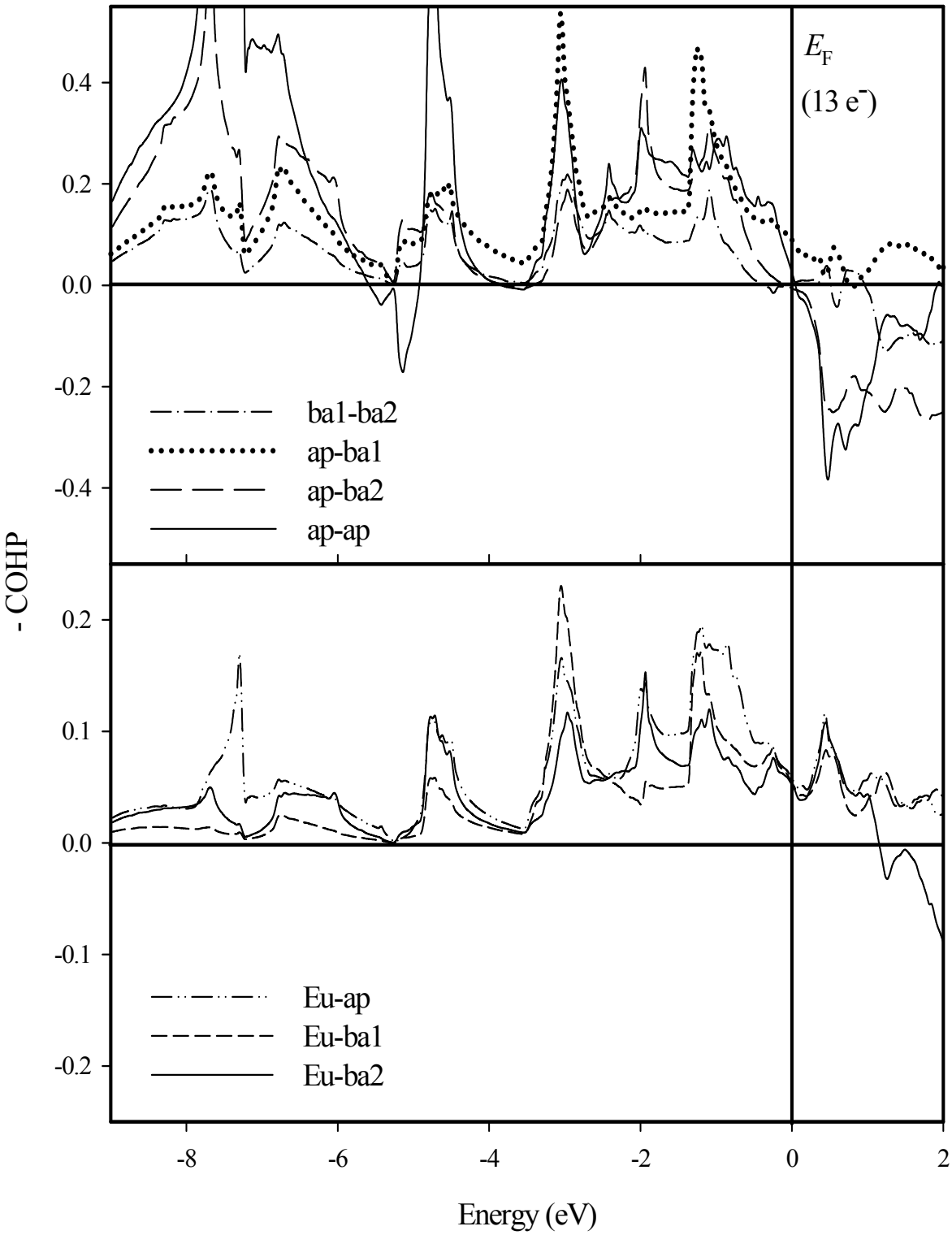

Figure 5.2 COHP curves of $EuMgGa_3$. The Fermi level is indicated by the bold line and is the energetic reference (0 eV). The numbers of valence electrons, which correspond to the Fermi level, are also shown

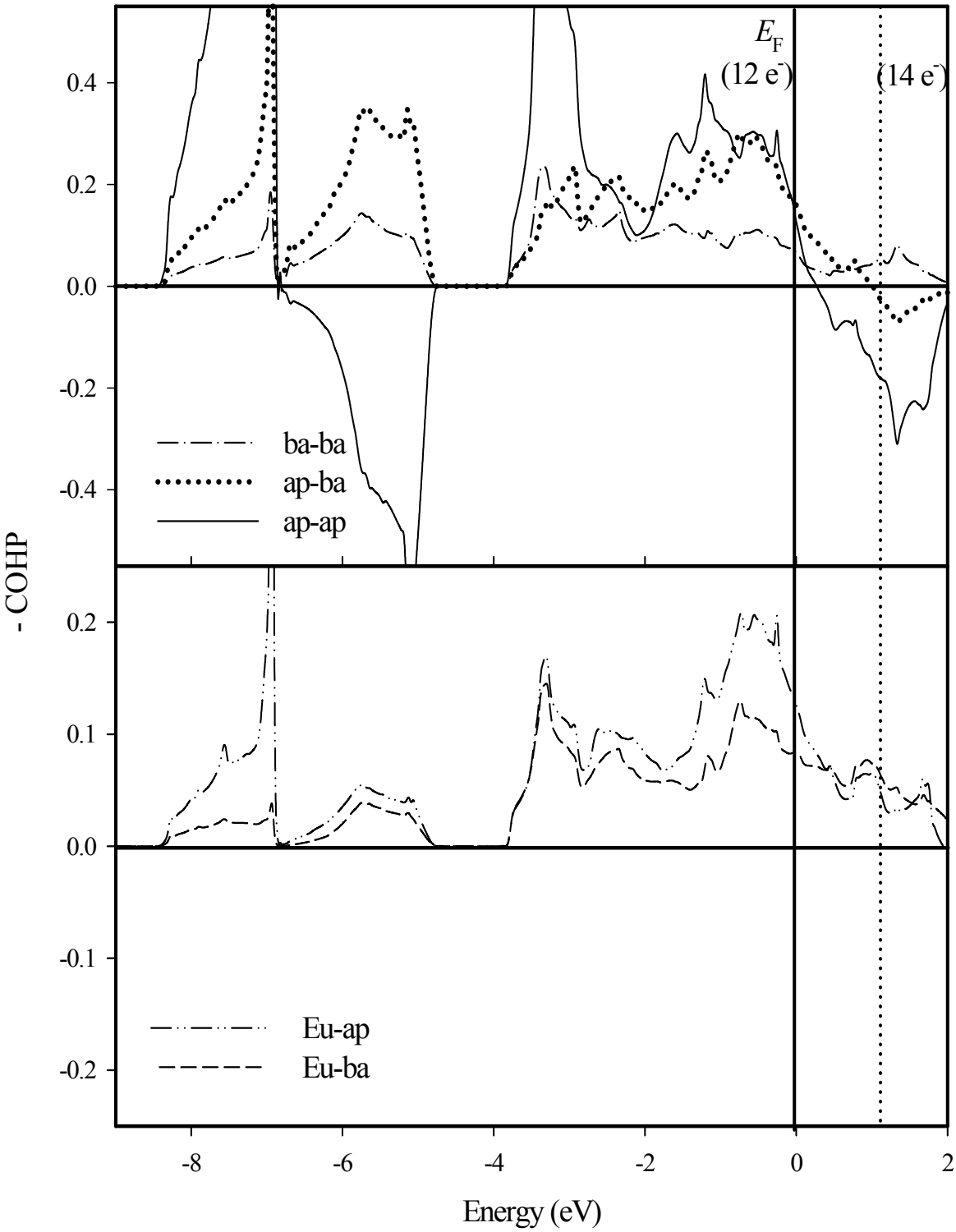

Figure 5. COHP curves of $EuMg_2Ga_2$. The Fermi level is indicated by the bold line and is the energetic reference (0 eV). The numbers of valence electrons, which correspond to the Fermi level, are also shown

that an increase of valence electron count toward the Ga-rich compositions would be possible, but that a decrease toward more Mg-rich compositions would be prohibited [43], which agrees with our experimental results.

To explore the influence of Mg content on the electronic structures of $EuMg_xGa_{4-x}$, DOS curves for $EuGa_4$ and $EuMgGa_3$ (Mg in a basal site) were also calculated and are also depicted in Figure 4. As the Mg content increases, the Ga valence *s* and *p* states show decreasing "delocalization" throughout the valence band. This effect on the DOS curves occurs through increasing heteroatomic Mg-Ga orbital interactions and simply fewer Ga atoms per formula unit. The DOS curves also indicate that a "rigid-band" approach to interpret the electronic structure of $EuMg_xGa_{4-x}$ is not valid; the COHP analysis of the various pairwise interactions further confirms this (see Figure 5.1, 5.2, 5.3). The stability of the observed $EuMg_xGa_{4-x}$ phases with respect to disproportionation occurs primarily from optimum apical-apical bonds in these $BaAl_4$-type structures. The apical-apical COHP curves for $EuMg_2Ga_2$, $EuMgGa_3$, and $EuGa_4$ also show Fermi levels located at the energy where apical-apical orbital interactions change from bonding (below E_F) to antibonding (above E_F). Thus, the optimal valence electron count depends on chemical composition. Furthermore, the DOS curves show a changing Ga character with increasing Mg content: the apical Ga atoms show more reduced character as demonstrated by the steadily increasing valence band centers for their 4*s* and 4*p* bands along the series $EuGa_4$-$EuMgGa_3$-$EuMg_2Ga_2$. The apical Ga 4*s* band centers (listed with respect to their corresponding E_F) increase from –9.52 ($EuGa_4$) to –9.31 ($EuMgGa_3$) to –9.02 eV ($EuMg_2Ga_2$); the 4*p* band centers also increase from +4.51 ($EuGa_4$) to +4.72 ($EuMgGa_3$) to +4.99 eV ($EuMg_2Ga_2$). Meanwhile, the valence band centers for Mg 3*s* and 3*p* orbitals remain essentially constant: 3*s*, –3.89 ($EuMgGa_3$) and –3.85 eV ($EuMg_2Ga_2$); 3*p*, +4.66 ($EuMgGa_3$) and +4.68 eV ($EuMg_2Ga_2$). Thus, the electronic structure does vary with chemical composition in the $EuMg_xGa_{4-x}$ series, but does control both the observed homogeneity width for stable phases as well as the site preference for Mg and Ga atoms.

7.5 Summary

Eight ternary compounds in the $EuMg_xGa_{4-x}$ series were synthesized and characterized using powder and single crystal X-ray diffraction as well as theoretical calculations to investigate the phase width and site preferences for Mg and Ga atoms. These compounds crystallize in the body-centered tetragonal $BaAl_4$-type structure with Mg atoms preferentially occupying the basal (4*d*) sites. This site preference leads to an unusual decrease then increase in the *a*-axis length in $EuMg_xGa_{4-x}$ as *x* increases, while the *c*-axis length increases. Furthermore, the site preferences between Mg and Ga atoms in the framework are influenced by both site-energy and bond-energy factors, with the more electronegative and smaller Ga atom occupying the apical sites. The electronic structures indicate that the DOS and COHP curves significantly depend on chemical composition, but provide a sound interpretation of the observed phase width and site preferences.

Acknowledgement

This work was supported by NSF DMR 02-41092 and 06-05949. The authors are grateful to Dr. Warren Straszheim for the EDS measurements at Iowa State University.

References

[1] U. Häussermann, S. Amerioun, L. Eriksson, C. -S. Lee, G. J. Miller, *J. Am. Chem. Soc*. **2002**, *124*, 4371.

[2] J. H. Westbrook, R. L. Fleischer (eds), *Intermetallic Compounds: Principle and Practice*, Wiley, New York 1995.

[3] H. Schäfer, *Ann. Rev. Mater. Sci*. **1985**, *5*, 1.

[4] R. Nesper, *Prog. Solid State Chem*. **1990**, *20*, 1.

[5] G. J. Miller, in: *Chemistry, Structure, and Bonding of Zintl Phases and Ions*, S. M. Kauzlarich (ed), VCH Publishers, New York 1996, p. 1.

[6] M. T. Klem, J. T. Vaughy, J. G. Harp, J. D. Corbett, *Inorg. Chem*. **2001**, *40*, 7020.

[7] J. S. von Fedorov, *Z. Kristallogr*. **1904**, *38*, 321.

[8] P. I. Kripyakevich, E. I. Gladyshevskii, D. I. Dzyana, *Sov. Phys. Crystallogr. (Engl. Transl.)* **1965**, *19*, 392.

[9] S. Bobev, E. D. Bauer, J. D. Thomson, J. L. Sarrao, *J. Magn Magn. Mater*. **2004**, *277*, 236.

[10] S. Cirafici, M. L. Fornasini, *J. Less-Common Met.* **1990**, *163*, 331.

[11] Yu. Grin, M. Ellner, K. Hiebl, P. Rogl, *J. Alloys Compd.* **1993**, *196*, 207.

[12] C. Zheng, R. Z. Hoffmann, *Z. Naturforsch B* **1986**, *41*, 292.

[13] J. K. Burdett, G. J. Miller, *Chem. Mater*. **1990**, *2*, 12.

[14] A. Szytula, J. Leciejewicz, *Handbook of Crystal Structures and Magnetic Properties of Rare Earth Intermetallics*, CRC Press, Boca Raton, FL 1994.

[15] A. Fedorchuk, Yu. Prots, Yu. Grin. *Z. Kristallogr. NCS* **2005**, *220*, 317.

[16] B. A. Hunter, C. J. Howard, Rietica, Australian Nuclear Science and Technology Organization, Menai, Australia 2000.

[17] XRD single crystal software, Bruker Analytical X-ray System, Madison, WI 2002.

[18] SHELXTL, version 5.1, Bruker AXS Inc., Madison, WI 1998.

[19] O. K. Anderson, *Phys. Rev. B* **1986**, *34*, 2439.

[20] O. Jepsen, A. Burkhardt, O. K. Andersen, The TB-LMTO-ASA Program, version 4.7, Max-Planck-Institut für Festkörperforschung, Stuttgart, Germany 1999.

[21] O. K. Anderson, O. Jepsen, *Phys. Rev. Lett*. **1984**, *53*, 2571.

[22] O. K. Anderson O. Jepsen, D. Glötzel, in: *Highlights of condensed matter theory*, F. Bassani, F. Fumi, M. Tosi (eds), New York, North−Holland, Lambrecht, W. R. L., 1985.

[23] O. Jepsen, O. K. Anderson, *Z. Phys. B* **1995**, *97*, 35.

[24] P. E. Blöchl, O. Jepsen, O. K. Anderson, *Phys. Rev. B* **1994**, *49*, 16223.

[25] L. Pauling, *The Nature of the Chemical Bond*, 3rd. ed., Cornell University Press, Ithaca, NY 1960.

[26] W. B. Pearson, *J. Less-Common Met*. **1985**, *L3*, 109.

[27] W. B. Pearson, *J. Solid State Che*m. **1985**, *56*, 278.

[28] B. Li, J. D. Corbett, *Inorg. Chem*. **2007**, *46*, 8812.

[29] S. P. Yatsenko, B. G. Semenov, K. A. Chuntonov, *Russ. Metall.* **1978***,* 173.

[30] D. B. Mooij, K. H. J. Buschow, *J. Less-Common Met*. **1985**, 109, 117.

[31] E-an Zen, *Am. Mineral* **1956**, 41, 523.

[32] K. H. J. Buschow; D. B. Mooij, *J. Less−Common Met*. **1984**, *97*, L5.

[33] A. M. Mills, A. Mar, *J. Am. Chem. Soc*. **2001**, *123*, 1151.

[34] X. He, R. A. Bartlett, M. M. Olmstead, K. Ruhlandt-Senge, B. E. Sturgeon, P. P. Power, *Angew. Chem. Int. Ed. Engl*., **1993**, *32*, 717

[35] F. A. Cotton, A. H. Cowley, X. Feng, *J. Am. Chem. Soc*., **1998**, *120*, 1795.

[36] J. Su, X. –W. Li, R. C. Crittendon, G. H. Robinson, *J. Am. Chem. Soc*, **1997**, *119*, 5471.

[37] J. K. Burdett, E. Canadell, *J. Am, Chem, Soc*. **1990**, *112*, 7202.

[38] J. Emsley, *The Elements*, Clarendon Press, Oxford 1998.

[39] A. Z. Ikromov, I. N. Ganiev, V. V. Kinjibalo, *Dokl. Akad. Nauk Tadzh. SSR* **1990**, *33*, 173.

[40] G. Cordier, E. Czech, H. Schäfer, P. Woll, *J. Less-Common Me*t. **1985**, *110*, 327.

[41] B. Stel'makhovych, O. Stel'makhovych, Yu. Kuz'ma, *J. Alloys Compd*. **2005**, *397*, 115.

[42] G. J. Miller, *Eur. J. Inorg. Chem.* **1998**, 523.

[43] R. Dronskowski, *Adv. Solid State Phys*. **2002**, *42*, 433.

CHAPTER 8

General Conclusion

In this dissertation, I have presented my investigations to understand the interrelationships among stoichiometry, crystal structure, and physical properties of various polar intermetallic compounds *RE*-*M*-*M*'. The observed trends in phase behavior and crystal structures along this series can be attributed to the interplay among atomic sizes, valence electron counts, and types of chemical bonding, which can be estimated by the atomic electronegativities and their differences.

Throughout the investigation of the Eu($M_{1-x}M'_x$)$_2$ series, I observed several different structure types, all of which are related to the AlB_2-type structure. For instance, in the Eu($M_{1-x}Tt_x$)$_2$ (*M* = Zn, Ga; *Tt* = Ge, Si) series, a structural variation was observed as the *Tt* content increased from the orthorhombic KHg_2-type to the hexagonal AlB_2-type, and finally to the trigonal $EuGe_2$-type for the Eu($Zn_{1-x}Ge_x$)$_2$ series or to the tetragonal $ThSi_2$-type for Eu($Ga_{1-x}Si_x$)$_2$ series, respectively. As mentioned in a recent analysis, the structural stability of 6-electron and 8-electron AB_2 phases can be understood using a structure map based on atomic size ratios and electronegativity differences. AlB_2-type structures are preferred for large size ratios (V_A/V_B) and electronegativity differences ($\chi_B - \chi_A$), whereas the KHg_2-type structure becomes preferred as the corresponding electronegativity difference becomes smaller while the size ratio remains constant. In our Eu($M_{1-x}Tt_x$)$_2$ (*M* = Zn, Ga; *Tt* = Ge, Si) series, the atomic size ratio between cationic Eu and anionic elements, such as Zn, Ga, Ge and Si, is large. In addition, an electronegativity difference becomes larger, respectively, for the Eu($Zn_{1-x}Ge_x$)$_2$ ($0 \le x \le 0.75$) series as Ge content increases and for the Eu($Ga_{1-x}Tt_x$)$_2$ (*Tt* = Si, $0 \le x \le 0.82$; *Tt* = Ge, $0 \le x \le 0.35$) series as *Tt* content increases. This implies a switch from orthorhombic KHg_2-type to the hexagonal AlB_2-type phases.

On the other hand, as the atomic size of *Tt* increases, in addition to the increasing number of valence electrons in the Eu($Ga_{1-x}Tt_x$)$_2$ (*Tt* = Ge, Sn, $x \ge 0.5$) series, the layered

hexagonal structure do not maintain its planar nets, but starts to pucker resulting in the YPtAs-type structure and more complex superstructures with expanded *c*-axis lengths. All of these structures may be described as puckered derivatives of the AlB_2-type structure.

The phase widths of the commonly observed AlB_2-type structure (see Figure 1), of course, vary in each compound series because of the different interplay between atomic sizes and valence electron counts. However, we observed that the minimum number of valence electrons for which the AlB_2-type phases remain stable with other arrangements should not be smaller than 8 throughout the whole system. Below this lower bound, the KHg_2-type structure dominated.

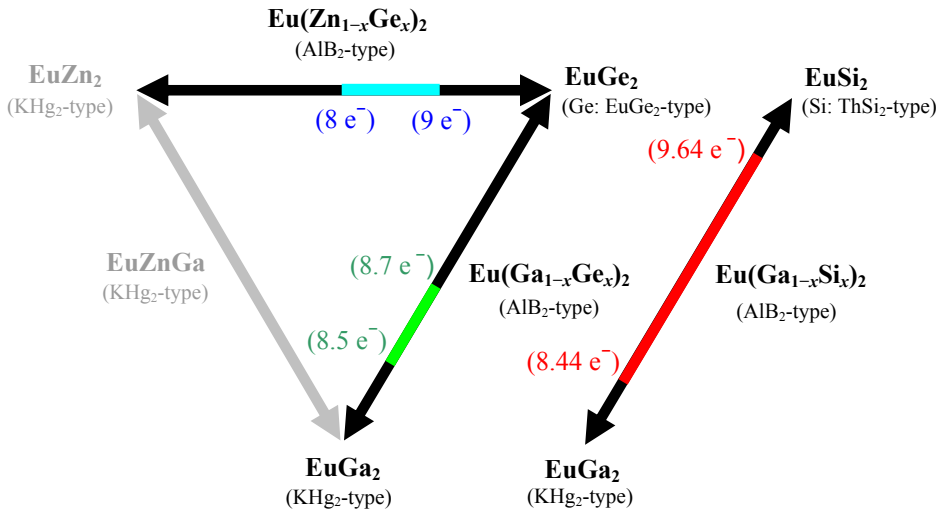

Figure 1. Phase width of the AlB_2-type structure and the corresponding number of valence electrons in various compound series.

For some compounds, all of which exhibited temperature-dependent electrical resistivities consistent with semiconducting or semimetallic character, the Zintl-Klemm electron counting rule is an attractive formalism to account for their structural and physical behavior. However, as presented in Chapter 3 for the $Eu(Zn_{1-x}Ge_x)_2$ series, this rule could account well for some compositions, but did not account for others. Therefore, theoretical electronic structure calculations are imperative, and have been conducted and analyzed to

complete these investigations, so as to understand the structural and bonding features of the entire Eu($M_{1-x}M'_x$)$_2$ series.

Theoretical electronic structure calculations using the TB-LMTO-ASA method were very powerful to understand phenomena, such as structural stability and site preferences among elements. In particular, electronic energy comparisons obtained using different structure models, which included both observed and hypothetical models, could show the preferred structure for a given composition. Moreover, DOS and COHP curves could be used to analyze specific orbital interactions and bonding character. ELF analysis was adopted to analyze the motion of electron pairs in real space, which included the direct interaction between atoms and lone pairs, and showed an unusual four-center interaction in EuGaSn. The VASP code was exploited extensively for many hypothetical as well as observed structural models. In particular, dynamic calculations, which allow relaxing a structure (cell shape, cell volume and atomic positions) were very useful to find energetically optimum structures.

During my investigation of the coloring problem of the YMg$_{1-x}$*Tr*$_{1+x}$ (*Tr* = Zn, Al, Ga, In) series, I found that the three elements presented a specific ordering to minimize *Tr*···*Tr* interactions while maximizing Y-*Tr* and Mg-*Tr* interactions. In the study about the phase width and site preferences of the EuMg$_x$Ga$_{4-x}$ series, I showed that the site preferences between Mg and Ga atoms in the framework were influenced by both site-energy and bond-energy factors as well as the electronegative and atomic size effects. In both investigations, the electronic structures indicated that the DOS and COHP curves significantly depended on chemical composition, but provided a sound interpretation of the observed phase widths and site preferences.

Appendix A: Reaction Composition and Product Identification

No.	Reaction Stoichiometry	Heating Methods	Reaction Products	Analysis
2-1-1	$SrAl_{1.4}Si_{0.6}$	arc-melting	$SrAl_{1.41}Si_{0.59}$	SXRD
8-1-1	EuAlSi	arc-melting	$EuAl_{1.12}Si_{0.88}$ + $EuAl_2$	PXRD,SXRD,EDS
10-1-1	$Sr\ Al_{0.8}\ Si_{1.2}$	arc-melting	$SrAl_{0.94}Si_{1.06}$ + $SrAl_2$	PXRD,SXRD,EDS
13-1-1	EuZnGe	furnace (1000°C, 600°C)	$EuZn_{0.66}Ge_{1.34}$ +$EuZn_2$	PXRD
13-5-2	$EuZn_{0.36}Ge_{1.64}$	furnace (1050°C, 650°C)	$EuZn_{1-x}Ge_{1+x}$+$EuGe_2$	PXRD
13-6-2	$EuZn_{0.62}Ge_{1.38}$	furnace (1050°C, 650°C)	$Eu_{0.98}Zn_{0.67}Ge_{1.33}$	SXRD,PXRD,EDS
13-6-3	$EuZn_{0.62}Ge_{1.38}$	furnace (1050°C, 650°C)	$EuZn_{0.5}Ge_{1.5}$ + ?	SXRD,PXRD,EDS
13-7-3	$EuZn_{0.66}Ge_{1.34}$	furnace (1050°C, 650°C)	$Eu_{0.99}Zn_{0.67}Ge_{1.33}$	SXRD,PXRD,EDS
13-8-3	$EuZn_{1.66}Ge_{0.34}$	furnace (1050°C, 650°C)	$EuZn_{1.05}Ge_{0.95}$ +?	SXRD,PXRD,EDS
13-9-1	EuZnGe	furnace (1050°C, 650°C)	$EuZn_{0.89}Ge_{1.11}$ + ?	PXRD,EDS
13-10-1	$EuZn_{0.3}Ge_{1.7}$	furnace (1050°C, 650°C)	EuZnGe + $EuGe_2$ + ?	SXRD,PXRD,EDS
13-11-1	$EuZn_{0.17}Ge_{1.83}$	furnace (1050°C, 650°C)	EuZnGe + $EuGe_2$ + ?	PXRD,EDS
13-12-1	$EuZn_{0.5}Ge_{1.5}$	furnace (1050°C, 650°C)	$EuZn_{1-x}Ge_{1+x}$ + ?	PXRD
13-13-1	$EuZn_{0.55}Ge_{1.45}$	furnace (1050°C, 650°C)	$EuZn_{0.5}Ge_{1.5}$ + ?	SXRD,PXRD
13-14-1	$EuZn_{0.75}Ge_{1.25}$	furnace (1050°C, 650°C)	$Eu_{1.00}Zn_{0.66}Ge_{1.34}$ + ?	SXRD,PXRD,EDS
13-15-1	$EuZn_{0.85}Ge_{1.15}$	furnace (1050°C, 650°C)	$Eu_{1.00}Zn_{0.97}Ge_{1.02}$ +?	SXRD,PXRD,EDS
13-16-1	$EuZn_{1.2}Ge_{0.8}$	furnace (1050°C, 650°C)	EuZnGe + $EuZn_2$	SXRD,PXRD,EDS
13-17-1	$EuZn_{1.4}Ge_{0.6}$	furnace (1050°C, 650°C)	$EuZn_{0.99}Ge_{1.01}$ + $EuZn_2$	SXRD,PXRD,EDS
13-18-1	$EuZn_{0.8}Ge_{1.2}$	furnace (1050°C, 650°C)	$EuZn_{0.81}Ge_{1.17}$	SXRD,PXRD,EDS
13-19-1	$EuZn_{0.4}Ge_{1.6}$	furnace (1050°C, 650°C)	$EuZn_{0.47}Ge_{1.53}$ + $EuGe_2$	SXRD,PXRD,EDS
13-20-1	$EuZn_{0.9}Ge_{1.1}$	furnace (1050°C, 650°C)	$EuZn_{0.9}Ge_{1.1}$ + ?	SXRD,PXRD,EDS
13-21-1	$EuZn_{1.1}Ge_{0.9}$	Induction-furnace (1000°C,600°C)	EuZnGe +$EuZn_2$ + ?	SXRD,PXRD,EDS
13-23-1	$EuZn_{0.44}Ge_{1.56}$	Induction-furnace (1000°C,600°C)	$EuZn_{0.48}Ge_{1.52}$ + ?	SXRD,PXRD,EDS

No.	Reaction Stoichiometry	Heating Methods	Reaction Products	Analysis
14-3-1	EuGaGe	arc-melting	EuGaGe	SXRD,PXRD
14-3-1A	EuGaGe	arc-melting + annealing(650°C)	EuGaGe	SXRD,PXRD,EDS
14-4-1	EuGaGe	furnace (1050°C, 650°C)	EuGaGe	SXRD,PXRD,EDS
14-Z4-1	EuGaGe	induction-melting (1050°C, 650°C)	EuGaGe	SXRD,PXRD,EDS
14-Z5-1	$EuGa_{0.8}Ge_{1.2}$	induction-melting (1050°C, 650°C)	$EuGa_{0.8}Ge_{1.2}$	SXRD,PXRD,EDS
14-Z9-1	$EuGa_{0.89}Ge_{1.11}$	induction-melting (1050°C, 650°C)	$EuGa_{0.89}Ge_{1.11}$	SXRD,PXRD,EDS
14-6-1	$EuGa_{1.5}Ge_{0.5}$	induction-melting (1050°C, 650°C)	$EuGa_{1.5}Ge_{0.5}$	SXRD,PXRD,EDS
14-7-1	$EuGa_{1.3}Ge_{0.7}$	induction-melting (1050°C, 650°C)	$EuGa_{1.3}Ge_{0.7}$	SXRD,PXRD,EDS
15-2-2	SrGaGe	arc-melting	$SrGa_{1-x}Ge_{1+x}$	SXRD,PXRD
15-2-2A	SrGaGe	arc-melting + annealing (650°C)	$SrGa_{1-x}Ge_{1+x}$	SXRD,PXRD
17-2-1	SrZnGe	furnace (1050°C, 650°C)	$SrZn_2Ge_2$ + ?	PXRD
18-1-1	EuFeGe	arc-melting	EuGe	SXRD,PXRD
19-1-1	$PdZn_4Ga$	furnace (700°C)	$Pd_{2+x}Zn_{11-x}$	SXRD,PXRD,EDS
20-1-1	EuYbGaGe	arc-melting	YGe + $Eu_{1-x}Yb_{1+x}GaGe$	SXRD,PXRD
20-1-1A	EuYbGaGe	arc-melting + annealing (650°C)	$Eu_{0.44}Yb_{0.56}GaGe$	SXRD,PXRD
20-2-1	EuYbGaGe	furncace (1050°C, 650°C)	$Eu_{1-x}Yb_{1+x}GaGe$ + ?	SXRD,PXRD
21-1-1	EuGaSn	arc-melting	EuGaSn	SXRD,PXRD,EDS
21-1-1A	EuGaSn	arc-melting + annealing (600°C)	EuGaSn	PXRD
21-1-D	EuGaSn	Induction-furnace (950°C,500°C)	EuGaSn + Eu_2O_3	PXRD
22-1-1	MgGaGe	furnace (1050°C, 600°C)	Mg_2Ge + ?	PXRD
24-1-1	EuGaSi	arc	EuGaSi	SXRD,PXRD,EDS
24-1-4	EuGaSi	furnace (850°C, 450°C)	EuGaSi + ?	SXRD,PXRD,EDS
24-1-D	EuGaSi	Induction-furnace (1500°C,650°C)	EuGaSi + ?	SXRD,PXRD,EDS
24-2-1	$EuGa_{1.33}Si_{0.66}$	arc-melting	$EuGa_{1.28}Si_{0.72}$	SXRD,PXRD,EDS

No.	Reaction Stoichiometry	Heating Methods	Reaction Products	Analysis
24-3-1	$EuGa_{1.66}Si_{0.33}$	arc-melting	$EuGa_{1+x}Si_{1-x} + EuGa_2$	PXRD
24-3-1A	$EuGa_{1.66}Si_{0.33}$	arc-melting +annealing (600°C)	$EuGa_{1+x}Si_{1-x} + EuGa_2$	PXRD
24-4-1	$EuGa_{0.66}Si_{1.33}$	arc-melting	$EuGa_{0.64}Si_{1.36}$	SXRD,PXRD,EDS
24-5-1	$EuGa_{0.33}Si_{1.66}$	arc-melting	$EuGa_{1+x}Si_{1-x} + EuGa_2$	PXRD
24-6-1	$EuGa_{1.50}Si_{0.50}$	arc-melting	$EuGa_{1.42}Si_{0.58}$	SXRD,PXRD,EDS
24-7-1	$EuGa_{1.33}Si_{0.66}$	arc-melting	$EuGa_{1.35}Si_{0.65}$	SXRD,PXRD,EDS
25-1-1	TbGaGe	arc-melting	$TbGa_{1+x}Ge_{1-x}$ + ?	PXRD
26-1-1	DyGaGe	arc-melting	$DyGa_{1+x}Ge_{1-x}$ + ?	PXRD
26-1-1A	DyGaGe	arc-melting +annealing (600°C)	$DyGa_{1+x}Ge_{1-x}$ + ?	PXRD
27-1-1	HoGaGe	arc-melting	$HoGa_{1+x}Ge_{1-x}$ + ?	PXRD
29-1-1	$EuMgGa_2$	furance (1050°C, 600°C)	$EuMg_{0.2}Ga_{1.8} + EuMg_{1.78}Ga_{2.22}$	SXRD,PXRD,EDS
29-2-1	$EuMg_2Ga_2$	furnace (900°C, 600°C)	$EuMg_{2+x}Ga_{2-x} + EuGa_2$	SXRD,PXRD,EDS
29-3-1	$EuMg_{1.7}Ga_{2.3}$	furnace (900°C, 600°C)	$EuMg_{1.5}Ga_{2.5}$ + ?	PXRD,EDS
29-4-2	$EuMg_{1.9}Ga_{2.1}$	furnace (900°C, 500°C)	$EuMg_{1.84}Ga_{2.16} + EuGa_2 + GaMg_2$	SXRD,PXRD,EDS
29-5-1	$EuMg_{2.2}Ga_{1.8}$	furnace (900°C, 500°C)	$EuMg_{1.94}Ga_{2.06} + EuGa_2$	SXRD,PXRD,EDS
29-6-1	$EuMg_{0.2}Ga_{3.8}$	furnace (900°C, 500°C)	$EuMg_{0.21}Ga_{3.79}$	SXRD,PXRD,EDS
29-7-1	$EuMgGa_3$	furnace (900°C, 500°C)	$EuMg_{0.91}Ga_{3.09}$ + ?	SXRD,PXRD,EDS
29-8-1	$EuMg_{1.2}Ga_{2.8}$	furnace (900°C, 500°C)	$EuMg_{1.22}Ga_{2.78}$ + ?	SXRD,PXRD,EDS
30-1-1	TmGaGe	arc-melting	$Tm_3Ga_2Ge_3$ + ?	S/PXRD
32-1-1	$EuGa_2$	arc-melting	$EuGa_2$	SXRD,PXRD
33-1-1	$EuSi_2$	arc-melting	$EuSi_2$	SXRD,PXRD
34-1-1	YMgZn	furnace (1150°C, 700°C)	$YMg_{0.95}Zn_{1.05}$	SXRD,PXRD,EDS
34-1-2	YMgZn	Induction-Furnace (1100°C)	$YMgZn + YMg_2$	PXRD
34-1-2A	YMgZn	Induction-Furnace (1050°C) + annealing (450°C)	$YMgZn + YMg_2$	PXRD

No.	Reaction Stoichiometry	Heating Methods	Reaction Products	Analysis
34-1-2B	YMgZn	Induction-Furnace (1050°C) + annealing (550°C)	$YMgZn + YMg_2$	PXRD
34-2-1	$YMg_{1.2}Zn_{0.8}$	Induction-Furnace (1050°C) + annealing (450°C)	$YMg_{1.1}Zn_{0.9} + YMg_2$	SXRD,PXRD,EDS
34-3-1	$YMg_{0.8}Zn_{1.2}$	Induction-Furnace (1050°C) + annealing (450°C)	$YMg_{0.8}Zn_{1.2}$	PXRD
34-4-1	$Y\ Mg_{0.6}Zn_{1.4}$	furnace (1050°C, 450°C)	$YMg_{0.83}Zn_{1.17} + ?$	SXRD,PXRD,EDS
34-5-1	$Y\ Mg_{1.4}Zn_{0.6}$	furnace (1050°C, 450°C)	YMgGa + ?	SXRD,PXRD,EDS
35-1-1	Y_5Mg_{24}	furnace (1000°C, 580°C)	$Y_{3.73}Mg_{25.27} + YMg$	SXRD,PXRD,EDS
37-1-1	$Y_5Mg_{36.65}$	furnace (1000°C, 580°C) + water-quenching	$Y_{3.92}Mg_{25.08} + Mg$	SXRD,PXRD,EDS
37-2-1	$Y_{3.6}Mg_{25.4}$	furnace (1000°C, 580°C) + water-quenching	$Y_{3.83}Mg_{25.17} + Mg$	SXRD,PXRD,EDS
37-3-1	$Y_{3.7}Mg_{25.3}$	furnace (1000°C, 580°C) + water-quenching	$Y_{3.8}Mg_{25.2\ +\ Mg} + Mg$	SXRD,PXRD,EDS
37-4-1	$Y_{3.9}Mg_{25.1}$	furnace (1000°C, 580°C) + water-quenching	$Y_{5-x}Mg_{25+x}$	PXRD
34-5-1	$Y_{4.2}Mg_{24.8}$	furnace (1000°C, 580°C) + water-quenching	$Y_{5-x}Mg_{25+x} + YMg$	PXRD
38-1-1	$Y_5Mg_{23}Ga$	furnace (1000°C, 580°C) + water-quenching	$Y_{0.715}\ Mg_{2.285} + Y_{5-x}Mg_{24+x} + YMgGa$	SXRD,PXRD,EDS
38-2-2	$Y_5Mg_{36.5}Ga$	furnace (1000°C, 580°C) + water-quenching	$Y_{3.71}\ Mg_{25.29} + YMgGa$	SXRD,PXRD,EDS
39-1-1	$Y_5Mg_{22}Ga_2$	furnace (1000°C, 580°C) + water-quenching	$Y_{3.85}\ Mg_{25.15} + YMgGa$	SXRD,PXRD,EDS
39-1-2	$Y_5Mg_{22}Ga_2$	furnace (1000°C, 580°C) + water-quenching	$Y_{5-x}Mg_{25+x} + YMgGa$	SXRD,PXRD,EDS
39-2-2	$Y_5Mg_{35.5}Ga_2$	furnace (1000°C, 580°C) + water-quenching	$Y_{5-x}Mg_{25+x} + YMgGa + Y_{0.13}Mg_{1.06}Ga_{5.94}$	SXRD,PXRD,EDS
40-1-1	$EuZn_2$	Induction-Furnace (880°C)	$EuZn_2$	SXRD,PXRD
41-1-1	$EuGe_2$	Induction-Furnace (1050°C) + annealing (670°C)	$EuGe_2$	PXRD
42-1-1	EuGaPb	furnace (850°C)	$Eu_3Ga_8 + Eu_5Pb_8 + EuPb_3$	SXRD,PXRD
42-1-2	EuGaPb	furnace (850°C) + water-quenching	Eu_4Pb_5	PXRD
43-1-1	NaGaSi	furnace (880°C, 520°C)	product rapidly decomposed	
44-1-2	$Y_5Mg_{35.2}In_2$	furnace (950°C, 580°C) + water-quenching	$YMg_{1.04}In_{0.96} + Y_{3.56}Mg_{25.44}$	SXRD.PXRD,EDS
45-1-1	$Y_5Mg_{36.5}Ge$	furnace (1050°C, 580°C)	$Y_{5-x}Mg_{24+x} + Y_5Ge_3$	SXRD,PXRD,EDS
45-1-2	$Y_5Mg_{36.5}Ge$	furnace (1050°C, 580°C) + water-quenching	$Y_{5-x}Mg_{24+x}\ + ?$	PXRD

No.	Reaction Stoichiometry	Heating Methods	Reaction Products	Analysis
46-1-1	$Y_5Mg_{35.5}Cu_2$	furnace (1050°C, 580°C)	$Y_{5-x}Mg_{24+x}$ + ?	PXRD
46-1-2	$Y_5Mg_{35.5}Cu_2$	furnace (1050°C, 730°C, 580°C)	$Y_{3.86}Mg_{25.44}$	PXRD
47-1-1	$Y_5Mg_{35.5}Zn_2$	furnace (880°C, 580°C)	$Y_{5-x}Mg_{24+x}$ + ?	PXRD
47-1-1B	$Y_5Mg_{35.5}Zn_2$	furnace (880°C, 580°C) + annealing (370°C)	$Y_{5-x}Mg_{24+x}$ + ?	PXRD
47-1-2	$Y_5Mg_{35.5}Zn_2$	furnace (900°C, 580°C)	$Y_{3.97}Mg_{25.03}$ + Y_2MgZn_2	SXRD,PXRD,EDS
47-2-1	$Y_3Mg_{24}Zn_2$	furnace (900°C, 580°C)	$Y_{5-x}Mg_{24+x}$ + ?	SXRD,PXRD,EDS
48-1-1	$Y_5Mg_{22}Fe_2$	furnace (1090°C, 730°C, 500°C)	$Y_{4.46}Mg_{24.54}$ + ?	SXRD,PXRD,EDS
49-1-1	$Y_5Mg_{22}Co_2$	furnace (1090°C, 730°C, 500°C)	$Y_{5-x}Mg_{24+x}$ + YCo_2 + YMg_3	SXRD,EDS
50-1-2	YMgIn	furnace (1100°C, 450°C)	YMgIn	SXRD
50-1-3	YMgIn	furnace (1100°C, 450°C)	YMgIn	SXRD,PXRD
51-1-1	YMgAl	furnace (1100°C, 450°C)	YMgAl	SXRD,PXRD,EDS
51-1-2	YMgAl	furnace (1100°C, 450°C)	YMgAl	PXRD,H-absorption
52-1-2	$Y_3Ti_2Mg_{24}$	furnace (1080°C, 580°C)	$Y_{3.86}Mg_{25.14}$ + ?	SXRD,PXRD,EDS
53-1-1	$Sc_{4.5}Mg_{24.5}$	furnace (1080°C, 600°C)	too ductile to conduct analysis	
54-1-1	ScMgAl	furnace (1080°C, 450°C)	ScAl + ?	PXRD
55-1-2	$Y_3Gd_2Mg_{24}$	furnace (1080°C, 580°C)	$Y_3Gd_{1.9}Mg_{33.5}$ + YMg_2	PXRD,EDS
56-1-1	$Y_3Ce_2Mg_{24}$	furnace (1080°C, 580°C)	$Y_3Ce_{1.9}Mg_{21.7}$ + ?	PXRD,EDS,SXRD
57-1-1	CeZnGe	furnace (1080°C, 550°C)	$Ce(Zn_xGe_{1-x})2$ + ?	PXRD,SXRD

Appendix B: Structural Information for VASP Calculation

Directory	Composition	Structure-type	Space group	Lattice para.	Atomic Coord.	kpoints	Relaxation
/EuZn2/11_2/	$EuZn_2$	AlB_2, hex	P6/mmm	a = 4.3262 c = 4.2651	Eu 0 0 0 Zn 1/3 2/3 1/2	Gamma (16 16 16)	shape, position
/EuZn2/11_3/	$EuZn_2$	$EuGe_2$	P-3m1	a = 4.3262 c = 4.2651	Eu 0 0 0 Zn 1/3 2/3 0.4	Gamma (16 16 16)	shape, position
/EuZn2/11_4/	$EuZn_2$	AlB_2, ortho	Imma	a = 4.3262 b = 7.650 c = 7.655	Eu 0 1/4 0.51 Zn 0 0.01 0.165	MonkHost (12 12 12)	shape, position
/EuZn2/11_5/	$EuZn_2$	AlB_2, ortho	Imma	a = 4.3262 b = 7.650 c = 7.655	Eu 0 1/4 0.53 Zn 0 0.03 0.165	MonkHost (16 16 16)	shape, position
/EuZn2/11_6/	$EuZn_2$	KHg_2	Imma	a = 4.3262 b = 7.650 c = 7.655	Eu 0 1/4 0.552 Zn 0 0.06 0.165	MonkHost (16 16 16)	shape, position
/EuZn2/41_2/	$EuZn_2$	$CaIn_2$	Pmm2	a = 4.3262 b = 7.650 c = 7.655	Eu1 0 0 0 Eu2 1/2 0 1/2 Eu3 1/2 1/2 1/2 Eu4 0 1/2 0 Zn1 1/2 0.2 0.165 Zn2 0 0.3 0.335 Zn3 0 0.2 0.665 Zn4 1/2 0.3 0.835	MonkHost (16 16 16)	shape, position
/EuZn2/31_1/	$EuZn_2$	KHg_2	Imma	a = 4.3262 b = 7.650 c = 7.655	Eu 0 1/4 0.552 Zn 0 0.06 0.165	MonkHost (16 16 16)	volume (a = 7.40-7.70)
/EuGa2/2/	$EuGa_2$	AlB_2, hex	P6/mmm	a = 4.345 c = 4.520	Eu 0 0 0 Ga 1/3 2/3 1/2	Gamma (16 16 16)	volume (a = 4.330-4.400)
/EuGa2/1/	$EuGa_2$	KHg_2	Imma	a = 4.6459 b = 7.6255 c = 7.6379	Eu 0 0 0 Ga 0 0.434 0.661	Gamma (16 16 16)	volume (a = 4.635-5.000)

Directory	Composition	Structure-type	Space group	Lattice para.	Atomic Coord.	Kpoints	Relaxation
/EuGe2/	$EuGe_2$	$EuGe_2$	P-3m1	a = 4.102 c = 4.995	Eu 0 0 0 Ga 1/3 2/3 0.405	Gamma (16 16 16)	shape, position, volume (test: a = 4.072-4.132; best a = 4.122)
/EuZnGe/GeRich/P121/	$Eu_{16}Zn_8Ge_{24}$	out-of-phase puckering	P121	a = 8.7262 b = 15.1142 c = 8.6028 β = 90	Eu1 0 0 0 Eu2 1/2 0 0 Eu3 1/4 1/4 0 Eu4 0 1/2 0 Eu5 1/2 1/2 0 Eu6 0 0 1/2 Eu7 1/2 0 1/2 Eu8 1/4 1/4 1/2 Eu9 0 1/2 1/2 Eu10 1/2 1/2 1/2 Eu11 3/4 1/2 0 Eu12 3/41/4 1/2 Ge1 0 1/6 0.3 Ge2 1/4 1/12 0.2 Ge3 1/2 1/6 0.3 Ge4 0 1/3 0.2 Ge5 1/4 0.4167 0.3 Ge6 1/2 1/3 0.2 Ge7 0 2/3 0.3 Ge8 1/2 2/3 0.3 Ge9 3/4 0.5833 0.2 Ge10 0 5/6 0.2 Ge11 1/2 5/6 0.2 Ge12 3/4 0.9167 0.3 Zn1 3/4 1/12 0.2 Zn2 3/4 0.4167 0.3 Zn3 1/4 0.5833 0.2 Zn4 1/4 0.9167 0.3	Monk Host (4 4 4)	

Directory	Composition	Structure-type	Space group	Lattice para.	Atomic Coord.	kpoints	Relaxation
/EuZnGe/GeRich/P121_2/	$Eu_{16}Zn_8Ge_{24}$	in-phase puckering	P121	a = 15.1142 b = 8.7262 c = 8.6028 β = 90	Eu1 0 0 0 Eu2 1/2 0 0 Eu3 1/4 1/4 0 Eu4 0 1/2 0 Eu5 1/2 1/2 0 Eu6 0 0 1/2 Eu7 1/2 0 1/2 Eu8 1/4 1/4 1/2 Eu9 0 1/2 1/2 Eu10 1/2 1/2 1/2 Eu11 3/4 1/2 0 Eu12 3/41/4 1/2 Ge1 0 1/6 0.3 Ge2 1/4 1/12 0.2 Ge3 1/2 1/6 0.3 Ge4 0 1/3 0.2 Ge5 1/4 0.4167 0.3 Ge6 1/2 1/3 0.2 Ge7 0 2/3 0.3 Ge8 1/2 2/3 0.3 Ge9 3/4 0.5833 0.2 Ge10 0 5/6 0.2 Ge11 1/2 5/6 0.2 Ge12 3/4 0.9167 0.3 Zn1 3/4 1/12 0.2 Zn2 3/4 0.4167 0.3 Zn3 1/4 0.5833 0.2 Zn4 1/4 0.9167 0.3	Monk Host (4 4 4)	
/EuZnGe/P222/planar/	$Eu_{16}Zn_8Ge_{24}$	planar layer	P222	a = 8.7262 b = 15.1142 c = 8.6028	Eu1 0 0 0 Eu2 1/2 0 0 Eu3 1/4 1/4 0 Eu4 0 1/2 0	Monk Host (4 4 4)	

Directory	Composition	Structure-type	Space group	Lattice para.	Atomic Coord.	kpoints	Relaxation
					Eu5 1/2 1/2 0 Eu6 0 0 1/2 Eu7 1/2 0 1/2 Eu8 1/4 1/4 1/2 Eu9 0 1/2 1/2 Eu10 1/2 1/2 1/2 Ge1 0 0.16667 0.25 Ge2 1/4 1/12 0.25 Ge3 1/2 1/6 0.25 Ge4 0 1/3 0.25 Ge5 1/4 0.4167 0.25 Ge6 1/2 1/3 0.25 Zn1 3/4 1/12 0.25 Zn2 3/4 0.4167 0.25		
/EuZnGe/P222/puckered/LREAL/	$Eu_{16}Zn_8Ge_{24}$	puckered layer	P222	a = 8.7262 b = 15.1142 c = 8.6028	Eu1 0 0 0 Eu2 1/2 0 0 Eu3 1/4 1/4 0 Eu4 0 1/2 0 Eu5 1/2 1/2 0 Eu6 0 0 1/2 Eu7 1/2 0 1/2 Eu8 1/4 1/4 1/2 Eu9 0 1/2 1/2 Eu10 1/2 1/2 1/2 Ge1 0 0.16667 0.3 Ge2 1/4 1/12 0.2 Ge3 1/2 1/6 0.3 Ge4 0 1/3 0.2 Ge5 1/4 0.4167 0.3 Ge6 1/2 1/3 0.2 Zn1 3/4 1/12 0.2667 Zn2 3/4 0.4167 0.2333	Monk Host (4 4 4)	shape, position

Directory	Composition	Structure-type	Space group	Lattice para.	Atomic Coord.	Kpoints	Relaxation
/EuZnGe/1/	EuZnGe		P6(3)/mmc	a = 4.3631 c = 8.6028	Eu 0 0 0 Zn 1/3 2/3 0.25 Ge 1/3 2/3 0.75	Gamma (16 16 16)	volume (test: a = 4.300-4.400; best: a = 4.342)
/EuZnGe/2/vol/	$Eu(Zn_{0.45}Ge_{0.55})_2$		P6(3)/mmc	a = 4.3116 c = 8.836	Eu 0 0 0 Zn 1/3 2/3 0.25 Ge 1/3 2/3 0.75	Gamma (16 16 16)	volume (test: a = 4.300-4.330; best: a = 4.304)
/EuZnGe/3/	$Eu(Zn_{0.33}Ge_{0.67})_2$		P6(3)/mmc	a = 4.2554 c = 9.0308	Eu 0 0 0 Zn 1/3 2/3 0.25 Ge 1/3 2/3 0.75	Gamma (16 16 16)	volume (test: a = 4.220-4.280; best: a = 4.27)
/EuZnGe/4/	$Eu(Zn_{0.25}Ge_{0.75})_2$		P6(3)/mmc	a = 4.2358 c = 9.1518	Eu 0 0 0 Zn 1/3 2/3 0.25 Ge 1/3 2/3 0.75	Gamma (16 16 16)	volume (test: a = 4.190-4.256; best: a = 4.252)
/EuZnGe/Ge2_1/	$Eu_3Zn_2Ge_4$		P3m1	a = 4.2358 c = 14.1468	Eu1 0 0 0 Eu2 0 0 0.3235 Eu3 0 0 0.6765 Zn1 1/3 2/3 1/6 Zn2 2/3 1/3 5/6 Ge1 2/3 1/3 1/6 Ge2 1/3 2/3 0.4665 Ge3 2/3 1/3 0.5335 Ge4 1/3 2/3 5/6	Gamma (6 6 6)	shape, position, volume (test: a = 4.200-4.236; best: a = 4.234)
/EuZnGe/Ge2_12/	$Eu_3Zn_2Ge_4$		P-3m1	a = 4.2358 c = 14.1468	Eu1 0 0 0 Eu2 0 0 0.3250 Zn1 1/2 2/3 0.1617 Zn2 2/3 1/3 0.1617 Ge2 1/3 2/3 0.4665	Gamma (12 12 12)	shape, position
/EuZnGe/Ge2_2/	$Eu_3Zn_2Ge_4$		P3m1	a = 4.2358 c = 13.7277	Eu1 0 0 0 Eu2 0 0 1/3 Eu3 0 0 2/3 Zn1 1/3 2/3 1/6 Zn2 2/3 1/3 5/6	Gamma (12 12 12)	shape, position

					Ge1 2/3 1/3 1/6 Ge2 1/3 2/3 0.4683 Ge3 2/3 1/3 0.53167 Ge4 1/3 2/3 5/6		
Directory	**Composition**	**Structure-type**	**Space group**	**Lattice para.**	**Atomic Coord.**	**kpoints**	**Relaxation**
/EuZnGe/Ge2_3/	Eu_2ZnGe_3		P-6m2	a = 4.2358 c = 19.1418	Eu1 0 0 0.1195 Eu2 0 0 0.3805 Zn1 1/3 2/3 0 Zn2 2/3 1/3 1/2 Ge1 2/3 1/3 0 Ge2 1/3 2/3 0.2263 Ge3 2/3 1/3 0.2738 Ge4 1/3 2/3 1/2	Gamma (12 12 12)	shape, position
/EuZnGe/Ge2_4/	Eu_2ZnGe_5		P-6m2	a = 4.2358 c = 29.1318	Eu1 0 0 0.0785 Eu2 0 0 1/4 Eu3 0 0 0.4215 Zn1 2/3 1/3 0 Zn2 1/3 2/3 1/2 Ge1 1/3 2/3 0 Ge2 1/3 2/3 0.1801 Ge3 2/3 1/3 0.1485 Ge4 1/3 2/3 0.3515 Ge5 2/3 1/3 0.3199 Ge6 2/3 1/3 1/2	Gamma (10 10 10)	shape, position
/EuGa4/1/	$EuGa_4$		I4/mmm	a = 4.42 c = 10.72	Eu 0 0 0 Ga1 0 1/2 1/4 Ga2 0 0 0.38	Gamma (16 16 16)	shape, position, volume (test: a = 4.380-4.445; best: a = 4.435)
/EuGa4/2/vol/	$EuGa_4$		I4/mmm	a = 4.407 c = 10.635	Eu 0 0 0 Ga1 0 1/2 1/4 Ga2 0 0 0.3833	Gamma (16 16 16)	shape, position, volume (test: a = 4.430-4.445; best: a = 4.436)
/EuGa4/	$EuGa_4$		I4/mmm	a = 4.497	Eu 0 0 0	Gamma	

				c = 11.733	Ga1 0 1/2 1/4 Ga2 0 0 0.3439	(16 16 16)	
/EuGaSi/EGSi1S/	EuGaSi		P-6m2	*a* = 4.1687	Eu 0 0 0	Gamma	shape, position,
Directory	**Composition**	**Structure-type**	**Space group**	**Lattice para.**	**Atomic Coord.**	**kpoints**	**Relaxation**
				c = 4.5543	Ga 2/3 1/2 1/2 Si 1/3 2/3 1/2	(18 18 18)	volume (test: *a* = 4.10-4.32; *a* = 4.26)
/EuGaSi/T12O/	EuGaSi		P6(3)mc	*a* = 4.1687 *c* = 8.3374	Eu 0 0 0 Ga 1/3 2/3 0.27 Si 1/3 2/3 0.73	Gamma (16 16 16)	shape, position,
/EuGaSi/T12S/	EuGaSi		P6(3)/mmc	*a* = 4.1687 *c* = 8.3374	Eu 0 0 0 Ga 1/3 2/3 0.25 Si 1/3 2/3 0.75	Gamma (16 16 16)	shape, position,
/EuGaSn/	EuGaSn		P6(3)/mmc	*a* = 4.5273 *c* = 18.067	Eu1 0 0 0 Eu2 0 0 1/4 Ga 2/3 1/3 0.1621 Sn 1/3 2/3 0.1168	Gamma (14 14 12)	shape, position,
/EuGaGe/a2/	EuGaGe		P6(3)/mmc	*a* = 4.2646 *c* = 18.041	Eu1 0 0 0 Eu2 0 0 1/4 Ga 2/3 1/3 0.1467 Ge 1/3 2/3 0.1142	Gamma (14 14 12)	shape, position, volume (test: *a* = 4.20-4.56; *a* = 4.39)
/EuGaGe/T24OS/	EuGaGe		P6(3)/mmc	*a* = 4.2646 *c* = 18.041	Eu1 0 0 0 Eu2 0 0 1/4 Ga 2/3 1/3 1/4 Sn 1/3 2/3 0.1/4	Gamma (14 14 12)	shape, position,

Appendix C: Single Crystal Structure of $Y_{0.82}Ce_{0.18}Mg_{4.07}$

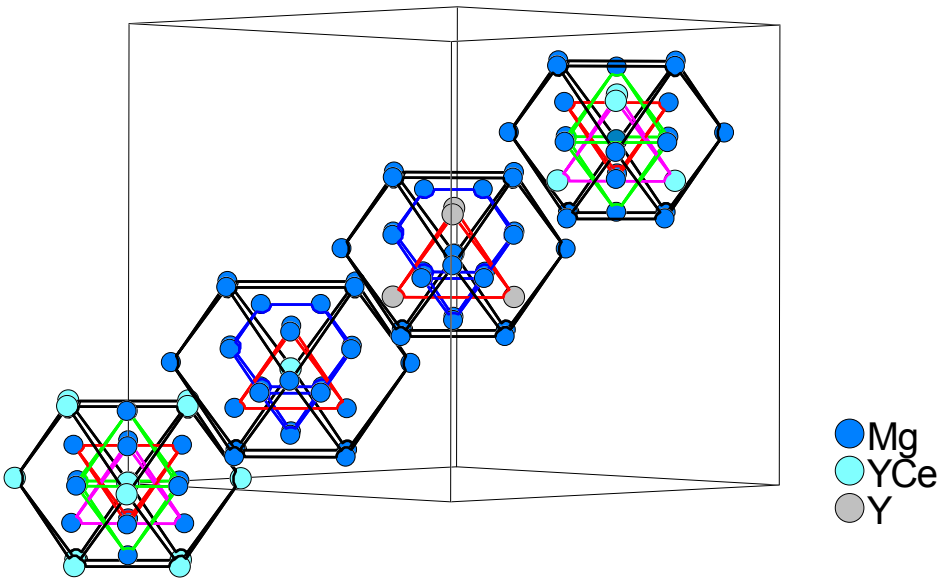

Table 1. Crystallographic Data of $Y_{0.82}Ce_{0.18}Mg_{4.07}$

Formula	$Y_{0.82}Ce_{0.18}Mg_{4.07}$ ($Y_{9.05}Ce_{1.95}Mg_{44.77}$)
Structure type	$GdMg_5$-type (defect type of $Sm_{11}Cd_{45}$)
Space Group	*F*-43*m* (no.216)
Lattice parameters (Å)	a = 22.443(2))
Volume (Å^3)	11303.7(1)
Z	88
Density calculated (g cm^{-3})	2.555
Theta range	1.57 to 28.29°
Index ranges	$-28 \le h \le 28$ $-29 \le k \le 29$ $-29 \le l \le 29$
Reflections collected	25038
Independent reflections	1425 [R_{init} = 0.1171]
Data/refined parameters	1425/74
GOF on F^2	1.038
Final R indices [$I > 2\sigma(I)$]	R1 = 0.0507, wR2 = 0.1040
R indices (all data)	R1 = 0.0688, wR2 = 0.1121
Largest diff. peak and hole (e$^-$/Å^3)	1.933 / –0.830

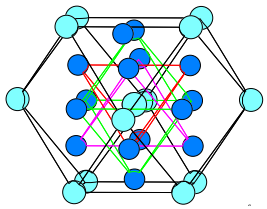

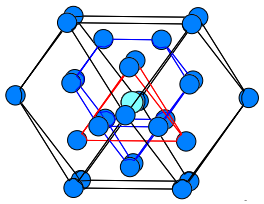

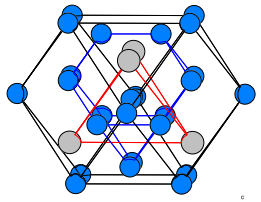

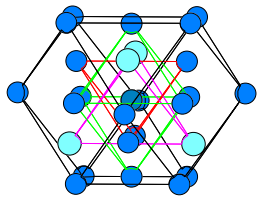

Table 2. Nested Polyhedra Unit sof $Y_{0.82}Ce_{0.18}Mg_{4.07}$

	atom	occupancy	*x*	*y*	*z*	*U* (eq)
***A* unit**						
A C	Y2/Ce2	0.42(3)/0.58(3)	0.25	0.25	0.75	0.018(1)
A IT	Mg5	0.89(4)	0.3336(3)	0.1664(3)	0.8336(3)	0.049(5)
A OT	Mg4		0.3368(2)	0.3368(2)	0.8368(2)	0.025(2)
A OH	Mg8	0.99(2)	0.25	0.0931(4)	0.75	0.039(3)
A CO	Y5/Ce5	0.84(1)/0.16(1)	0.2612(1)	0.0766(1)	0.9235(1)	0.018(1)
***B* Unit**						
B C	Y1/Ce1	0.86(3)/0.14(3)	0.5	0	0	0.010(1)
B TT	Mg9		0.3596(2)	0.9540(2)	0.9540(2)	0.027(1)
B T	Mg6		0.4139(2)	0.0861(2)	0.9139(2)	0.019(2)
B CO	Mg11		0.3161(2)	0.9872(2)	0.8161(2)	0.022(1)
***C* Unit**						
C C	Mg2		0.25	0.75	0.75	0.022(5)
C T	Y4		0.3430(1)	0.8430(1)	0.8430(1)	0.016(1)
C TT	Mg12		0.2952(1)	0.8908(2)	0.7048(1)	0.012(1)
C CO	Mg10		0.2380(2)	0.9223(2)	0.9223(2)	0.017(1)
***D* Unit**						
D C	Mg1		0	0	0	0.027(5)
D IT	Mg3		0.0803(3)	0.0803(3)	0.9197(3)	0.027(2)
D OT	Y3/Ce3	0.70(3)/0.30(3)	0.0900(1)	0.9100(1)	0.9100(1)	0.010(1)
D OH	Mg7		0.1576(4)	0	0	0.019(2)
D CO	Mg13		0.1654(2)	0.0152(3)	0.8346(2)	0.047(2)

Appendix D: Crystal structure of the $Y_{5-x}Mg_{24+x}$ Series

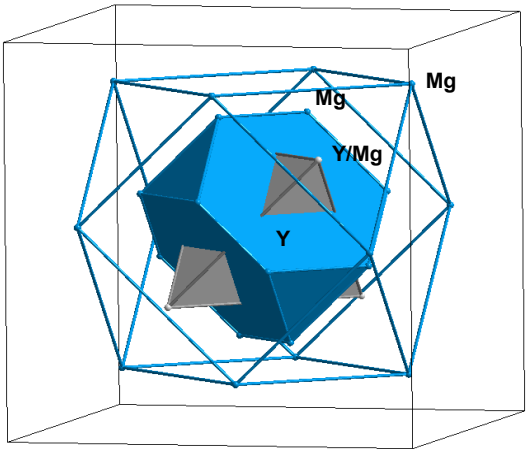

Table 1. Crystallographic data of $Y_{5-x}Mg_{24+x}$ (x = 0.18)

Formula	$Y_{3.82(2)}Mg_{25.18(2)}$
Structure type	α-Mg
Space Group	I-43m (no.217)
Lattice parameters (Å)	a = 11.253(1)
Volume (Å^3)	1425.0(2)
Z	2
Density calculated (g cm^{-3})	2.396
Theta range	2.56 to 27.79°
Index ranges	$-14 \le h \le 14$ $-14 \le k \le 14$ $-14 \le l \le 14$
Reflections collected	6268
Independent reflections	350 [R_{init} = 0.520]
Data/refined parameters	350/18
GOF on F^2	0.968
Final R indices [$I > 2\sigma(I)$]	R1 = 0.0164, wR2 = 0.0262
R indices (all data)	R1 = 0.0199, wR2 = 0.0266
Largest diff. peak and hole (e$^-$/Å^3)	0.243 / –0.165

Table 2. Atomic Coordinates and Equivalent Isotropic Displacement Parameters of $Y_{5-x}Mg_{24+x}$ (x = 0.18)

Atom	Wyck.	Occ.	x	y	z	U_{eq}
Y1	2a		0	0	0	0.013(1)
Y2/Mg1	8c	0.706(3)/0.293(3)	0.1867	0.1867	0.1867	0.015(1)
Mg2	24g		0.0906	0.0906	0.2805	0.019(1)
Mg3	24g		0.3572	0.3572	0.0351	0.022(1)

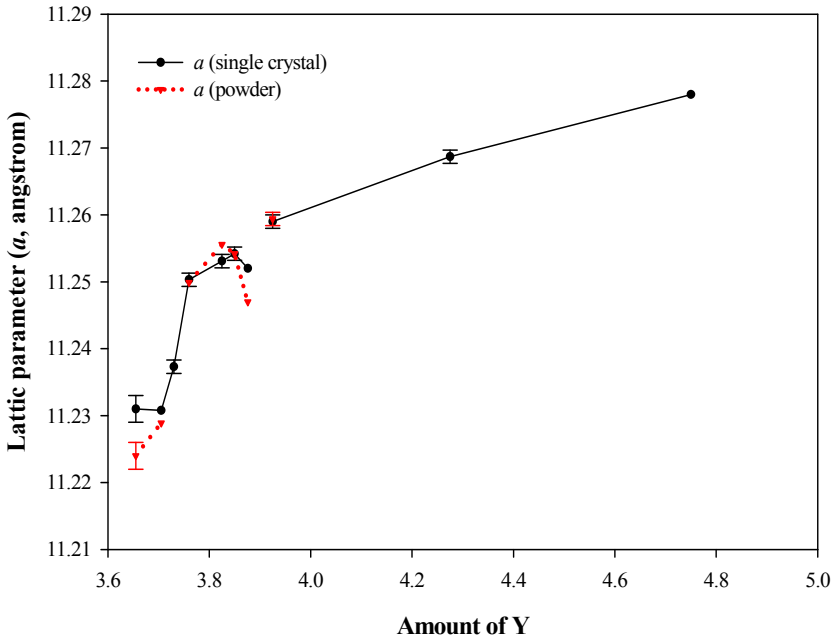

Figure 8. Lattice Parameter Changes as a Function of the Y amounts for the $Y_{5-x}Mg_{24+x}$ Series

Table 3. Lattice Parameters of the $Y_{5-x}Mg_{24+x}$ Series

Loaded	Refined (SXRD)	Lattice parameters	
		SXRD	PXRD
Y/Mg/In (5/35.2/2)	3.56(1)/25.44(1)	a = 11.231(2)	a = 11.224(2)
Y/Mg/Ga (5/36.5/1)	3.705 / 25.295	a = 11.231()	a = 11.229(0)
Y/Mg/Ga (5/23/1)	3.73 / 25.27	a = 11.237(1)	-----
Y/Mg/Ga (5/23/1)	3.76 / 25.24	a = 11.250(1)	a = 11.250(0)
Y/Mg (3.6/25.4)	3.88 / 25.12	a = 11.252(2)	a = 11.247(0)
Y/Mg (3.9/25.1)	-----	-----	a = 11.248(0)
Y/Mg (4.2/24.8)	-----	-----	a = 11.249(1)
Y/Mg (3.7/25.3)	3.82 / 25.18	a = 11.253(1)	a = 11.256(0)
Y/Mg/Ga (5/22/2)	3.85 / 25.15	a = 11.254(1)	a = 11.254(0)
Y/Mg (5/36.65)	3.93 / 25.07	a = 11.259(1)	a = 11.259(1)
Literature	*4.750 / 24.250*	*a = 11.278*	---

ACKNOWLEDGEMENTS

"We know that God is always at work for the good of everyone who loves him.
They are the ones God has chosen for his purpose,"

- Romans 8: 28

I want to express my sincere thanks to my advisor, Professor Gordon Miller for his patience, commitment, and encouragement to me and my graduate research. It has been my great pleasure to work with Gordie and learn more than I could have imagined. Especially, I thank him for giving me an opportunity to visit MPI-Dresden and harvest more than *just* fruitful academic results.

I want to thank many people who helped my learning and research at Iowa State University. Thanks to Dr. Warren Straszheim for EDXS measurements, Jim Anderegg for XPS measurements, Dr. Sergey Bud'ko for magnetization measurements, and Dr. Yaqiao Wu for TEM measurements.

I also want to thank people in MPI-Dresden. Thanks to Prof. Yuri Grin for the invitation to the prestigious institute and many advice for my research, Dr. Ulrich Burkhardt for XAS measurements, Dr. Walter Schnelle for magnetization measurements, Dr. Alexei Baranov for teaching me ELF calculations and his FPLO calculations, Dr. Frank Wagner and Dr. Miroslav Kohout for a helpful discussion for my computational calculation research.

I want acknowledge the current and former members of the Miller group for the valuable discussions about my research in the lab, and for the invaluable discussions about life and science during the group lunch. Thanks to Prof. Yurij Mozharivskyi, Dr. German Samolyuk, Dr. Mi-Kyung Han, Dr. Hynjin Ko, Dr. Sumohan Misra, Dr. Srinivasa Thimmaiah, Fei Wang and Jakoah Brgoch.

I thank the KCRC family for the faithful fellowship and many prayers to support and strengthen me throughout my precious time in Ames.

Finally, many thanks to my wife Hyun-Jung, for her endless love and encouragement, and to my parents, for their unconditional love, support and many prayers.